Molecular dynamics and photoionisation processes: from strong-fields to soft X-rays

Ruaridh Forbes

Thesis submitted for the Degree of

Doctor of Philosophy of

University College London

Department of Physics and Astronomy

University College London

December 18, 2018

I, Ruaridh Forbes, confirm that the work presented in this thesis is my own. Where information has been derived from other sources, I confirm that this has been indicated in the work.

Abstract

This thesis comprises of a set of time and energy-resolved photoelectron spectroscopy studies of polyatomic molecules exposed to radiation ranging from the IR to soft X-ray region of the spectrum. Chapter 1 provides an introduction to molecular photochemistry, wavepacket dynamics and ionisation mechanism ranging from weak single photon ionisation to strong-field ionisation in intense laser fields. In Chapter 2 an experiment to probe excited state wavepacket dynamics in the molecule NO_2 is presented. This experiment is based on using the channel-resolved above-threshold ionisation technique as a multi-dimensional probe of non-adiabatic dynamics in polayatomics molecules. The complex roles of one-photon excitation, multiphoton excitation to higher-lying neutral states, multi-channel neutral and ionic dissociation are examined and complications of using strong-fields to probe photochemistry are outlined. Chapter 3 deals with a VUV/UV time-resolved photoelectron velocity map imaging (VMI) study of Rydberg-valence mixing in high-lying excited states of acetone (CH_3-CO-CH_3). Details are provided of the implementation of a high-flux femtosecond VUV source based on non-collinear four-wave mixing. The VMI results show evidence of non-adiabatic evolution from the initially prepared $3d_{yz}$ electronic state to the lower-lying 3p/3s states and subsequent relaxation of these Rydberg states to the $\pi\pi^*$ electronic state on a few hundred femtosecond timescale. Chapters 4 and 5 deal with energy-resolved synchrotron radiation studies of the core-level ionisation, excitation and Auger decay in CH_3I. Detailed assignments and analysis of the angular distributions connected with the I 4s, 4p and 3d orbitals are provided. These studies are a necessary precursor to aid in the interpretation of time-resolved data obtained using recently developed labora-

tory and facility based soft X-ray sources. Finally, Chapter 6 provides a summary of the different opportunities offered by performing time-resolved photoelectron spectroscopy in various wavelength regimes and provides an outlook for future work utilising novel ultrafast light sources.

This thesis is based on the following publications:

Chapter 2

R. Forbes, A. E. Boguslavskiy, I. Wilkinson, J. G. Underwood and A. Stolow, *"Excited state wavepacket dynamics in NO_2 probed by strong-field ionization"*, J. Chem. Phys. 147, 054305 (2017).

Chapter 3

R. Forbes, M. A. B. Larsen, S. P. Neville, A. E. Boguslavskiy, I. Wilkinson, T. I. Sølling, R. Lausten, M. S. Schuurman and A. Stolow *"Femtosecond photoelectron imaging of Rydberg-valence coupling in acetone"*, in preparation.

Chapter 4

R. Forbes, A. De Fanis, C. Bomme, D. Rolles, S. T. Pratt, I. Powis, N. A. Besley, M. Simon, S. Nandi, A. R. Milosavljević, C. Nicolas, J. D. Bozek, J. G. Underwood, and D.M.P. Holland, *"Photoionization of the iodine 3d, 4s and 4p orbitals in methyl iodide"*, Accepted to J. Chem. Phys, 149, (2018).

Chapter 4

R. Forbes, A. De Fanis, C. Bomme, D. Rolles, S. T. Pratt, I. Powis, N. A. Besley, S. Nandi, A. R. Milosavljević, C. Nicolas, J. D. Bozek, J. G. Underwood, and D.M.P. Holland, *"Auger electron angular distributions following excitation or ionization of the I 3d level in methyl iodide"*, J. Chem. Phys, 149, 094304, (2018).

In addition, contributions were made to the following publications:

R. Forbes, V. Makhija, K. Veyrinas, A. Stolow, J. W. L. Lee, M. Burt, M. Brouard, C. Vallance, I. Wilkinson, R. Lausten, and P. Hockett, *"Time-resolved multi-mass ion imaging: Femtosecond UV-VUV pump-probe spectroscopy with the PImMS camera"*, J. Chem. Phys. 147, 013911 (2017).

R. Forbes, V. Makhija, J. G. Underwood, A. Stolow, I. Wilkinson, P. Hockett and R. Lausten *"Quantum Beat Photoelectron Imaging Spectroscopy of Xe in the VUV"*, Phys. Rev. A. 97, 063417, (2018).

M. R. Coates, M. A. B. Larsen, R. Forbes, S. P. Neville, A. E. Boguslavskiy, I. Wilkinson, T. I. Sølling, R. Lausten, A. Stolow and M. S. Schuurman *"Vacuum Ultraviolet Excited State Dynamics of the smallest ring, Cyclopropane: II. Time-Resolved Photoelectron Spectroscopy and Ab Initio Dynamics"*, Accepted to J. Chem. Phys., 149 (2018).

Acknowledgements

I would like to express my sincere thanks to the following people who made this PhD possible and an unforgettable experience. My supervisors Dr. Jonathan Underwood and Prof. Albert Stolow for giving me the opportunity to purse a PhD in experimental atomic, molecular and optical physics and for their supervision. I would like to thank Jonathan for his patience, support and pragmatism. I am particularly grateful to him for teaching me the following: (i) taking a step back when you cannot "see the wood for the trees" and; (ii) about the importance of not "shifting gears" between projects too often. Jonathan, despite most of our contact being via email, you taught me more than you are likely aware of. Albert, I am indebted to you for all your guidance and mentorship across the past 4 years. You have definitely had a massive input on how I think about light-matter interactions. Thank you for also helping to facilitate my stay in Ottawa and for being so welcoming and hospitable. I also thank my secondary supervisor Prof. Peter Barker for becoming my primary UCL supervisor after Jonathan's departure from academia and for reading this thesis.

Despite the unifying theme of photoionisation in this thesis, each chapter has a specific group of people who deserve thanks, therefore, chapter specific acknowledgments are given below. I would however like to express my gratitude to Dr. Paul Hockett for kindly and carefully proof reading this thesis. Much of the VUV work which did not make it into this thesis was carried out in close collaboration with Dr. Hockett as well as Dr. Varun Makhija, both of whom were excellent collaborators and became good friends. Thanks also go to the whole molecular photonics group at the National Research Council in Ottawa for creating a good working environ-

ment. Particular thanks in this regard should go to my office mate and friend Dr. Andrey Boguslavskiy.

Outside the world of physics, I would like to thank all my friends, particularly for their continued friendship despite moving across the Atlantic. Special thanks go to Tom, Richard, Jenny and Caitlin for being present whenever I needed them. I would like to thank my parents for their help and support throughout my whole university career, and of course life in general. Lastly, I would to thank Renaude for her support and encouragement across the last third of my PhD, I am excited for what is to come with our move to California.

Strong-field ionisation of NO_2

The experimental work presented in this chapter on nitrogen dioxide was undertaken under the guidance and help of Drs. Iain Wilkinson and Andrey Boguslavskiy. Andrey I thank you for kindly processing the experimental data through your covariance code and Iain for multiple phone call discussions since your move to Berlin. The optical set-up utilised in this experiment was constructed with significant advice and input from Dr. Rune Lausten, to whom I am grateful for all the help and training you provided me during my first real experience of ultrafast laser physics.

Femtosecond VUV and Rydberg valence coupling in acetone

The construction and characterisation of the VUV femtosecond laser source outlined in this chapter was done with the help and guidance of Dr. Rune Lausten. Rune I thank you for all the advice and technical help you have given me during the various reiterations of the VUV box design and implementation. Without this everything would have taken a great deal longer to implement! The data acquisition and preliminarily analysis codes used for the Ottawa electron VMI were written by Dr. Andrey Boguslavskiy to whom I am very grateful for making these available. Thanks also go to Andrey for leading the effort to identify and minimise contributions associated with acetone clusters.

These experiments, as well as many others, were conducted in collaboration with Mr Martin Larsen a visitor to the NRC group from University of Copenhagen. I am not sure both Martin and myself want to recount the number of times we left NRC at 2-6am. It was, however, always exciting to see a new dataset!

CH_3I core-level ionisation

By their very nature and 24 hour operation large scale user facility beamtimes typically involve somewhat larger group of people compared to table top/in house experiments. With this in mind I would like to give thanks Drs. Alberto De Fanis, Cédric Bomme, David Holland and Jonathan Underwood who all put in long hours with me during our 5 day beamtime at synchrotron SOLEIL to collect the data presented in Chapters 4 and 5. In addition, I am grateful to Profs. Ivan Powis and Nick Besley for providing theoretical support for this project and for making their data available for inclusion within this thesis. Thanks also go to the SOLEIL staff for running the facility and providing beamtime under Project No. 20150786. Finally, I would like to give particular thanks to David for supervising large parts of this project after Jonathan's departure from academic science. I am extremely grateful for the discussion I had with David across the past few years, which have undoubtedly shaped the way I view VUV photoionisation.

Auger electron angular distributions following excitation or ionisation of the I 3d level in CH_3I

The acknowledgements associated with this chapter are similar to those outlined at the start of Chapter 4 but with a few noteworthy exceptions. Particular thanks goes to Dr Alberto De Fanis for his advice on how to treat and fit the Auger electron angular distributions. I am grateful to Profs. Daniel Rolles and Artem Rudenko for providing me with unpublished LCLS data on CH_3I used to generate Fig. 6.1 in the thesis conclusions and for numerous discussions I had with them both across my PhD. Finally, I am grateful to Dr. David Holland for his help in supervising this project.

Impact Statement

The research included in this PhD thesis provides a detailed analysis of the various photoionisation mechanisms applied to the study of polyatomic molecules. This research is particularly timely as the work involves the use of a variety of novel femtosecond laser sources and high-resolution synchrotron measurements to investigate photochemical dynamics. With the on-going development and construction of X-ray Free Electron Lasers (FELs) around the globe the previously quite disparate fields of ultrafast lasers and synchrotron radiation physics are becoming closely linked. Many of the ideas outlined in this thesis will be of interest to members of both these communities.

The laboratory results shown on NO_2 and acetone (CH_3-CO-CH_3) are of interest to a large number of research groups at interaction of chemical and atomic, molecular and optical (AMO) physics. In particular the results on strong-field ionisation of NO_2, have received considerable attention and resulted in several invited talks. These included talks at the EU-COST Action XUV/X-ray light and fast ions for ultrafast chemistry meeting in 2016 and the Photon Science Seminar Series at the Stanford Linear Accelerator Centre (SLAC) in 2017. The detailed description of the design of the femtosecond VUV source provides a useful resource to researchers interested in accessing previously challenging wavelength for conventional solid state laser technology. This could, for example, have implications outside AMO physics and be utilised in angle-resolved photoemission spectroscopy (ARPES) of solid state samples.

It is anticipated the energy-resolved synchrotron radiation results on core-shell photoionisation and Auger decay in methyl iodide (CH_3I) will directly feed into on-going analysis of unpublished FEL data recorded at the Linac Coherent Light Source (LCLS) at Stanford University. These results will also serve as a helpful basis for future photoelectron spectroscopy experiments utilising high repitiation rate seeded X-ray FELs, which have, to date, been challenging.

Contents

1 Introduction **22**

1.1 Pump probe methodology 27

1.2 The Born-Oppenheimer approximation 30

1.3 Franck-Condon principle 31

1.4 Photoionisation dynamics 32

1.5 The role of vibration in photoionisation 34

1.6 Photoionisation with X-rays 36

1.6.1 Relaxation of core ionised systems: Auger decay 38

1.7 Strong-field ionisation 43

1.7.1 Multiple continua in strong-field ionisation 48

1.8 Photoelectron angular distributions 51

1.9 Time-resolved photoelectron spectroscopy (TRPES) 54

1.9.1 Probing non-adiabatic dynamics 55

1.9.2 Photoelectron kinetic energies in TRPES 57

1.10 Outline of the thesis 58

2 Strong-field ionisation of NO_2 **59**

2.1 Introduction 59

2.2 Experimental set-up 63

2.3 Data analysis 68

2.4 Intensity calibration of the experimental data 70

2.5 Experimental results 71

2.6 Discussion 84

2.6.1 Single photon excitation and relaxation dynamics 84
2.6.2 The role of multiphoton pump excitation and relaxation dynamics 91
2.7 Conclusions 95

3 Femtosecond VUV and Rydberg valence coupling in acetone 98
3.1 Introduction 98
3.2 Experimental set-up 104
3.2.1 VUV generation and optical setup 104
3.2.2 Velocity map imaging (VMI) spectrometer 118
3.2.3 Data acquisition and image processing 119
3.2.4 VMI energy calibration 121
3.2.5 VUV energy and time-resolution calibration 121
3.2.6 Fitting methods 126
3.3 Acetone experimental results 128
3.3.1 Elimination of cluster signals 128
3.3.2 VUV absorption spectrum 129
3.3.3 Time-resolved photoelectron spectra 132
3.4 Discussion 143
3.5 Conclusion 150

4 CH_3I core-level ionisation 153
4.1 Introduction 153
4.2 Experimental apparatus and data analysis 156
4.2.1 Experimental setup 156
4.2.2 The effect of post collision interaction on the I 3d photoelectron peak shape 162
4.3 Theoretical techniques 164
4.3.1 X-ray absorption spectrum 164
4.3.2 Photoionisation cross section 165
4.4 Results and discussion 166

4.4.1 Ion yield, x-ray absorption and photoionisation cross section spectra . . . 166
4.4.2 Photoelectron spectra . . . 172
4.5 Conclusions . . . 190

5 Auger electron angular distributions following excitation or ionisation of the I 3d level in CH_3I 192
5.1 Introduction . . . 192
5.2 Experimental apparatus and procedure . . . 199
5.2.1 Experimental setup . . . 199
5.2.2 Auger electron peak fitting procedure . . . 201
5.3 Results and discussion . . . 203
5.3.1 Overview . . . 203
5.3.2 Auger electron band structure . . . 204
5.3.3 Auger electron angular distributions . . . 221
5.4 Conclusions . . . 229

6 General conclusions and outlook 231
6.1 Strong-field ionisation of NO_2 . . . 231
6.2 Femtosecond VUV and Rydberg valence coupling in acetone . . . 233
6.3 CH_3I core-level ionisation . . . 236
6.4 Auger electron angular distributions for the I 3d level in CH_3I . . . 238
6.5 Concluding remarks . . . 240

Appendices 241

A Fitting of the Auger spectra in CH_3I 241
A.1 Fitting of the non-resonant Auger spectra . . . 241
A.2 Fitting of the resonant Auger spectra . . . 244

Bibliography 247

List of Figures

1.1 Schematic diagram of the creation, evolution and detection of an excited state wavepacket. 29

1.2 The valence photoelectron spectrum of methyl iodide (CH_3I) recorded at $\hbar\omega$ = 60 eV. 34

1.3 Schematic diagrams of core-level photoionisation and associated satellite processes. 37

1.4 The I 4d shake-up/shake-off spectra of CH_3I recorded at $\hbar\omega$ = 120eV. 39

1.5 Schematic diagrams relaxation mechanism that can occur after core-level photoionisation. 40

1.6 Electron spectra of the major Auger decay pathways following 3d photoionisation of Xe. 42

1.7 Schematic diagrams of various strong-field ionisation processes. . . 43

1.8 Above-threshold ionisation photoelectron spectra for (a) Xe/Ar and (b) 1,3-butadiene 48

1.9 Fragment correlated above-threshold ionisation photoelectron spectra for 1,3-butadiene 51

1.10 Angle-resolved above-threshold ionisation photoelectron spectra of Xe 53

1.11 Schematic diagram showing TRPES applied to disentangling electronic and vibrational dynamics in an excited polyatomic molecule. 56

2.1 Potential energy surfaces as a function of ONO bending angle for the important electronic states of NO_2 and $NO_2{}^+$ involved in single-photon excitation and subsequent strong-field probing at 798 nm. . . 61

2.2 Schematic overview of the optical setup used in strong-field ionisation experiments on NO_2. 64

2.3 Sample spectral for the 399 nm and 798 nm pump and probe pulses. 65

2.4 Schematic diagram of the PEPICO used in strong-field ionisation experiments on NO_2. 67

2.5 Probe alone ATI photoelectron spectra of (a) NO_2 and (b) H_2O as a function of laser pulse intensity. 73

2.6 NO_2 mass spectra for various pump probe time delays. 74

2.7 Time-resolved ion yield spectra for the NO_2^+, NO^+ and O^+ channels 75

2.8 Time and channel-resolved above-threshold ionisation spectra correlated with NO_2^+, NO^+ and O^+ ions. 77

2.9 Pump laser intensity dependence of the NO_2^+, NO^+ and O^+ time-resolved ion yield spectra. 78

2.10 Pump laser intensity dependence of the NO_2^+, NO^+ and O^+ time-resolved linear dichroism. 79

2.11 TRCRATI spectra associated with NO^+ (left column) and O^+ (right column) channels as a function of pump laser intensity 80

2.12 Probe laser intensity dependence of the NO_2^+, NO^+ and O^+ time-resolved ion yield spectra. 82

2.13 Probe laser intensity dependence of the NO_2^+, NO^+ and O^+ time-resolved channel-resolved ATI spectra. 83

2.14 Schematic diagram of the ground state equilibrium structure of NO_2 with the molecular axes labeled in C_{2v} symmetry 84

2.15 Energy levels relevant for possible multiphoton pump excitation pathways in neutral NO_2. 92

3.1 Schematic overview of the optical setup used VUV/UV pump-probe experiments on acetone. 105

3.2 Sample spectral for the 266.63 nm and 798 nm pulses utilised for generation of femtosecond VUV pulses. 106

3.3 Energy and phase matching diagrams for the non-collinear four-wave difference frequency mixing process used to generate femtosecond VUV pulses. 107

3.4 Solid works rendered drawing of the vacuum chamber utilised for generation of the femtosecond VUV pulses. 108

3.5 Pressure dependence of the 5ω flux recorded with a VUV monochromator and photodiode. 110

3.6 Sample spectral for 5ω pulses generated using non-collinear four-wave difference frequency mixing 111

3.7 Sample spectral for 3ω pulses generated with different thicknesses of BBO. 114

3.8 Autocorrelation traces for the 3ω probe pulses after adjustment of the CaF_2 prism compressor for the shortest UV pulse. 115

3.9 Schematic overview of the optical setup used to generate the 4th harmonic of Ti:sapphire 116

3.10 Sample spectral for 4ω pulses used in the VUV experiments. 117

3.11 Sample raw and inverted VMI photoelectron images for multiphoton ionisation of Xe. 120

3.12 Radial velocity and photoelectron kinetic energy distributions for multiphoton ionisation of Xe. 122

3.13 Time-integrated photoelectron spectra for Xe produced via 5ω+3ω photoionisation. 123

3.14 TRPES for Xe produced via 5ω+3ω photoionisation. 124

3.15 Mass spectrum of acetone recorded as a function of Even-Lavie pulse valve backing pressure for $1+1'$ photoionisation with 7.78 eV and 4.65 eV pulses. The spectra was recorded at Δt = 120 fs, which corresponded to the position of maximal signal strength. 130

3.16 High resolution VUV photoabsorption spectrum of acetone in the 7.3-8.2 eV energy region recorded using synchrotron radiation . . . 132

3.17 Time-resolved photoelectron spectra for acetone pumped with 7.78 eV photons and subsequently probed at 4.65 eV. 133

3.18 One dimensional cuts of the acetone time-resolved photoelectron spectra at various positive pump-probe time-delays 134

3.19 Transient photoelectron anisotropy (β) parameters for various features photoelectron peaks observed in Fig. 3.17. 135

3.20 Fits, residuals and decay associated spectra for acetone probed with 4.65 eV light. 137

3.21 Time-resolved photoelectron spectra for acetone pumped with 7.77 eV photons and subsequently probed at 6.20 eV. 139

3.22 Transient photoelectron yields for various features photoelectron peaks observed in Fig. 3.21. 140

3.23 Fits, residuals and decay associated spectra for acetone probed with 6.20 eV light. 141

4.1 Calibration of the synchrotron photon energy scale using established transition energies of Xe and O_2 159

4.2 Angular distribution calibration of the SCIENTA electron spectrometer using Xe 3d ionisation 161

4.3 CH_3I Experimental total ion yield and theoretical X-ray absorption spectra in the viscinity of the I $3d_{5/2}$ and I $3d_{3/2}$ ionisation thresholds 166

4.4 Experimental total ion yield and theoretical X-ray absorption spectra in the I $3d_{5/2}$ pre-edge region. Plots of the valance and Rydberg orbitals associated with excitation from the I $3d_{5/2}$ orbital 167

4.5 (a) Orbital plots of state involved in transition that give rise to the continuum oscillator strength. (b) Theoretical above-threshold X-ray absorption spectra, calculated using TDDFT, as a function of employed basis set. 171

4.6 Photoionisation cross section for the I 3d levels in CH_3I, calculated using the CMS-Xα 173

4.7 Angularly-resolved CH_3I core-level electron spectra recorded at (a) 614.0 eV and (b) 666.2 eV, respectively. 174

4.8 (a) Angularly-resolved photoelectron spectrum of CH_3I, recorded at $\hbar\omega$ = 614.0 eV, in the binding energy range encompassing structure due to the I 4s and I 4p orbitals. (b) The corresponding photoelectron anisotropy parameter. 176

4.9 A Voigt profile fit to the photoelectron band due to I 4s photoionisation. 178

4.10 Angularly-resolved photoelectron spectra for the I $3d_{5/2}$ and I $3d_{3/2}$ levels recorded at a photon energy of 665.6 eV. 180

4.11 CH_3I 3d photoline fit parameters as a function of photon energy. . . 181

4.12 Photoelectron anisotropy parameters for the I $3d_{5/2}$ and I $3d_{3/2}$ levels in CH_3I 183

4.13 The I $3d_{5/2}$:I $3d_{3/2}$ intensity branching ratio. 184

4.14 Angularly-resolved photoelectron spectra of CH_3I, recorded at $\hbar\omega$ = 740 eV, in the binding energy range encompassing structure due to the I $3d_{5/2,3/2}$ main-lines and the associated shake-up/shake-off satellites. 186

4.15 The $M_4N_{45}N_{45}$ and $M_5N_{45}N_{45}$ Auger electron yields of CH_3I recorded with horizontally plane polarised radiation. 187

4.16 Auger electron spectra for the (a) $M_4N_{45}N_{45}$ and (b) $M_5N_{45}N_{45}$ transitions as a function of photon energy. 189

5.1 Xe $M_{45}N_{45}N_{45}$ Auger spectra recorded at $\hbar\omega$ = 709 eV. 200

5.2 CH_3I Auger electron spectrum spanning all transitions associated with the $3d_{5/2}^{-1}$ and $3d_{5/2}^{-1}$ core-holes. 204

5.4 CH_3I $M_{45}N_{45}N_{45}$ angularly-resolved Auger electron spectra recorded at $\hbar\omega$ = 666.2 eV. 206

5.5 Angularly-resolved resonant Auger spectra recorded at photon energies $\hbar\omega$ = 620.4 and 632.0 eV 207

5.6 Angularly-resolved Auger spectra for the $M_{45}N_{45}O_{23}$ and $M_{45}N_{45}V$ transitions recorded at photon energies $\hbar\omega$ = 666.2 and 646.0 eV 211

5.7 Angularly-resolved Auger spectra and associated β_{Auger} parameters for the $M_{45}N_{23}N_{45}$ transitions 214

5.8 Angularly-resolved Auger spectra and associated β_{Auger} parameters for the $M_{45}N_1N_{45}$ transitions 216

5.9 Branching ratios for the $M_4N_{45}N_{45}$:$M_5N_{45}N_{45}$, $M_4N_{45}O_{23}$:$M_5N_{45}O_{23}$ Auger transitions compared with the I $3d_{5/2}$:$3d_{3/2}$ photoelectrons. . 218

5.10 The calculated, normalised, angular distribution parameter (β_{ion}) characterising the spatial distribution of molecular axes in CH_3I in the I $3d^{-1}$ ionised state. 222

5.11 Auger electron anisotropy parameters, β_{Auger}, extracted from fits to the $M_{45}N_{45}N_{45}$ transitions in CH_3I. 227

5.12 β_{Auger} parameters extracted from fits to the $M_{45}N_{45}O_{23}$ Auger transitions in CH_3I. 228

6.1 Time-resolved Auger spectra of CH_3I recorded at the Linac Coherent Light Source (LCLS) 238

List of Tables

2.1 Estimated and calibrated 399 and 798 nm pump and probe intensities, respectively. The values were obtained using the procedure outlined in Sec. 2.4. 71

3.1 Adiabatic excitation energies of the valence and Rydberg states of acetone of interest in this work. Experimental ionisation potentials for the D_0 and D_1 channels are also shown. 131

3.2 Summary of the extracted 2D global fit parameters extracted from the time-resolved spectra presented in Figs. 3.17 (4.65 eV - 3ω) and 3.21 (6.2 eV - 4ω). 142

4.1 Excitation energies and proposed assignments for the structure in the CH_3I $3d_{5/2,3/2}$ pre-edge region. 170

4.2 Energies and assignments of the observed transitions in the electron spectrum of CH_3I shown in Fig. 4.7. Explanation of the nomenclature for the Auger transition labeling is given in Sec. 1.6.1. 175

5.1 Experimental Auger electron kinetic energies and final state assignments for the Xe $M_{45}N_{45}N_{45}$ transitions. 201

5.2 Experimental Auger electron kinetic energies and intrinsic anisotropy parameters for the I $M_{45}N_{45}N_{45}$ transitions in CH_3I, and calculated intrinsic anisotropy parameters for the $M_{45}N_{45}N_{45}$ transitions in Xe. 209

5.3 Experimental Auger electron kinetic energies, β_{Auger} parameters and intrinsic anisotropy parameters (α_2) for the I $M_{45}N_{45}N_{45}$ transitions in CH_3I following resonant excitation at 620.4 eV ($3d_{5/2} \rightarrow \sigma^*$) or 632.0 eV ($3d_{3/2} \rightarrow \sigma^*$) 210

5.4 Auger electron kinetic energies for the iodine $M_{45}N_{45}O_{23}$, $M_{45}N_{23}N_{45}$ and $M_{45}N_1N_{45}$ transitions in CH_3I 213

5.5 Theoretical orbital ionisation energies for I 3d ionised and I 3d core excited states ($3d^{-1}\sigma^*$) in CH_3I 220

Chapter 1

Introduction

In general the dynamics of photoexcited polyatomic molecules involve a complex redistribution of both electronic and nuclear energy. Typically these degrees of freedom are coupled and this coupling gives rise to a variety of radiationless transitions, such as internal conversion, intersystem crossing, isomerisation, proton and electron transfer [1–4]. Non-radiative processes often occur in regions of configuration space where electronic states lie together in energy and are particularly prominent when multiple electronic states cross each other. These crossings, often termed conical intersections, allow population to be transferred from a single or manifold of electronic state(s) to another. This crossing typically takes place on a femtosecond (1 fs = 10^{-15} s) timescale and therefore provides a very efficient route for non-radiative decay pathways to happen. The above processes play key roles in the primary steps in the photochemistry of almost all polyatomic systems as well as being critical in photobiological processes such as vision and photosynthesis [5–8].

Conical intersections are an example of a situation where charge and energy flow become strongly coupled. This coupling is described as a breakdown of the Born-Oppenheimer Approximation (BOA), which is an adiabatic separation of the electronic and nuclear degrees of freedom. The BOA is appealing to use as it allows the construction of a potential energy surface for a particular electronic state, which can then be used to describe both the molecular structure and the nuclear trajectories, thus permitting the construction of a mechanistic view of molecular dynamics. Spectroscopically, the non-adiabatic coupling of electronic and nuclear degrees of

freedom results in complex broadened absorption spectra due to a large density of vibrational states, which in turn results in large variations of transition dipole moment as a function of nuclear coordinate. A general treatment of the breakdown of the BOA remains a huge challenge in molecular physics as does the experimental effort in the energy/frequency domain to study these process [9–11]. Complementary time-resolved methods, mainly based on ultrafast laser technology, have been developed over the past few decades [12–14].

Ultrafast time-resolved methods, which relate to a substantial portion of the work presented in this thesis, can be considered as the direct successor of flash photolysis pioneered by Norrish and Porter in the 1950s and subsequently resulted in a Noble Prize in Chemistry in 1967. In the original experiments performed by Norrish and Porter, millisecond bursts of light produced from discharge lamps were used to trigger photochemical reactions, the ensuing dynamics of the reaction were then captured by taking "photographs" of the absorption of the sample at different time delays after excitation. This was achieved by exposing the sample to a second flash, comprising of a continuous spectrum of white light, the transmitted component was then dispersed by a grating before being recorded by photoplates [15, 16]. The above represents a intuitive and useful picture of any time-resolved measurement with the dynamics being incited by a "pump" and at a later time delay observed with a "probe". Both the achievable time resolution and experimental capabilities increased significantly in the early 1990s with the advent of femtosecond wavelength tunable laser systems, which allowed for the investigation of fundamental vibrational and dissociation dynamics in molecular systems [17]. Subsequent work to develop ultrashort pulses, in the vacuum ultraviolet (VUV) and soft X-ray regions of the spectrum also resulted in the generation of attosecond (1 as = 10^{-18} s) pulses, which currently are at the forefront of achievable time-resolution in a time-resolved measurement [18].

The information content obtainable from a time-resolved measurement is intimately linked to the particular probe scheme used, as well as the nature of the final state of the system. A variety of optical probe schemes have been considered,

which include transient absorption, non-linear wave mixing, laser-induced fluorescence, resonant enhanced multiphoton ionisation (REMPI). However, the above are somewhat limited by the constraints that the probe light has to be resonant with an electronic transition in the system being studied and the transition has to obey strict angular momentum and symmetry selection rules. An alternative probe scheme that overcomes these limitations, and is utilised for the majority of the work presented in this thesis, is photoionisation spectroscopy. In a photoionisation experiment the selection rules are relaxed due to the fact that the outgoing photoelectron can adopt a range of symmetries. Hence, in a photoionisation experiment there are no forbidden transitions/optically dark states. In particular, time-resolved photoelectron spectroscopy (TRPES) is well suited for the study of non-adiabatic dynamics in molecules due to the sensitivity of ionisation to both electronic and vibrational dynamics [13, 14, 19, 20]. Aside from the above a number of additional advantages are offered by TRPES as a technique:

- Charge particle detection is extremely sensitive and detailed information can be obtained through analysing an outgoing photoelectrons kinetic energy and angular distribution [21].

- Detection of the ion provides mass information relating to a particular photoelectron spectrum [22, 23].

- Higher order (multiphoton) processes are easily identifiable in the photoelectron spectra, compared to other energy integrated measurements.

- Photoelectron-photoion coincidence (PEPICO) measurements can allow for studies of the scalar and vector correlations in photodissociation [24] as well as the effect of differently sized clusters on ionisation [25].

- Combing photoelectron angular distributions with laser induced alignment methods allows molecular frame properties to be studied [26–28].

The combination of femtosecond laser technology and photoelectron spectroscopy therefore provides a means to study ultrafast non-adiabatic dynamics and has been

applied to study a large number of processes, including internal conversion [29–33], intersystem crossing [32, 34, 35] and photodissociation [36–40].

Although TRPES has arguably emerged as one of the gold standard techniques, for the investigation of ultrafast non-adiabatic dynamics in neutral excited states in polyatomic molecules, novel probe techniques are always being developed. This is in part due to the research field being comprised of a mix of groups focusing of laser/accelerator development and those utilising this technology to address questions in atomic, molecular or solid state systems. These new probe techniques can very roughly be divided into a few categories:

- **High intensity** - The first set is based on the fact that ultrafast lasers provide, as well as short pulse duration, high intensity pulses, which have allowed the application of strong electric fields to matter, opening up a new regime of non-perturbative light-matter interactions [41]. Investigation of these non-perturbative processes led to the discovery of phenomena of above-threshold ionisation (ATI) [42–44], high-harmonic generation (HHG) [45, 46] and recollision/scattering [47] processes, such as laser induced electron diffraction (LIED) [48]. These process all occur within a single laser optical cycle and hence, when applied as a probe technique, offers potentially high temporal resolution. A few noteworthy, but by no means exhaustive, examples of these techniques applied to time-resolved molecular dynamics include: the work from Marangos and co-workers who applied high-harmonic spectroscopy to track nuclear dynamics in CH_4 on a subfemtosecond timescale [49], high-harmonic spectroscopy applied to photodissociation dynamics in Br_2 by Wörner *et al.* [50, 51] and laser induced electron diffraction work on bond elongation in N_2/O_2 [52] and bond breakage in di-ionised acetylene [53]. The latter method LIED also falls into the next category of structure.

- **Nuclear frame structure** - The development of high flux ultrafast X-ray [54, 55] and electron [56–58] sources has opened up the possibility performing diffraction experiments in a time-resolved manner, which allows structural

information to be extracted during photochemical reactions [59–62]. These techniques offer complementary information to those extractable via TRPES in the sense that they are uniquely sensitive to the evolution of the nuclear degrees of freedom. A second promising avenue is to use Coulomb explosion imaging [63] as a method by which to determine molecular structure [64, 65]. This technique has recently been applied in both laser [66] and FEL [67, 68] based experiments to track processes like isomerisation in ionised acetylene and to track photodissociation dynamics in halomethanes [69, 70] and halobenzenes [70].

- **Site specificity** - The final category refers to the probe processes being sensitive to the dynamics occurring at a particular atomic constituent of a molecular system. Access to this information has been made achievable by the development of tabletop soft X-ray [71–74], as well as X-ray free-electron lasers (FEL) sources [54, 55], with photon energies reaching core level binding energies. Some notable applications of these sources to molecular dynamics include the work from Leone and co-workers on tracking ring-opening dynamics in 1,3-cyclohexadiene [75] using transient X-ray absorption spectroscopy at the Carbon K-edge. The FEL investigation by Erk *et al.* on imaging charge transfer in dissociating CH_3I [76] and the hetero-site-specific X-ray pump-probe spectroscopy work of Southworth and co-workers on tracking fragmentation dynamics in XeF_2 [77].

Contained within the subsequent chapters of this thesis are a mixture of both time-resolved and energy/frequency-resolved studies which exploit different photoionisation mechanisms to study excited state and photoionisation dynamics, respectively. The latter energy-resolved ground state spectroscopic studies constitute an important precursor to any time-resolved measurement. The remainder of this first chapter provides introduction to excited state dynamics in isolated molecules and provides a framework by which the time-resolved measurements presented subsequently can be interpreted. A description of how pump-probe experiments can be viewed within a wavepacket picture is presented. This is followed by discussions

of the commonly evoked approximations in such experiments, namely, the Born-Oppenheimer approximation, the molecular orbital or Koopmans' picture of photoionisation, and the Franck-Condon principle. The chapter is then concluded by giving a overview of the different ionisation mechanisms that can occur following interaction with a molecular systems with different wavelengths and intensities of electromagnetic radiation. A brief discussion of their application in time-resolved experiments is also given.

1.1 Pump probe methodology

In general, as alluded to in the introduction, any time-resolved measurement can be viewed as three components [17, 78, 79]:

- A well-defined start time, t_0, which is given by the excitation of the molecule by a pump laser pulse, $E_{\text{pump}}(\omega_{\text{pump}})$, which prepares an excited state wavepacket. Here ω_{pump} describes the finite bandwidth associated with the pump laser pulse, which typically spans more than a single quantum state. The excitation of multiple excited states results in a coherent superposition, otherwise known as a wavepacket.

- A well-defined time delay, Δt, the wavepacket (Eq 1.1), $|\Psi(t)\rangle$, then evolves freely according to the energy phase factors contained within the superposition of exact (non Born Oppenheimer) molecular eigenstates $|\Psi_n\rangle$.

$$|\Psi(t)\rangle = \sum_n a_n \mathrm{e}^{-iE_n\Delta t/\hbar}|\Psi_n\rangle \tag{1.1}$$

  where the complex coefficients, a_n, contain both the amplitudes and phases of $|\Psi_n\rangle$ and E_n are the eigenenergies of the states in question.

- A well-defined end time, given by the interaction of the probe laser pulse, $E_{\text{probe}}(\omega_{\text{probe}})$, with the wavepacket, which projects the wavepacket onto a specific final state at Δt. The final state therefore acts as a "template" onto which the wavepacket dynamics are projected.

The time dependence of observed differential signal, $S_f(\Delta t)$, for projection onto a single final state can be expressed, using time dependent perturbation theory, as:

$$S_f(t) = |\langle \Psi_f | E_{\text{probe}}(\omega_{\text{probe}}) \cdot d | \Psi(t) \rangle|^2 = \left| \sum_n B_n e^{-iE_n \Delta t/\hbar} \right|^2 \tag{1.2}$$

where d is the transition dipole moment of the probe excitation and the complex coefficients, B_n, contain both the state amplitudes, a_n, and the transition dipole matrix elements connecting each state within the wavepacket to a single final state.

$$B_n = a_n \langle \Psi_f | E_{\text{probe}}(\omega_{\text{probe}}) \cdot d | \Psi(t) \rangle \tag{1.3}$$

Eq. 1.2 can be rewritten as:

$$S_f(\Delta t) = 2 \sum_n \sum_{n \leq m} |B_n||B_m| \cos[(E_n - E_m)\Delta t/\hbar + \Phi_{nm}] \tag{1.4}$$

where the phase factor, Φ_{nm}, contains the initial phase difference between the molecular eigenstates, $|\Psi_n\rangle$ and $|\Psi_m\rangle$, and the phase of the probe transition dipole matrix elements between these states and the final state, $|\Psi_f\rangle$. The form of Eq. 1.4 highlights that the final state accessed is a coherent sum over all two-photon transitions amplitudes, covered by the bandwidth of the pump and probe laser pulses, ω_{pump} and ω_{probe}, respectively, as well as the interferences between all degenerate two-photon transitions. Additionally, the resultant signal contains time-dependent modulation frequencies, (E_n-E_m)/$\hbar$, which correspond to the set of level spacings in the coherent superposition. Eq. 1.4 therefore represents the relationship between the initially prepared wavepacket and the observed time-dependent pump-probe signal. This relationship is critically important as, in general, each of the molecular eigenstates will have different overlaps with the final state and therefore add a different weight to the observed signal. Consequently, the choice of which final state(s) act as the "template" that the wavepacket dynamics are being projected onto also matters, as does the choice of experimental technique. A schematic diagram of the pump-probe scheme is provided in Fig. 1.1.

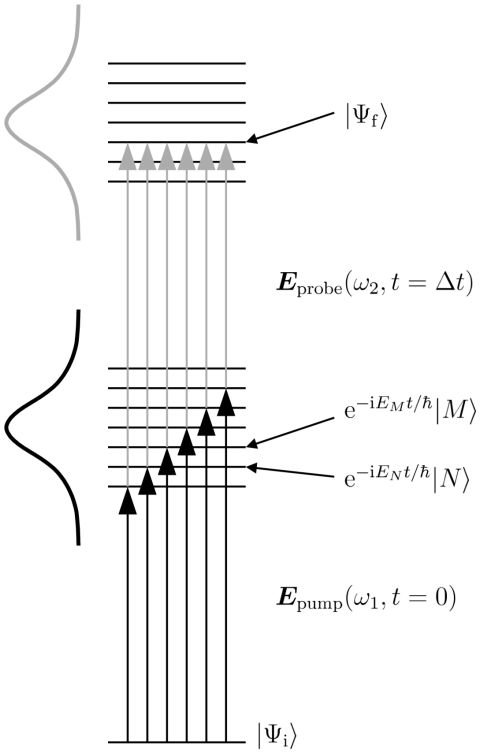

Figure 1.1: A schematic diagram showing the excitation, evolution and detection of an excited state wavepacket. Initially a pump laser pulse, E_pump creates a coherent superposition of excited eigenstates at $t = 0$ from the ground state $|\Psi_i\rangle$. At later time $t = \Delta t$ the wavepacket is projected by a probe pulse (E_probe) onto a set of final states $|\Psi_f\rangle$ which act as a "template" for the excited state wavepacket dynamics. Figure adapted from Fig. 1 of Ref. [14].

In particular, it is important to make the distinction between integral and differential detection techniques. For integral detection techniques, such as total fluorescence or ion-yield, the measured signal, $S_f(\Delta t)$, is proportional to the total population in all final states (i.e. $S_f^\mathrm{tot}(t) = \sum_f S_f(\Delta t)$) and is therefore unable to distinguish between specific $|\Psi_f\rangle$. Typically, this summation over final states results in a loss of information, since individual final states may have different overlaps with the initially prepared wavepacket. Conversely, differential techniques, such as translational energy spectroscopy or photoelectron spectroscopy, are more information rich, due to the signal being dispersed with respect to final state. For the experimental work presented in this thesis the "template" is the ionisation continuum, which

is comprised of the final state of the molecular ion and the ejected photoelectron. The probe process can therefore be considered as the excited state projecting onto the molecular ionisation continuum. Finally, the photoelectron yield, kinetic energy or angular distribution is measured, thus providing a time-dependent signal.

1.2 The Born-Oppenheimer approximation

In general the temporal evolution of the excited state wavepacket is complex due to the coupling between electronic and nuclear degrees of freedom, this is particularly prevalent in polyatomic molecules where there is a large density of electronic and vibrational states, lying close together in energy [80, 81]. In order to construct a more physically insightful picture it is typical to invoke approximations, such as the Born-Oppenheimer Approximation (BOA). This is an adiabatic approximation where the molecular wavefunction, $\Psi_n(r,R)$, is factored into electronic, $\psi_\alpha(r, R)$, and nuclear, $\phi_{\nu_\alpha}(R)$, components

$$\Psi_{\alpha,\nu_\alpha}(r,R) = \psi_\alpha(r,R)\phi_{\nu_\alpha}(R) \tag{1.5}$$

where r and R represent the electronic and nuclear coordinates, respectively. The subscripts α and ν_α represent a particular electronic state and vibrational levels within that state, respectively. The above separation is justified since the mass of the nuclei is three orders of magnitude larger than the electrons mass and therefore the nuclear motion is much slower than the electronic dynamics. In this approximation the electrons can be considered to rapidly adjust to the evolving nuclear motion, while in turn the nuclei experience only an average potential due to the electrons. Further approximations are typically applied where the nuclear wavefunction $\phi(R)$ is separated into vibrational and rotational parts [82–85].

The adiabatic approximation then permits the electronic time-independent Schrödinger equation to be solved by setting the nuclear part of the Hamiltonian, $H_{\text{nuclear}}(R)$, to zero (i.e. for fixed nuclei)

$$H_{\text{elec}}(r,R)\psi_\alpha(r,R) = E_\alpha(R)\psi_\alpha(r,R) \tag{1.6}$$

where $H_{\text{elec}}(r, R)$ is the electronic part of the molecular Hamiltonian and $E_\alpha(R)$ is the electronic energy of the system. Eq. 1.6 is then solved for each value of R (i.e. for various nuclear coordinates), allowing the construction of a potential energy surface by mapping out the electronic energy of the system as a function of nuclear coordinates. In the above picture the initial population, prepared by excitation from the ground state by the pump pulse, exists in some region of the excited state potential energy surface, defined by $E_\alpha(R)$. The initial population then evolves according to the topography of the excited state surface and is probed at Δt via photoionisation.

1.3 Franck-Condon principle

The first step in the above outlined pump-probe methodology, when applied to a molecular photochemistry experiment, is the excitation of a molecule to a higher-lying electronic state. Typically it is assumed that these electronic transitions can be treated as instantaneous, meaning they occur on a timescale much faster than the motion of the nuclei and is a consequence of the comparatively large mass of the nuclei compared to the electrons (i.e. an adiabatic, Born-Oppenheimer, type picture as outlined above). This approximation is the Franck-Condon (FC) principle [86,87] and permits transitions to be represented as vertical excitations from a point on the lower energy potential surface to the same nuclear configuration on an upper surface. Within the FC principle electronic transitions between two vibronic states, Ψ and Ψ', can be described by the following transition moment:

$$R_{\Psi\rightarrow\Psi'} = \int \Psi^*_{v_\alpha} \Psi^*_\alpha \mu \Psi_{v'_\alpha} \Psi_{\alpha'} \mathrm{d}r\mathrm{d}R \tag{1.7}$$

where μ is the operator of the dipole moment, which can be defined in terms of nuclear μ_v and electronic μ_e components. The BO total wave function presented in Eq. 1.7 can further expanded as:

$$\begin{aligned} R_{\Psi\rightarrow\Psi'} &= \int \Psi^*_{v_\alpha} \Psi^*_\alpha (\mu_v + \mu_e) \Psi_{v'_\alpha} \Psi_{\alpha'} \mathrm{d}r\mathrm{d}R \\ &= \int \Psi^*_{v_\alpha} (\int \Psi^*_\alpha \mu_e \Psi_{\alpha'} \mathrm{d}r) \Psi_{v'_\alpha} \mathrm{d}R + \int \Psi^*_{v_\alpha} \mu_v (\int \Psi^*_\alpha \Psi_{\alpha'} \mathrm{d}r) \Psi_{v'_\alpha} \mathrm{d}R \end{aligned} \tag{1.8}$$

The electronic (second) term in the final line of Eq. 1.8 is zero, due to the the electronic wave functions being orthogonal at any nuclear configurations. Within the FC framework the electronic transition moment, $R_{\alpha\to\alpha'} = \int \Psi^*_{\alpha}\mu_e\Psi_{\alpha'}\mathrm{d}r$, is assumed to be independent of R, and Eq. 1.8 can be expressed as:

$$R_{\Psi\to\Psi'} = R_{\alpha\to\alpha'}\int \Psi^*_{\alpha_v}\Psi_{\alpha'_v}\mathrm{d}R \tag{1.9}$$

The form of Eq. 1.9 highlights that the total transition moment between two states is dictated by a transition dipole moment between the electronic states and a vibrational overlap term. A consequence of the above separation is that value of the electric dipole transition moment is largest when the initial and final vibrational states have the greatest overlap. The probability, P_{FC}, of populating a particular final state vibrational level is given by the square of the vibrational overlap term, which is commonly known as a FC factor [86–88]:

$$P_{\mathrm{FC}} \propto |\int \Psi^*_{\nu_\alpha}\Psi_{\nu'_\alpha}\mathrm{d}R|^2 \tag{1.10}$$

1.4 Photoionisation dynamics

The common thread that links all the experiments presented in this thesis, regardless of whether these measurements were time or energy-resolved, is the detection of electrons and/or positively charged ions after interaction of electromagnetic radiation with a molecular system. These are referred to as photoelectron and photoion spectroscopy, respectively. In the case of photoelectron spectroscopy, analysis of kinetic energy, integrated flux, as well as angular distribution, of the outgoing electron has been shown to be a powerful method for determining the nature of the individual states (i.e. molecular orbitals) from which they originate [89–91]. This ability to separate out individual molecular orbitals, and therefore examine molecular electronic structure, is particularly advantageous for studying non-adiabatic dynamics as will be outlined in Sec. 1.9.1.

The quantity typically measured in photoelectron spectroscopy is kinetic en-

ergy of emitted photoelectron which, through an approximation known as Koopmans' theorem, can be related to the ionisation potential of a specific molecular orbital. According to this approximation the photoelectron kinetic energy, E_{kin}, is given by:

$$E_{\text{kin}} = \hbar\omega - I_{\text{p}}^{j} \tag{1.11}$$

where I_{p}^{j} is the ionisation potential of the jth ionisation channel (where $j = 0$ signifies the D_0 ground electronic state of the ion, $j = 1$ the D_1 first excited electronic state of the ion, and so forth), and $\hbar\omega$ is the energy of the incident photon. In general Eq. 1.11 should be extended to include the additional possibility of vibrational and/or rotational excitation during ionisation, which may result in a decrease in the photoelectron kinetic energy:

$$E_{\text{kin}} = \hbar\omega - I_{\text{p}}^{j} - E_{\text{vib}} - E_{\text{rot}} \tag{1.12}$$

Here E_{vib} and E_{rot} denote energy deposited in the vibrational and rotational degrees of freedom, respectively. Consequently, the resulting photoelectron spectrum may contain multiple vibrational features for each ionised molecular orbital. The system of lines, originating from ionisation of the single molecular orbital, is typically referred to as a band. To serve as an example to clarify the above points, presented in Fig. 1.2 is the photoelectron spectra of CH_3I recorded at a photon energy of 60 eV at the Synchrotron SOLEIL [92]. Details of the experimental apparatus used to record this spectra are provided in Sec. 4.2.1 of Chapter 4. In the binding energy range spanning 9-18 eV, the spectra is dominated by a series of well separated bands centred at approximately 9.7, 10.3, 12.5 and 15 eV, respectively. These peaks have been associated with photoionisation of particular molecular orbitals (i.e. a well-defined single-hole state) and have been thoroughly characterised [93–97]. At large binding energies (>20 eV) the spectra is comprised of a dense progression of overlapping broad features. This region, typically referred to as the inner valence spectrum, represents a situation where the independent particle picture of photoionisation (i.e. Koopmans' theorem) breaks down due to the role of electron correlation

effects in the ionisation process [98].

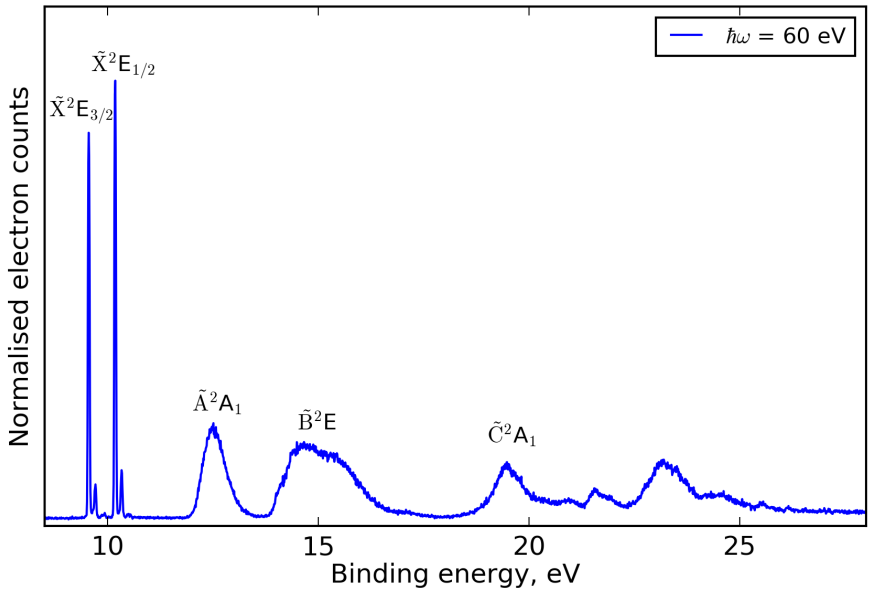

Figure 1.2: .The valence photoelectron spectrum of methyl iodide (CH_3I) recorded at $\hbar\omega$ = 60 eV at the Synchrotron SOLEIL [92]. Assignments of the various photoelectron bands between 9-18 eV are taken from the earlier investigation of Holland and co-workers [97]. Further discussion of these features in the context of Koopmans' theorem is provided in the main text.

The goal of the remainder of this chapter is to provide a general overview of several different photoionisation, as well as associated decay mechanisms relevant to the experimental work presented later in the thesis. As photoionisation has been the subject of numerous review articles and textbooks the goal is not to present an exhaustive literature review but simply outline a conceptual framework for interpreting the experimental results.

1.5 The role of vibration in photoionisation

The discussion surrounding the FC principle (see Sec. 1.3) highlighted that: (i) the timescale of an electronic transition is typically short when compared with that required for the execution of vibrational motion and; (ii) the associated transition

dipole moment can be approximately considered as slowly varying with internuclear coordinates (see Eq. 1.9 and 1.10 as well as surrounding text). These points have important implications for the structure typically observed in photoelectron spectra since, in particular point (ii), governs the relative probabilities of ionisation occurring to various ionic vibrational states [89]. The electron flux for each resolved vibrational peak therefore provides either a direct or indirect measure of the probability of ionisation (Eq. 1.10) at specific photon energy. In general, the photoelectron spectra will exhibit a distribution of vibrational peaks, the so-called "Franck-Condon envelope", centered around where initial and final vibrational state have the greatest overlap (i.e where the transition dipole moment is maximised).

The valence photoelectron spectra of CH_3I (see Fig. 1.2) conveniently serves as an illustrative example of the role of vibration in a photoionisation experiment and helps clarify some of the aforementioned points. Firstly, the vibrational structure associated with the $^2E_{3/2,1/2}$ doublet exhibits a limited progression of relatively sharp peaks in the symmetric CH_3 deform/umbrella (ν_2) mode, for both spin-orbit split states. The maximum intensity peak in this progression coincides with the vibrational origin of these states and therefore implies that the ground state equilibrium geometries of both neutral and ionic CH_3I are similar. This point is however unsurprising when the composition (a doubly degenerate pair of iodine p_x and p_y atomic orbitals [93, 94]) of the highest occupied molecular orbital (HOMO) in neutral CH_3I is considered, as the removal of an electron from this orbital is unlikely to effect molecular bonding. The photoelectron band associated with the next lowest-lying (HOMO-1) orbital, $\tilde{A}^2A_1$, exhibits a broad Franck-Condon envelope, with at least 3 vibrational progressions observed in high-resolution He I spectra [94]. These three progressions have been assigned as excitation of C-I symmetric stretch (ν_3) as well as combinations bands of that with either C-H symmetric stretch (ν_1) or CH_3 umbrella. Based on the broad nature of the band and maximisation of the FC envelope at peaks corresponding to significant excitation of the ν_1-ν_3 modes the equilibrium geometry of the $\tilde{A}^2A_1$ state must be substantially different from the ground state of CH_3I. This point is again unsurprising as the HOMO-1 orbital is

characterised as a C-I σ-bonding orbital.

The above, although outlined for the specific case of valence photoionisation of CH_3I, outlines a few useful generalities: (i) If the photoelectron spectra exhibits limited vibrational structure then the geometries of the state undergoing ionisation and the final catonic state are similar and; (ii) broad FC envelopes are indicative of a large geometry change between the two states involved and as a consequence typically maximise at peak position corresponding to significant vibrational excitation. In the experimental results presented in Chapter 3, on VUV excited state dynamics in acetone, FC based arguments are used extensively to aid in the assignment of various transient photoelectron bands.

1.6 Photoionisation with X-rays

If the incident photon energy continues to be increased then ionisation can occur from more deeply bound (core) orbitals within a molecule. These states, unlike the valence shell, tend to be: (i) energetically isolated and; (ii) have electron density well localised about a specific atomic site (i.e. these orbital should behave fairly atomic-like). The opposite is true for valence electrons, which often directly participate in chemical bonding and can be delocalised across the whole molecule. Despite the large photon energies required to ionise core-shell orbitals these processes have been extensively studied, particularly in atomic systems, due to the fact that probability for photon absorption (i.e. the absorption cross section) generally increases at each ionisation threshold [99]. This shell-specific dependency to the cross section, when coupled with wavelength tunable synchrotron radiation, has permitted inner-shell photoionisation processes to be investigated with relative ease.

The photoionisation cross section $\sigma(\hbar\omega)$, at a given photon energy, is defined as the sum of the partial cross sections of all sub-shells and is given simply by a photoionisation matrix element between the initial and final states. For the simplest case of a one-electron atom or ion, the total photoionisation cross section can be expressed as [83]:

$$\sigma(\hbar\omega) \approx \frac{16\sqrt{2}\pi}{3}\alpha^8 Z^5 (\frac{m_e c}{\hbar\omega})^{7/2} a_0^2 \tag{1.13}$$

here α is the fine structure constant, m_e is the mass of the electron, Z is the atomic number of the element undergoing ionisation and a_0 is the Bohr radius. Although this expression is not strictly correct for inner-shell photoionisation processes a number of interesting points can still be highlighted from Eq. 1.13, namely: (i) the photoabsorption rapidly decreases with higher photon energy and; (ii) the Z^5 terms implies that heavier elements have significantly larger X-ray absorption cross sections than lighter elements. Point (ii) has resulted in a significant amount of synchrotron radiation investigations being conducted on heavy rare gases like Xe [100–110] and for molecular systems containing heavy elements, like iodine, a popular choice for FEL investigations [40, 76, 111–116]. The experimental work presented in Chapter 4 of this thesis deals with characterisation of the core-level photoionisation dynamics, including photoelectron angular distributions (see Sec. 1.8), of the I 3d, 4s and 4p shells in the molecule CH_3I using plane polarised synchrotron radiation.

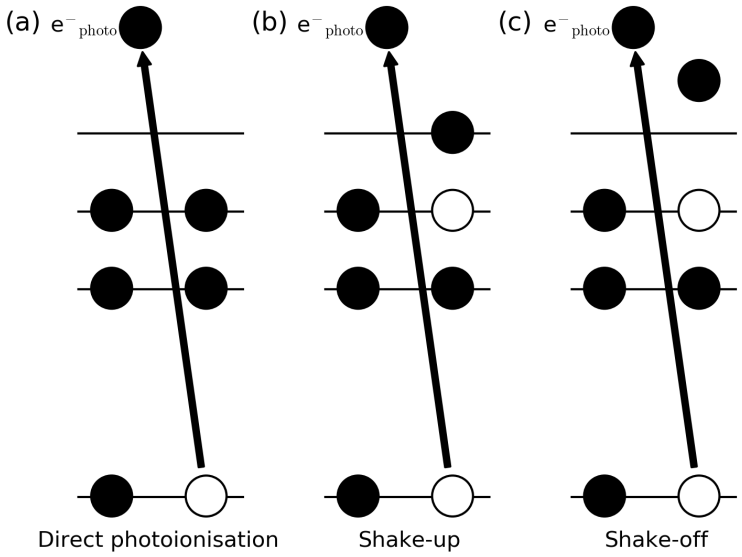

Figure 1.3: Schematic diagrams of (a) core-level photoionisation and associated satellite processes of (b) shake-up and (c) shake-off.

Another interesting set of features that show up much more prevalently in X-

ray photoelectron spectra, when compared to valence, are so called photoelectron "satellites", which are a direct consequence of electron correlation (in valence shell photoionisation, this is known as the 'breakdown' of the molecular orbital or Koopmans' picture) during photoionisation [99, 117]. These features appear at higher binding energies ($\sim$5-50 eV) than the main photoelectron band for a particular shell and are classified into two categories, either shake-up or shake-off. Presented in Fig. 1.3 are schematic diagrams for both these processes. Shake-up can be viewed as the outgoing photoelectron interacting with valence shell electrons and exciting one (or more) electron to a higher-lying previously unoccupied orbital. Spectrally these transitions will appear as a series of discrete peaks below the main photoline, which become more closely spaced at higher binding energies due to a higher density of states (Rydberg) approaching the IP. If the energy of this transition extends past the IP a valence electron is ejected from the ion completely and the PES now exhibits a continuum structure; this process is known as shake-off. To serve as an example of these two mechanisms, the satellite spectra associated with the I 4d level in CH_3I is shown in Fig. 1.4. Assignments of the individual shake-up features in this spectra are not provided but can be found in Ref. [97]. Finally, unlike in atomic systems where the structure of the shake-up transitions is relatively sharp [118], the shake-up structure in molecular systems is often broad and featureless [90]. This observation is linked to the fact that typically shake-up/shake-off transitions cause excitation of bonding valence electrons into highly excited states which may be dissociative in nature.

1.6.1 Relaxation of core ionised systems: Auger decay

The ejection of an core-level electron through photoionisation results in an ion left in an excited state with a hole in the inner-shell (see Fig. 1.5(a)). This system is highly unstable and undergoes relaxation via one of two pathways, both of which initially involve the filling of the inner-shell vacancy with a higher-lying core or valence electron. The first mechanism, known as X-ray fluorescence, liberates the

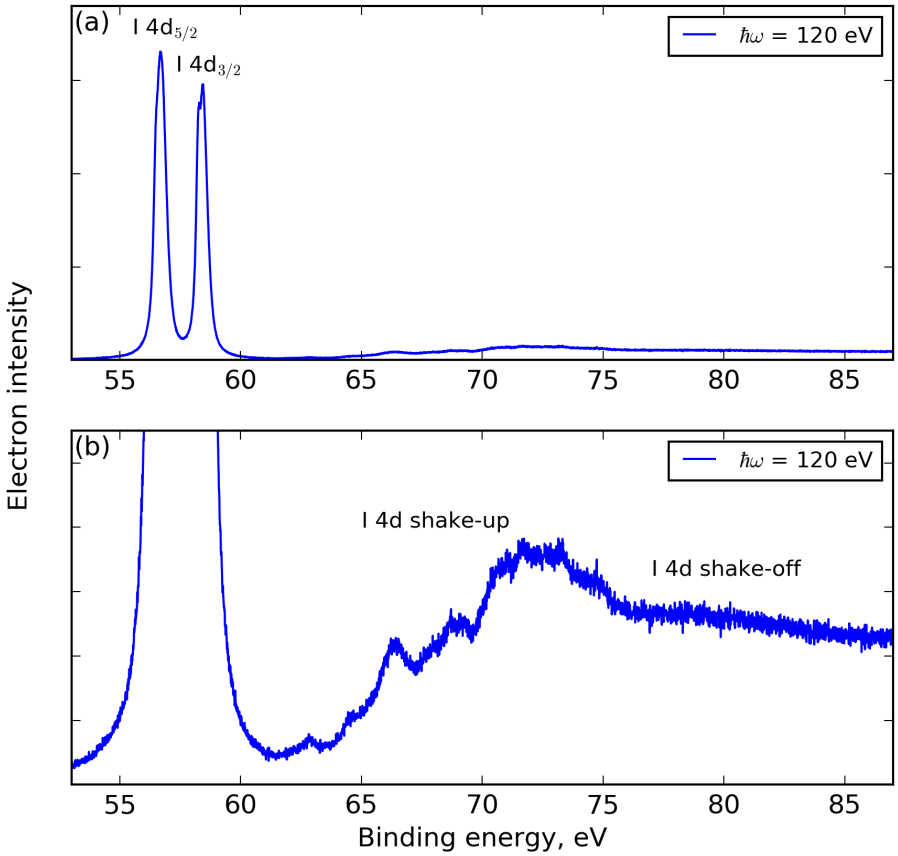

Figure 1.4: (a) The photoelectron spectrum of CH_3I recorded at a photon energy of 120 eV at Synchrotron SOLEIL [92]. The spectra is dominated by two peak due to spin orbit split I $4d_{5/2,3/2}$ levels but some weaker associated satellite structure is observed at higher binding energies. (b) Zoom of panel (a) in binding energy range spanning the satellite features. Discussion of the typical structure observed in the shake-up and shake-off portions of the spectrum is provided in the main text.

excess energy of the higher-lying electron refilling the core-hole by emitting a photon, where $\hbar\omega$ is simply given by the difference between the two energy levels involved. The second is a non-radiative relaxation process called Auger decay, where one or more secondary electrons are emitted from the system following refilling of the inner-shell vacancy. Schematic diagrams for these two processes are shown in panels (b) and (c) of Fig. 1.5.

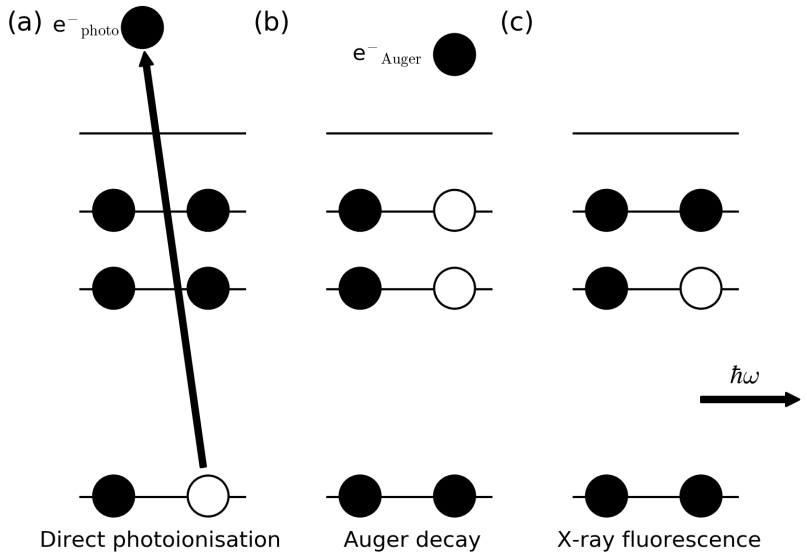

Figure 1.5: Schematic diagrams of electronic relaxation processes that can occur after core-level photoionisation (panel (a)). (b) Auger decay is non-radiative processes where the initial core-level vacancy is filled by an electron from a higher-lying state and the excess energy is released in the kinetic energy of a secondary electron. (c) X-ray fluorescence is a radiative process where this excess energy is liberated in the form of a photon.

In general there exists a competition between Auger decay and X-ray flores-cence, with the former dominating in low Z elements. In Chapter 5 results are presented for possible Auger relaxation pathways following ionisation of I 3d shell in CH_3I. Despite the fact that iodine is a relatively large Z atom the discussion herein is limited to non-radiative decay as only electron spectroscopy measurements were conducted in this investigation.

Conceptually Auger decay is typically considered as a two step process and can be expressed as follows:

$$\begin{aligned} A + \hbar\omega &\rightarrow [A^+]^* + e^-_{\text{photo}} \\ [A^+]^* &\rightarrow A^{2+} + e^-_{\text{Auger}} \end{aligned} \tag{1.14}$$

here the charge state of the system A is changing to that of a doubly charged ion through the ejection of one photoelectron and one, subsequently emitted Auger electron. A consequence of this separation of the Auger process into two distinct steps

is that the refilling of the core vacancy, in the second step, is independent of the exact formation process (i.e. the hole could be created via interaction with an electron beam or with X-ray photoionisation), which in turn implies that the kinetic energy of the Auger electron is independent of photoexcitation energy. An Auger transition is therefore characterised primarily by: (i) the location of the initial core-hole and; (ii) the location of the final two holes in the doubly ionised system. The energetic difference between these two states gives the Auger electron kinetic energy.

In general scientists working with X-rays tend use an alternative nomenclature to label atomic states, with K, L, M, N and O shell denoting a state with a principle quantum number of 1, 2, 3, 4 and 5, respectively. These labels are also generally accompanied by a numerical subscript to describes levels with a non-zero value of the orbital angular momentum quantum number ($l > 0$), i.e. p,d,f,.. levels, as well as to highlight spin-orbit splitting. For example a 2p state would be labeled as $L_{2,3}$ in X-ray/Auger nomenclature with 2 referring to J = 1/2 state and 3 referring to the J = 3/2 state, respectively. This choice of labeling results in Auger transitions being characterised by a series of three letters which denote the locations of the initial core-hole state and the final two holes. To illustrate this nomenclature and to highlight the large number of channels which can occur during Auger decay, presented in Fig. 1.6 is an electron spectra containing the major Auger decay channels following photoionisation of the 3d shell of Xe. The spectra is dominated by two groups of peaks centred at $\sim$525 and $\sim$530 eV which correspond to the $M_5N_{45}N_{45}$ and $M_4N_{45}N_{45}$ transitions, respectively. The former of these would correspond to a $3d_{5/2}$ vacancy being refilled by a 4d electron and another 4d electron being ejected. Note that the substructure observed in these Auger groups is associated with the population of different electronic states in the final doubly-ionised system and fine structure peaks are typically observed in high-resolution measurements of atoms [119].

Despite the complex structure typically observed in Auger electron spectra, like Fig. 1.6, assignment of features to either Auger transitions or photoelectrons

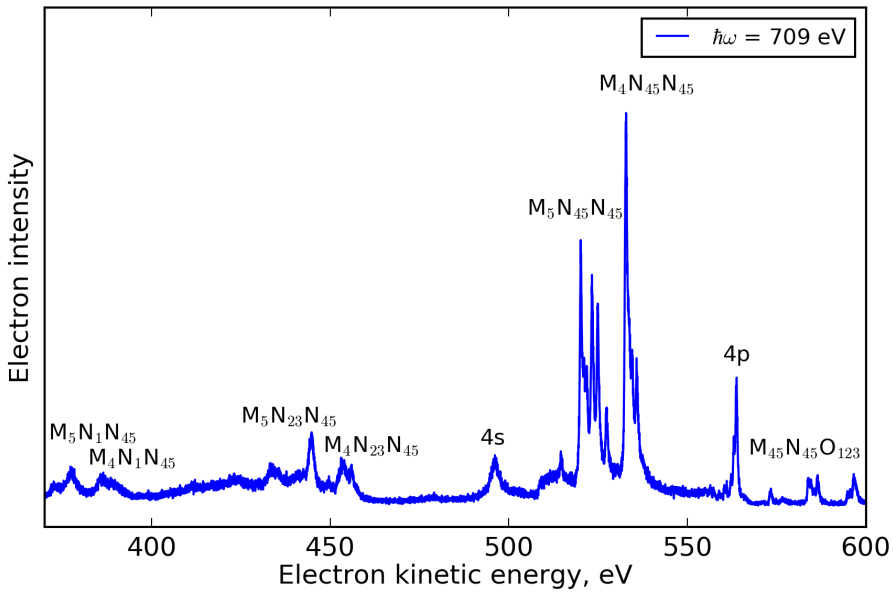

Figure 1.6: Electron spectra of the major Auger decay pathways following 3d photoionisation of Xe, recorded at $\hbar\omega = 709$ eV using the experimental apparatus outlined in later chapters (see Secs. 4.2.1 and 5.2.1). In addition of the Auger transitions, the spectra also contained peaks associated with core-level photoionisation of the 4s and 4p level of Xe at ∼495 and ∼565 eV, respectively.

(and associated satellites) when using tunable synchrotron radiation is relatively trivial as Auger transition kinetic energies, unlike direct photoelectrons, are independent of excess energy. Another method, which is exploited in Chapter 5 to disentangle satellite structure and Auger peaks, is to use plane polarised radiation to record electron angular distributions (see Sec. 1.8). In general the electron angular distributions for Auger transitions are fairly isotropic, whereas those associated with direct photoelectrons are often highly directional.

Finally, beyond the simple mechanism of Auger decay outlined in Fig. 1.6 there are multitude of other complex processes which involve the emission of multiple Auger electrons. For example in a triple ionisation process the emission of two Auger electrons can either occur simultaneously or sequentially. The former, typically called double-Auger decay, can be considered as the Auger equivalent of shake-off and was first observed by Carlson and Krause [120, 121]. The latter, step-wise process, is referred to as Auger-cascade [110]. Disentangling the relative contributions of these two processes, although interesting from the point of view of

studying electron-electron correlation, is experimentally challenging as it requires two electron coincidence detection [110, 122].

1.7 Strong-field ionisation

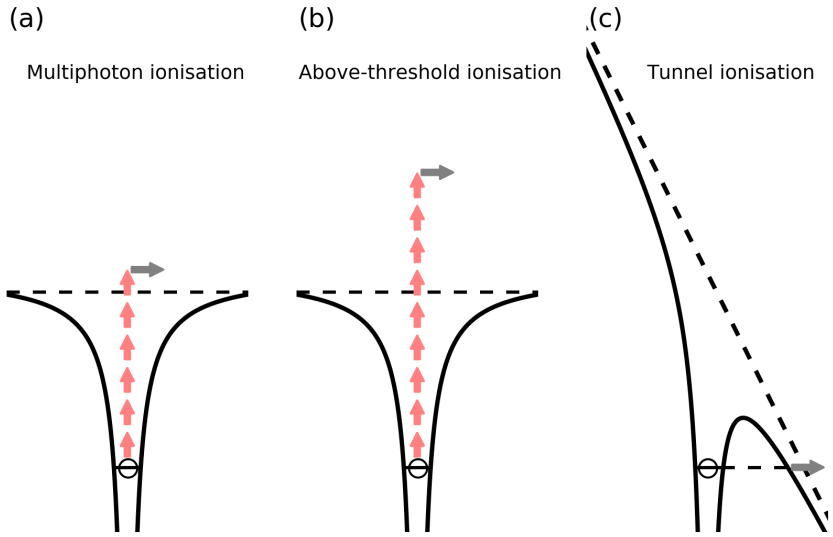

Figure 1.7: Schematic diagrams of strong-field ionisation processes: (a) mutiphoton ionisation (MPI); (b) above-threshold ionisation (ATI) and; (c) tunnel ionisation (TI). Note, in panel (c) the solid lines represent the potential in presence of the laser field.

In the preceding discussion the ionisation mechanisms occurred via the interaction of a single photon with the molecular system, however, as mentioned in the introductory remarks, the intense nature of ultrashort laser fields can result in higher order/non-perturbative processes which also cause ionisation. Photoionisation caused by the interaction of an intense laser field with an atomic or molecular system is conceptually very different from both valence and core single photon ionisation, therefore, the aim of this section is to provide a review of some basic ideas in non-perturbative ionisation.

In general, all atoms and molecules which experience laser intensities $>10^{13}$ Wcm^{-2} will experience some level of ionisation, however, the exact mech-

anism by which this process occurs depends strong on both the intensity and frequency of the laser pulse as well as the IP [123]. There exists four commonly discussed mechanisms, known as multiphoton ionisation (MPI), above-threshold ionisation (ATI), tunnel ionisation (TI), and over the barrier ionisation (OTBI) [124, 125], which will be briefly discussed for atomic systems. The general framework is also appropriate for molecular systems with a few caveats which will be outlined towards then end of the section.

In the limit where the laser electric field strength is insufficient to distort the Coulomb potential experienced by the electrons, the laser interaction can be consider as a perturbation and therefore the only way photoionisation can occur is through the absorption of multiple photons, such that $N\hbar\omega > I_{\mathrm{p}}^{j}$, where N is the number of photons (see Fig. 1.7(a)). The absorption of the photons occurs as a series of transitions through virtual states until the electron reaches the continuum. This process is known as multiphoton ionisation and has an ionisation rate, Γ_N, which depends on the laser intensity, I, to the the power N, and is given by [42,126]:

$$\Gamma_N = \sigma_N I^N \tag{1.15}$$

where N is the minimum number of photons needed for ionisation, σ_N is the generalised cross section. This relatively simple situation can however become more complex by the presence of a resonance at a particular photon order. Further discussion of resonant versus non-resonant multiphoton processes in the context of photoexcitation is provided in Sec. 3.1.

At higher laser intensities (10^{12}-10^{13} Wcm^{-2}) another ionisation mechanism occurs by which an atom absorbs multiple photons above the ionisation threshold. This is referred to as ATI and results in a photoelectron spectra containing a series of peaks spaced, to first order, by modulo the photon energy. Deviations from the expected spacing have been observed [44] and have been attributed to, for example, intensity dependent resonance effects [127]. A schematic diagram of ATI is presented in panel (b) of Fig. 1.7. For the case of ATI, the intensity dependence of the

ionisation rate is given by [128]:

$$\Gamma_{N+S} = \sigma_{N+S} I^{N+S} \tag{1.16}$$

where S is the number of excess photons absorbed and all other terms were previously defined for Eq. 1.15. Note the form of Eq. 1.16 implies that the electron flux at a particular photon order strongly decreases as the photon number increases and hence ATI spectra, like the ones presented in Chapter 2, are typically displayed on logarithmic scales. Further details surrounding the appearance of ATI in photoelectron spectra given in Sec. 1.7.1.

As the intensity of the laser field is further increased ($I > 10^{13}$ Wcm^{-2}), the electric field of the laser, V_{L}, can no longer be considered as a perturbation to the system anymore and can in fact begin to distort the Coulomb potential of the system [129]. This distortion of the potential barrier manifests itself as a raising of the potential on one side of the well and a lowering of the barrier on the other side (see Fig. 1.7(c)). As V_{L} reaches its peak, the bound electron in the distorted Coulomb potential will see a barrier of finite width, which will have an finite probability of quantum mechanical tunnelling associated with it. Provided that the electron can adiabatically follow the laser electric field cycles the ionisation rate can by calculated in the quasi-static approximation with Ammosov, Delone and Krainov (ADK) theory [129], and is expressed in atomic units as:

$$\Gamma = 4 I_{\mathrm{p}} \left[\frac{2(2I_{\mathrm{p}}^{j})^{3/2}}{E_0} \right]^{2n-m-l} \exp\left[-\frac{2(2I_{\mathrm{p}}^{j})^{3/2}}{3E_0} \right] \tag{1.17}$$

where n, l, and m define the effective principal, angular and magnetic quantum numbers of the ionising electron, respectively, and E_0 is the peak of the electric field experienced by the electron. In many cases ionisation occurs in the intensity regime between MPI and TI, for typical experimental conditions [130], and disentangling the relative contributions of each is challenging. In spite of this it is often useful to characterise the transition between the two through the Keldysh parameter, which

is defined as [131]:

$$\gamma = \sqrt{\frac{I_{\mathrm{p}}^{j}}{2U_{\mathrm{P}}}} \tag{1.18}$$

where U_{P} is the ponderomotive potential, which is related to the ponderomotive (quiver) force (i.e. the non-linear force that charged particles experience in an inhomogeneous oscillating electromagnetic field) of a free electron of charge, e, and mass, m_{e}. The ponderomotive potential is related to the electric field strength and angular frequency of the laser field, ω, through the following relation:

$$U_{\mathrm{P}} = \frac{e^2 E_0^2}{4 m_e \omega^2} \propto \lambda^2 I \tag{1.19}$$

for $\gamma << 1$ the ionisation process is well described by TI, whereas for $\gamma >> 1$ the opposite applies, and the MPI picture is more appropriate, as the external electric field is weak compared to the Coulomb potential experienced by the valence electron.

Within the tunneling regime, if the intensity of laser field continues to increase ($I > 10^{15}$ Wcm^{-2}) the Coulomb potential barrier can be distorted to the point that the electron is no longer bound and the electron is free to reach the continuum without tunneling through the barrier. This mechanism is referred to as over the barrier ionisation. As this mechanism occurs at significantly higher laser intensity than those utilised in this thesis ($\sim 10^{13}$ Wcm^{-2}) no further discussion will be provided. Finally, despite the above mechanisms representing intuitive pictures of how to understand SFI these are limiting cases and the boundary/intensity regime where one mechanism becomes dominant over another is not well defined.

Similarly to the case of an atom, a molecule placed in an intense laser field can also be ionised through various mechanisms outlined above. However, there are a few critical differences. Firstly, in a molecular system the ionisation rate depends strongly on the molecular symmetry and on the spatial orientation of the molecules with respect to the laser field [132–136]. For TI there also exists a new phenomena related to the fact that molecular ionic potential contains multiple wells, which can drastically effect ionisation rates. It has been shown, for example, that

TI ionisation rates are very sensitive to internuclear separation in the molecular ion [123, 125, 137–141]. Secondly, in the commonly studied atomic systems (i.e. noble gases) the energy gap between the ground and first electronically excited state of the cation is large. This point has resulted in the assumption that the ionisation dynamics are generally dominated by a single continua, which, when one considers the exponential dependence of the ionisation rate to I_p in Eq. 1.17, appears reasonable. However, in other atoms (e.g. transition metals) and molecular systems this is not the case and there can be multiple electronic states residing within $\sim$1 eV of each other and therefore multiple continua (i.e. ionisation into an electronically excited state of the ion) contributing to the ionisation dynamics. It has been experimental demonstrated that even in even in simple molecules such as N_2 [142], HCl [143], CO_2 [144, 145], N_2O_4 [146, 147], C_2H_2 [148] and SF_6 [149] that the simple picture can breakdown and SFI has the possibility of accessing multiple electronic continua.

The extent to which multielectron dynamics play a role varies between molecules but it can potentially be assessed experimentally by examining the ratios of channel-resolved ionisation yields to different final ionic states. Typically, the excited ionic states of polyatomic molecules undergo rapid radiationless transitions, which often results in fragmentation [99]. Monitoring the degree and channel of fragmentation, through methods such as mass spectrometry following SFI, therefore also allows assessment of the role of multielectron dynamics. However, typical femtosecond laser pulses comprise multiple optical cycles, which means that a bound electron within an ionised molecule can be further excited within the same laser pulse. This post-ionisation excitation therefore presents another route to SFI-induced molecular ion fragmentation. Finally, even within a single laser field cycle, non-resonant, non-adiabatic excitations to cation excited states may occur. This field-driven, inter-channel coupling process has been termed non-adiabatic multielectron (NME) ionisation [150, 151]. The observation of ionic fragmentation alone, therefore, does not suffice to disentangle direct ionisation to excited states of the ion from post-ionisation excitation from the ionic ground state. A method which

is sensitive to direct ionisation to electronically excited states will be outlined in the following subsection.

1.7.1 Multiple continua in strong-field ionisation

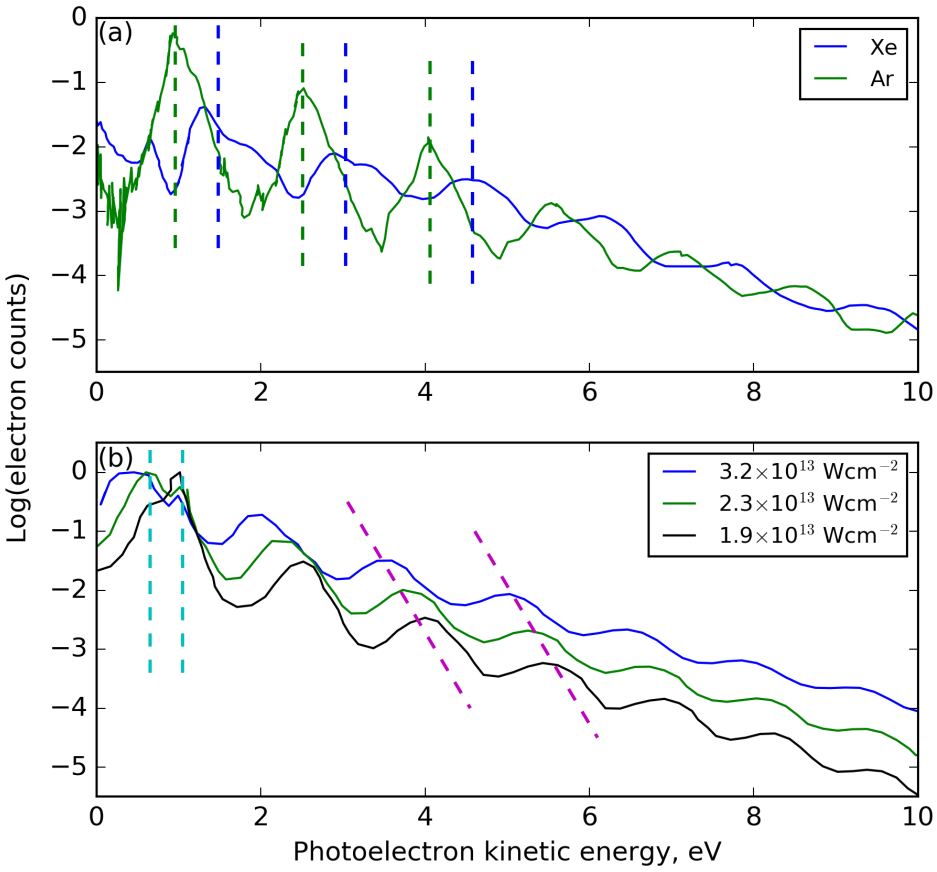

Figure 1.8: (a) ATI photoelectron spectra of Xe and Ar recorded using a photoelectron-electron photo-ion coincidence (PEPICO) spectrometer (details provided in Sec. 2.2) with a 80 fs pulse from a 800 nm Ti-Sapphire femtosecond laser. The laser intensity was 8×10^{13} Wcm^{-2}. Highlighted is a shift in the ATI comb peak positions due to differences in $I^{j}_{\mathrm{p,Stark}}$ of the atomic targets. (b) ATI photoelectron spectra of 1,3-butadiene as a function of ionising laser intensity recorded using the same experimental apparatus. Note the ATI peaks shift (dashed magenta lines) monotonically with laser intensity (see Eqs. 1.19 and 1.20), whereas the so-called "Freeman resonances", observed at low energy, are independent of laser intensity (dashed cyan lines). Data used to produce panel (b) was taken from the supplementary information of Ref. [152].

In order to resolve the contributions associated with the aforementioned mul-

tiple continuum in molecular strong-field ionisation it is first useful to summarise a few basic ideas of how ATI manifests itself in photoelectron spectra. In SFI a photoelectron is ejected into the continuum around the peak of the laser field within a single optical cycle and this process is then repeated for every optical cycle within the laser pulse. This, as was briefly mentioned in Sec. 1.7, results in an photoelectron spectra containing a series of discrete peaks, spaced by the photon energy of the ionising laser, with central peak positions given by the following:

$$E_{\mathrm{kin}} = (N+S)\hbar\omega - [I^{j}_{\mathrm{p,Stark}} - U_{\mathrm{p}}] \tag{1.20}$$

where $I_{\mathrm{p,Stark}}$ is the Stark shifted molecular ionisation potential of the jth ionisation channel, which accounts for the relative Stark shifts between the neutral and ionic states and all other symbols have been previously defined. The form of Eq. 1.20 is similar to that of Eq. 1.11 apart from the incident photon energy is now assumed to be much smaller and hence multiple photons are required to reach the IP, which now also differs from Eq. 1.11 due to the presence of the Stark shift. This dependence of the ATI comb peak position on $I^{j}_{\mathrm{p,Stark}}$ is highlighted in Fig. 1.8(a) for SFI of Xe and Ar. This data was collected using a photoelectron-electron photo-ion coincidence (PEPICO) spectrometer, which will be outlined in detail in Sec. 2.2. The energy separation of the peak maxima in the Ar and Xe correlated ATI combs roughly reflects the difference in ionisation potential between the two species (modulo $\hbar\omega$) if the assumption that the Stark shift is negligible at this intensity in evoked.

The ATI comb peak position is also affected by both the intensity and wavelength of the ionising laser through U_{p} (see Eq. 1.19). An example of these intensity dependent effects are highlighted in Fig. 1.8(b) for the SFI of 1,3-butadiene. In addition to the expected shift of the ATI comb peaks to lower kinetic energies at higher laser intensities (magenta dashed lines) there is a collection of sharp spectral features superimposed on the comb structure at low kinetic energies. The peak positions of these features, known as Freeman resonances [43], are independent of laser intensity and are a result of Stark shifting a neutral Rydberg state into multiphoton resonance with the driving laser field. Further discussion of Freeman resonances

and also a method to use ATI combs as an *in-situ* intensity calibration are provided in Sec. 2.4.

The method which utilised in this thesis to disentangle the role of multiple continua in molecular SFI is known as Channel-Resolved ATI (CRATI) [152,153]. This method is essentially a strong-field version of PEPICO spectroscopy where ATI photoelectrons are detected in coincidence with either parent or fragment ions. In a CRATI experiment, the ability to distinguish between different ionisation continua is based on that the ATI comb peak position is directly sensitive to the ionisation potential through Eq. 1.20 and secondly, that excited cationic state are generally unstable, which results in fragmentation [99]. For ionisation channels correlated with direct preparation (i.e. within a single optical cycle) of a cationic electronically excited state, due to the difference in vertical IP the ATI comb may be shifted (modulo the photon energy) energetically compared to that for ionisation correlating to the cation ground state. Conversely, if excited ionic states were populated by absorption post-ionisation, the ATI photoelectron would have departed before subsequent excitation could occur. The resultant ATI comb would therefore be the same as the comb prepared by direct ionisation to the ground state (i.e., post-ionisation excitation cannot influence the departed continuum electron). An example of this technique applied to SFI of 1,3-butadiene is shown in Fig. 1.9. Highlighted in this data is shift in ATI comb peak position between electrons correlated with the parent ion ($C_4H_6^+$) and both the fragment ($C_4H_5^+$/$C_3H_3^+$) ions, which is due to direct population of an electronically excited state of the cation in a single optical cycle [152]. Complimentary methods which utilise rotational wavepackets created through laser induced alignment schemes have also been proposed [148, 154], which exploit that different ionisation channels are expected to have a characteristic angular dependence in the SFI yield.

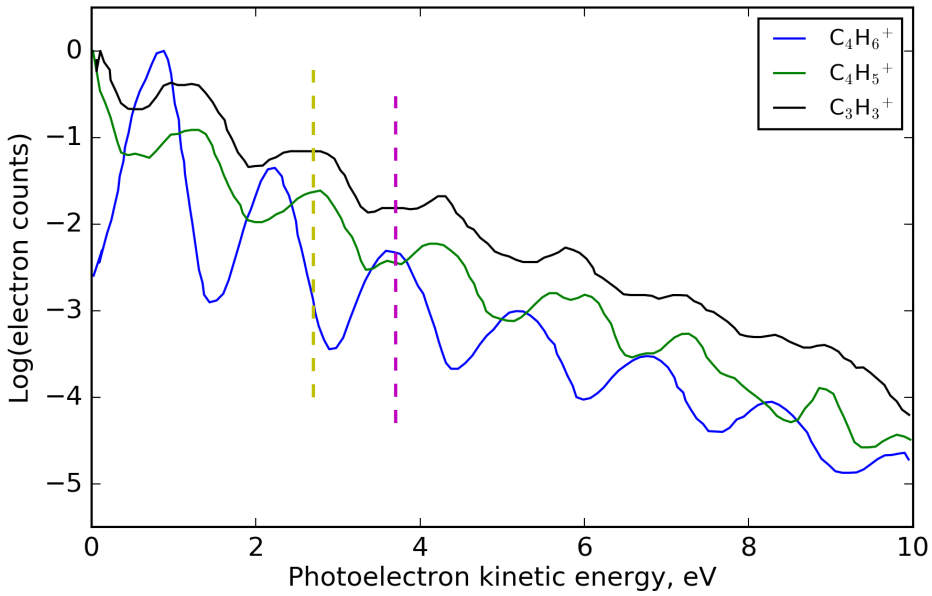

Figure 1.9: Fragment correlated ATI photoelectron spectra of 1,3-butadiene recorded using a PEPICO spectrometer with a 80 fs pulse from a 800 nm Ti-Sapphire femtosecond laser. The peak laser intensity was 1.9×10^{13} Wcm^{-2}. Highlighted is a shift in the ATI comb peak positions between the fragments due to differences in $I^{j}_{\mathrm{p,Stark}}$ between the ground and first electronically excited state of the cation (yellow and magenta dashed lines). Data used to produce this figure was taken from Ref. [152].

1.8 Photoelectron angular distributions

In addition to the photoelectron energy distributions, as discussed in Sec. 1.4, more information can be obtained about the state undergoing ionisation from the angular distribution of the emitted electron [14, 21, 27]. Following symmetry arguments, it is possible to determine which photoionisation matrix elements are allowed (non-vanishing). This is useful as it means a signature of symmetry of the state undergoing ionisation is directly reflected in the photoelectron angular distribution (PAD) [155]. In order for a dipole matrix element to be non-zero, group theory dictates that it is required that the direct product of the representations of the initial state, final state and dipole operator symmetry representations, denoted by Γ_{i}, Γ_{f} and Γ_{dipole}, respectively, must contain the totally symmetric representation of the molecular symmetry (MS) group, denoted Γ^{s}. For photoionisation, Γ_{f} can be split

into the symmetry species associated with the photoelectron, Γ_e, and ion [155]:

$$\Gamma_e \otimes \Gamma_f \otimes \Gamma_{dipole} \otimes \Gamma_i \supset \Gamma^s \tag{1.21}$$

Here Γ_i and Γ_f denote the symmetry of the full vibronic wavefunction, further separation of the vibrational, Γ_v, and electronic, Γ_α, symmetry components is possible when the Franck-Condon principle is applied (see Sec. 1.3):

$$\Gamma_{\alpha_v^+} \otimes \Gamma_{\alpha_v} \supset \Gamma^s \tag{1.22}$$

$$\Gamma_e \otimes \Gamma_{\alpha_v^+} \otimes \Gamma_{dipole} \otimes \Gamma_{\alpha_v} \supset \Gamma^s \tag{1.23}$$

The most general form of the angle-resolved flux, $I(\theta,\phi)$, originally developed for nuclear reaction measurements [156], can be expressed as:

$$I(\theta,\phi) = \sum_{L}^{L_{max}} \sum_{M=-L}^{L} \beta_{L,M} Y_{L,M}(\theta,\phi) \tag{1.24}$$

where $Y_{L,M}(\theta,\phi)$ is a spherical harmonic function of rank and order L and M, respectively. $\beta_{L,M}$ are the expansion parameters, often termed anisotropy parameters which contain information on the underlying photoionisation dynamics of the system. The allowed values of L and M which appear in Eq. 1.24 depend on the experimental geometry (i.e. the polarisation state of the light) and properties of the molecule undergoing ionisation.

For all experiments presented in this thesis the reference frame of the photoionisation dynamics is the lab frame. This places a limit on the maximum allowed value of L in Eq. 1.24 such that $L_{max} = 2N$, where N is the number of photons which interact with the system. Truncating this expansion at a particular value of L also determined the maximum anisotropy that can be created in the lab frame from an initially isotropic distribution [21]. This point is exemplified in the data presented in Fig. 1.10, where angle-resolved photoelectron spectra are shown for ATI of Xe. Due to the large number of photons involved in ATI processes the resultant spectra can exhibit complex angular structure, well beyond what is typically observed in

either single photon ionisation or most time-resolved measurements, since Eq. 1.24 is truncated at relatively low rank.

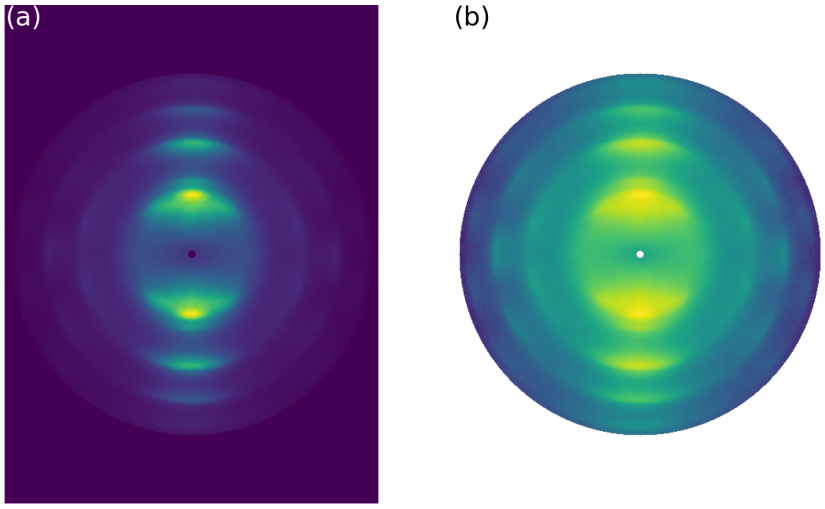

Figure 1.10: Angle-resolved ATI photoelectron spectra of Xe recorded using a velocity map imaging (VMI) spectrometer. The estimated laser intensity was $\sim 5\times10^{13}\mathrm{Wcm}^{-2}$ and the polarisation is aligned vertically. Details of the spectrometer used to record this data are given in Sec. 3.2.2

Constraints can also be placed on the allowed values of both L and M by symmetry. For example, if reflection symmetry is present, L must be even, and cylindrical symmetry restricts terms to $M = 0$ only, due to the the system exhibiting no dependence on the azimuthal emission angle ϕ. These symmetry constraints are present in each of the experiments, be it time-resolved (Chapter 3) and energy-resolved (Chapters 4-5), where PADs are measured and hence the common place alternative representation of Eq. 1.24 in terms of Legendre polynomials will be adopted throughout the thesis. This mapping is possible because $Y_{L,0} \propto P_L(\cos(\theta))$, where $P_L(\cos(\theta))$ are Legendre polynomials in $\cos(\theta)$ and results in the following expression:

$$I(\theta) = \sum_{L}^{L_{max}} \beta_L P_L(\cos(\theta)) \tag{1.25}$$

It is important to note β_L in Eq. 1.25 and $\beta_{L,M}$ in Eq. 1.24 are not equivalent as the angular functions have different normalisation factors.

Finally, if a photoionisation experiment is conducted in the molecular frame, the allowed terms in Eq. 1.24 no longer depend on the experimental geometry (i.e. number of photons involved and/or polarisation geometry) and are determined by molecular symmetry and the maximum angular momentum component of the photoelectron wavefunction [21, 157]. This generally results in the molecular frame PADs containing much richer angular structure than those recorded in LF measurements as has been demonstrated, in for example, inner shell energy-resolved [91] and time-resolved experiments [26, 27].

1.9 Time-resolved photoelectron spectroscopy (TRPES)

In essence TRPES can be viewed as the wavepacket methodology (Sec. 1.1) with the probe step as photoionisation. This, as mentioned in the introduction, is an advantageous choice compared other techniques since it has the ability to detect any final state (provided the photon energy is sufficient) because of the relaxed selection rules for photoionisation. Typically TRPES experiments are conducted with a femtosecond pulse pair in the UV region of the spectrum (see for example Refs. [30–32, 37] and references therein) but can also be conducted with VUV [31, 33, 158], XUV [159, 160] and soft X-ray [40] pulses or using SFI. Each of these probe techniques have their unique advantages, such as site specificity or improved temporal resolution, as well as caveats, and hence are all actively being explored in the context of TRPES by many research groups. This is area of research is often referred to as “the physics of the probe”.

Despite differences in photon energy and intensity, the experiments generally share a common aim of tracking non-adiabatic photochemical dynamics in molecular systems by exploiting the sensitivity of TRPES to both electronic and nuclear configurations [13, 14]. In Chapter 2 of this thesis a UV pump+SFI probe CRATI experiment on probing non-adiabatic in the polyatomic molecule NO_2 is presented.

This study, to our knowledge, is the first time-resolved SFI based TRPES experiment and hence significant discussion is provided on the information content extractable in this type of experimental method. Chapter 3 deals with VUV pump + UV probe angle-resolved TRPES measurement of Rydberg valence coupling in acetone (CH_3COCH_3). This study, although not dealing with a new regime of photoionisation in the probe step, exploited a novel VUV femtosecond laser source as the pump.

The aim of the remainder of the section is to provide an intuitive picture of TRPES with the role of non-adiabatic dynamics discussed in Sec. 1.9.1 and the expected energy correlations in TRPES outlined in Sec. 1.9.2.

1.9.1 Probing non-adiabatic dynamics

Although the BOA (see Sec. 1.2) provides a simple and intuitive description of molecular dynamics on a single electronic state, non-adiabatic processes occur when several electronic states are coupled by vibrational motions [1–4]. In Fig 1.11 a schematic diagram to illustrate this concept is presented. Here some "fraction" of the excited state wavepacket crosses from one electronic state, α, to another, β, clearly representing a breakdown of the BOA. In a TRPES experiment the goal is to have the ability to track both the excited state vibrational dynamics, via the FC envelope, and evolving excited state electronic configurations. The latter are understood to be projected out via the continuum electronic structures (i.e. the final state of the photoelectron plus residual ion). Typically it is useful to invoke a Koopmans' picture of the probe photoionisation step and hence assume that the electron emission occurs without the simultaneous electronic reorganisation of the ionic or neutral core (see Sec 1.4). This simplification results in a set of simple and intuitive correlation rules which indicate the possible final cationic state formed upon photoionisation of a given neutral state.

Although not a complete generality, it is common place for the partial photoionisation cross sections for a particular cationic electronic state to differ drastically with respect to the electronic structure of the probed neutral state. Therefore,

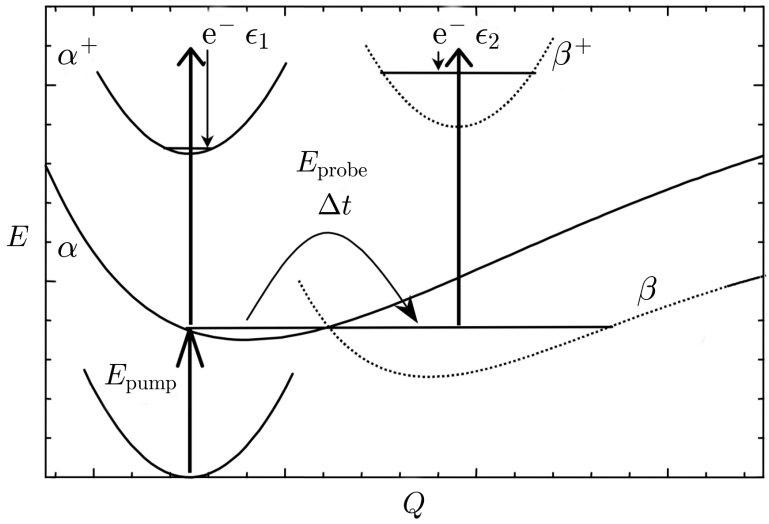

Figure 1.11: A schematic diagram showing TRPES applied to disentangling electronic and vibrational dynamics in an excited polyatomic molecule. A femtosecond pump pulse (E_{pump}) excites an electronic state α which subsequently decays, via a non-adiabatic process, to a vibrationally hot lower-lying electronic state, β. This particular scheme exhibits Type(I) Koopmans' correlations and therefore these two states will be ionised by the probe pulse (E_{probe}) into different electronic continua: $\alpha \rightarrow \alpha^+ + e^-(\varepsilon_1)$ and $\beta \rightarrow \beta^+ + e^-(\varepsilon_2)$. Figure adapted from Fig. 2 of Ref. [14].

in the ideal case, the electronic states of the cation can provide a "template" of evolving electronic population dynamics in the neutral prior to ionisation, if different electronic neutral states correlate with different final ionic states. This correlation may, for example, result in the appearance of a new band in the photoelectron spectrum at a different energy due to differences in ionisation potential between the sets of neutral and ionic states. The above represents the ideal case of Koopmans' Type(I) correlations [161] and is illustrated in Fig. 1.11, where ionisation from α correlates with α^+ and β with β^+. However, a second situation is possible where the neutral states α and β have ionisation correlations to the same final state, which can make disentangling non-adiabatic dynamics by photoelectron kinetic energy

distributions alone challenging. Measurement of PADs (see Sec. 1.8) can however provide a means to extract this due to the angular distribution being sensitive to neutral electronic configurations and symmetries as well as FC factors. The case of ionisation correlating to the same final state corresponds to a Type(II) Koopmans' correlation [162]. Examples of Type (I) Koopmans' correlations are presented in the acetone data shown in Chapter 3.

1.9.2 Photoelectron kinetic energies in TRPES

In a TRPES experiment according to the energy conservation principle, the following equality must hold:

$$E_0(v) + \hbar\omega_{\text{pump}} + \hbar\omega_{\text{probe}} = I_{\text{p}}^{j} + E_{\text{ion}}(v) + E_{\text{kin}}, \tag{1.26}$$

where $E_0(v)$ refers to the internal energy of the initial state, $\hbar\omega_{\text{pump}}$ and $\hbar\omega_{\text{pump}}$ are the photon energies of the pump and probe pulses, respectively and $E_{\text{ion}}(v)$ refers to the vibrational energy retained in the ion. In gas-phase experiments it is typical to make the approximation that the rovibrational energy of the initial state is negligible as experiments are conducted in ultrasonic expansions and therefore rewrite Eq. 1.26 as:

$$E_{\text{kin}} \approx \hbar\omega_{\text{pump}} + \hbar\omega_{\text{probe}} - [I_{\text{p}}^{j} + E_{\text{ion}}(v)] \tag{1.27}$$

this expression, under the proviso that $\hbar\omega_{\text{pump}}$ and $\hbar\omega_{\text{pump}}$ are known, relates the kinetic energy of outgoing photoelectron to a particular final cationic state. The internal vibrational energy deposited in the cation ($E_{\text{ion}}(v)$) depends on the FC factors (see Eq. 1.10 and surrounding text). In certain cases a further approximation can be applied which assumes that no vibrational excitation occurs during photoionisation (i.e. $E_{\text{n}}(v) \approx E_{\text{ion}}(v)$, where $E_{\text{n}}(v)$ is the vibrational excess energies in the electronically excited intermediate state) and therefore that the FC factors are diagonal. This is commonly referred to as the $\Delta v = 0$ propensity rule and is generally a good first order approximation in, for example, photoionisation of molecular Rydberg states [163] or non-bonding orbitals. Although not for an excited state, a good

example of the latter is the ground state valence photoelectron spectra of CH_3I correlating to the $\tilde{X}^2A_1$ doublet presented in Fig. 1.2. The above assumption allows E_{kin} to be related to the energy of the photoexcited electronic state, E_n:

$$E_{kin} \approx E_n + \hbar\omega_{probe} - I_p^j. \tag{1.28}$$

This type of analysis is used extensively for assignment of various molecular Rydberg states of acetone in Chapter 3.

As only a handful of experimental investigations have been carried on probing non-adiabatic dynamics using core-level photoionisation or SFI it remains to be seen how the relatively intuitive ideas on how to interpret/understand energy-resolved TRPES will map onto different regimes of photoionisation.

1.10 Outline of the thesis

This thesis is structured as follows. Chapter 2 describes a femtosecond UV pump-SFI probe CRATI experiment aiming to disentangle non-adiabatic dynamics in NO_2 and better understand how SFI probes excited states in polyatomics. In Chapter 3 the construction and implementation of a femtosecond VUV source based on four-wave mixing is outlined. This source was then utilised in various VUV pump-UV probe schemes to study Rydberg-valence coupling in the acetone. Chapters 4 and 5 contain results on the ground state core-level photoionisation and subsequent Auger decay dynamics of the 3d shell in CH_3I. These experiments were carried out to provide foundational data and understanding for forthcoming dynamical experiments at, for example, FELs that use Auger spectra or core level photoionisation as a probe. Finally, a summary of the thesis is presented in Chapter 6.

Chapter 2

Strong-field ionisation of NO_2

2.1 Introduction

The use of strong-field ionisation (SFI) based probe techniques, such as high-harmonic generation (HHG) and above-threshold ionisation (ATI), as a probe technique in the study of molecular electronic dynamics has received considerable attention [49, 50, 144, 146, 152, 153, 164]. This is in part due to both ATI and HHG being subcycle phenomena, meaning that subfemtosecond time-resolution may be achievable in experimental measurements. For example, UV pump-HHG probe spectroscopy has been applied to study molecular wavepacket dynamics in the molecules N_2O_4 [146], Br_2 [50], NO_2 [165–167], CH_3I and CF_3I [168]. In the interpretation of these HHG experiments, extensive use was made of the three-step model [47, 169].

Recent studies from Villeneuve and co-workers, where UV pump-HHG probe spectroscopy was applied to the photodissociation in Br_2 [50, 51], highlighted that HHG is particularly sensitive to: (i) variation of the vertical ionisation potential along the reaction coordinate, through the phase of the emitted harmonics and; (ii) electronic structure of the dissociating molecule through the photorecombination matrix elements [170, 171]. In contrast to Br_2, the vast majority of photochemical processes in polyatomic molecules involve multiple electronic states and significant geometry changes during the reaction. This means that, within the narrative of the three-step model, both the first step - involving SFI rates - and the third step

- involving recombination dipole matrix elements - will vary as the wavepacket evolves. It will therefore be critically important, for the interpretation of strong-field experiments on molecular dynamics, to understand the relative roles of both the SFI rate and recombination dipoles as a function of wavepacket evolution.

To further benchmark the use of SFI based probes of molecular dynamics, an experimental UV pump-SFI probe study on non-adiabatic wavepacket dynamics in the polyatomic NO_2 is presented in this chapter. In order to disentangle the role of multiple ionisation continua (see Sec 1.7.1), which may be operative during molecular SFI, this study made use of a previously developed an ATI probe technique, termed Channel-Resolved ATI (CRATI) [152, 153]. The NO_2 molecule is an exemplary system with which to study strong-field probing of photoexcited polyatomic molecules due the presence of non-adiabatic couplings between electronic states, intramolecular vibrational energy redistribution (IVR) and neutral dissociation pathways. The literature associated with this system is extensive in both the frequency [172–180] and time domains [165–167, 181–187] and hence adds to the suitability of NO_2 as an important system for studying the nature of pump-SFI probe spectroscopies in polyatomics. The photodynamics of NO_2 have been reviewed and summarised by Wilkinson and Whitaker [188].

For the experimental study presented here, the primary focus is on the photochemical dynamics close to the first dissociation limit of NO_2 located at 3.1155 eV [188]. Single-photon vertical photoexcitation at wavelengths around this dissociation limit transfers population from the ground electronic state, $\tilde{X}\ ^2A_1$ (labeled in C_{2v} symmetry), to the first optically bright electronic state, $\tilde{A}\ ^2B_2$. Initially, the wavepacket motion on the excited state is quasi-one-dimensional along the bending coordinate and moves rapidly towards a conical intersection between the $\tilde{A}\ ^2B_2$ and $\tilde{X}\ ^2A_1$ states. The wavepacket can either cross the intersection diabatically or adiabatically or both (i.e. a non-adiabatic process) [189,190]. The diabatic component is expected to make several passes of the intersection, but significant population transfer back to the ground state does occur within 50 fs and the majority of population is transfered back to the ground state within approximately 200 fs [190]. In addition,

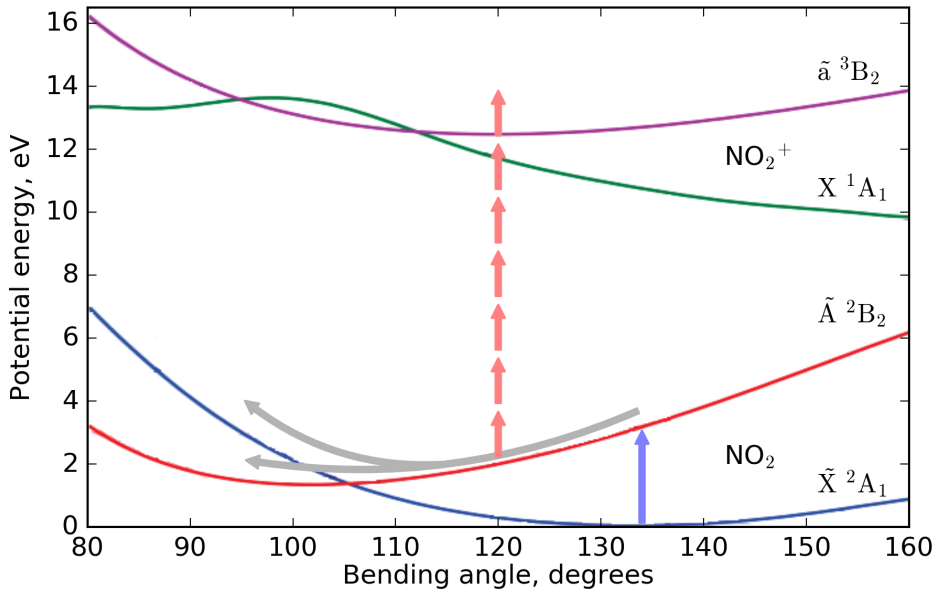

Figure 2.1: Potential energy surfaces as a function of ONO bending angle for the important electronic states of NO_2 and NO_2^+ involved in single-photon excitation and subsequent strong-field probing at 798 nm (red arrows). Photoexcitation at 399 nm (blue arrow) prepares a vibrational wavepacket on the $\tilde{A}\ ^2B_2$ state which subsequently transfers population back to the $\tilde{X}\ ^2A_1$ state via a conical intersection.

within a few hundred femtoseconds, IVR results in the wavepacket spreading into the asymmetric (and symmetric) stretch coordinate and, for molecules with an internal energy above 3.1155 eV, eventual neutral dissociation producing NO ($X^2\Pi$) and O (^3P) via unimolecular decay on a picosecond time scale [191].

Numerous femtosecond time-resolved studies have been carried out to investigate the dynamics originating from the $\tilde{A}\ ^2B_2$ state, employing a range of technique such as two-colour fluorescence depletion [181], mass spectrometry [185] and velocity map imaging (VMI) of photoions and photoelectrons [183, 187], coincidence imaging studies [184, 186] and novel high-harmonic probes [165–167]. Recently, a series of femtosecond time-resolved imaging experiments employing pulses at 400 nm and 266 nm have investigated photofragmentation dynamics in NO_2. These experimental studies reported time-dependent oscillations in the NO^+ fragment and slow (near 0 eV) photoelectron yields with periods in the range of 500-850 fs [182, 183, 186, 187]. A series of differing interpretations have been sug-

gested as to the origin of the observed modulations, including: the energy level spacing between coupled levels in the $\tilde{A}\ ^2B_2$ and $\tilde{X}\ ^2A_1$ states close to their conical intersection [182]; wavepacket motion along a "soft coordinate" with a corresponding energy level spacing of 40 cm^{-1}, with the motion potentially linked to a free rotation of an oxygen atom around an NO core at large NO-O bond lengths [183] (roaming atom mechanism [192]); motion in the asymmetric stretch coordinate; and resonances between symmetric stretch and bend vibrations at energies close to the NO ($X^2\Pi$) and O (^3P) dissociation threshold [193].

Recently, time-resolved HHG studies reported a small number of oscillations in high harmonic signals with a period on the order of 100 fs, which was assigned to $\tilde{A}\ ^2B_2/\tilde{X}\ ^2A_1$ vibronic coupling [165] due to its similar appearance to the theoretical predictions [167, 190]. In contrast to both the imaging and HHG studies, 200 fs oscillations were observed in time-resolved mass spectrometry studies [185], which have again been tentatively assigned to conical intersection dynamics. However, recent coincidence imaging studies employing pulses at 400 nm and 266 nm have identified a number of different competing multiphoton pump laser channels leading to the formation of NO_2^+ or NO^+ cations and corresponding photoelectrons [184, 186]. The participation of multiphoton pump laser channels may equally occur but be obfuscated in less differential (i.e. not channel-specific) measurements such as time-resolved mass spectrometry or high harmonic spectroscopy. This, therefore, may effect the interpretation of the previous experimental results. With this in mind and the ambiguity in the interpretation of the oscillations observed via different probe schemes, we revisit here the excited state dynamics of NO_2. In the present study, 399 nm weak field pump and 798 nm strong-field probe femtosecond laser pulses, in conjunction with PEPICO spectroscopy, were utilised to investigate the dynamics following excitation to the $\tilde{A}\ ^2B_2$ state and to assess contributions of multiphoton pump excitation channels in the observed dynamics (see Fig. 2.1).

The remainder of this chapter is structured as follows. In Sec. 2.2, a description of the experimental set-up is given, in Sec. 2.3 the data analysis tools used in the interpretation of the PEPICO spectra are presented. Details of the procedure used to

calibrate the probe, and estimate the pump, laser intensities are outlined in Sec.. 2.4 and in Sec.. 2.5 the experimental results are shown. In Sec. 2.6, the experimental results are interpreted in terms of both single and multiphoton pump laser dynamics and, finally, the conclusions are summarised in Sec. 2.7.

2.2 Experimental set-up

The NRC laser system, an amplified Coherent Legend Elite Duo, delivered 35 fs pulses at 798 nm with a pulse energy of 8.0 mJ at a repetition rate of 1 kHz. Fig. 2.2 provides a schematic illustration of the optical set-up employed in these experiments. Part of the output (0.5 mJ) of the Legend Elite Duo was beamsplit and passed through a 2:1 reflecting telescope, which utilised curved mirrors with high reflectivity at 798 nm. Further attenuation, if required, to this beam was provided by a half ($\lambda/2$) waveplate and a set of thin film polarizers (TFP). The 0.5 mJ beam was passed through a 85:15 beamsplitter to provide the pump and probe beams, respectively. The reflected 85% was frequency doubled using a 200 μm Beta Barium Borate (β-BaB_2O_4), BBO, crystal cut at 29.2°, to provide 399 nm pulses with an estimated pulse duration of 45 fs. A $\lambda/2$ waveplate at 798 nm was placed before the BBO crystal in order to provide independent attenuation of the pump pulse power. Presented in Fig. 2.3 are typical spectra of the pump and probe pulses recorded using a spectrometer (USB4000 Ocean Optics Inc.).

Dichroic mirrors with high reflectivity (HR) at 399 nm and high transmission (HT) at 798 nm were used for separating the fundamental and second harmonic, and also for recombining the pump and probe beams in a collinear geometry. To ensure minimal dispersion of the 798 nm probe pulse during recombination, with the pump pulse, a minimal thickness dichroic mirror (3 mm fused silica substrate) was chosen. However, despite the careful choice of this optic, some self-phase modulation of 798 nm probe beam was observed after recombination. This is evident by the plateau in the shorter wavelength region of the 798 nm spectra in Fig. 2.3(b). The collinear beams were then focused into the coincidence spectrometer

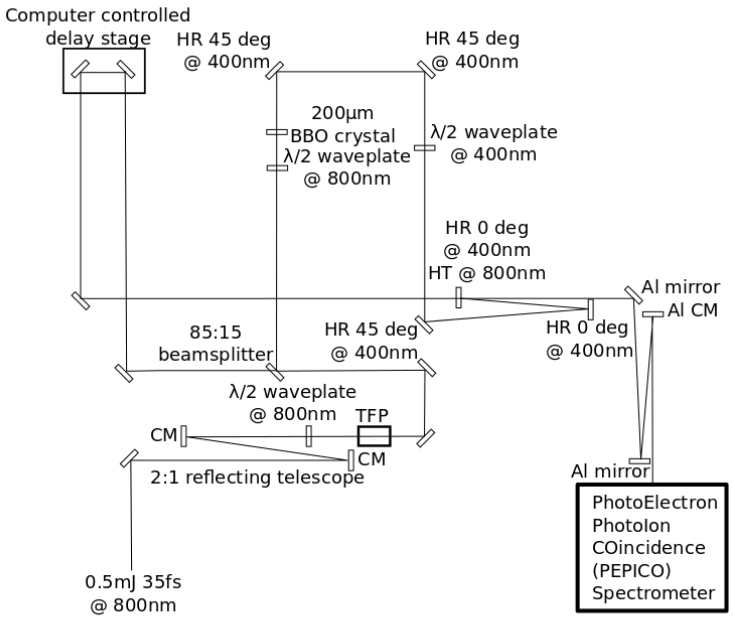

Figure 2.2: Schematic overview of the optical setup used in strong-field ionisation experiments on NO_2. Optical elements labels are further explained in the main text. All optics absent of labels are dielectric high reflecting mirrors at 800 nm.

using an f = 0.5 m spherical reflective Al mirror (Al CM). The Rayleigh range of each beam at the foci was estimated to be 10 mm and 5 mm, and the approximate Gaussian beam radii at the foci was 50 μm and 25 μm at 798 nm and 399 nm, respectively. The relatively long Rayleigh range of the laser focii ensured a constant axial intensity in the laser ionisation volume, thus minimizing the effects of volume spatial intensity averaging [194]. Additionally, the smaller Gaussian beam radii of the pump compared to probe pulses, at the laser focus, served to reduce the effect of intensity averaging in the pump-probe data.

The time delay between the pump and probe beams was varied using a computer controlled delay stage (Newport XML210) and a set of retroflector mirrors. The temporal overlap of the pump and probes pulses was determined *in-situ* by examining the non-resonant ionisation signal of background H_2O and co-expanded O_2 in the spectrometer and fitting the associated parent ion channels with a Gaussian

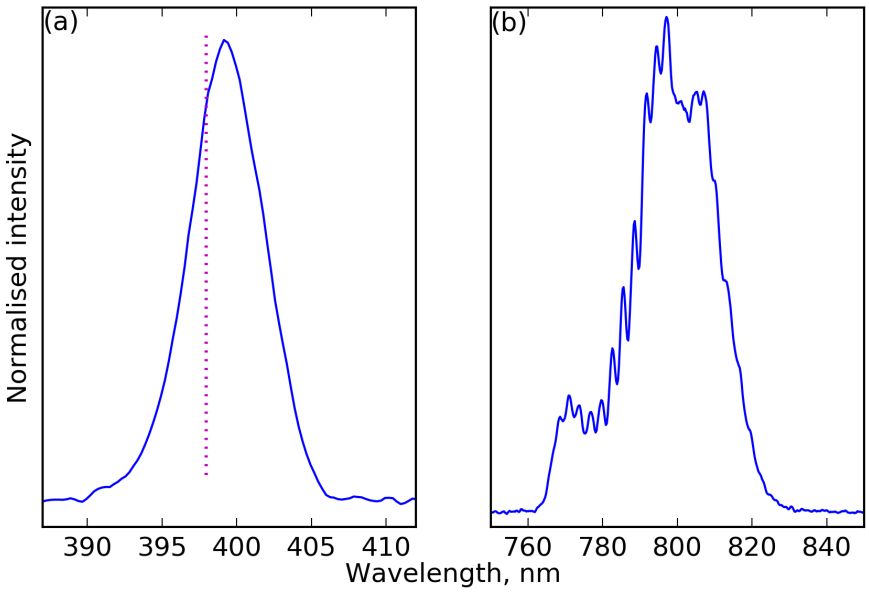

Figure 2.3: Typical spectra of the (a) pump and (b) probe pulses, measured with an Ocean Optics HR400 spectrometer. The dashed magenta line in panel (a) denotes the first NO ($X^2\Pi$) and O (^3P) dissociation limit at 397.96 nm.

function. The average temporal cross-correlation was determined to be 55 fs Full Width at Half Maximum (FWHM). Linearly polarised laser pulses were employed throughout the measurements, with the relative polarisation between the two beams being controlled and varied using a $\lambda/2$ waveplate at 399 nm mounted in a computer controlled rotation stage placed in the pump beamline prior to pump-probe recombination. The polarisation of the 798 nm probe remained parallel to the spectrometer Time-of-Flight (ToF) axis. This ensured ensured that the electron detection efficiency was independent of probe laser polarisation throughout the experiments.

The PEPICO/CRATI spectrometer used to carry out these experiments was described previously in Refs. [152, 153, 195, 196]. A gas mixture of 1.5% NO_2 (Praxair Canada Inc., 99.5%) seeded in He (BOC GAZ, 5N purity) was continuously expanded through a 50 μm pinhole into a source chamber held at a pressure of around 3×10^{-6} Torr (molecular beam on). Additionally, 3% O_2 (Praxair Canada Inc., 5N purity) was added to the mixture to help ensure the equilibrium between NO and NO_2 was displaced towards NO_2. To ensure that the experimental signals reported here are free from contributions associated with NO_2 dimer the expansion

was created using a nozzle held at 350 K to yield a NO_2/N_2O_4 equilibrium of 99.8% in favor of the monomer. Additionally, it should be noted that absorption of NO_2 dominates at 399 nm where N_2O_4 has an extremely low single-photon excitation probability [197].

The molecular beam passed through a 1 mm skimmer and subsequently entered a differentially pumped interaction chamber. A second skimmer, 0.75 mm, was then used to yield a beam of approximately 1 mm diameter at the center of the detection chamber. This chamber was typically held at a base pressure of 1×10^{-8} Torr during the molecular beam experiment. The laser propagated perpendicularly to the molecular beam and intersected at a distance of 600 mm from the second skimmer. Photoelectrons were extracted from the laser-molecular beam interaction region by a large bore (20 mm inner diameter) icosapole (20-pole) permanent magnet, magnetic bottle spectrometer [198]. The spectrometer has a 30 cm ToF length and is designed to ensure efficient collection of photoelectrons, >75% (i.e. magnetic mirror mode), by placing the interaction region on the negative slope of the axial magnetic field intensity. This geometry allows collection of a large solid angle of electrons, including a subset of electrons emitted in the opposite direction to the electron ToF region, at the expenses of slightly poorer energy resolution. The kinetic energy resolution of the magnetic bottle spectrometer, determined via (1+1′) photoionisation of NO, was $\Delta E/E$ = 160 meV at 1 eV and electrons were collected up to an energy of approximately 15 eV. Coincident ion detection was achieved by means of a coaxial pulsed Wiley-McLaren ToF mass spectrometer [199]. The ion ToF was operated under Wiley-McLaren space and energy focusing conditions to maximize mass resolution. The TOF mass resolution was measured to be M = 1 amu at 100 amu. The ToF axis in the detection chamber was oriented orthogonally to both the laser and molecular beam propagation directions and detection of ions and electrons from a single ionisation event was performed using two sets of 40 mm (outer diameter) triple-stack microchannel plate detectors (MCPs). The electron and ion signals were amplified (Philips Scientific 300 MHz Bipolar Amplifier 6950), passed through a constant fraction discriminator (Philips Scientific 300 MHz Discrimina-

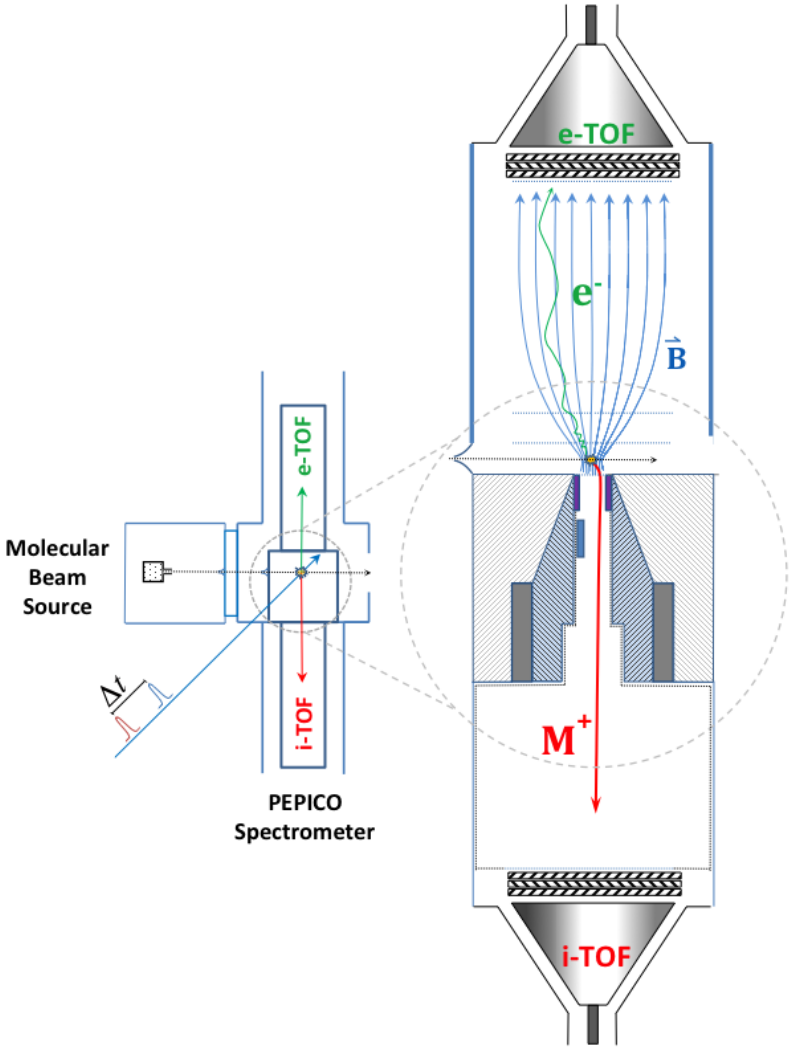

Figure 2.4: A depiction of the Photoelectron-Photoion Coincidence (PEPICO) spectrometer utilised in the experiments presented here. A skimmed molecular beam introduced NO_2 molecules to the interaction region of a dual time-of-flight (TOF) PEPICO spectrometer. Photoelectrons (e^-) were collected along the e-TOF, yielding the kinetic energy resolved photoelectron spectrum, whereas coincident ions (M^+) were collected along the i-TOF, yielding the mass spectrum. The total TRCRATI spectra was then generated by scanning the pump-probe time-delay (Δt) between the pump (blue) and probe (red) laser pulses. A detail description of the spectrometer, as well as the data acquisition procedure, is given in the main text.

tor 6904) and their arrival time recorded using a multichannel scaler card (FAST Comtec GmbH P788). A conceptual diagram of the magnetic bottle PEPICO spectrometer and the experimental setup utilised in this study, and described above, is presented in Fig. 2.4. Further technical details concerning the PEPICO spectrometer design can be found in Ref. [196].

The total TRCRATI spectrum was then generated by scanning the pump-probe time-delay over a range between -250 and +10000 fs, with variable step sizes. Pump-probe delay scans were performed with high-temporal resolution (step size 10-20 fs) between -250 and +500 fs only. At each time delay, pump-probe and time-independent probe-alone signals were recorded for 5000 and 1000 laser shots, respectively. Additionally, time-independent pump-alone signals were recorded for 1000 laser shots in higher intensity experiments where pump-alone counts were observed. Typically, negligible signals were observed in the pump-alone case. The experimental data were recorded for two linear polarization geometries: (i) pump and probe polarisation vectors set parallel to the ToF axis of the spectrometer, referred to as the parallel geometry; and (ii) with the pump set perpendicularly to the probe polarisation and the ToF axis, referred to as the perpendicular geometry. The polarisation between the pump and probe pulses was rotated between the two geometries every consecutive time-delay scan. This was done to mitigate the effects of long term drifts of the laser system and ensure consistency between two polarisation geometry datasets. The pump-probe delay range was swept through 20-30 times, depending on the signal strength, for each of the polarisation geometries. This resulted in acquisition times of approximately 12 hours for a given set of experimental conditions. Finally, spectra similar to those presented in Fig. 2.3 were recorded before and after each of the experimental runs to ensure consistency between different datasets.

2.3 Data analysis

Typically the correlation between photoelectron and photoion ToF signals, such as the ones presented in this chapter, is achieved by coincident detection. In true

coincidence mode, the average number of ionisation events per laser shot is required to be less than one in order to prevent false coincidences where, due to the finite detection efficiency of the spectrometer, ion and electrons from different events may be erroneously correlated. This places stringent requirements on the data acquisition rate and, when combined with superfluous ionisation events from background gases within the extended laser focal volume, makes true coincidence measurements of quite tedious [152]. This is particularly true in these experiments where data was collected over 85 pump-probe time delays and photoelectron spectra correlated with multiple ionic channels are considered.

To help ease the requirements on the data acquisition rate the photoelectron and photoion ToF signals were correlated using covariance mapping, a method introduced by Frasinski and co-workers [200, 201]. The covariance between a photoelectron ToF, t_e (corresponding to kinetic energy, E_e) and a ion ToF, t_i (corresponding to mass, m_i) and is given by

$$\mathrm{cov}[I(t_i), E(t_e)] = \overline{I(t_i)E(t_e)} - \overline{I(t_i)} \cdot \overline{E(t_e)} \tag{2.1}$$

where the electron-ion covariance is determined for each laser shot and the average is evaluated over all laser shots. For a particular laser shot, $I(t_i)$ and $E(t_e)$ are the number of ions at a specific mass, and photoelectrons at a specific kinetic energy, respectively. The TRCRATI spectra, shown in Sec. 2.5, were then generated by performing the covariance analysis at each Δt and integrating the resulting covariance map over individual ion masses. In all experiments presented here, background counts were observed from the probe laser alone and therefore covariant probe-alone signals were subtracted from the pump-probe signal. Typically, in all but the highest pump intensity experiments, covariant pump-alone signals were not observed and, therefore, were only subtracted when required.

The recording of the two orthogonal relative polarisation geometries permits the linear dichroism (LD) to be extracted. The LD provides a measure of the photoionisation anisotropy between the two polarization geometries and assesses any dependence on the alignment created in the excited state by the pump pulse. The

time-dependent linear dichroism (TDLD) is expressed as

$$\mathrm{LD}(\parallel,\perp,E,t) = \frac{I(\parallel,E,t) - I(\perp,E,t)}{\max(I(\parallel,E,t) - I(\perp,E,t))} \tag{2.2}$$

where $\parallel$ and $\perp$ refer to the parallel and perpendicular polarisation geometries, respectively and I refers to the intensity of the photoelectron or photoion signals. Eq. 2.2 has been normalised to the maximum value of the difference between the parallel and perpendicular signals. In the case of the LD associated with the time-resolved ion-yields, we note that the kinetic energy dependence can be neglected due to the ion-yield (in our implementation) being a kinetic energy integrated observable.

2.4 Intensity calibration of the experimental data

The absolute intensities of the probe laser pulses were extracted by examining the intensity dependence of the ATI comb correlated with the H_2O molecule, trace amount of which are always found in the spectrometer vacuum chamber. This background gas served as a convenient calibrant during each experimental data run as ionisation occurs in the same laser interaction region as the target molecule NO_2. For H_2O the absolute laser intensity can directly be extracted from the ATI comb peak position due to the fact that the polarisability, and hence the molecular Stark shift, is negligible across the intensity ranges used in this, as well as previous [152], SFI studies conducted on the same apparatus. If the Stark shift to the ionisation potential is neglected (see Eq. 1.20), then the ATI comb peak position can be directly related to the pondermotive shift, U_P. The probe laser intensity can then simply be extracted for specific U_P through Eq. 1.19.

In the fitting of the peak electron kinetic energy positions, initial guesses of U_P were provided from intensity estimates calculated assuming a Gaussian beam, focused using a mirror, f = 0.5 m, and pulse duration of 40 fs. The pre-focused beam diameter, d, was measured using a power head and an iris closed until 87 % (1-1/e^2) transmission was achieved. Finally, unlike the probe pulses, estimation of the intensity of the 399 nm pump pulse is a more challenging task due since no

ionisation, and by extension, ATI peaks are observed from pump pulse alone. It is therefore assumed that the Gaussian beam intensity estimates method outlined above are applicable. A 399 nm pulse duration of 45 fs was used, which appears reasonable based on the *in-situ* cross correlation measurements outlined in Sec. 2.2. The results of this calibration processes are outlined in Table 2.1 in the subsequent section.

2.5 Experimental results

The intense nature of ultrashort laser fields can often result in the absorption of multiple photons during the duration of a pulse. This is egregious for the interpretation of time-resolved experiments since it leads to complications in understanding the nature of the wavepacket prepared initially by the pump pulse. In order to ensure the dynamics associated with single-photon excitation of NO_2 molecules are correctly identified, the TRCRATI spectra were recorded at three different pump intensities and, at each pump intensity, three different probe intensities. The latter probe intensity study was undertaken to help evaluate the role of processes such as intensity averaging during strong-field probing. The estimated pump and calibrated probe intensities (see Sec. 2.4), as well as the beam parameters, utilised in this study are summarised in Table 2.1.

Table 2.1: Estimated and calibrated 399 and 798 nm pump and probe intensities, respectively. The values were obtained using the procedure outlined in Sec. 2.4.

λ (nm)	1-1/e^2 d (mm)	Pulse energy (μJ)	Estimated intensity (Wcm^{-2})	Calibrated intensity (Wcm^{-2})
798	5.17	58	1.9×10^{13}	1.7×10^{13}
		70	2.3×10^{13}	1.9×10^{13}
		90	3.0×10^{13}	2.2×10^{13}
399	4.7	1	9.6×10^{11}	
		5	4.8×10^{12}	
		15	1.4×10^{13}	

Before the time-resolved coincidence data is presented, the role of geometric

intensity averaging in the laser focal volume is considered. In Fig. 2.5 the probe alone ATI electron spectra correlated with (a) NO_2^+ and (b) H_2O^+ ions are presented for the three probe intensities outlined above. Numerous observations can be drawn from the intensity dependence of the ATI combs: (i) There is clearly no significant loss in contrast in combs structure at higher probe intensities which suggests that intensity averaging does not play a significant role; (ii) The whole ATI comb shifts with laser intensity, as described by Eq. 1.20 in Sec. 1.7.1; (iii) By contrast, there exists several sharp peaks seen at low electron kinetic energies whose positions are invariant with respect to laser intensity. These peaks are known as Freeman resonances [43].

Freeman resonances originate from the fact that laser focal volume can be considered a series of hyperbolic shells of different constant intensities, which range from zero to the maximum intensity, I_{max}. Within the focal volume there exists shells of specific intensities where neutral Rydberg states are Stark-shifted into multiphoton resonance with the strong laser field. An electron in a Rydberg state, by its very nature, will experience a ponderomotive potential similar to that of a continuum electron and result in spectral features independent of laser intensity. The Freeman resonances also vanish more quickly than the normal ATI peaks due a difference in scaling with the number of absorbed photons (i.e. the Rydberg states involved have a low IP and cannot survive in the laser field). Therefore, in the analysis of the ATI combs presented here, any conclusions drawn were checked to be apparent for several ATI comb orders and not only for the lowest energy ATI peak, which is most effected by Freeman resonances.

Initially, experiments with the pump and probe intensities set at 4.8×10^{12} W cm^{-2} and 1.7×10^{13} W cm^{-2}, respectively, are considered. In order to assess which ionisation channels contribute significantly the simplest observable, the mass spectrum, is first examined for the employed experimental conditions. In Fig. 2.6 example mass spectra are shown for the parallel polarisation geometry at several time delays (0 fs, 300 fs and 1000 fs). At the temporal overlap of the pump and probe pulses

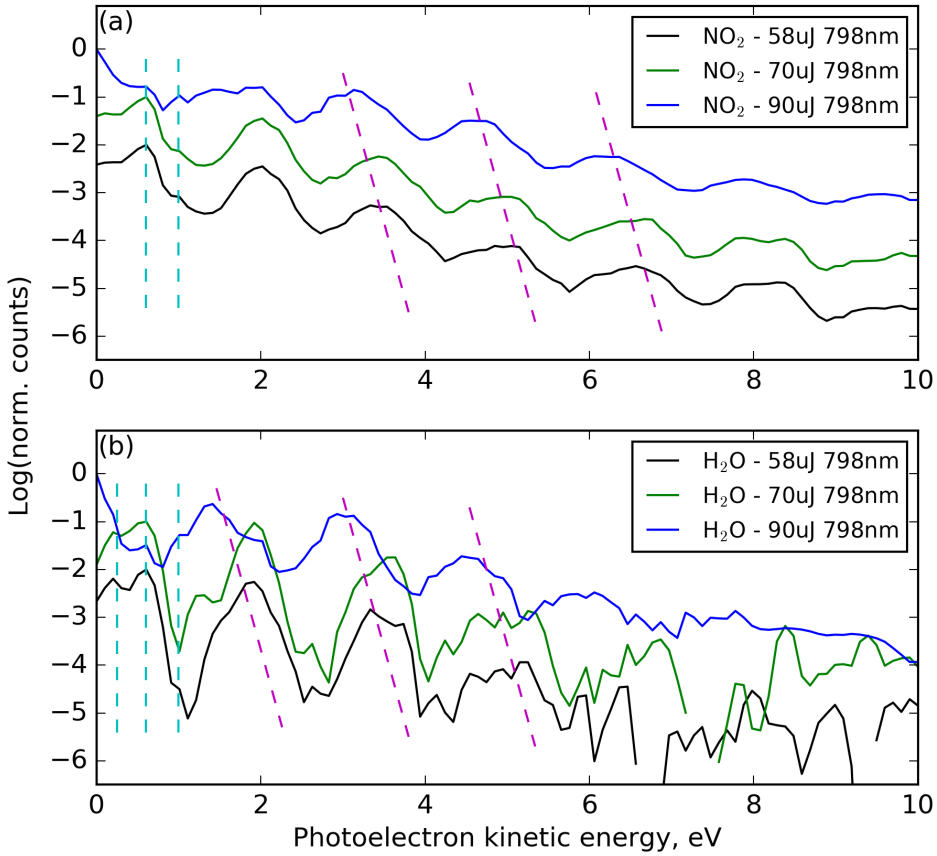

Figure 2.5: Probe alone ATI photoelectron spectra of (a) NO_2 and (b) H_2O as a function of laser pulse energy and therefore intensity. In both cases the ATI peaks shift (dashed magenta lines) monotonically with intensity, whereas the Freeman resonances (see main text), seen at low electron kinetic energies, are independent of laser intensity (dashed cyan lines).

(0 fs) it is evident that the NO_2^+ parent ion signal dominates the mass spectra. Outside of this region however, the dominant channel is fragmentation to form NO^+. The counts in this channel vary between 0.25 and 8 times that of NO_2^+ time-zero counts depending on the pump and probe intensities, as well as on the polarisation geometry. In contrast, the signals associated with O^+ and N^+ atomic fragments always remained smaller, typically 20% and 2%, respectively, of the parent ion channel. Small amounts of ionisation from background H_2O and O_2 were also observed, but as they do not contribute to the time-resolved dynamics of NO_2 they will not be further considered. The H_2O signal was however used for the intensity

and cross correlation calibration previously outlined in Secs. 2.2 and 2.4. Based on the above information on count rates only time-resolved ion-yield spectra (TRIYS) and TRCRATI spectra will be shown for the NO_2^+, NO^+ and O^+ channels.

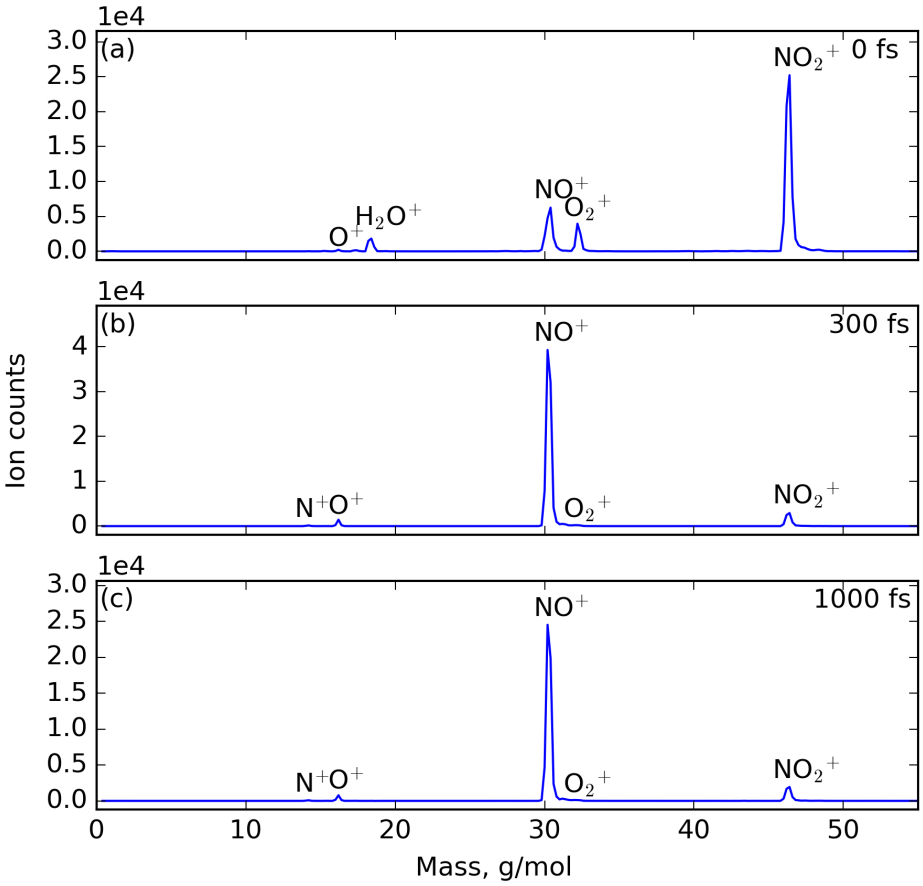

Figure 2.6: Mass spectra recorded in the parallel polarization geometry at (a) 0 fs, (b) 300 fs, (c) 1000 fs time delay. The spectra were recorded with an estimated pump and probe intensity of 4.8×10^{12} W cm^{-2} and 1.7×10^{13} W cm^{-2}, respectively.

In Fig. 2.7 we show time-resolved ion-yield (TRIY) spectra for NO_2^+ (panel (a)), NO^+ (panel (b)) and O^+ (panel (c)) for the parallel and perpendicular polarization geometries, as well as the TDLD. All TRIYS exhibited time-dependent modulations and have non-monotonic behavior. At the temporal overlap of the pump and probe pulses (time-zero) a sharp non-resonant signal is observed in the NO_2^+ signal.

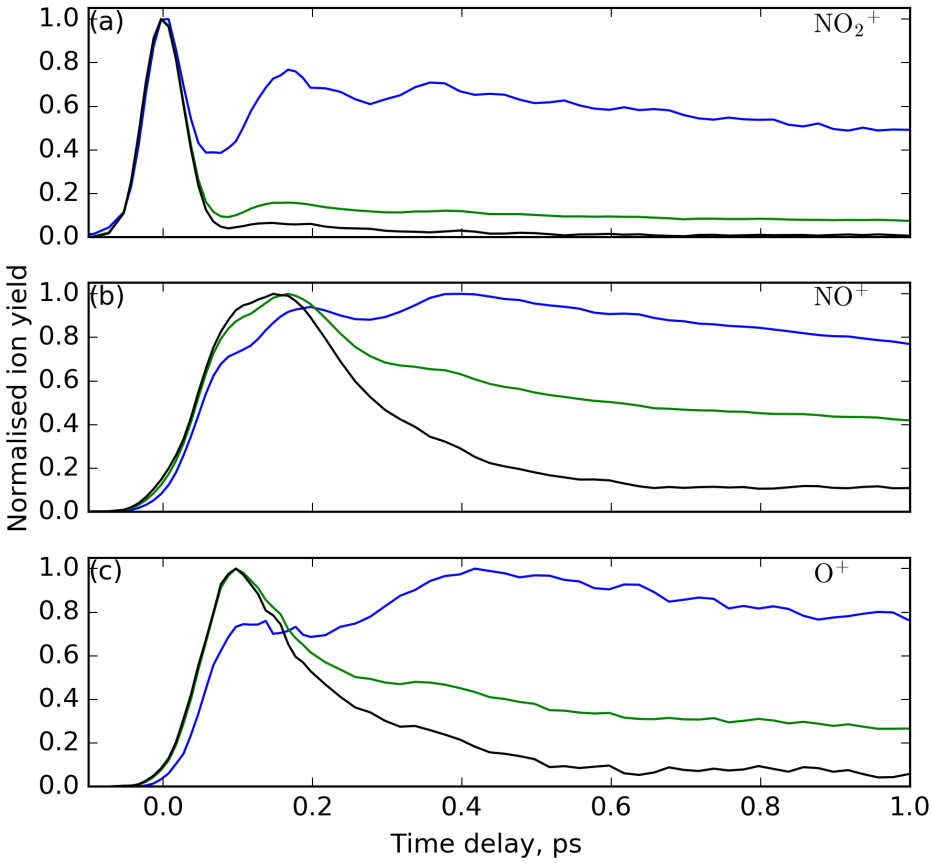

Figure 2.7: Time-resolved ion-yield (TRIY) spectra recorded for NO_2^+ (a), NO^+ (b) and O^+ (c) at a pump and probe intensity of 4.8×10^{12} W cm^{-2} and 1.7×10^{13} W cm^{-2}, respectively. Data are presented for both the perpendicular (blue) and parallel (green) polarisation geometries as well as the TDLD signal (black). Note, for each polarisation geometry the spectra were normalised to maximum per channel.

Outside this region, a series of rising signals were observed in all channels, initially peaking at approximately 110 fs in O^+ and at 180 fs in both NO^+ and NO_2^+. Additionally, the NO^+ signal exhibits a local maximum at 80 fs time delay. All channels exhibited a subsequent peak in their signals at later time delays (380-400 fs), which itself then decays on a picosecond timescale. The TDLD signals (black) display behaviour different from the ion yields in all channels within the first 500 fs, but decaying towards zero outside this region (see Fig.2.7).

The TRCRATI spectra for the NO_2^+ (panel (a)), NO^+ (panel (b)) and O^+ (panel (c)) ion channels are presented in Fig. 2.8 for the parallel polarization geometry. Outside the temporal overlap of the two pulses, a sharp ATI comb is observed in the TRCRATI spectra for all three channels, which persists out to the maximum measured pump-probe delay. A number of interesting observations can be drawn from the comparison of TRCRATI spectra associated with different cations. Firstly, the NO_2^+ correlated spectra exhibits two distinct ATI combs outside the cross-correlation region, which indicates that the stable parent ion can be formed via multiple strong-field ionisation channels, with distinct vertical ionisation potentials. The lower energy ATI comb (0.55+n$\hbar\omega$ eV - black dashed lines) is also present in both the NO^+ and O^+ fragment correlated spectra, suggesting that sequential processes are participating in the ionisation dynamics, whereas the higher energy ATI comb (0.95+n$\hbar\omega$ eV - magenta dashed lines) appears only in the NO_2^+ channel. Secondly, temporal modulations were only observed in the ATI comb intensity and not in the comb kinetic energy peak position. These intensity modulation broadly exhibit the same temporal behaviour as the photoion signals (Fig. 2.7). Finally, a number of less intense short lived features at approximately 1 eV were observed in the NO^+ and O^+ fragment channels and have a limited progression at higher photoelectron kinetic energy. The onset of the short lived ATI comb matches the features observed at 80 fs in the NO^+ and O^+ TRIYS (see Fig. 2.7(b)-(c)).

In order to investigate the possible origins of these differences and the temporal modulations observed in the photoelectron spectra and ion yields, we systematically varied the intensities of both the pump and probe pulses. These studies allowed us to determine if: (i) there are contribution in the time-resolved signals associated with multi-photon excitations to higher-lying neutral states in the pump step, which can often occur when when using femtosecond laser pulses [184, 186, 187, 195] and; (ii) whether additional ionisation channels become operative at higher probe intensities.

In Fig. 2.9, the TRIY spectra is shown for NO_2^+ (panel (a)), NO^+ (panel (b)) and O^+ (panel (c)) as a function of pump laser intensity. The dynamics in the NO_2^+ parent ion channel are essentially independent of pump intensity, apart from the ex-

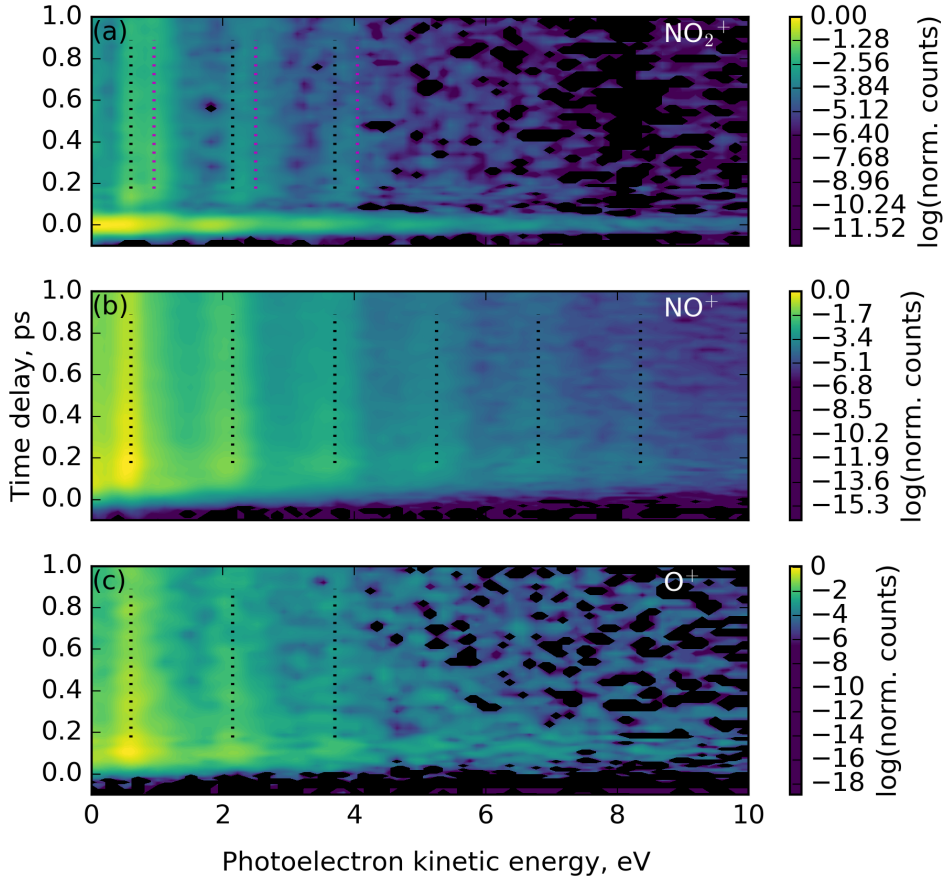

Figure 2.8: TRCRATI spectra for the NO_2^+ (a), NO^+ (b) and O^+ (c) ion channels. The spectra were recorded in the parallel polarization geometry with an estimated pump and probe intensity of 4.8×10^{12} W cm^{-2} and 1.7×10^{13} W cm^{-2}, respectively. It should be noted that the appearance of empty data bins in the spectra originates from the probe-alone background subtraction. In cases where a negative counts value was generated, the data point in question was not displayed during plotting; negative counts would result in errors in the log scale.

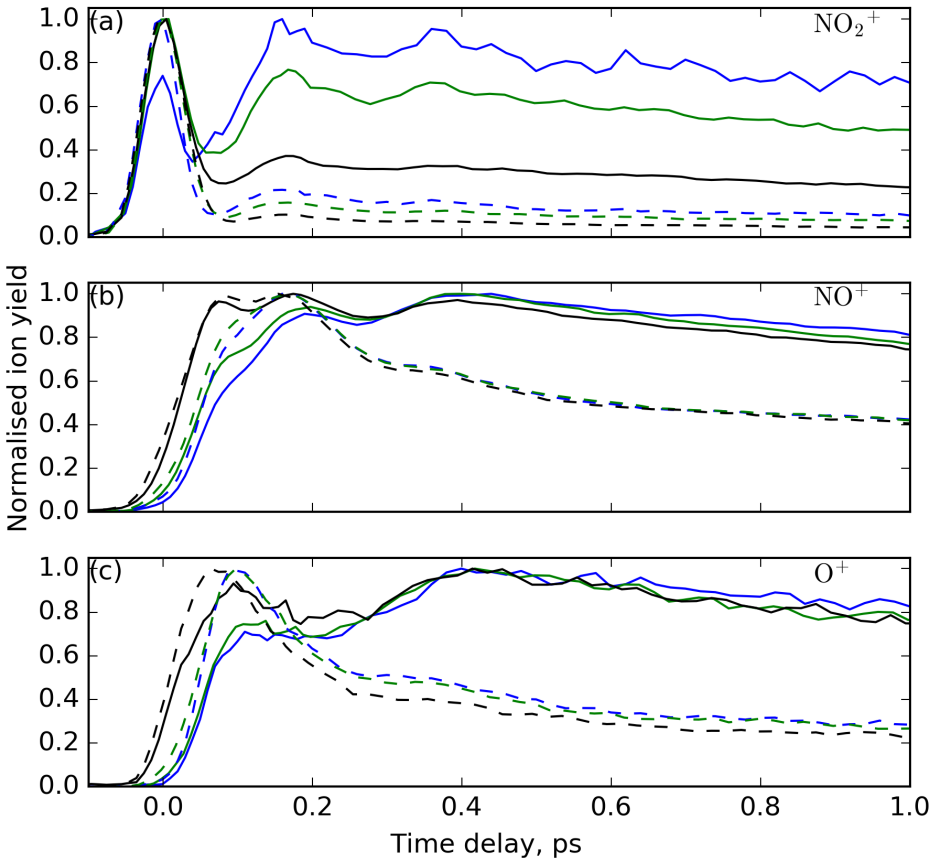

Figure 2.9: Pump laser intensity dependence of the TRIY spectra recorded for NO_2^+ (a), NO^+ (b) and O^+ (c) in the parallel (dashed lines) and perpendicular (solid lines) relative polarization geometries. The data was collected with three different estimated pump intensities, 9.8×10^{11} W cm^{-2} (blue), 4.8×10^{12} W cm^{-2} (green) and 1.4×10^{13} W cm^{-2} (black) at a constant probe laser intensity of 1.7×10^{13} W cm^{-2}.

pected increase in the non-resonant ionisation signal at temporal overlap of the two pulses. Conversely, the two fragment channels show the opposite behaviour, at short time delays, where features become much more prevalent at higher pump intensities. This pump intensity dependence unambiguously shows that higher-lying electronically excited states, in neutral NO_2, are being populated via multiphoton pump excitations. These features at short time delays also exhibit a strong dependence on the relative polarisation geometry, with enhancement in the signal observed in the parallel geometry. The intensity dependence is evident from the TDLDs presented

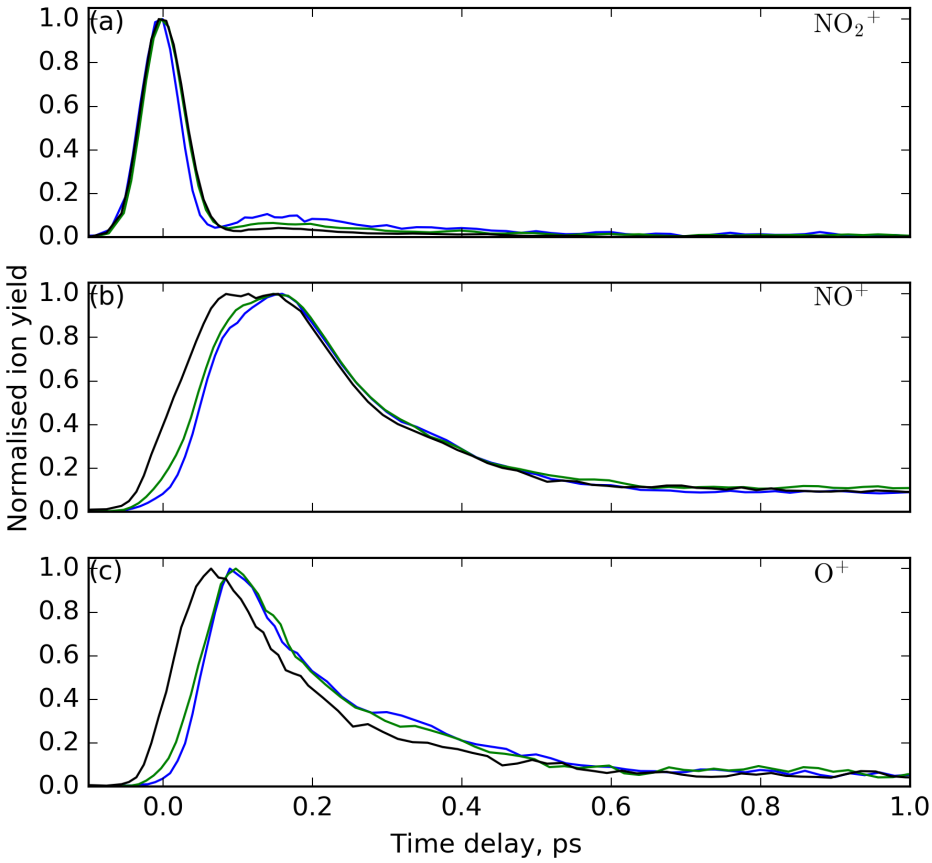

Figure 2.10: Pump laser intensity dependence of the TDLD for NO_2^+ (a), NO^+ (b) and O^+ (c) channels. The data was collected with three different estimated pump intensities, 9.8×10^{11} W cm^{-2} (blue), 4.8×10^{12} W cm^{-2} (green) and 1.4×10^{13} W cm^{-2} (black) at a constant probe laser intensity of 1.7×10^{13} W cm^{-2}.

in Fig. 2.10, where larger values of the LD are observed for time delays $<$100 fs for both the NO^+ and O^+ fragment channels. Finally, at all time delays $>$100 fs the TDLD signals essentially display the same temporal dependence regardless of pump laser intensity and decays towards zero by approximately 500 fs.

To further examine the origins of the pump-power-dependent features observed in the TRIY and TDLD spectra, presented in Fig. 2.11 are TRCRATI spectra, for the lowest (9.8×10^{11} W cm^{-2}) and highest (1.4×10^{13} W cm^{-2}) pump intensities for the parallel polarization geometry. It can be clearly seen that, at short time delays ($<$100 fs), the modulation structure of the ATI combs becomes significantly less

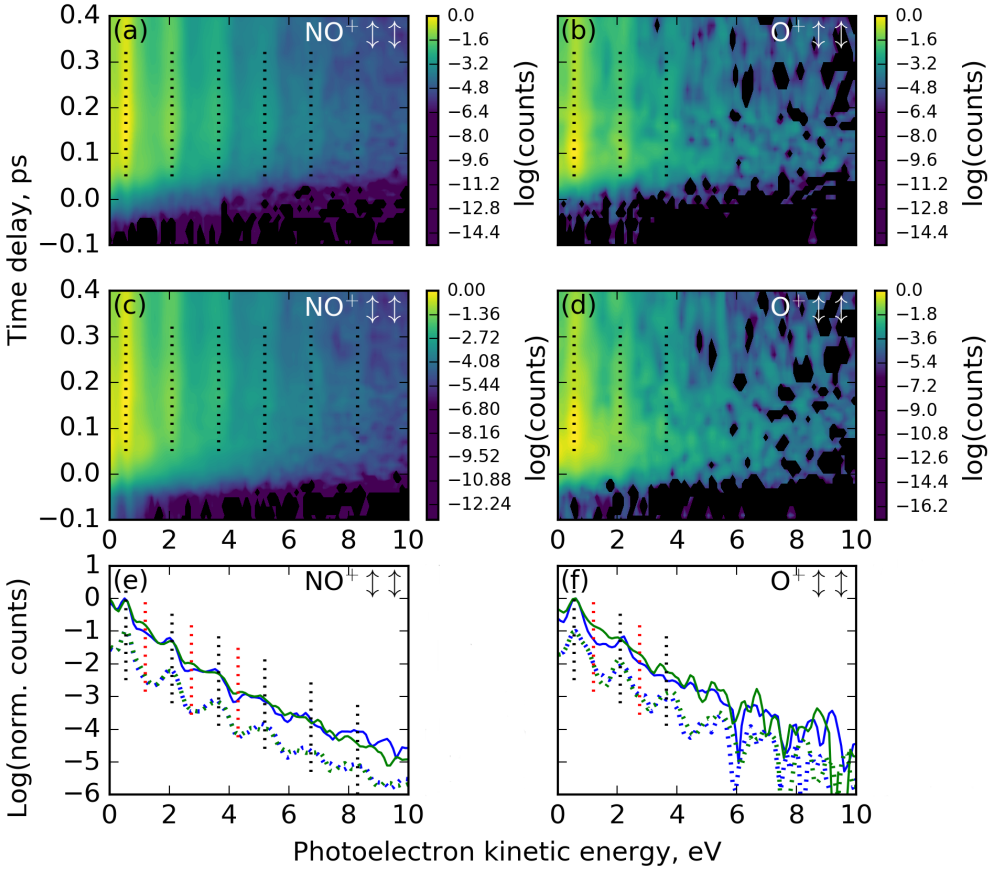

Figure 2.11: TRCRATI spectra associated with NO^+ (left column) and O^+ (right column) channels at two pump laser intensities: Panels (a), (b) $I_{pump} = 9.6\times10^{11}$ W cm^{-2}; Panels (c), (d) $I_{pump} = 1.4\times10^{13}$ W cm^{-2}. The spectra were recorded with a constant probe intensity of 1.7×10^{13} W cm^{-2} and data is presented for the parallel polarization geometry. Panels (e), (f) show line-outs of the TRCRATI spectra at Δt = 80 (solid line) and 180 fs (dashed line) for the two pump intensities, 9.6×10^{11} W cm^{-2} (blue), 1.4×10^{13} W cm^{-2} (green). The dotted black lines in all panels indicate the main ATI comb observed. In panel (e), the red dotted line indicates a second ATI comb which appears at the 80 fs time delay (solid line), most prominently for the higher intensity pump (green). This transient, high pump intensity ATI comb, which vanishes at longer time delays, is seen only weakly in panel (f), due to the low count rate in the O^+ channel.

pronounced at higher pump intensities (Fig. 2.11(c)-(d)). Furthermore, in the correlated photoelectron spectra for both fragments, the less intense short lived spectral features at around 1 eV (and higher ATI order photoelectron peaks) become more pronounced at higher pump intensities. This latter point is highlighted in Fig. 2.11(e)-(f) (red dashed lines), where temporal line outs, integration regions Δt = 50-110 and 150-210 fs, of photoelectron spectra are shown for the two pump laser intensities. Interestingly, no signature of the 1 eV+$h\omega$ ATI peaks are observed in the photoelectron spectra at 180 fs which, similarly to the TRIY spectra (see Fig. 2.9), implies the short-lived nature of this ionisation channel.

Finally, the effect of the probe laser intensity on the experimental observables is considered. In Fig. 2.12 TRIY spectra for NO_2^+, NO^+ and O^+ as a function of probe laser intensity are presented. The spectra are essentially unchanged for the intensities considered within this study, with no additional ionisation channels being observed at higher probe laser intensities.

In Fig 2.13 the TRCRATI spectra are shown for all three channels, in the parallel polarisation geometry, for the lowest (1.7×10^{13} W cm^{-2}) and highest (2.2×10^{13} W cm^{-2}) 798 nm probe intensities studied here. In the fragment channels, it is evident that the modulation structure of the ATI combs diminishes in the higher probe intensity data set (Fig 2.13(d)-(f)). This point is evident in panels (g) and (h), where line-outs, integrated over Δt = 150-210 fs (i.e. across the temporal cross-correlation width), of the NO_2^+ and NO^+ TRCRATI spectra are shown for both the aforementioned probe intensities. The ATI comb structure associated with the NO_2^+ parent ion exhibits very little broadening as a function of probe laser intensity, whereas the ATI comb correlated with the NO^+ fragment exhibit large broadening. Analysis of the ground state, probe-alone, CRATI spectra (see Fig. 2.5) highlighted that no significant broadening of the H_2O^+ and NO_2^+ ATI comb was observed at the higher probe laser intensity. This point suggests that intensity averaging, due to an increased interaction volume of the probe laser with the molecular beam, is not operative under the experimentally conditions employed here. Another possible cause of the loss of comb contrast in the fragment channels is the partici-

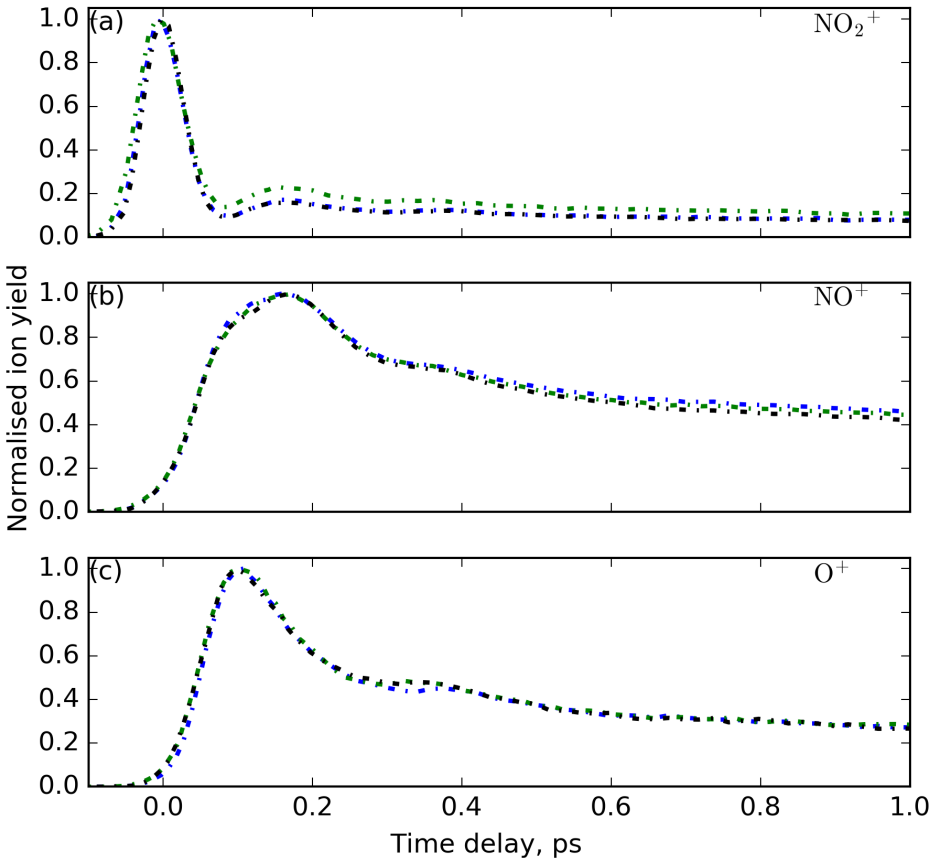

Figure 2.12: Probe laser intensity dependence of the TRIY spectra recorded for NO_2^+ (a), NO^+ (b) and O^+ (c) in the parallel relative polarisation geometry. The data was collected with three different calibrated probe intensities, 1.7×10^{13} W cm^{-2} (blue), 1.9×10^{13} W cm^{-2} (green) and 2.2×10^{13} W cm^{-2} (black), while the pump was held constant at an estimated intensity of 4.8×10^{12} W cm^{-2}.

pation of additional ionisation channels. This would be due to the higher intensity probe ionising from broader regions of molecular configurations and/or accessing higher-lying ionisation continua. Finally, if multiple ionisation channels are contributing to the NO^+ ATI comb, then Stark shifting of the multiple overlapping combs, likely by different energetic values for each final state, could result in an apparent broadening/loss of contrast in the comb structure. Disentangling the relative contributions of and/or ruling out each of these possible mechanisms from the observe signal remains challenging and would require further experimental work.

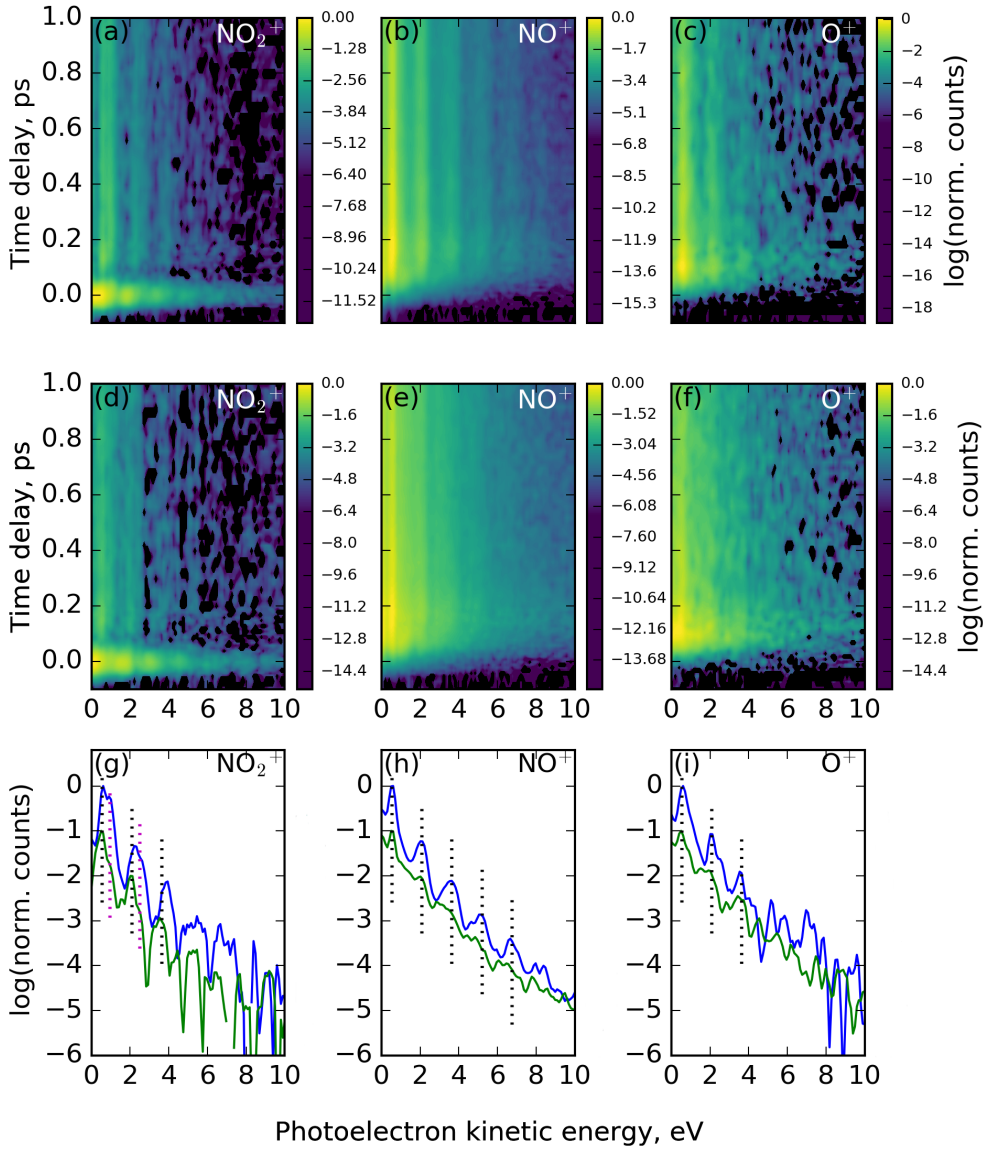

Figure 2.13: TRCRATI spectra associated with the NO_2^+, NO^+ and O^+ channels for two calibrated probe intensities, 1.7×10^{13} W cm^{-2} [top row, (a)–(c)] and 2.2×10^{13} W cm^{-2} [middle row, (d)–(f)]. In bottom row [panels (g)-(i)] line-outs of the TRCRATI spectra, integrated between Δt = 150-210 fs, are shown for both probe intensities (1.7×10^{13} W cm^{-2} (blue) and 2.2×10^{13} W cm^{-2} (green)). The black and magenta dashed lines denote the ATI combs at 0.55+n$\hbar\omega$ eV and 0.95+n$\hbar\omega$ eV, respectively, these ionisation channels are discussed in the main text. All presented data were recorded with a constant estimated pump intensity of 4.8×10^{12} W cm^{-2}, in the parallel polarisation geometry.

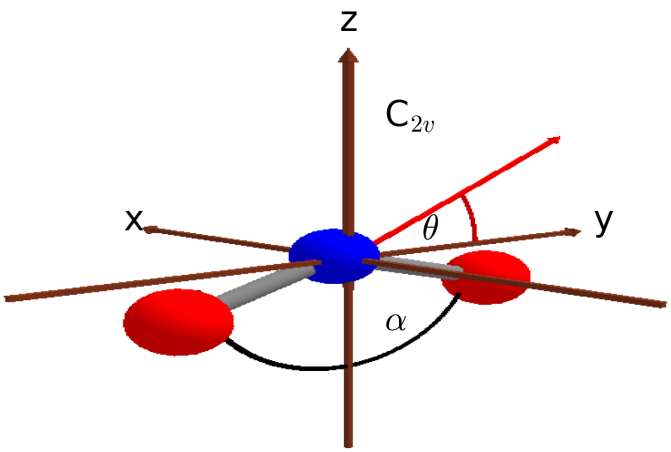

Figure 2.14: Schematic diagram of the ground state equilibrium structure of NO_2 with the molecular axes labeled in C_{2v} symmetry. α is the ONO bending angle and θ is the angle between the molecular y-axis (oxygen-oxygen axis) and the linear pump laser polarization vector (red).

2.6 Discussion

2.6.1 Single photon excitation and relaxation dynamics

In these experiments, single photon absorption at 399 nm transfers population from the $\tilde{X}\,^2A_1$ ground state to the $\tilde{A}\,^2B_2$ excited state. The dipole matrix element for this transition lies along the y-axis, the oxygen-oxygen axis (see Fig. 2.14), within C_{2v} symmetry and excitation therefore produced a $\cos^2(\theta)$ distribution of the molecular y-axes in the laboratory frame. Here, θ denotes the angle between the molecular y-axis and polarisation of the linear pump pulse. As outlined in Sec. 2.1, the excited state wavepacket moves rapidly towards the conical intersection that exists between the $\tilde{X}\,^2A_1$ and the $\tilde{A}\,^2B_2$ states, with the initial motion expected to be somewhat localised within the bending coordinate, where the potential energy gradient is greatest. The wavepacket is expected to make several passages of the conical intersection, with substantial population transfer to the ground state typically occurring in approximately 200 fs [190].

In previous experimental and theoretical work performed by Wörner *et al.*, all-

electron, coupled-channel time-dependent Schrödinger equation calculations were carried out for SFI of NO_2 [165]. The calculations made use of a mixed orbital/grid-based approach and calculated both the SFI yield and angular-dependence [202, 203] for a series of final cationic states at a specific set of geometries, within C_{2v} symmetry. Ionisation channels were considered for both $\tilde{A}\ ^2B_2$ and $\tilde{X}\ ^2A_1$ acting as the initial electronic state from which ionisation occurs. For the geometries considered on the $\tilde{A}\ ^2B_2$ surface, ionisation predominately correlates to the first electronically excited cationic state, $\tilde{a}\ ^3B_2$, which likely results in fragmentation to produce NO^+. Calculations performed by Hirst indicate that the $\tilde{a}\ ^3B_2$ state correlates, adiabatically, with the $NO^+(X\ ^2\Sigma^+)$ + $O(^3P)$ dissociation limit [204]. The angular dependence of these SFI channels, correlating to the $\tilde{a}\ ^3B_2$ state, is strongly peaked along the molecular z-axis for all considered nuclear geometries. It would therefore be expected that ionisation from the $\tilde{A}\ ^2B_2$ state (and therefore NO^+ production) should be enhanced for the perpendicular polarisation geometry, given that the initial distribution of molecular axes, created upon photoexcitation, is peaked along the y-axis.

In contrast with this expectation, increased ionisation in the NO^+ channel was observed in the parallel polarisation geometry, on a timescales comparable that of the expected timescale for significant population transfer ($<$200 fs). The prior study by Wörner *et al*. additionally reported SFI calculations from the $\tilde{X}\ ^2A_1$ ground state of NO_2 at two geometries corresponding to (i) the $\tilde{X}\ ^2A_1$ equilibrium geometry at an ONO bond angle ($\angle$ONO) of 134° and (ii) the conical intersection geometry of the $\tilde{A}\ ^2B_2$ state at $\angle$ONO = 102°. The calculations highlighted that, at bond angles in the region of 102°, the energetic ordering of the ionic $X\ ^1A_1$ and $\tilde{a}\ ^3B_2$ diabatic states switches (see Fig. 2.1), resulting in approximately an order of magnitude higher SFI yield for ionisation correlating to the $\tilde{a}\ ^3B_2$ state at that calculated geometry. Furthermore, the angular dependence of the SFI yield for this geometry was calculated to be strongly peaked along the molecular y-axis. This result is in accord with the polarisation dependence observed in the NO^+ channel. However, we note that the previously reported SFI calculations were conducted at a higher intensity

(1.0×10^{14} Wcm^{-2}) than the measurements we report here and that the calculations were performed for a single half-cycle of a 800 nm driving laser. These two factors mean that quantitative comparison with the previous calculation is not possible as: (i) intensity dependent angular dependences have previously been observed in even simple atomic and molecular systems such as Xe [205] and H_2 [206], respectively and; (ii) multi-cycle effects, i.e. post-ionisation excitation (see Sec. 1.7), may play a role here.

Consolidating the SFI calculations from Wörner *et al.* with (i) the expected molecular axis distribution due to the initial pump excitation, (ii) the observed enhancement of SFI in the parallel polarisation geometry for the NO^+ channel at approximately 180 fs, and (iii) the timescale associated with ground state re-population from wavepacket calculations [190, 207], it appears the likely origin of the enhanced ionisation feature observed at Δt = 180 fs in the NO^+ channel is SFI from the excited molecule returning to the ground electronic state of NO_2 at bent molecular geometries. It is important to note that the feature observed in the NO^+ channel (see Figs. 2.12-2.11) at shorter time delays, $<$100 fs, is associated with higher pump intensities and can be attributed to multiple pump photon dynamics occurring in higher-lying neutral excited states in NO_2; this will be discussed in Sec. 2.6.2.

At approximately Δt = 180 fs, the NO_2^+ channel also exhibits peaks in the TR-CRATI spectra. The lower energy ATI comb (0.55+n$\hbar\omega$ eV) appears at the same electron kinetic energies as the ATI comb observed in the NO^+ and O^+ TRCRATI spectra, indicating that the y-polarized SFI channel from the $\tilde{X}\ ^2A_1$ ground state surface to $\tilde{a}\ ^3B_2$ excited cationic state can also result in the formation of stable parent ions. This assertion appears reasonable based on the VUV synchrotron work from Eland and Karlsson [208], where stable NO_2^+ can be observed for ionisation correlating to $\tilde{a}\ ^3B_2$ depending on the vibrational state accessed in this electronic manifold. The higher energy ATI comb (0.95+n$\hbar\omega$ eV - magenta dashed line in Fig. 2.8) may be due to the z-polarized ionisation route which correlates with the $X\ ^1A_1$ cationic state. This assignment is supported by the fact that the wavepacket

returns to the ground state with an internal energy just below the first dissociation limit of NO_2 and, therefore, is expected to explore a large range of nuclear geometries far away from neutral NO_2 equilibrium geometry. Of particular interest is the wavepacket exploring regions on the $\tilde{X}\,^2A_1$ surface at large ∠ONO, where the geometry approaches the linear equilibrium structure of the $X\,^1A_1$ cationic state. Accessing near-linear geometries therefore provides good Franck-Condon (FC) overlap for ionisation as well as an effectively lower vertical IP [204], resulting in an increased SFI rate [165]. This mechanism is further supported by: (i) the wavepacket calculations, which indicate that such regions of nuclear coordinate space are accessed on similar timescales [189, 190] and; (ii) the relatively small calculated SFI yields for ionisation channels from the neutral excited $\tilde{A}\,^2B_2$ state displaced significantly from the pump FC geometry [165]. Finally, it is of note that the reduced sensitivity of the NO_2^+, compared to the NO^+, ion yields to the relative polarization geometry (see Figs. 2.7 and 2.10) is perhaps related to participation of these aforementioned multiple continua, correlating to the $X\,^1A_1$ and $\tilde{a}\,^3B_2$ cationic states. These associated SFI channels exhibit peaks in their angle dependent yields along the molecular y-axis and z-axis, respectively. This would result in an averaging away of the NO_2^+ ion yield sensitivity, when compared to NO^+, to the relative polarisation geometry.

The $\tilde{X}\,^2A_1$ ground state wavepacket is expected to remain somewhat localised within the bending and symmetric stretch coordinates for the first few hundred femtoseconds, meaning that ground state IVR is likely to be incomplete on a timescale of a few hundred femtoseconds. At later times, as the dynamics progress, IVR will induce the ground state wavepacket to explore geometries at extended ON-O bond lengths (r_{ON-O}), as well as larger ∠ONO. Indeed, it is IVR and coupling into the asymmetric stretch coordinate that gives rise to the neutral dissociation process on the ground state surface, yielding free NO ($X^2\Pi$) and O (^3P) products. This spreading of the wavepacket, over multiple degrees of freedom, on the $\tilde{X}\,^2A_1$ surface leads to a decay of the ionisation signal associated with the $\tilde{a}\,^3B_2$ SFI channel. This is in part due to the increase in IP away from the $\tilde{a}\,^3B_2$ equilibrium geometry, as well as the reduced wavepacket density in the low IP region. Conversely, an increase in SFI

rate correlating to X $\Sigma_g^+/^1A_1/^1A'$ state of the cation is expected due to a reduction in IP in regions of coordinate space near its equilibrium geometry [204]. Ionisation of the wavepacket on the neutral ground state from a broad range of both bond angles and bond lengths is likely, therefore, to result in the formation of stable NO_2^+ as well as fragmentation to form NO^+.

Based on the above observations and arguments, it can be speculated that the peaks observed in all three ion/electron channels at 380-400 fs are signatures of an increase in the ionisation rate to the ground state of the cation from the vibrationally 'hot' neutral ground state. The participation of the aforementioned multiple SFI continua, at 180 fs and 380-400 fs, is supported by the insensitivity of the latter peak (380-400 fs) to the relative laser polarisation geometry, due to the fact that the two accessible ion states are reached via cross-polarized transitions (see Figs. 2.7 and 2.10). Alternatively, this insensitivity could, in part, be linked to loss of the initial axis alignment, induced by the pump pulse, through rotational dephasing. The timescale associated with this dephasing depends on the exact rotational temperature within the molecular beam. This is challenging to estimate in the employed PEPICO apparatus. A timescale on the order of 1 ps would however not be unexpected, and therefore, makes ruling out this mechanism challenging. It is of note that in the former mechanism, where at least two SFI channels participate, this should result in a loss of ATI comb contrast in the NO^+ correlated ATI spectra at 380 fs with respect to the earlier 180 fs peak, to some degree. However, under the proviso that ionisation to the $\tilde{a}\ ^3B_2$ state and NO^+ production dominates, an ATI comb shift need not be observed. The dominance of the $\tilde{X}\ ^2A_1 \rightarrow \tilde{a}\ ^3B_2$ channel is substantiated by the previous SFI calculations performed by Wörner *et al*. [165] as well as the ion state literature [204].

On longer (picosecond) timescales, the ground state wavepacket spreading into the asymmetric stretch coordinate results in a reduction of wavepacket density in the regions of coordinate space participating in the previously outlined ionisation channels associated with SFI to the X $\Sigma_g^+/^1A_1/^1A'$ and $\tilde{a}\ ^3B_2$ cationic states. This would therefore result in the decay of the NO_2^+, NO^+ and O^+ ion/electron signals. At the

pump photon energy employed in the experiments (see Fig. 2.3), a fraction of the excited molecules which return to the ground state will have an internal energy just above the NO ($X^2\Pi$) and O (^3P) dissociation limits, the first of which is located at 3.1155 eV ($\sim$397.96 nm) [191]. These molecules will dissociate on a few picosecond timescale, as discussed in detail in previous time-resolved laser induced fluorescence studies [191]. However, as is evident from Fig. 2.3, the majority of the wavepacket will remain bound. This in turn implies that the associated ion/electron signals do not decay to zero due to the continued but reduced possibility of ionisation to the X $\Sigma_g^+/^1A_1/^1A'$ and $\tilde{a}$ $^3B_2$ states at intermediate bond angles and bond lengths. Furthermore, it is of note that a persistent and clear ATI comb structure was observed in all TRCRATI spectra at long pump-probe delays (see Fig. 2.8), suggesting that SFI of free neutral photofragments and/or fragmentation of weakly bound NO_2^+ does not contribute significantly to the observed ion/electron signals. If these ionisation routes contributed significantly to the ionisation yields, one might expect a shift of the ATI comb peak positions and/or a reduction in ATI comb contrast at longer pump-probe delays, in contradiction with what was observed. Additionally, if SFI of neutral NO or O photoproducts contributed significantly, then either a constant or increasing values should be observed in the associated ion/electrons yields at long time delay, whereas all ion/electron yields exhibited decreasing values. It therefore appears reasonable to conclude that the SFI pathways observed at Δt between 100 fs and 400 fs remain operative at on a picosecond timescale. This is supported by the temporal invariance of the ATI comb structures. However, the yield of these ATI electrons decreases with time, most likely due to wavepacket spreading.

Finally, the possible origins of the O^+ signal is considered. Based purely on energetics, this must undoubtedly be due to accessing even higher-lying ionisation continua. PEPICO spectra recorded by Eland and Karlsson show that dissociative ionisation to produce O^+ ($^4S_{3/2}$) in correlation with NO ($X^2\Pi_{3/2}$) can only occur at excitation energies above 16.63 eV and that the O^+ signal increases significantly above 17.4 eV [208]. Of note, however, is that the assignment of a par-

ticular electronic configuration becomes difficult at high excitation energies due to the broad photoelectron bands associated with electron correlation and multiple electronic configurations describing the excited cation states [204, 209]. The TR-CRATI spectra (Fig. 2.8) highlights that the production of the O^+ atomic fragment is likely linked to an indirect/sequential ionisation mechanism (see Sec. 1.7). This assignment is supported by the fact that the O^+ ATI comb peak position appears at identical kinetic energies (0.55+n$\hbar\omega$ eV) to the ATI combs present in both the NO_2^+ parent and NO^+ fragment ion correlated electron spectra. This ionisation channel was assigned in the preceding paragraphs to SFI from the $\tilde{X}\ ^2A_1$ ground state surface to the $\tilde{a}\ ^3B_2$ excited cationic state. The production of atomic O^+ is therefore likely linked to post-ionisation excitation of the $\tilde{a}\ ^3B_2$ state by multiple 798 nm photons.

It should be noted that O^+ and N^+ atomic fragments were previously observed in a study by Singhal *et al.* which investigated multiphoton ionisation pathways in NO_2 [210]. That study employed 375 nm photons with a pulse duration of 50 fs and an estimated maximum intensity of 5×10^{13} Wcm^{-2}. The authors assigned dissociative ionisation of neutral NO photoproducts as the origin of the atomic ion fragments. This interpretation is, however, inconsistent with the dynamics observed at long time delays (>500 fs), as the ion/photoelectron yields associated with O^+ signal decreases as a function of time. The opposite (increasing) behaviour would be expected for the ionisation of a neutral photo-product (products, once formed, do not vanish with time delay). Furthermore, if dissociative ionisation of free NO fragments, to produce O^+, contributed significantly, a shift of the ATI combs kinetic energy position and/or a reduction of ATI comb contrast could be observed at longer time delays. Finally, the short lived feature observed at Δt = 80 fs in the O^+ correlated spectra can, as suggested by the pump intensity study (see Figs. 2.9 and 2.11), be attributed to dynamics occurring on higher-lying state of neutral NO_2. This channel will be discussed in detail in Sec. 2.6.2. With the single-pump photon dynamics discussed above in mind, the most likely processes contributing to the neutral state wavepacket evolution are:

$$\tilde{A}^2B_2 \underset{180fs}{\overset{IC}{\rightarrow}} \tilde{X}^2A_1^{\dagger} \underset{380fs}{\overset{IVR}{\rightarrow}} \tilde{X}^2A_1^{\dagger\dagger} \underset{10ps}{\rightarrow} NO(X^2\Pi) + O(^3P) \tag{2.3}$$

To conclude, in contrast to other closely related work [185], the above interpretation of the transient ion/photoelectron signals is favoured over a periodic vibronic wavepacket explanation. This assertion is reasonable based purely on the absorption spectrum of NO_2, where no signatures of periodic wavepacket motion are observed [211]. Additionally, no clear oscillatory frequencies can be extracted from Fourier transform maps of the TRCRATI spectra (not shown).

2.6.2 The role of multiphoton pump excitation and relaxation dynamics

The intense nature of ultrashort laser pulses and the expected high absorption cross-sections for multiphoton pump excitations often result in complications in the interpretation of results in many femtosecond time-resolved studies [184, 186, 187, 195]. This is particularly true if the measured observable is not directly sensitive to the number of pump photons absorbed, for example in energy integrated measurements such as mass spectrometry. At the relatively high pump photon intensities employed in the experiments presented here, two-and three-photon excitations could occur to the higher-lying (neutral) $\tilde{D}\ ^2B_2$ excited state and the Rydberg manifold, respectively (see Fig. 2.15). Both of these processes would be resonantly enhanced by the one-photon resonance with the $\tilde{A}\ ^2B_2$ state. Signatures of these multiphoton excitation pathways were directly observed in the higher pump intensity dependent data presented in Sec. 2.5, for both the NO^+ and O^+ fragment channels at short delay times (< 100 fs). This has important consequences for the interpretation of all pump-probe experiments on NO_2 using strong laser fields.

Excitation to the $\tilde{D}\ ^2B_2$ state is considered first; although accessing the state directly via two-photon absorption is dipole allowed, additionally, two resonantly enhanced excitation pathways are possible. Excitation to the $\tilde{D}\ ^2B_2$ state can occur by using $\tilde{A}\ ^2B_2$ as a doorway state and subsequent single-photon excitation to the

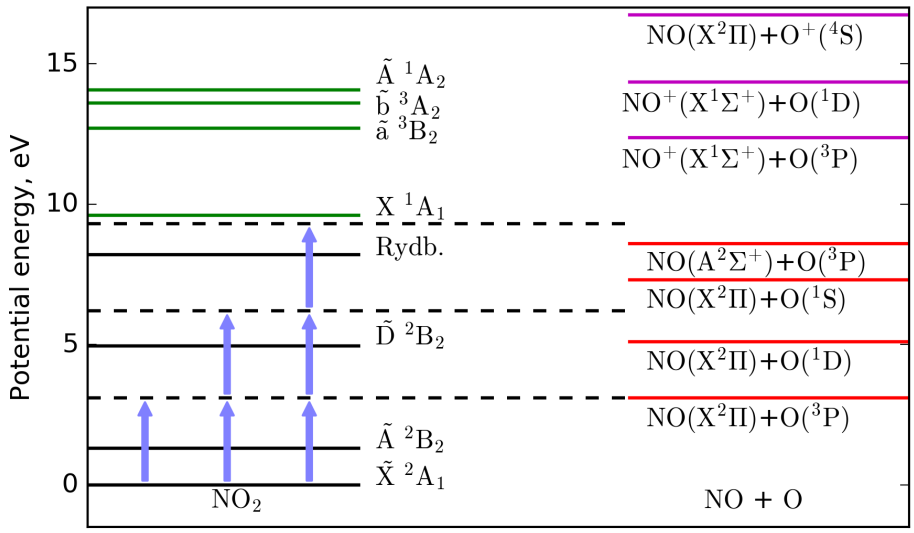

Figure 2.15: Energy levels of NO_2 (black solid lines) and NO_2^+ (green solid lines) as well as various neutral dissociation thresholds and photofragmentation channels (black dashed lines), indicated are the possible multiphoton excitation pathways to the $\tilde{D}\ ^2B_2$ state and the Rydberg manifold. The 399 nm pump photon is represented as a blue arrow and the neutral (red solid lines) and ionic (magenta solid lines) states of the NO and O fragments are shown to the right of the figure.

$\tilde{D}\ ^2B_2$ state is a z-polarised dipole allowed transition:

$$\tilde{X}^2A_1 \xrightarrow[y]{h\nu} \tilde{A}^2B_2 \xrightarrow[z]{h\nu} \tilde{D}^2B_2 \tag{2.4}$$

A second excitation route is possible due to the wavepacket being able to make the first pass through the conical intersection within the duration of the ∼50 fs pump pulse [189, 190]. This would lead to the initially populated state dynamically acquiring considerable $\tilde{X}\ ^2A_1$ character within the pump pulse duration, allowing the $\tilde{D}\ ^2B_2$ state to be accessed through the absorption of a second 399 nm photon. Here the transition would be dipole allowed and y-polarised in C_{2v} symmetry:

$$\tilde{X}^2A_1 \xrightarrow[y]{h\nu} \tilde{A}^2B_2 \xrightarrow{IC} \tilde{X}^2A_1^\dagger \xrightarrow[y]{h\nu} \tilde{D}^2B_2 \tag{2.5}$$

The two-photon excited $\tilde{D}\ ^2B_2$ state is expected to predissociate within 100 fs

[212] via one of two dissociation thresholds, producing either NO($^2\Pi$) + O(^{1}D) (the second dissociation limit at 5.08 eV) or NO($^2\Pi$) + O(^{3}P) (the first dissociation limit at 3.11 eV, see Fig. 2.15) [175, 213]. The production of both NO^+ and O^+ due to ionisation of free neutral photofragments giving rise to the features observed at $<$100 fs can be ruled out, since the ion/electron signals observed in both fragment channels rapidly decay after reaching a maximum. Similarly to the discussion outlined for the long time delay (picosecond) dynamics in Sec. 2.6.1, ionisation of neutral photofragments would yield a signal which would increase asymptotically and then effectively remain constant [174, 175, 188]. This is in contrast to what was observed. A decrease in a photo-product yield could be observed at very long (nanosecond) time delays but this would not contribute on the timescale relevant to any of the data presented here.

The primary ionisation routes from the $\tilde{D}\ ^2B_2$ state will result in the population of unstable electronically and vibrationally excited states in NO_2^+, likely the $\tilde{b}\ ^3A_2$ and $\tilde{A}\ ^1A_2$ states. Both these states are likely to fragment and produce NO^+ ions [177]. This is in accord with the higher pump intensity results presented in Fig. 2.9, where no signatures associated with dynamics occurring on higher-lying neutral states were observed in the NO_2^+ correlated data. Additionally, the well structured single ATI comb observed at later time delays in the high pump intensity fragment channel data sets (see Fig. 2.11(c)-(d)) are notably absent at pump-probe delays $<$100 fs. The participation of multiple ionisation continua is clearly evident in the line-out spectra at Δt = 80 fs, where a second ATI comb, with a distinct vertical IP, is observed at 1.2+n$\hbar\omega$ eV.

A second possibility is that the multiphoton pump features are due to dynamics occurring on the Rydberg manifold, excited via three-photon absorption. This process would be resonantly enhanced at both single and potentially the two-photon level. Similar to the discussion of two-pump-photon excitation, it is possible that, following single-photon excitation to the $\tilde{A}\ ^2B_2$ manifold, subsequent excitation occurs from vibrationally excited levels on the $\tilde{X}\ ^2A_1$ state following passage through the conical intersection. Accessing the $\tilde{X}\ ^2A_1$ state results in many nuclear geome-

tries being sampled, along the bending coordinate and, therefore, provides good FC overlap with the linear geometry Rydberg series, converging on the cationic ground state. Typically, linear Rydberg states would have poor FC overlap for direct single-photon excitation from the bent $\tilde{X}\ ^2A_1$ ground state [214–216]. At excitation energies corresponding to three-photons at 399 nm, multiple dissociation thresholds and non-adiabatic couplings are expected to play a role in the ensuing fragmentation dynamics [188]. However, similarly to the case of two-pump-photon excitation, we can rule out that the signal originates from ionisation of free neutral photofragments produced through neutral dissociation.

The structure of the ATI comb observed at 1.2+n$\hbar\omega$ eV in the NO^+ and O^+, fragment channels at 80 fs provides tentative evidence for ionisation of the Rydberg manifold. Direct SFI of Rydberg states should result in the well-known Freeman resonances [43]: these were discussed in Sec. 2.5 and can clearly be observed in Fig. 2.5 (dashed cyan lines). As is well-known, due to their low IP, such features in an ATI comb cannot persist out to higher orders of the comb. The data presented in panels (e) and (f) in Fig. 2.11 highlights that this comb only has progression out to perhaps two higher orders, whereas the ATI comb observed at 0.55+n$\hbar\omega$ eV proceeds out for at least five higher orders. This is consistent with the 1.2 eV feature being due to a Freeman resonance - the SFI of higher-lying Rydberg states.

Finally, the polarisation geometry dependence of the features correlated with multiphoton pump excitation in the NO^+ and O^+ channels (see Figs. 2.9 and 2.11) is considered. As discussed in the Sec. 2.6.1, the transition dipole moment associated with single-photon-pump excitation lies along the molecular y axis. The transition dipole moment associated with the absorption of a second 399 nm photon can potentially lie along either the z-axis (see Eq. 2.4) or y-axis (see Eq. 2.5) depending upon if the population undergoing a second pump photon excitation possess $\tilde{A}\ ^2B_2$ or $\tilde{X}\ ^2A_1$ character, respectively. Therefore, a sequential excitation process will either result in a complex (cross polarised) molecular axis distribution, if the transition dipole moments for each of the single-photon excitations lie along different molecular axes, or a sharpening of the initial lab frame molecular

axis distribution, producing a $\cos^4(\theta)$ distribution about the y molecular axis. In the case of three-photon excitation to the Rydberg manifold, population of a particular Rydberg state will primarily be selected based upon the electronic character of the state. However, at excitation energies corresponding to two or three-photons at 399 nm, a large number of non-adiabatic couplings are expected to play a role in the ensuing dynamics [188]. It is therefore possible that the sensitivity of the polarisation geometry and the observed enhancement of the fragment ion/electron signals could reflect a transient change in electronic character rather than originating from alignment created by the pump laser photoexcitation.

Given the information content in the current experimental data, disentangling whether the multiphoton contributions originate from two or three-pump-photon excitation remains challenging. The timescale of the features observed in the fragment channels is somewhat indicative of the predissociating $\tilde{D}\ ^2B_2$ state but the spectral features at 1.2+n$\hbar\omega$ eV extending to limited progression in the NO^+ TRCRATI spectrum appears to favour SFI of a Rydberg state. The origin of the O^+ signal is also hard to assign but it appears reasonable to speculate that a similar interpretation to the sequential/indirect ionisation mechanism outlined in Sec. 2.6.1, may be appropriate, where the increase in signal originates from ionisation of molecules at extended r_{ON-O}. Although the fragment channels show a clear sensitivity to the relative polarisation geometry, identifying the origin of this is difficult without SFI calculations from higher-lying excited states in neutral NO_2. Both the two and three-pump-photon excitation processes have been identified previously in both femtosecond time-resolved imaging and coincidence imaging experiments [184, 186, 187] but a more detailed experimental study would be required to examine this in the SFI case. This is beyond the scope of the work presented here.

2.7 Conclusions

In Chapter 2, a femtosecond time-resolved study utilising SFI and PEPICO spectroscopy to investigate excited state wavepacket dynamics in NO_2 has been presented. The CRATI experiments revealed modulations in both the photoelectron

and photoion yields for all channels considered. Examination of the TRCRATI spectra as a function of both pump laser intensity, as well as polarisation geometry, highlighted that the origin of the observed modulations is due to an incoherent combination of single and multiphoton pump excitations and their subsequent dynamics. This is in direct contradiction with previous time-resolved mass spectroscopy work, which attributed these apparent modulations to periodic vibronic wavepacket motion [185].

The contributions of non-adiabatic coupling rapidly re-populating the ground electronic state of neutral NO_2 was recognised through comparing the relative polarisation geometry dependence of the ion/electron yields with previously published SFI [165] and wavepacket calculations [189, 190]. In addition, the effects of two/three-pump-photon excitation dynamics, at short time delays, $<$100 fs, were identified through the dependence of the NO^+ and O^+ correlated spectra on the pump laser intensity. The longer timescale dynamics are tentatively attributed to signatures of ionisation of the vibrationally 'hot' ground state wavepacket, due to an increase in SFI rate to the cationic ground state.

By utilising the coincident detection of both photoelectrons and ions, several subtle features of the underlying probe ionisation dynamics could be clearly identified. Firstly, a weak ATI comb structure at 0.95+n$\hbar\omega$ eV was observed only in the NO_2^+ correlated electron spectra, likely originating from an ionisation channel correlating to the X $^1A_1$ cationic ground state. Secondly, the dominant ionisation channel, which produced an ATI comb at 0.55+n$\hbar\omega$ eV, was observed in all ion correlated electron spectra. This point is particularly important in the NO_2^+ channel, since it highlights that multiple ionisation channels are able to produce a stable parent ion. Finally, for the O^+ TRCRATI spectra both, the observable ATI comb peak positions, located at 0.55+n$\hbar\omega$ eV and 1.2+n$\hbar\omega$ eV, respectively, also appear at identical kinetic energies in the NO^+ fragment. This observation, coupled with the relatively high expected appearance energy of atomic O^+, provides a strong indication that sequential ionisation mechanisms are operative. It is particularly noteworthy that if a non differential detection scheme, such as mass spectroscopy,

had been employed the majority of the above channels would not be discernible. Even techniques like energy-resolved photoelectron spectroscopy would struggle to identify the aforementioned minor ionisation channels, since the ionisation signal associated with NO^+ constitutes $\sim$80 % of the ionisation events at most time delays.

Chapter 3

Femtosecond VUV and Rydberg valence coupling in acetone

3.1 Introduction

The introduction highlighted that TRPES is a very useful tool for monitoring non-adiabatic dynamics in polyatomic molecules, due to its sensitivity to both electronic and vibrational dynamics. However, as was evident in previous chapter, the use of multiphoton/strong-field ionisation to probe prototypical photochemical processes, like internal conversion and photodissociation, results in complex and difficult to interpret experimental observables. A far more tractable, and widely used, method to interrogate such dynamics is a pump-probe scheme employing both weak single photon excitation and ionisation, so called "1+1′" photoionisation (see the following reviews and references therein [13, 14, 217, 218]). This pump-probe scheme, when coupled with energy-resolved measurements, permits extraction of binding energies, through the known photon energies, for the populated electronic states with relative ease. Despite this clear advantage, time-resolved studies employing 1+1′ photoionisation schemes have been somewhat limited by the wavelength coverage (>200 nm) of conventional femtosecond laser systems. In particular, the lack of femtosecond sources in the VUV/XUV has resulted in the majority of studies: (i) focusing on non-adiabatic dynamics in relatively low-lying electronic states and; (ii) being unable to fully track dynamics from the initially prepared (reactant)

wavepacket along reaction coordinates to dissociated photoproducts.

The latter point is often phrased in the context of a "windowing effect" where, along certain reaction coordinates, a <6.2 eV (200 nm) photon is energetically insufficient to ionise the evolving wavepacket. This has resulted in the necessity to infer reaction mechanisms from partial measurements [26,27] or employment of multiphoton ionisation probe schemes [24, 184, 195, 196]. In seminal work, Leone and co-workers [159, 219] used tabletop femtosecond XUV pulses from a HHG source as a photoelectron spectroscopy probe to map the complete reaction pathway of dissociating diatomic (Br_2) molecules. These investigations, and subsequent related works [220, 221], allowed a complete description of the valence electron rearrangement during bond cleavage to be obtained. Recently, this has also been extended to track all of the relevant electronic states and molecular geometries associated with competing dissociation pathways in the polyatomic molecule CS_2 [160].

An alternative use of femtosecond VUV sources, which directly addresses the aforementioned point (i) and will be subject of this chapter, is to perform time-resolved studies on high-lying excited states in molecular systems [222–224]. In this chapter the construction of a femtosecond VUV source, based on non-resonant Difference Frequency Four-Wave Mixing (DFFWM) [225], will be outlined and applied to study Rydberg-valence coupling in acetone. Highly excited electronic states near 7-10 eV, despite their importance for ionospheric and interstellar chemistry, remain relatively poorly understood and are generally complex due to a high density of states. In particular, non-adiabatic coupling within this dense manifold of states typically results in processes such as internal conversion [226, 227] or dissociation [228] occurring on ultrafast timescales. To date, a significant portion of the experimental pump-probe studies investigating highly excited states in the VUV region of the spectrum have employed two (or more) photon excitation schemes [184, 229–233]. This is a direct consequence of the previously mentioned lack of wavelength coverage for femtosecond pulses in the VUV region. In order to ensure that only the single state of interest is prepared by the pump pulse, it is required that any multiphoton excitation be non-resonant at the intermediate stages. However,

in many molecular systems there is the possibility of accessing lower-lying excited states during the multiphoton excitation process. This is the case for acetone and will be discussed in the following paragraphs. If the excitation process is resonantly enhanced then the measured time-dependent pump-probe signal of the state of interest also carries a signature of any intermediate levels accessed during the excitation process. In addition to this, the relatively high pulse intensities required to drive the desired non-resonant multiphoton excitation can result in higher-order processes occurring where more than the desired number of photons can be absorbed. Both these points have led to complications in the interpretation of experimental data due to difficulties in assigning the nature of the populated state under investigation. To summarise, the recent development of femtosecond vacuum-ultraviolet (VUV) or extreme-ultraviolet (XUV) light sources, based on either low-order high harmonic generation [234, 235] or wave-mixing schemes [225, 236–238], provides an ideal means by which highly-excited states can be accessed at the single-photon level, avoiding the above outlined complications.

Before details of the experimental apparatus and results are given, this section ends with a brief of the excited state dynamics of the acetone molecule. Acetone represents an exemplary system to study photochemical dynamics in ketones due to it being the simplest aliphatic ketone. UV photolysis of acetone, to produce the acetyl and methyl radicals, has attracted considerable attention as it the prototypical example of the so-called Norrish type I (NT1) reaction (C-C bond cleavage) [239]. Therefore constructing a dynamical picture of the NT1 reaction will have important implications for the photochemistry of all aldehydes and ketones. The electronic ground state of acetone, 1^1A_1 character, has C_{2v} symmetry with principal molecular axis lying along the C-O bond. Acetone's electronic absorption spectra is comprised of a series of transitions to valence ($n_y \rightarrow \pi^*, \pi \rightarrow \pi^*, \pi \rightarrow \sigma^*$) and n = 3,4,.. Rydberg states. The lowest lying excited state 1^1A_2 ($n_y \rightarrow \pi^*$) has a vertical excitation energy of 3.774 eV [239]. This weak transition is forbidden in C_{2v} symmetry but gains oscillator strength by means of Herzberg-Teller intensity borrowing [240]. The intense absorption line at 6.348 eV marks the first transition to the Rydberg series

(3s) [241]. Between 7.0-8.0 eV a broad structured continuum appears, superposed by a series of intense Rydberg absorption lines [242]. Previous experimental work assigned these sharp features to the $^1A_2(n_y \rightarrow 3p_x)$, $^1A_1(n_y \rightarrow 3p_y)$ and $^1B_2(n_y \rightarrow 3p_z)$ Rydberg states located at 7.36 eV, 7.41 eV and 7.45 eV, respectively [243]. Evidence of Rydberg-valence coupling between the $^1A_1(n_y \rightarrow 3p_y)$ and $^1A_1(\pi \rightarrow \pi^*)$ was also determined from multiphoton photoacoustic and resonantly enhanced multiphoton ionisation (REMPI) experiments [243, 244]. Although the energetic minimum of $\pi\pi^*$ state is thought to be $\sim$7.4 eV, it enters the Franck-Condon region at 8.35 eV and hence adds to role of coupling between the Rydberg and valence states [245]. This conclusion was also supported by *ab initio* calculations which predict that the $(\pi \rightarrow \pi^*)$ state also plays a role in this spectral region [246]. Despite the vibrational structure in the 3p manifold being assigned up to energies of $\sim$7.9 eV, there exist numerous conflicting assignments with, in some cases, up to three vibrational state being assigned by different authors to the same single peak [242]. Vibrational structure associated with the higher-lying $3d_{yz}$ state (onset 7.715 eV) have been observed, but accurate assignments of these states have remained challenging due to an underlying broad continua. This likely has its origin in a valence state, perhaps $\pi\pi^*$ with a significantly geometry change with respect to the ground state equilibrium geometry. Both theoretical and experimental work suggested that coupling exists between the $\pi\pi^*$ state to the 3d Rydberg states with the same symmetry [245].

The majority of the femtosecond time-resolved studies have focused on dynamics following excitation of the low-lying $n_y \rightarrow \pi^*/S_1$ [232, 247–249] and $n_y \rightarrow 3s$ (S_2) [247, 250–252] states. The primary focus of these early studies was trying to disentangle whether these states can rapidly decompose on an ultrafast timescale to form long lived acetyl radicals [247, 253] or if the fragmentation is mediated by intersystem crossing from S_1 to T_1 and then subsequent decomposition [254, 255]. The majority of these investigations employed TRMS as the experiment technique and also utilised multiphoton ionisation detection schemes. The existence of multiple proposals on how to interpret the TRMS data is perhaps unsurprising given that evidence of C-C bond cleavage was observation of the acetyl fragment ion

[247, 247, 250–252, 255], which can be formed by at least two pathways. The first, photoionisation of a neutral photoproduct, is the one directly related to C-C bond cleavage, whereas, the second, dissociative photoionisation or post-ionisation excitation of the cation (see Sec. 1.7) can produce the same fragment ion but through an entirely different mechanism. Further ambiguity in the interpretation of these data are also linked to the use of multiphoton ionisation based detection schemes and potentially had contributions associated with multiphoton pump processes. The latter point is linked to the very low $S_0 \rightarrow S_1$ excitation cross section [242], which typically results in the use of higher pump laser fluences and hence a higher probability for two-photon excitation. Even in TRPES measurements there are difficulties in data interpretation because multiple pump-probe ionisation channels are active [232] and complex pathways, such as initial excitation to S_1, ultrafast nuclear/geometry relaxation and absorption of a second pump photon to reach S_3 are required to explain the photoelectron transients [232, 256].

In contrast to the lower-lying S_1 and S_2 state the dynamics initiated by photoexcitation of the 3p and 3d Rydberg manifolds, which is the photon energy range consider in this work, are governed by Rydberg-valence coupling [241, 245, 257]. Some femtosecond pump-probe studies of states located near 8 eV have observed decays ranging from from 50 to 330 fs and have attributed these to dissociation on the excited state surface [228, 258–260]. The earliest investigation in this region (8.09 eV) was performed by Zewail and co-workers who extracted an extremely short decay constant of 50 fs in the acetone parent ion signal to C-C bond cleavage due to the initially populated Rydberg state being crossed by a state of σ^* character [258]. However, this study did employ both TRMS and mulitphoton excitation, which comes with the many ambiguities in data interpretation outlined above. A subsequent TRMS study by Farmanara *et al.*, utilising direct single-photon excitation at 8.0 eV, observed a significantly longer decay constant (330 fs) associated with the parent ion. The authors attributed this difference to dynamics occurring on a different state due to excitation of the lower-lying $3d_{yz}$ Rydberg compared to $3d_{x^2-y^2}$ in the Zewail work [228]. A long-lived (>10 ps) acetyl peak was also

observed and assigned to the acetyl radical being formed in an excited state by photodissociation of the initially prepared state [228].

Recent TRPES work by Hüter and Temps, employing two-photon excitation between 320-250 nm (3.87-4.96 eV), observed a photoelectron peak consistent with $3d_{yz}$ ionisation at wavelength comparable to Farmanara *et al.*, which decayed rapidly within their cross correlation [259]. The same study also provided some evidence that the decay time associated with the lower-lying 3p Rydberg states depended strongly on the level of vibrational excitation [259]. Investigations into the dynamics of even higher-lying Rydberg state have been undertaken by several groups [232, 261, 262] and in each of these studies photoelectron bands at the expected appearance energy of the 3p Rydberg states have been observed. This state has been suggested to be a bottleneck of the electronic relaxation of acetone within the Rydberg manifold.

One of the least ambiguous studies to date on relaxation dynamics of lower Rydberg manifolds was conducted by the Murnane and Kapteyn group where PEPICO spectroscopy and a waveguide based HHG source was used to provide single-photon VUV excitation [260]. The TRPES following excitation at 8 eV were dominated by a single peak, which was attributed to photoionisation 3p manifold. This transient feature exhibited an identical decay constant to the TRMS work of Farmanara *et al.* suggesting an incorrect assignments in the earlier work [228]. A weak feature consistent with photoionisation of the 3s Rydberg state was also identified in the time-integrated photoelectron spectra, for time-delays $>$100 fs. However, most likely due to limited statistics associated with the PEPICO detection scheme, no information was obtained on the timescale of the appearance of this feature. Population of the 3s (S_2) Rydberg state from the 3p has been proposed theoretically [248] so the appearance of this transient appears reasonable. Finally, the authors provide a tentative assignment of slow (near 0 eV) photoelectrons to photoionisation of the elusive $\pi\pi^*$ state correlating D_1 (π^{-1} [263]) cationic state, through a Koopmans' type argument (see Sec. 1.9.1). However, given the quality of the TRPES data, further experimental and theoretical work would be required to verify this assignment.

With the above ambiguities surrounding the excited state wavepacket dynamics of the 3p state and the role of the elusive $\pi\pi^*$ state in the dynamics in mind, this chapter is concerned with a single-photon VUV pump + single photon probe TRPES study of acetone. The rest of Chapter 3 is structured as follows. In Sec. 3.2, a description of the experimental apparatus is given, which includes details of the femtosecond VUV source and the Velocity-Map Imaging (VMI) spectrometer employed in this study. Details of the calibration of the VMI instrument as well as the VUV pulses are outlined in Secs. 3.2.4-3.2.5 and in Sec. 3.4 the experimental results are shown and discussed. This section is split into two-parts depending on the employed probe photon energy. Finally, the conclusions are summarised in Sec. 3.5.

3.2 Experimental set-up

3.2.1 VUV generation and optical setup

The 1 kHz 35 fs Ti:sapphire laser system employed in these experiments is the same as that outlined in Sec. 2.2. Fig. 3.1 shows, from the left, how a 3.25 mJ component of the total laser output was used for the VUV generation detailed here. Using a beamsplitter, a 0.75 mJ component (split (1) in Fig. 3.1) of total beam was separated to either generate a second color for pump-probe studies or for performing pulse duration measurements. The other arm was further split into two arms: the reflected component (1.5 mJ - split (2)) was for third harmonic generation (THG) in a tripling stage by first generating the second harmonic (2ω) in a first nonlinear crystal and successive combination with the remaining fundamental (ω) in a second crystal for THG (see lower section of Fig. 3.1); and the transmitted component (1 mJ - split (3)) remained at the fundamental frequency. Presented in Fig. 3.2 are sample spectra for the third harmonic and ω pulses used for the VUV generation scheme discussed below.

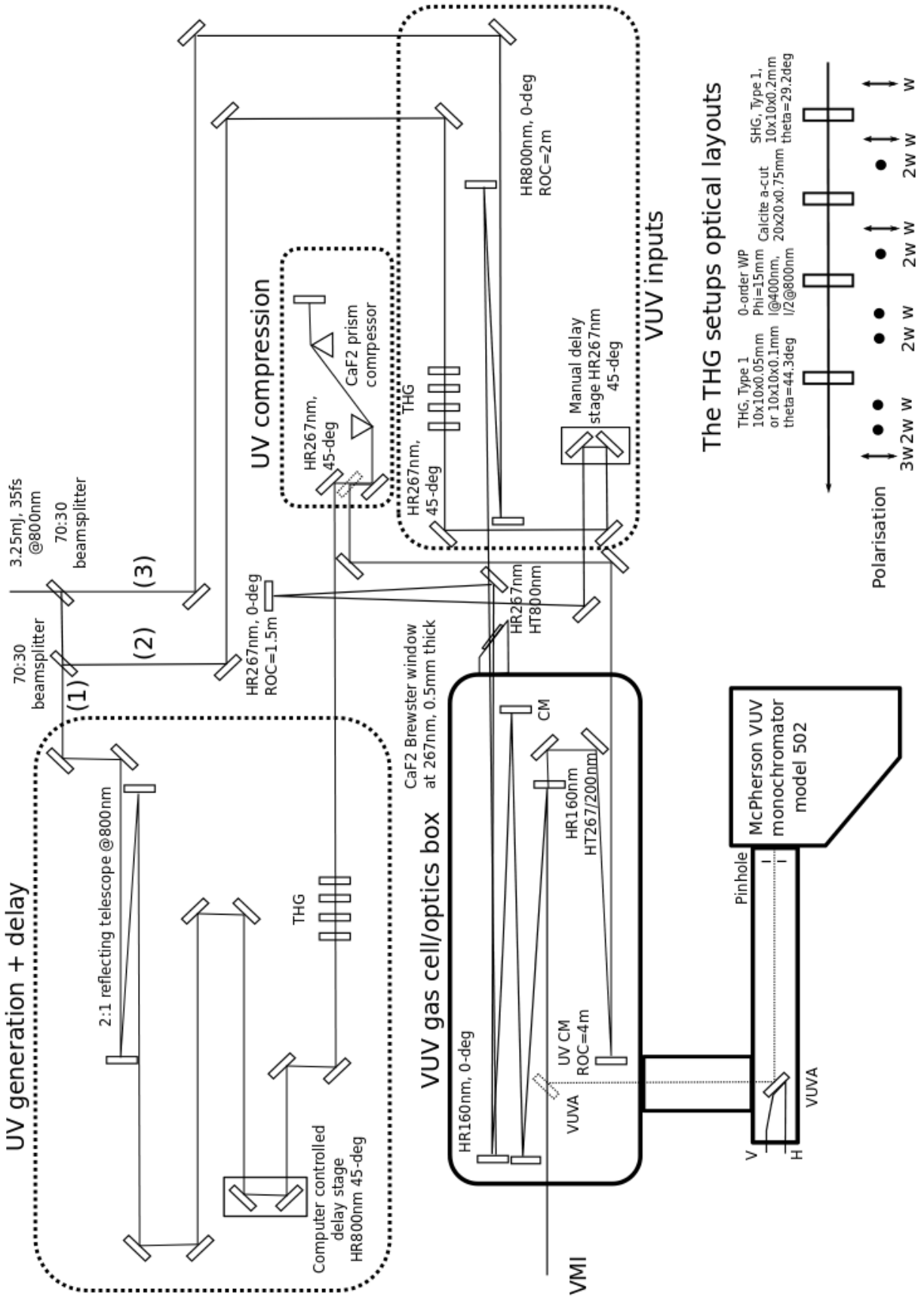

Figure 3.1: Schematic overview of the optical setup used in VUV-UV experiments on acetone. A detailed description of the optical elements is given in the main text. All optics absent of labels are dielectric high reflecting mirrors at either 160, 267 or 800 nm, depending on the specific arm of the experimental setup and if these optics are located after a frequency conversion scheme.

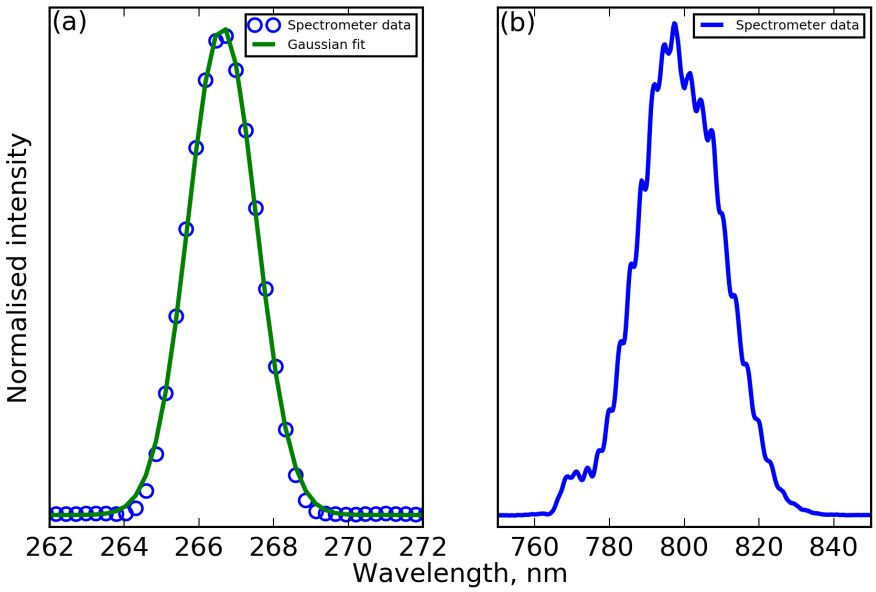

Figure 3.2: Typical spectra of the (a) third harmonic and (b) fundamental pulses used for VUV generation, measured with an Ocean Optics HR4000 spectrometer. Shown in panel (a) is a Gaussian fit (green) to the measured spectrum and yields a central wavelength as well as bandwidth of 266.63 nm and 2.15 nm (FWHM), respectively. This would correspond to a Fourier transform limited pulse duration of 49 fs, assuming a Gaussian pulse envelope.

The tripling stage was set-up in the following manner, 2ω pulses were generated in a 200 μm thick β-BBO crystal cut at 29.2° for Type I phase matching. In order to ensure efficient conversion to the third harmonic from the residual ω and the 2ω the effect of group velocity mismatch (GVM) needed to be considered. GVM refers to the fact that when different optical frequencies, or polarisation directions, propagate in a transparent medium, their group velocities will typically be different. In the context of nonlinear frequency conversion this is typically called temporal "walk-off" and essentially limits the effective interaction length in the nonlinear crystals. A birefringent calcite plate introduced into the beam-path compensates for GVM between the 2ω and ω pulses. A $\lambda/2$ plate for 800 nm and λ plate for 400 nm then rotates the polarisation of the pair of the pulses such that THG can be performed via Type I phase matching. The third harmonic (3ω) is generated by collinear sum-frequency-generation between 2ω and ω in a 100 μm β-BBO crystal cut at 44.3°. This setup generates 130 μJ at 266.63 nm with an estimated

pulse duration of approximately 50 fs (see Fig. 3.2). The residual 2ω and ω light was separated from the 3ω light by a series of dielectric mirrors with high reflectivity at 267 nm (HR 267nm, Eksma Optics). Attenuation of the 3ω pulses, required in some experiments where the VUV pulse energy was too high, was achieved by insertion of a $\lambda/2$ plate for 800 nm before the tripler setup and rotating the fundamental polarisation.

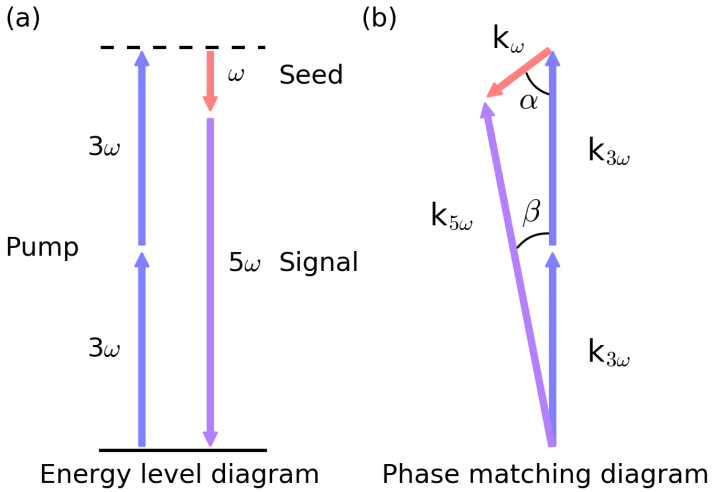

Figure 3.3: (a) Energy and (b) phase matching diagrams for the non-collinear difference frequency four-wave mixing process used to generate femtosecond VUV pulse.

The VUV fifth harmonic (5ω) light was generated by a non-collinear Difference Frequency Four-Wave Mixing (DFFWM) scheme first demonstrated and described in detail by Noack and coworkers [225]. Here, the choice of a non-collinear geometry permits the phase-matching condition to be satisfied for DFFWM at higher pressures, when compared with a collinear geometry [264]. This increase in phase matching pressure directly translates into an increase in VUV flux due to the quadratic dependence of the efficiency on the pressure [265]. In Fig. 3.3 an energy and wave-vector diagram (i.e. non-collinear phase matching) diagram for

DFFWM process is shown. In particular, panel (b) highlights the non-collinear nature of the process and the angle between the 3ω and ω beams. It is of note that for a particular pressure, the phase matching condition is satisfied at a particular angle (i.e. there is both a pressure and angle dependence to phase matching and therefore VUV flux) [265].

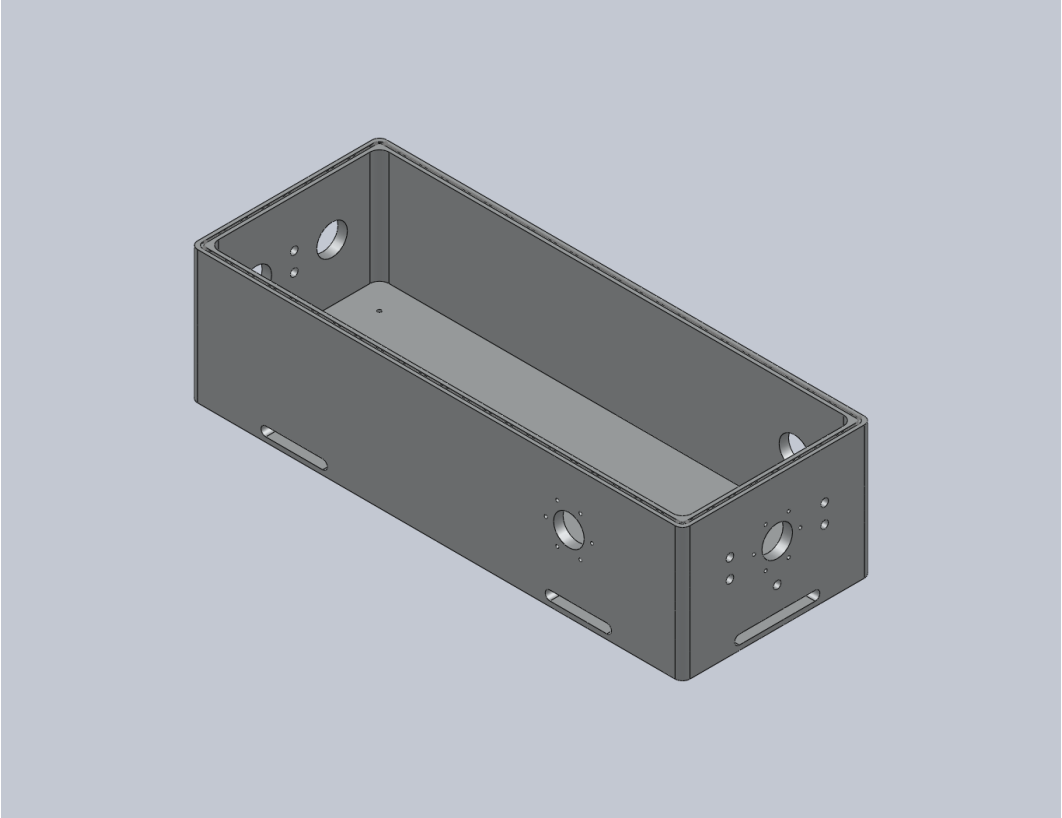

Figure 3.4: Solid works rendered drawing of the vacuum chamber utilised for generation of the femtosecond VUV pulses. Details of the optical elements and the VUV generation are provided in the main text.

For the particular realisation of the VUV source outlined here, the 3ω and the ω pulses are focused into a vacuum box using curved high reflector mirrors: HR 267 nm radius of curvature (ROC)=1.5 m and HR 800 nm ROC=2 m, respectively (f=R/2 for spherical mirrors). The vacuum box served as both the Ar gas cell for the DFFWM as well as an optics box for separation/recombination of the 5ω light with another femtosecond pump or probe pulse, typically in the UV or DUV region. In

Fig. 3.4 a Solid Works rendered drawing of the vacuum box is presented. The gas cell/VUV optics chamber was designed to incorporate a 24"×8" breadboard (Thorlabs - part number MB824) for an optical setup shown in Fig. 3.1. In order to ensure efficient VUV generation and experimental ease of use the following design choices were implemented during construction, or subsequent rebuilds, of this source:

- A thin (0.5 mm) CaF_2 window, mounted at Brewster's angle for 267 nm, was used as the entrance window; this ensured minimal dispersion and low reflection losses of the 3ω pulses.

- The top of chamber was sealed with an O-ring and a transparent plexiglass lid. This permitted the two filaments of ionised gas, associated with the focused 3ω and ω pulses, to be viewed during operation of gas cell and was essential for finding overlap of the pulse pair. If spatial and temporal overlap was achieved, the length and brightness of the filament would significantly increase.

- All *in vacuo* optical mounts, electrical cabling and motors were chosen and cleaned so as to be ultrahigh vacuum compatible; thus minimising the effects of outgassing. Failure to do this in the earliest implementation of the source resulted in irreversible damage to optics, as well as substantial decreases in VUV flux over time. This was attributed to build-up and photochemical deposition of outgassed hydrocarbons on optical elements.

- A pair of motorised mirror mounts were used to steer 5ω pulses and to optimise overlap with the gas jet in the centre of the VMI spectrometer (see Sec. 3.2.2).

A set of multilayer dichroic mirrors (HR160 nm), optimised with high reflection at 160 nm (Layertech GmbH, $R_{160\pm4\text{ nm}} > 90\%$) and high transmission at 267 nm and 800 nm ($R < 5\times10^{-2}$), were used to separate the residual driving beams in the wave mixing process and for recombining with a second pulse, for pump-probe studies, in a collinear geometry. Prior to recombination a curved,

ROC=2.8 m, VUV grade metal mirror (Acton optics - VUVA) was used to relay image the focus of VUV generation filament into the centre of a VMI spectrometer (see Sec. 3.2.2). The UV probe beam was focused independently using another curved optic ROC=4 m (UV CM), again prior to recombination. The choice of long focal length optics in both arms allowed for relatively "loose" focusing of VUV/UV pulses and helped to minimise spectroscopic signals associated with multiphoton processes.

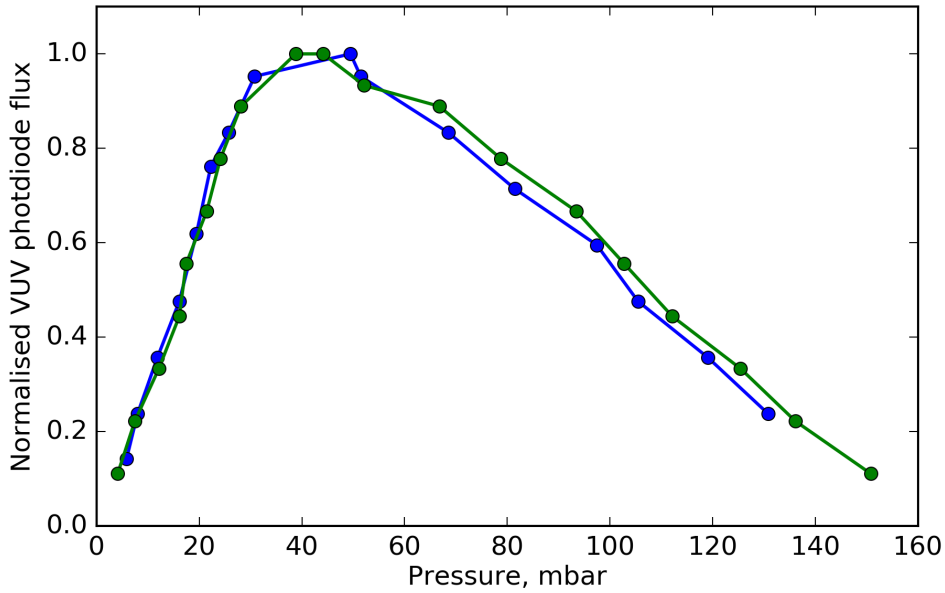

Figure 3.5: Pressure dependence of the 5ω flux recorded with a VUV monochromator and photodiode on two separate days (blue and green points).

In vacuo diagnostics of the VUV and UV pulses were provided by means of a VUV monochromator (McPherson model 502) and photodiode (OSI Optoelectronics XUV 100) as shown at the bottom of Fig. 3.1. Here, a set of metal mirrors (Acton optics - VUVA) and a motorised flip mirror were used to change the beam path between the VMI spectrometer and the monochromator. The inclusion of the monochromator in the VUV diagnostics proved essential for the operation of the VUV source as it allowed the signals associated with the 5ω, 3ω and ω beams to be isolated and optimised. Although significant attenuation of the 3ω and ω driving

beams was achieved by the inclusion of three 160 nm dichroic mirrors, bypassing the monochromator resulted in the photodiode response being dominated by signals associated with direct, as well as scattered, ω light. Due to the strong coupling of the 3ω and ω fields when the DFFWM process is optimised, 3ω, and ω scattering will depend on both spatial overlap of the 3ω, ω foci, and timing. Based on the above it was essential to have the ability to monitor the 5ω flux without any background and thus to utilise a monochromator. Inclusion of the monochromator also provided a means for the following parameters to be explored or optimised:

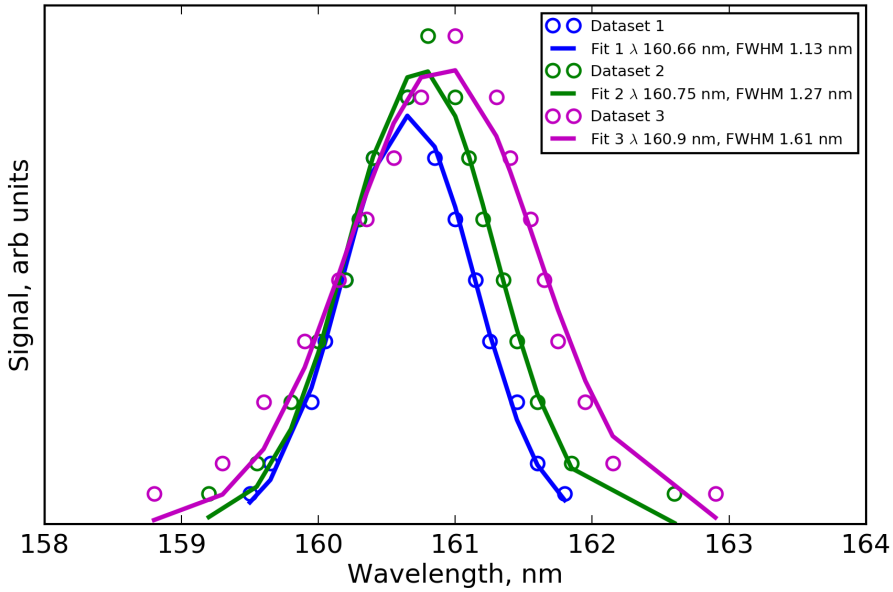

Figure 3.6: Sample spectral for 5ω pulses generated using non-collinear four-wave difference frequency mixing. The spectra were measured by hand using a VUV monochromator (McPherson model 502) and photodiode (OSI Optoelectronics XUV 100). It is of note that the wavelength axis is uncalibrated and therefore the quoted central wavelength should be treated with caution.

- The phase-matching conditions (i.e. Ar pressure and 3ω+ω spatial/temporal overlap) could be optimised for maximal VUV flux on a day-to-day basis. In Fig. 3.5 the pressure dependence of the normalised VUV flux is shown for a fixed non-collinear angle and two separate experimental runs. This pressure dependence was reproducible, as is evident for the overlapping data points, on

a day-to-day basis provided no change was made to the VUV generation beam paths, and hence phase matching angle. The observed trend in the pressure dependence is broadly in accord with the results of Noack and coworkers [225].

- The spectrum of the VUV pulse could be coarsely measured (by hand) using the monochromator and photodiode signal. However, due to this process being very time consuming and only providing low resolution data, spectra were infrequently measured. Shown in Fig. 3.6 are sample VUV spectra recorded on three separate experimental runs. All presented spectra exhibit significantly different bandwidths and central wavelengths, which are likely related to the exact spatial and temporal overlap of the 3ω and ω pulses for a given dataset. In particular, these changes in bandwidth could result in large variation of VUV pulse duration between different experimental measurements. For the spectra presented here, Fourier transform limited pulse durations of 34 fs and 24 fs would be expected for the smallest and largest bandwidths, assuming Gaussian pulse envelopes. In the case of the central wavelengths the absolute values should be treated with some caution as the wavelength scale of the VUV monochromator was not calibrated. Determination of the central wavelength was however possible using photoelectron spectra recorded using the VMI spectrometer; this will be discussed in Sec. 3.2.5. The observations outlined above suggest that it would be desirable to record the VUV spectra, and not the flux alone, during optimisation of the 3ω and ω spatial and temporal overlap. Finally, similarly to first point above, the experimental results were in accord with those presented in Ref. [225], where the authors report bandwidth of 1.3 nm (FWHM).

- Spatial overlap of the VUV pump and the UV probe pulse was also be found using the photodiode/monochromator setup. For this purpose, a 200μm pinhole was place at the monochromator entrance flange and position of the flange chosen to be at the foci of the VUV/UV beams. This distance approximately matches that of the foci in the centre of the VMI spectrometer and

hence provided an effective method for finding spatial overlap of the pump and probe pulse pair.

The final part of this section will deal with generation of a separate UV pulse, which, as previously mentioned, can be utilised as both: (i) a probe in the VUV excited state dynamics study of acetone and; (ii) a means to characterise the 5ω pulse duration through cross-correlation measurements. In comparison to VUV generation, the generation of UV light, either the third (3ω) or fourth (4ω) harmonic of Ti:sapphire, was relatively straightforward and used sum frequency mixing in β-BBO crystals. The final 0.75 mJ component of the total 3.25 mJ 800 nm output passed through a 2:1 reflecting telescope to reduce the beam diameter to approximately 5.0 mm (measured using the same procedure outlined in Sec. 2.4 of Chapter 2). Here reduction of the spot size resulted in an increase conversion efficiency in the various mixing stages. The ω beam then passed through a set of dielectric mirrors mounted on a computer controlled delay stage (Newport XML210) before entering the mixing stage. The 0.75 mJ beam was then passed through a 85:15 beamsplitter, the transmitted (15 %) component remained at the fundamental ω, whereas the reflected component (85 %) was frequency tripled using an "in-line" mixing scheme similar to the one described earlier for the 3ω VUV generation arm (see lower right hand side of Fig. 3.1). The exact choice of β-BBO crystal thickness used in the mixing schemes for 3ω or 4ω pulses differed and will be discussed separately.

For the 3ω pulses, the only significant change to the "in-line" mixing scheme outlined above was reducing the BBO crystal thickness from 100 μm to 50 μm in the final sum-frequency-generation step. THG was performed via Type-I phase matching and, therefore, the crystal cut remained at 44.3°. Incorporation of a thinner crystal for THG results in an increase of bandwidth at 3ω and opportunity to produce shorter pulse durations. Pulse energies up to 12 μJ were generated using this setup but typical pulse energies used for pump-probe experiments were considerably less (on the order of 0.5-3μJ) in order to achieve the best possible contrast between the pump-probe and probe-alone/pump-alone signals. In Fig. 3.7 sample

spectra shown for 3ω pulses generated with either 50 μm or 100 μm β-BBO crystals, these spectra highlight the increase in bandwidth associated with the thinner crystal.

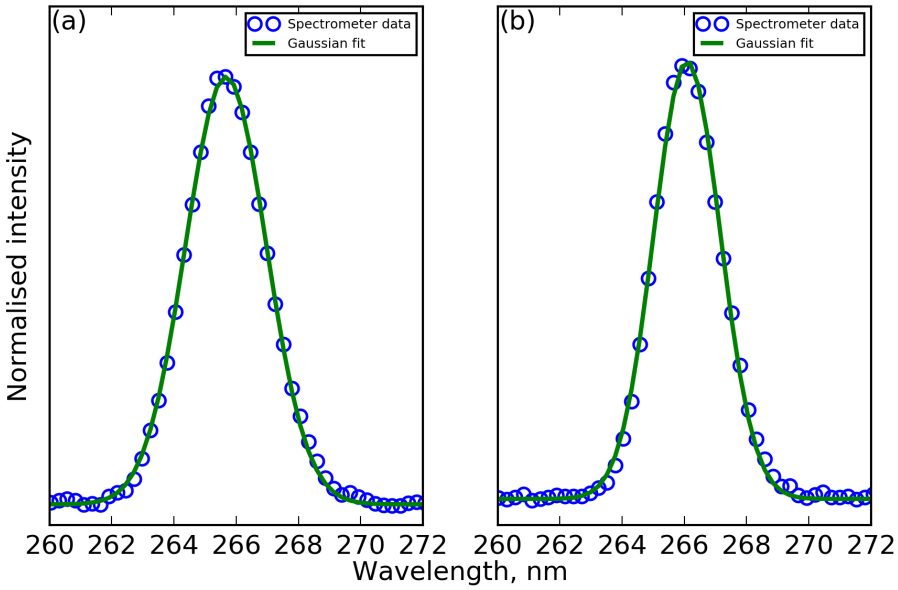

Figure 3.7: Third harmonic spectra recorded using a Ocean Optics HR4000 spectrometer for two different β-BBO crystal thicknesses. Gaussian fits to these spectra yield central wavelengths/bandwidths for (a) 50 μm and (b) 100 μm β-BBO crystals of 265.67/3.06 nm and 266.08/2.52 nm, respectively.

The 3ω beam was subsequently separated from the generating beam by a set of dielectric mirrors with high reflectivity at 267 nm (HR 267nm) before entering a prism compressor. The prism compressor was constructed in a folded geometry (see Fig. 3.1) using a matched pair of custom CaF_2 prisms (Laseroptex excimer 157 nm grade, cut at Brewster's angle for 267 nm); the distance between the two prisms was determined using estimates of the dispersion in various optical elements (windows/recombination optic) within the setup. Characterisation of the compressed 3ω pulse duration was performed using a homebuilt UV Two-Photon Absorption Auto-Correlator (TPA-AC) based on the design of Riedle and coworkers [266]. The autocorrelator utilises beam attenuation by two-photon absorption in thin material

for directly measuring the intensity autocorrelation of femtosecond pulses and is broadly tunable from visible to deep UV wavelengths. Presented in Fig. 3.8 is a typical autocorrelation trace of the 3ω pulse obtained via this method. This yielded a pulse duration of approximately 39 fs, close to the transform limit, assuming a Gaussian pulse envelope, for the available bandwidth shown in Fig. 3.7 (34 fs). The optimally compressed 3ω pulses were subsequently routed into the VUV generation vacuum box, where, as outlined above, they were focused and recombined with the 5ω pulses.

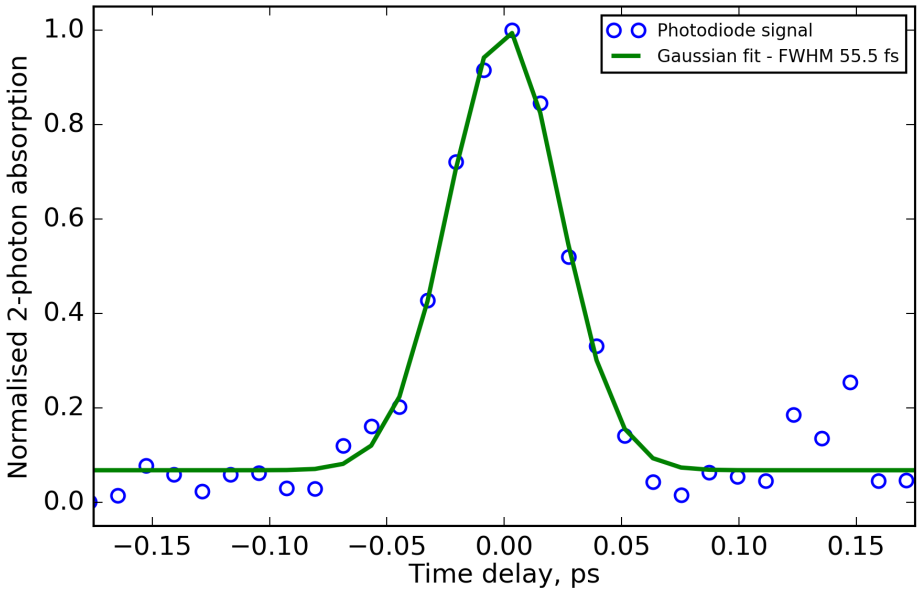

Figure 3.8: Autocorrelation traces for the 3ω probe pulses recorded using the two-photon absorption autocorrelator outlined in the main text. This autocorrelation trace was recorded after adjustment of the CaF_2 prism compressor for the shortest UV pulse. A Gaussian fit extracts a width of 55.5 fs (FWHM), this can be directly related to the 3ω pulse duration through $\sigma_{\text{autocorr}} = \sqrt{2\sigma_{3\omega}^2}$ and yields a pulse length of $\sigma_{3\omega} = 39$ fs.

For the generation of 4ω pulses an additional sum frequency mixing stage, between 3ω and ω pulses, was required. This scheme made use of the "in-line" tripler described above but with a few notable changes (see Fig. 3.9): (i) in order

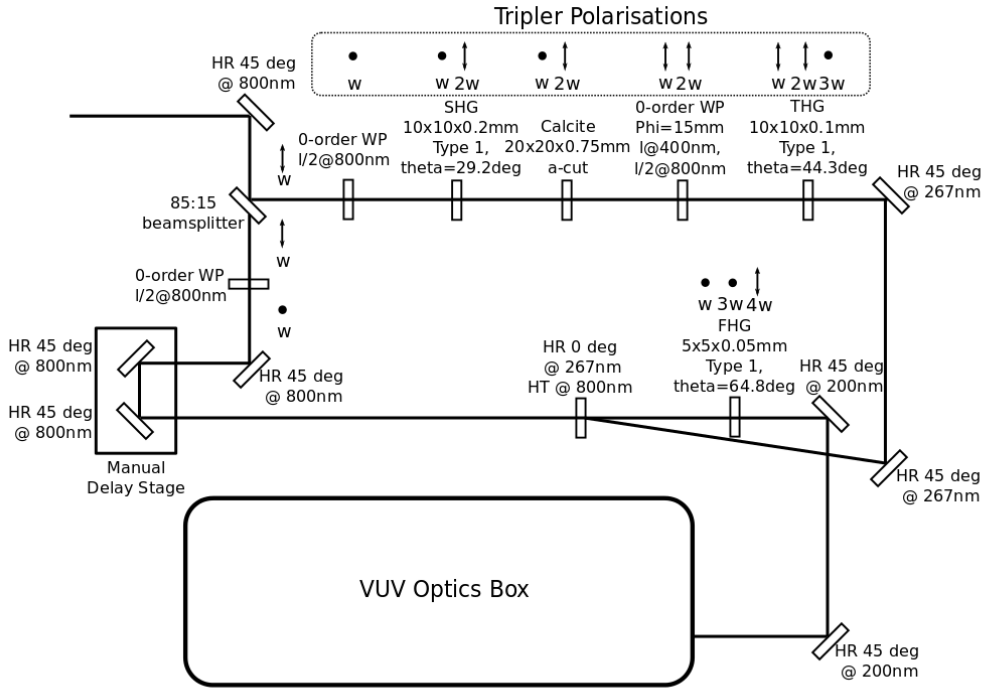

Figure 3.9: Schematic overview of the optical setup used to generate the 4th harmonic of Ti:sapphire. A detailed description of this setup, as well as rationalisation of the chosen non-linear crystal thicknesses, are provided in the main text.

to increase the conversion efficiency of this final stage a thicker, 100 μm, β-BBO crystal was used; (ii) to ensure that the 5ω and $3\omega/4\omega$ pulses have the same polarisation state within the VMI chamber the initial p-polarised ω beam was rotated to s-polarisation along with all elements of the THG setup. This choice of a parallel polarisation geometry is typically a requirement in the data processing for experiments utilising VMI techniques (see Sec. 3.2.3). Given the above requirement, all mixing stages in the generation of 4ω pulses were performed using Type-I phase matching.

Presented in Fig. 3.9 is a diagram of the above optical setup, details are given on all crystal thicknesses and cuts as well as polarisation rotations. The above mixing scheme produced approximately 30μJ of s-polarised 3ω pulse with a spectra similar to Fig. 3.7(b). Dielectric mirrors were used to transport the 3ω pulses, which were subsequently recombined at 0° on a minimal thickness dichroic mirror (3 mm fuse silica substrate) with the 15% transmitted component of the 0.75 mJ. Before

recombination the transmitted component passed through a $\lambda/2$ plate and manual delay stage to yield s-polarisation and a variable time-delay for the final mixing stage. Type-I sum frequency mixing to the fourth harmonic was performed in a 50 μm β-BBO crystal cut at 64.8°. Dielectric mirrors (CVI laser optics) with high reflectivity at 200 nm were then used to separate the 4ω pulses from the residual 3ω and ω pulses. The 4ω pulses were subsequently routed into the VUV optics box, where both focusing and recombination was performed in the same manner as for the previously discussed 3ω pulses. Fig. 3.10 shows a sample spectra for the 4ω pulse in the VUV excited state dynamics study of acetone; here the sparsity of data points with limited resolution of the employed Ocean Optics spectrometer in the deep UV.

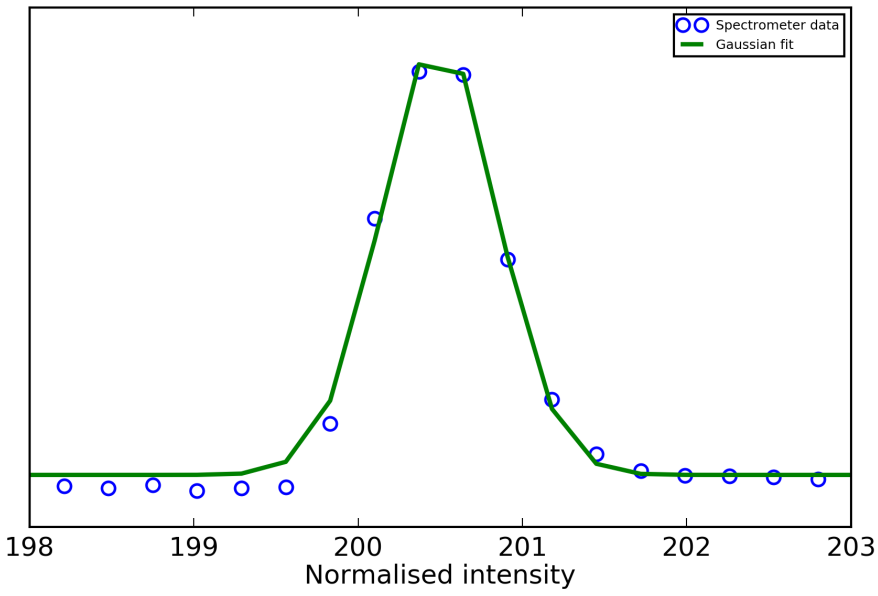

Figure 3.10: Fourth harmonic spectra generated using the optical setup shown in Fig. 3.9. Gaussian fits to the spectra yield central wavelength and bandwidth of 200.5 nm and 0.8 nm, respectively. Based on the bandwidth this would correspond to a Fourier transform limited pulse of 71 fs, again assuming a Gaussian pulse envelope.

3.2.2 Velocity map imaging (VMI) spectrometer

The pump and probe pulse pair outlined above was routed into the VMI spectrometer via a set of input baffles that minimised the transmission of scattered VUV/UV light to the laser-sample interaction region. Exit baffles were also incorporated to further reduce deleterious signals from scattered VUV/UV light. No line of sight from the input window of the machine to any part of the spectrometer electrode stack is allowed, since the photon energy of the DUV/VUV pulses is well above the work functions of the materials used (Au coated non-magnetic stainless steel, SS316). The VMI spectrometer consisted of a source and interaction chamber. The sample gases, typically a few percent of the molecule/atom of interest seeded in He, were introduced into the spectrometer by means of a Even-Lavie pulse valve operating at 1 kHz producing a molecular beam in a supersonic expansion [267]. The pulse valve was heated to 55°C throughout the experiments, which helped to reduce the presence of clusters. The molecular beam was expanded through a 250 μm conical nozzle into a source chamber typically held at a base pressure of 1×10^{-6} Torr. A 0.75 mm skimmer was used reduce the beam diameter selecting the central and coldest part of the beam, before the beam entered the separate interaction chamber, typically held at a base pressure of 1×10^{-8} Torr, along the spectrometer ToF axis. The co-propagating pump and probe laser pulses intersected the molecular beam pulses at 90°. A delay generator (Stanford Instruments DG535) was used to optimise the temporal overlap of the 1 kHz molecular beam and laser pulses.

Photoelectrons were extracted from the interaction region and focused onto an MCP and phosphor-based detector setup using electrostatic optics. The electrostatic optic system, similar to that described in Ref. [268], incorporated a three-stage, open aperture repeller electrode system. This was used to help to minimise spurious signals from scattered VUV/UV light and background gas in the ionisation chamber. The electrostatic optics additionally incorporated a set of eight Einzel lenses that allowed VMI conditions [269] to be achieved with a range of initial field gradients, facilitating tuning of the electron cloud compression/expansion along the ToF axis of the spectrometer. Following transit through the Einzel lens system, the electrons

were accelerated for detection using a high transmission grid electrode and detected using a pair of 40 mm Microchannel Plates (MCPs) and a phosphor screen (P47), the emission from which was relay imaged onto a charge-coupled device (CCD) camera operating at 30 Hz using an achromatic lens telescope.

3.2.3 Data acquisition and image processing

In the experiments reported here, photoelectron images were recorded as a function of pump-probe delay, with 200 frames (6666 laser shots) per step. The first 100 of which were recorded at the maximum overlap of the molecular beam and laser pulses, the second 100 were recorded with the pulse valve delayed 200 μs with respect to the laser. The latter was used to account for ionisation of residual background gases in the interaction chamber, which can also exhibit a time-dependent signal during the experiment. Each sequence of delays, a single experimental cycle, was kept short in order to minimise the effects of slow drifts over the cycle (primarily affecting the VUV/UV laser power), but a number of cycles were run in order to build up good statistics. At end of each experimental cycle single color pump and probe alone data, 200 frames (6666 laser shots) each, were recorded to help account for any single-color multiphoton ionisation with either pulse. Typically, however, the pump and probe intensities were set sufficiently low to help minimise any single-color multiphoton ionisation from either pulse. Typical datasets contained approximately 100 time-steps and approximately 25-40 identical pump-probe delay scans were averaged, depending on the signal strength, to achieve to the presented data.

The recorded photoelectron images were then processed using the following method:

- An image centre was defined, either manually or by finding the centre of mass, and the images rotated to ensure the polarisation axis was aligned correctly to the axis used in the inversion procedure.

- Both the time-independent and time-dependent background signals, associated with single-color multiphoton ionisation and residual background gases,

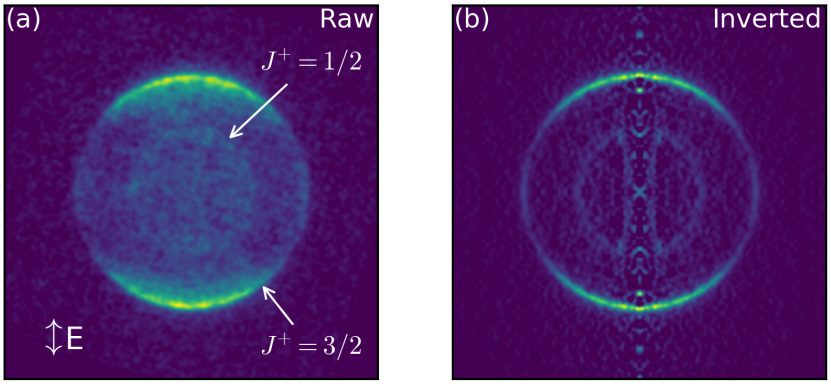

Figure 3.11: Sample (a) raw and (b) inverted VMI photoelectron images recorded using the apparatus outlined in Sec. 3.2.2 for 3-photon ionisation of Xe with 266.45 nm pulses. Here the polarisation direction of the linearly polarised pump and probe pulses is denoted by the vertical white arrow. The observed structure is discussed in detail in Sec. 3.2.4.

respectively, were then subtracted at each pump-probe time-delay.

- The resultant images were symmetrised by dividing the image into quadrants and determining the mean values from these four sections.

- A matrix inversion method [270] was then applied to each image within the pump-probe time-delay image stack to obtain the inverse Abel transform. This inversion procedure requires that the experimental geometry possesses cylindrical symmetry, which in turn, places constraints of the pump and probe polarisation geometry. In Fig. 3.11 sample images of both the raw and inverted data are shown for 3-photon (3×266.45 nm) ionisation of atomic Xe.

- Finally, the time-resolved photoelectron spectra (uncalibrated) was then obtained via radial integration of the inverted image stack. Calibration of this spectrum was achieved using the method outlined in the following section.

3.2.4 VMI energy calibration

The VMI spectrometer projects the velocity distribution of the photoelectrons emitted in the interaction region onto a position sensitive electron detector, thus producing a velocity map image [269]. After using the matrix inversion algorithm, the photoelectrons velocities, and therefore kinetic energies, can be extracted from the image. If a known photoelectron distribution is recorded, under the same focusing conditions (voltages) utilised in the experiments on the sample of interest, then the absolute kinetic energy scale, as well as detector resolution, can be extracted. For this purpose, a multiphoton ionisation photoelectron spectrum of Xe was used to calibrate the detector. The relationship between the photoelectron velocity v, kinetic energy E_{kin} and detector radius r can be expressed as follows [269]:

$$E_{\mathrm{kin}} = \frac{m_{\mathrm{e}} v^2}{2} = ar^2 \tag{3.1}$$

where m_{e} is the mass of the electron, r is the radial position on the detector and a is the calibration factor, which is dependent on the VMI focusing conditions.

For the pump probe studies presented here, Xe was multiphoton ionised using either $3\times3\omega$ or $2\times4\omega$ photons, these corresponded to the third and fourth harmonic of the Ti:sapphire laser system utilised in this study. Xe has two relevant and well characterised IPs: $\mathrm{Xe}(^1\mathrm{S}_0)\rightarrow\mathrm{Xe}^+(\ ^2\mathrm{P}_{3/2})$ with an IP of 12.1298 eV and $\mathrm{Xe}(^1\mathrm{S}_0)\rightarrow\mathrm{Xe}^+(^2\mathrm{P}_{1/2})$ with an IP of 13.4363 eV [271]. An example of the energy calibration procedure is shown in Fig. 3.12. Xe was ionised with three 266.45 nm (4.65 eV) photons, resulting in two photoelectron bands at 1.8202 eV and 0.5137 eV and providing a simple means to determine the calibration factor using Eq. 3.2.4.

3.2.5 VUV energy and time-resolution calibration

The measurement of the 5ω spectra using the monochromator and a photodiode (see Fig. 3.6) provided a means to estimate the typical bandwidth of the VUV

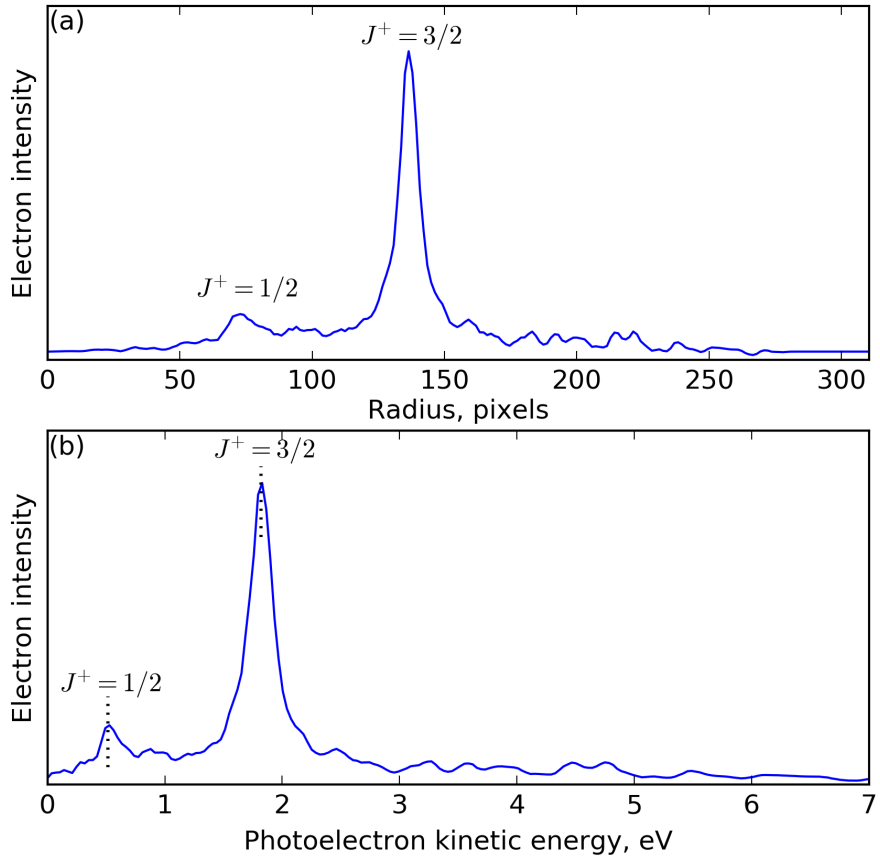

Figure 3.12: (a) The velocity spectrum obtained from the Abel inverted images shown in Fig. 3.11. Using the known IPs, and therefore the peak spacing, of the two spin-orbit split states of Xe^+ ($^2P_{3/2}$ and $^2P_{1/2}$) the calibration factor could be obtained. (b) Photoelectron kinetic energy spectrum obtained after rebinning from pixels to energy. Note, the relative spacing of the peaks changes due to the non-linear relationship between velocity and photoelectron kinetic energy.

pulse generated via DFFWM. However, as discussed in Sec. 3.2.1, the exact photon energy could not be reliably extracted due to uncertainties in the calibration of the monochromator wavelength axis. Obtaining a reliable measurement of this photon energy is a necessity for performing the TRPES measurements presented in this chapter. A relatively simple method to extract this value, given the available apparatus, is to perform 1+1′ photoionisation of Xe with the VUV pulse and another pulse of known photon energy. Presented in Fig. 3.14 is a time-integrated photoelectron spectrum of Xe^+ produced with 5ω+3ω ionisation; here the photon

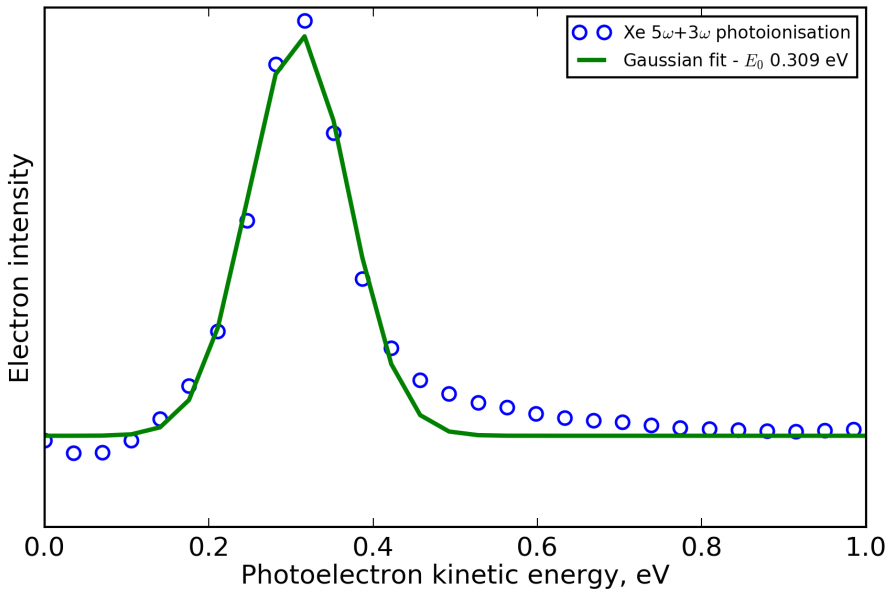

Figure 3.13: Time-integrated photoelectron spectra for Xe produced via 5ω+3ω photoionisation. A Gaussian fit (green) to the photoelectron peak yields a central energy of 0.309 eV. A central photon energy of 7.786 eV can therefore be extracted for the 5ω pulses based on the known IP of Xe ($^1S_0 \rightarrow Xe^{+2}P_{3/2}$ - 12.1298 eV) and known photon energy of the 3ω pulse (4.65 eV).

energy of the 3ω pulse could be determined accurately using a conventional UV spectrometer (Ocean Optics HR4000) and independent verified using the procedure outlined in Sec. 3.2.4. A Gaussian fit to the photoelectron peak observed in Fig. 3.14 extracts a central photoelectron kinetic energy of 0.309 eV and, therefore, a central photon energy/wavelength of 7.786 eV/159.24 nm for the 5ω pulse. This value did however fluctuate on a day-to-day basis due to small changes in the exact spatial and temporal alignment of the VUV driving beams and the above procedure was applied to each experimental run if accurate knowledge of the photon energy was required.

In addition to the calibration of the 5ω pulse photon energy, the analysis of the temporal dependence of the Xe 1+1′ non-resonant photoionisation signal also permitted extraction of the "time zero" (i.e. the temporal overlap of the pump and probe pulses) position and the cross correlation width. Shown in Fig. 3.14 is the

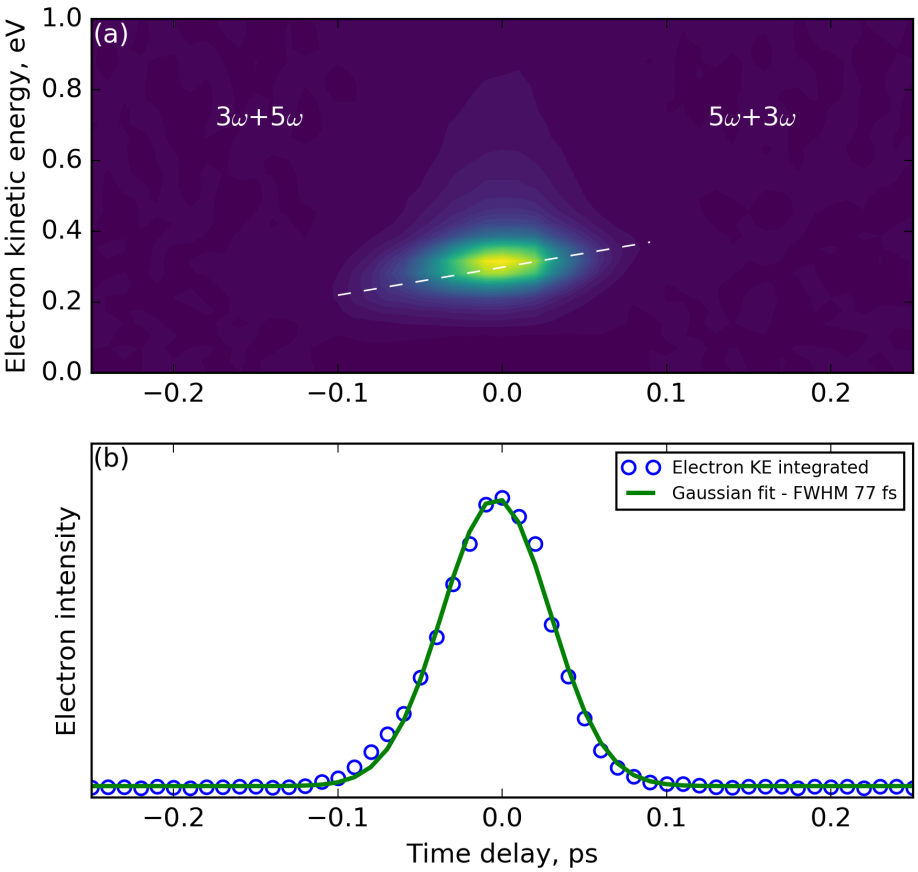

Figure 3.14: (a) Time-resolved photoelectron spectra for Xe produced via 5ω+3ω photoionisation. Negative time-delays refers to where the 3ω pulse proceeds the 5ω pulse, whereas positive time-delays refer to the opposite situation. A significant amount of variation in the photoelectron kinetic energies (dashed white line) is observed across the peak as a function of time-delay. This is attributed to a chirp of the 5ω pulse and is discussed in detail in the main text. (b) Time-dependence of the kinetic energy integrated photoelectron signal. A Gaussian fit to this yield extracts a width (FWHM) of 77 fs.

time-resolved photoelectron spectra for non-resonant ionisation of Xe with 5ω+3ω pulse pair. In panel (b) the time-dependence of the energy-integrated (0.0-1.0 eV integration window) photoelectron signal is presented. A Gaussian fit to this data extracts a FWHM of 77 fs, which can be directly related to the durations of the 5ω and 3ω pulses through $\sigma_{\text{xcorr}} = \sqrt{\sigma_{5\omega}^2 + \sigma_{3\omega}^2}$. Here $\sigma_{5\omega}$ and $\sigma_{3\omega}$ refer to the individual durations of the 5ω and 3ω pulses, respectively, assuming Gaussian pulse envelopes. This value was seen to vary due to either misalignment of the UV prism

compressor, resulting in a change of $\sigma_{3\omega}$, and/or changes in the VUV generation process (i.e. differing bandwidths on a day-to-day basis) which will effect $\sigma_{5\omega}$. In order to ensure constancy across the course of an experimental run and between different datasets the cross correlation was recorded before and after each experiment. This procedure was also performed for the 5ω+4ω pulse pair but as the analysis is identical to the discussion above no spectra are presented. Values are however quoted, where relevant, in the experimental result section (Sec. 3.4).

An estimate of $\sigma_{5\omega}$ can be determined by utilising the independent measurements of $\sigma_{3\omega}$ performed using a homebuilt UV autocorrelator (see Sec. 3.2.1). Note that during the autocorrelation measurements 4 mm of CaF_2 was inserted into 3ω beam path and the prism compressor distances adjusted accordingly. This allowed for the dispersion associated with the VUV/UV recombination optic (3 mm) and two thin (0.5 mm) CaF_2 windows to be properly accounted for during the extraction of $\sigma_{5\omega}$. Based on $\sigma_{3\omega}$ = 39 fs and σ_{xcorr} = 77 fs the VUV pulse duration was determined to be 62 fs. This is significantly larger than the Fourier transform limited values of 24-34 fs (see Fig. 3.6). This discrepancy can, in part, be attributed to the dispersion experienced by the 5ω pulse in the 0.5 mm CaF_2 window which separates the VUV optics box and the VMI spectrometer. However, by considering a 30 fs pulse, centred at 159.24 nm, propagating through 0.5 mm piece of CaF_2 one would only expect approximately 10 fs of temporal broadening. A possible source of additional dispersion is plasma contributions associated with the ionised filament where the DFFWM process takes place. This hypothesis was in keeping with an experimental observation where the 5ω+3ω cross-correlation was seen to vary as a function of VUV input pulse ($3\omega/\omega$) power but this was not systematically investigated.

Finally, the photoelectron spectra shown in panel (a) of Fig. 3.14 exhibits a slight energy dependent variation (white dashed line) as a function of pump-probe delay; this is indicative of one and/or both of the ionising pulses being chirped. The change in the photoelectron kinetic energies from low to high between the negative and positive sides of time-zero is consistent with a setup where the 3ω pulse is

close to its Transform Limited (TL) pulse duration, and the 5ω pulse has positive dispersion as expected assuming it was generated close to TL, and then propagates through 0.5 mm of CaF_2 on its way to the interaction region. This is in complete accord with the discussion in the preceding paragraph related to the duration of the 5ω pulse from the Xe cross-correlation measurements.

3.2.6 Fitting methods

A further consequence of the cylindrically symmetric laser polarisation geometry required for inverse Abel transform is that the observed laboratory frame PAD is only dependent upon a single angle, θ. Here θ denotes the ejection angle with respect to the symmetry (polarisation) axis. The presence of cylindrical symmetry therefore allows the general form of the angle-resolved flux (see Sec. 1.8) to be re-expressed in terms of Legendre polynomials rather than spherical harmonics (i.e. the ϕ dependence of the spherical harmonics is redundant after the choice of a cylindrically symmetric polarisation geometry). The angle-resolved flux (Eq. 1.24), for isotropically oriented molecules ionised by linearly polarised light, can therefore be re-expressed for the case of $1+1'$ photoionisation (i.e. L=4) as [21, 218]:

$$I(\theta) = \beta_0 P_0(\cos(\theta)) + \beta_2 P_2(\cos(\theta)) + \beta_4 P_4(\cos(\theta)) \tag{3.2}$$

here β_L are expansion coefficients, commonly termed photoelectron anisotropy or β parameters, and P_L are Legendre polynomials of order L. β_2 and β_4 are the anisotropy parameters describing the shape of the observed PAD. Here, the angles $\theta = 0^\circ$ and $\theta = 180^\circ$ are defined along the direction of the laser polarisation. For the femtosecond experiments presented in this chapter, Eq. 3.2 will exhibit a photoelectron kinetic energy dependence and vary with pump-probe time-delay.

In order to model the time-dependent excited state wavepacket dynamics of acetone, time-resolved photoelectron spectra were analysed using a 2D global least-squares fitting routine, which has been described in detail previously [272]. Briefly, the time-resolved (angle integrated) spectra, $S(E, \Delta t)$, was modelled by a series of exponentially decaying functions, $P_i(\Delta t)$, that are convoluted with the experimental

cross-correlation, $g(\Delta t)$. The fitting routine utilised FWHM of the cross-correlation, as well as time-zero position, determined from separate Gaussian fits to the temporal profiles of Xe photoelectron signals outlined in Sec. 3.2.5. Based on the above $S(E,\Delta t)$ can therefore expressed as:

$$S(E,\Delta t) = \sum_{i=1}^{n} A_i(E) \cdot P_i(\Delta t) \otimes g(\Delta t) \tag{3.3}$$

here $A_i(E)$ are the energy-dependent amplitudes for a particular $P_i(\Delta t)$ and i are the number of exponential functions employed in the fitting routine. Eq, 3.3 was then optimised by adjusting both $A_i(E)$ and the exponential decay constants to minimise the value of χ^2 for the experimental data and the fit using a mixture of Levenberg-Marquardt, stochastic, and exhaustive search routines. The 2D global fit returns the $1/e$ decay lifetime τ_i as well as $A_i(E)$, which is therefore a photoelectron spectrum associated with a particular decay time. These spectra are commonly referred to as decay associated spectra (DAS) and are attributed to a dynamical process occurring on a specific timescale. Such data can be fit using only parallel models (i.e. all fit functions originate from time-zero). With this choice of model, any negative amplitude present in the DAS is indicative of signal growth and sequential dynamical process, whereas positive amplitudes are signatures of decaying signal [272, 273].

Finally, the adopted 2D fitting procedure has two noteworthy drawbacks. Firstly, if the time-resolved spectra contain multiple features with similar time-dependence the fitting procedure will be unable to reliably extract multiple time constants occurring within the same decade. This is due to coupling between the two similar time-constants within the fit. Secondly, if the excited state wavepacket undergoes large amplitude nuclear motion, on a single electronic state, this can produce a time-and energy-dependent changes to the photoelectron spectra and be misinterpreted as dynamics evolving across multiple electronic states [274]. In general, the 2D global fit method employed here is unable to account for time- and energy-dependent changes (i.e. photoelectron kinetic energy chirps) to the spectra induced by large amplitude motion. An alternative strategy to analyse these spectral features has been discussed in a recent paper by Boguslavskiy *et al.* on excited state

non-adiabatic dynamics of trans 1,3-butadiene [196].

3.3 Acetone experimental results

The experimental results are divided according to the particular probe, either 3ω or 4ω, used to ionise the excited state wavepacket produced by the VUV pulse. By employing these two quite disparate photon energies it may be possible to access higher-lying electronic states of the acetone cation, which in turn may give complimentary information on the excited state dynamics (see Koopmans in the introduction). Initially however, a short discussions on: (i) the steps that were taken to eliminate the contributions associated with acetone clusters from the experimental data and; (ii) the assignments and nature of the wavepacket prepared by the 5ω pulse are provided.

3.3.1 Elimination of cluster signals

A concern of performing experiments on a molecules with a dipole moment, such as acetone, is that the recorded results can contain contributions associated with dimers and higher-order clusters. The presence of which can lead to difficulty in the interpretation of the time-resolved signals. To ensure the photoelectron signals presented here originated only from the acetone monomer, the mass spectra (MS) was recorded as a function of Even-Lavie pulse valve backing pressure. Note, throughout these measurements a 0.675 % mix of spectroscopic grade acetone (ACP Canada, 99.5 % purity) seeded in He (BOC GAZ, 5N purity) was used to back the Even-Lavie valve. In Fig. 3.15 acetone MS, for $1+1'$ ionization with 7.78 eV and 4.65 eV photons, is presented for a variety of backing pressures. It is evident that for all pressures considered here that, above 0.5 bar, the spectra contain significant contributions associated with acetone clusters. Multiple high-order clusters, up to $[CH_3\text{-}CO\text{-}CH_3]_5$, are observed in the 4.0 bar data and in both the dimer and trimer channels there are peaks observed associated with CH_3 loss.

Given the above, a backing pressure of 0.5 bar was used throughout this study to try to reduce any contributions associated with acetone clusters. It should be noted that, although no ToF peaks associated with clusters are observed at this pres-

sure, this method cannot unambiguously rule out the presence of clusters in the molecular beam. If, for example, photoionisation of the 5ω+3ω pulse pair correlated to a final cationic state which was unstable (i.e. resulted in fragmentation) then this could produce, for example, an acetone parent ion and a neutral acetone co-fragment. These photoproducts would be identical to those formed by photoionisation of the acetone monomer and hence could not be distinguished from one another. In order to cleanly rule out any contributions associated with clusters an experiment would have to be performed using either 3D (or 2D slice/mass gated) ion VMI under identical molecular beam conditions. If clusters were present this would result in a non-zero recoil in the parent ion correlated VMI image and not just the expected zero kinetic energy peak. This capability was however not implemented on the current Ottawa VMI apparatus but could be achieved by utilising state-of-the-art time-stamping cameras such as the Pixel Imaging Mass Spectrometry (PImMS) camera [275] and TPX3Cam [276]. The former of which has been previously integrated with the Ottawa VUV+VMI set-up [277].

Finally, it is of note that the 0.5 bar MS is broadly in-accord with the results of Farmanara *et al.*, namely that peaks associated with the acetone parent ion as well as the acetyl (CH_3-CO^+) and methyl fragments are present [228]. The appearance potentials connected with the acetyl and methyl ion fragmentation channels are 10.4 eV and 13.8 eV [263], respectively, implying that CH_3^+ production requires ionisation with two 4.65 eV (3ω) photons to be produced, based on the total $1+1'$ photon energy in the experiment of 12.43 eV.

3.3.2 VUV absorption spectrum

The introductory material to this chapter highlighted that the photochemical dynamics occurring in high-lying excited states of polyatomic molecules are generally complex due to large state densities and non-adiabatic coupling between them. This complexity is evident in the VUV absorption spectrum of acetone [278], which is shown in Fig. 3.16 between 7.3-8.2 eV. The spectrum is dominated by a series of sharp spectral features, which belong to the various vibrational states on

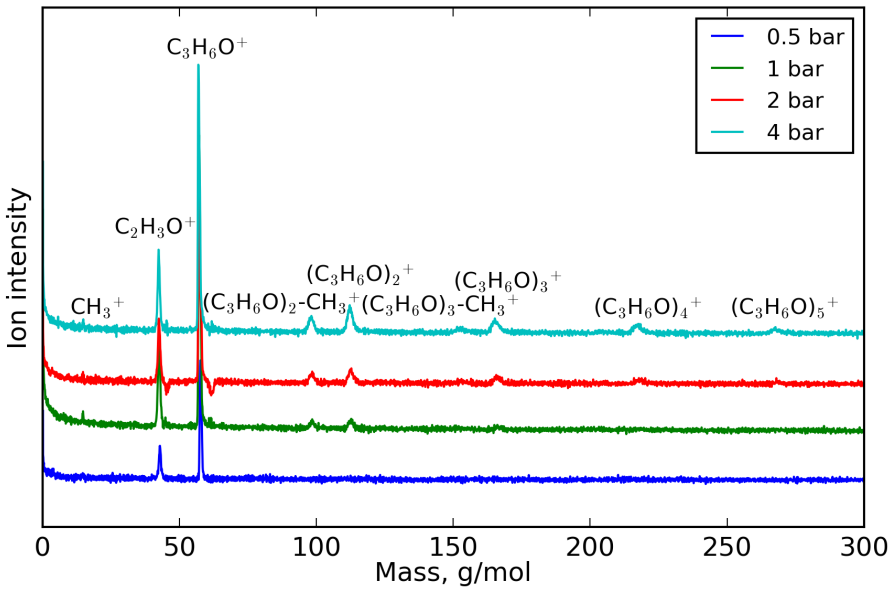

Figure 3.15: Mass spectrum of acetone recorded as a function of Even-Lavie pulse valve backing pressure for 1+1′ photoionisation with 7.78 eV and 4.65 eV pulses. The spectra was recorded at Δt = 120 fs, which corresponded to the position of maximal signal strength.

the $3p_y$, $3p_z$, $3d_{yz}$ and $3d_{x^2-y^2}$ Rydberg manifolds, superimposed on a broad diffuse continuum. This continuum has been attributed to three distinct valence states at approximately 7.454, 7.715 and 8.09 eV [242, 279]. Assignment of the lowest energy valence band has been the subject of considerable discussion, particular since the assignment of $n_y \rightarrow \sigma^*$ by Barnes and Simpson [280], which is at odds theoretical predictions. The valence states located at approximately 7.715 and 8.09 eV have also been the subject of debate but it is generally accepted that a state of $\pi\pi^*$ character plays a role in this region. The exact vertical excitation energy of this state is debated with the most detailed synchrotron radiation study placing this at ∼7.85 eV [242], whereas energy loss measurements have given a value of ∼8.1 eV [280].

A summary of the vertical excitation energies for the origins of the aforementioned bands, as well as their symmetries is provided in Table. 3.1. Despite VUV vibronic absorption spectrum of acetone being the subject of numerous experimental [242,257,281] and theoretical [240,245] investigations, spectral assignment dif-

fer, and are often contradictory. This is particularly true in the excitation region ($\sim$7.7-7.85 eV) considered in this study, where various vibrational states have multiple electronic assignments [242]. A normalised VUV spectrum to represent the series of vibrational states which can be accessed during pumping with the 5ω pulse is also presented in Fig. 3.16, here the spectral shape is assumed to be Gaussian. Note, a bandwidth of 1.3 nm/0.063 eV was used for this sample spectra, which appeared reasonable based on the fits extracted from Fig. 3.6. The central photon energy was taken directly from Sec. 3.2.5. The sample spectra spans a series of at least two vibrational peaks at 7.756 and 7.803 eV which have been attributed to $3d_{yz}$+$1\nu_8$ and $3d_{yz}$+$2\nu_8$, respectively [242] and perhaps a shoulder at $\sim$7.78 eV, which is unassigned. It therefore appears reasonable to suggest that the initially prepared wavepacket in the experiments presented here possesses predominately $3d_{yz}$ (3^1A_1) character but may exhibit some $\pi\pi$ contribution also.

Table 3.1: Adiabatic excitation energies of the valence and Rydberg states of acetone of interest in this work. Experimental ionisation potentials for the D_0 and D_1 channels are also shown.

Transition	Symmetry	Excitation energy (eV)
Valence States		
$n_y \rightarrow \pi^*$	1^1A_2	3.774 [239]
$n_y \rightarrow \sigma^*$		$\sim$7.454 [280]
$\pi \rightarrow \pi^*$	4^1A_1	$\sim$7.85 [242]
Rydberg States		
$n_y \rightarrow 3s$	1^1B_2	6.355 [242]
$n_y \rightarrow 3p_y$	2^1A_1	7.40 [242]
$n_y \rightarrow 3p_z$	2^1B_2	7.454 [242]
$n_y \rightarrow 3d_{yz}$	3^1A_1	7.715 [242]
$n_y \rightarrow 3d_{x^2-y^2}$	3^1B_2	8.090 [242]
Cationic states		
$D_0(n^{-1})$	1^2B_2	9.708 [263]
$D_1(\pi^{-1}CO)$	1^2B_1	12.45 [263]

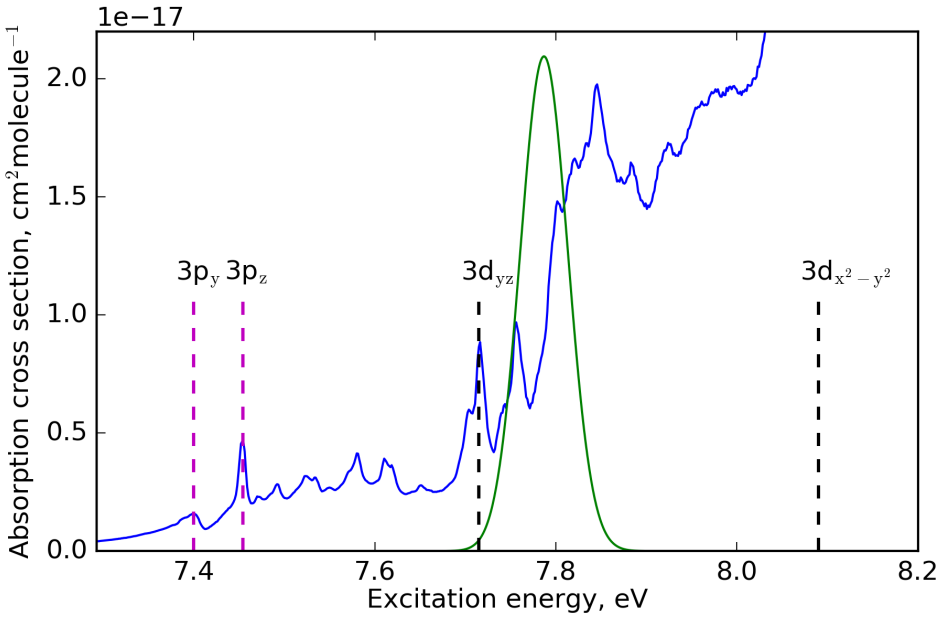

Figure 3.16: High resolution VUV photoabsorption spectrum of acetone in the 7.3-8.2 eV energy region recorded using synchrotron radiation by Cheng *et al.* [278]. An overlay of Gaussian spectrum representing the 5ω pulse is shown to highlight the states populated by photoexcitation. Dashed magenta and black lines denote the vertical excitation energies of the onset of various members of the 3p and 3d Rydberg manifold, respectively. The data used to generate this figure was taken from the Max Planck Institute-Mainz UV/VIS Spectral Atlas of Gaseous Molecules of Atmospheric Interest [282] and was originally presented in Ref. [278].

3.3.3 Time-resolved photoelectron spectra

3.3.3.1 Probing with 4.65 eV (3ω) photons

First, the results using the lower energy, 4.65 eV (3ω), probe are discussed. In Fig. 3.17 the time-resolved photoelectron spectra associated with excitation of acetone by the 5ω (7.78 eV) pulse and subsequent probing by the 3ω pulse is presented for both linear (a) and logarithmic (b) scales and for pump-probe delays up to 3 ps. The total available photon energy given the pump and probe pulses, $\hbar\omega_{\text{max}}$ is 12.43 eV. This photon energy would allow for ionisation correlating to both the electronic ground (D_0) and first excited (D_1) states of the acetone cation located at 9.708 eV and 12.4 eV, respectively [263]. Based on these values, the maximal pho-

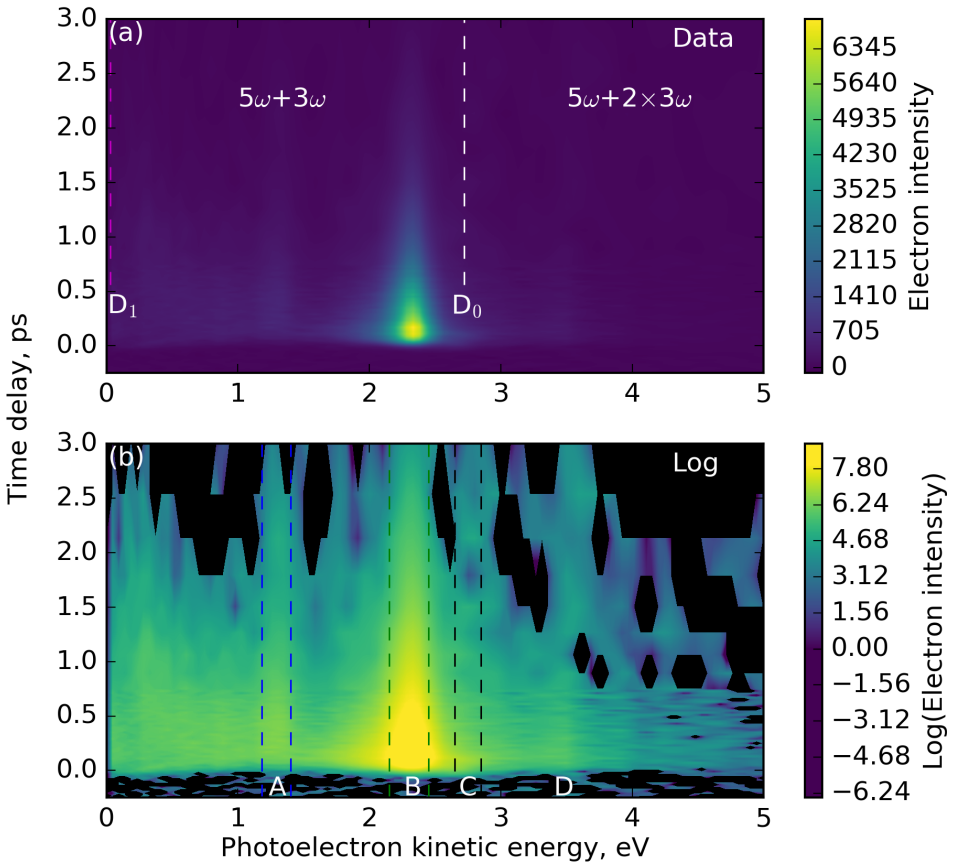

Figure 3.17: Time-resolved photoelectron spectra for acetone pumped with 7.78 eV (5ω) photons and subsequently probed at 4.65 eV (3ω). Positive time-delays indicate that the pump pulse precedes the probe pulse. The spectra is displayed on both (a) linear and (b) logarithmic scales. The maximum possible photoelectron kinetic energies for ionisation correlating to the ground (D_0) and first electronically excited (D_1) states of the acetone cation are denoted by the white and magenta dashed vertical lines in panel (a), respectively. Photoelectrons with higher kinetic energies than the D_0 cut-off must originate from 2-photon ionisation with the 4.65 eV 3ω pulse. Discussions of the features labeled A-D are provided in the main text. The dashed colored line signify the integration regions used for the 1D transients shown in Fig. 3.19.

toelectron kinetic expected for ionisation correlating to D_0 and D_1 would be 2.72 eV and 0.03 eV. However, given the very low electron kinetic energies associated with D_1 ionisation continuum, this latter channel would be unlikely to show up for single photon ionisation, particularly when the role of FC overlap in the photoelectron spectrum is considered.

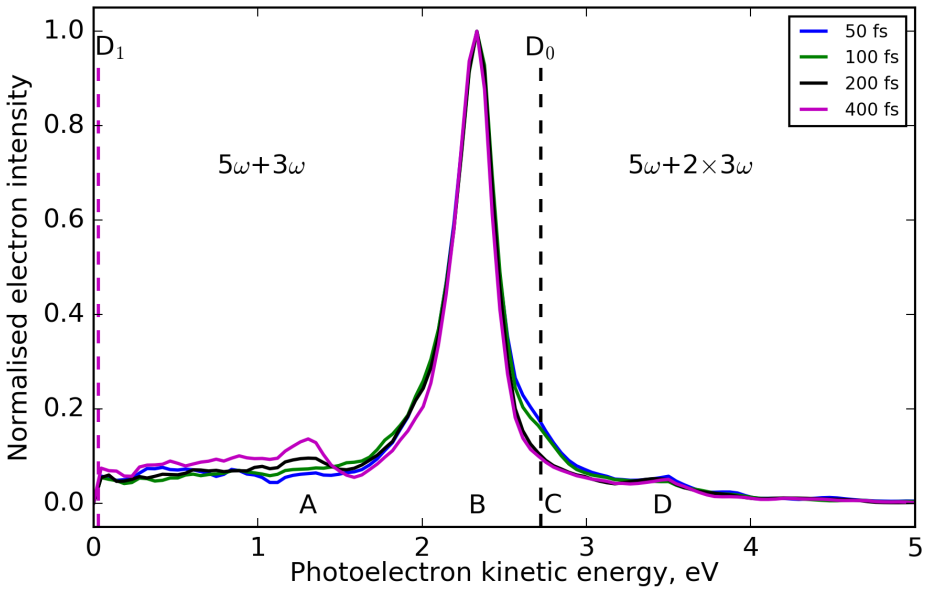

Figure 3.18: One dimensional cuts of the acetone time-resolved photoelectron spectra (see Fig. 3.17) at various positive time-delays. Similarly to Fig. 3.17 labels are provided for the maximum possible photoelectron kinetic energies for D_0 (black dashed line) and D_1 (magenta dashed line) ionisation channels and for peaks A-D. Note, each individual one dimensional cut was normalised to the maximum photoelectron intensity at a particular pump-probe delay and the cuts are integrated over a 60 fs window centred around the values shown in the legend.

In order to highlight the weaker spectral features, Fig. 3.17(b) shows the data on a logarithmic scale. In addition normalised, one-dimensional, cuts of the total time-resolved spectra are shown in Fig. 3.18 for various positive time-delays. Figs. 3.17 and 3.18 highlight that the spectra is dominated by a narrow band, with limited photoelectron KE progression, centered at approximately 2.3 eV (peak B in Fig. 3.17). Several weaker features are also observed: (i) a small narrow peak located at 1.3 eV (peak A); (ii) a "shoulder" extending up to the highest possible KE, based on 1+1′ ionisation (peak C), and; (iii) a weak band at approximately 3.45 eV, which must originate from ionisation with multiple photons since this photoelectron energy is higher than the energy we can access with the 1+1′ process (peak D). Although care was taken to minimise contributions associated with multiphoton processes, through the choice of long focal length optics and small fluences for

both the pump and probe pulses, weak signal such as point (iii) were observed in some datasets. These signals however did not provide any significant insight in the excited state wavepacket evolution and, therefore, will not be discussed further.

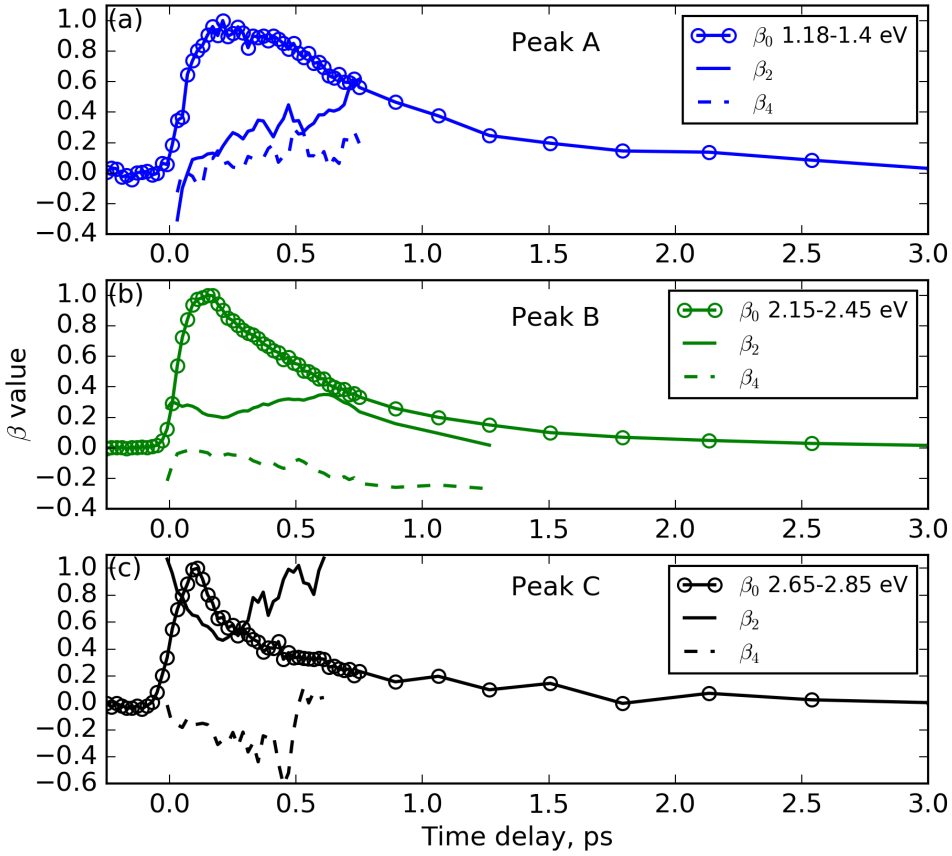

Figure 3.19: Transient photoelectron anisotropy (β) parameters for features A-C observed in Figs. 3.17 and 3.18. The electron kinetic energy integration regions are highlighted in each panel. The β_2 and β_4 parameters are normalised to β_0 (i.e. the contributions associated with the time-dependent photoelectron yield are removed), whereas β_0 is normalised to the maximum. Note, a three-point moving average was applied to β_2 and β_4 to improve the signal-to-noise

Presented in Fig. 3.19 are the transient (energy integrated) electron anisotropy (β) parameters obtained through fitting of the photoelectron images, using Eq. 3.2, as a function of time delay. Note, the values of the chosen integration region are highlighted in the legend of each subplot. The lowest order expansion coefficient,

β_0 is directly proportional to the photoelectron yield (i.e. the photoionisation cross section) and is independent of photoelectron emission angle. This observable therefore exhibits the same temporal behaviour as simply integrating the time-resolved photoelectron spectrum (Fig. 3.17) over the same regions. Each of the β_0 transients show different temporal dynamics for both onset/rise and decay timescales. For example, the lowest kinetic energy (peak A/1.18-1.4 eV) transient has delayed rise with respect to the higher energy features, with the band exhibiting negligible intensity at "time-zero". Conversely, the highest energy (peak C/2.65-2.85 eV) "shoulder" exhibits a much more rapid rise and decay, as was evident from the one-dimensional temporal cuts shown in Fig. 3.17.

The higher-order coefficients, β_2 and β_4, contain all the angularly dependences and display different levels of anisotropy for each of the photoelectron bands. Large positive and slight negative values of β_2 = 0.6-1.0 and β_4 = $\sim$-0.2 were observed for the high energy "shoulder" (peak C), whereas considerably smaller values were observed for the main photoelectron peak (peak B) at 2.35 eV (β_2 = 0.2-0.3 and β_4 = $\sim$0.0). However, despite these large differences in absolute values, the global time-dependence of the β_2 parameters of these two features is remarkably similar. Initially, the β_2 values decrease rapidly from time-zero and reach a global minimum at approximately 200 fs. The values then steadily increase out to the maximum plotted time-delay of $\sim$600-700 fs. It is noteworthy that the temporal behaviour of the β_2 parameters connected with these two higher-lying features is somewhat reminiscent of that expected for rotational dephasing [283]. For the lower energy feature (peak A/1.18-1.4 eV), the β_2 parameter does not exhibit the same time-dependent modulation but does slowly increase across the pump-probe window shown here. The temporal dynamics of the β_2 and β_4 parameters are considered to be beyond the scope of the current work, however, absolute values of these parameters at specific time delays, corresponding to the maximum of a photoelectron transient, will be used as supporting arguments in Sec. 3.4.

Fits to the spectra presented in Fig. 3.17 were performed using Eq. 3.3 and

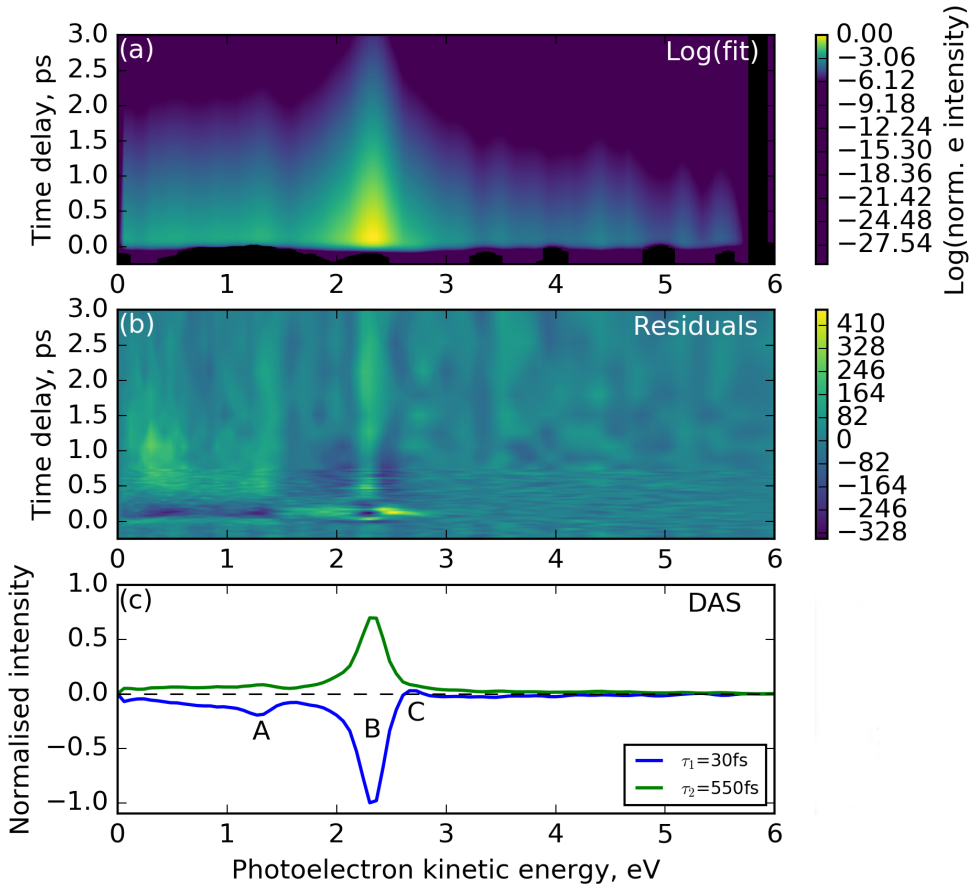

Figure 3.20: (a) A two exponential fit, using Eq. 3.3, to the photoelectron spectra in Fig. 3.17. The spectrum is presented on a logarithmic scale to highlight the weak features. (b) 2D plots of the residuals (i.e. global fit subtracted from raw data). (c) Decay associated spectra (DAS) obtained from data shown in panel (a). Time constants for the two exponentials are shown in the legend of panel (c). Peak labels are the same as those defined previously in Fig. 3.17.

two exponentially decaying functions. An instrument response function/cross correlation, independently extracted from non-resonant 1+1´ photoionisation of Xe, of 93 fs was utilised here (see Sec. 3.2.6). The resultant fit and extracted DAS are shown in Fig. 3.20. The DAS extracted for acetone, probed at 266.45 nm, includes two different components with time constants of $\tau_1^{3\omega}$ = 30 fs and $\tau_2^{3\omega}$ = 550 fs for the presented data. The 30 fs time constant appears to describe the initial evolution of the main photoelectron band (peak B) located at 2.35 eV, where the negative amplitude confirms the delayed onset of this feature. A small positive amplitude

was observed for the higher kinetic energy "shoulder" (peak C), which could be indicative of population transfer (i.e. sequential dynamics) between this and the state producing the 2.35 eV photoelectrons (peak B). The longer time constant, $\tau_2^{3\omega}$, accounts for the decay of main photoelectron band. Note, the robustness of fit was qualitatively checked by fitting multiple datasets using the model outlined above. These series of fits produced $\tau_1^{3\omega}$ = 10-30 fs and $\tau_2^{3\omega}$ = 500-600 fs and observed the same global trends, such as a weak positive amplitude of the high energy "shoulder".

In order to demonstrate the quality of the fit, the associated residuals (i.e. the fit subtracted from the raw data) are also presented in panel (b) of Fig. 3.20. Overall the residuals are fairly randomly distributed through the dataset, however, there are several noteworthy discrepancies (i.e. large values in the residuals): (i) a feature at short Δt (0-200 fs) extending from approximately 1.8-2.8 eV, which may be connected to large amplitude motion of the initially prepared state; (ii) a modulation (both positive and negative) at lower kinetic energies, which is, in part, attributed to failure of the model to capture the growth of the lower energy (peak A) narrow feature (see β_0 in Fig.3.19). The lower energy residuals could be improved significantly through the inclusion of a third time constant. However, this resulted in the fit becoming unstable due to two time constants being within the same decade (see Sec. 3.2.6).

3.3.3.2 Probing with 6.20 eV (4ω) photons

The time-resolved spectra associated with the higher energy, 6.20 eV, probe photon is presented in Fig. 3.21, for both linear (panel (a)) and logarithmic (panel (b)) scales. Based on the 5ω central photon energy (7.77 eV) extracted for this datasets (see Sec. 3.2.5) the total available photon energy, $\hbar\omega_{\max}$, is 13.97 eV. This would correspond to maximal photoelectron kinetic energies of 4.26 eV and 1.56 eV for ionisation correlating to D_0 and D_1, respectively and are denoted by the black and magenta dashed vertical lines in Fig. 3.21. The spectra above 1.55 eV (i.e. the portion which could be ionised with the lower energy probe photon (3ω))

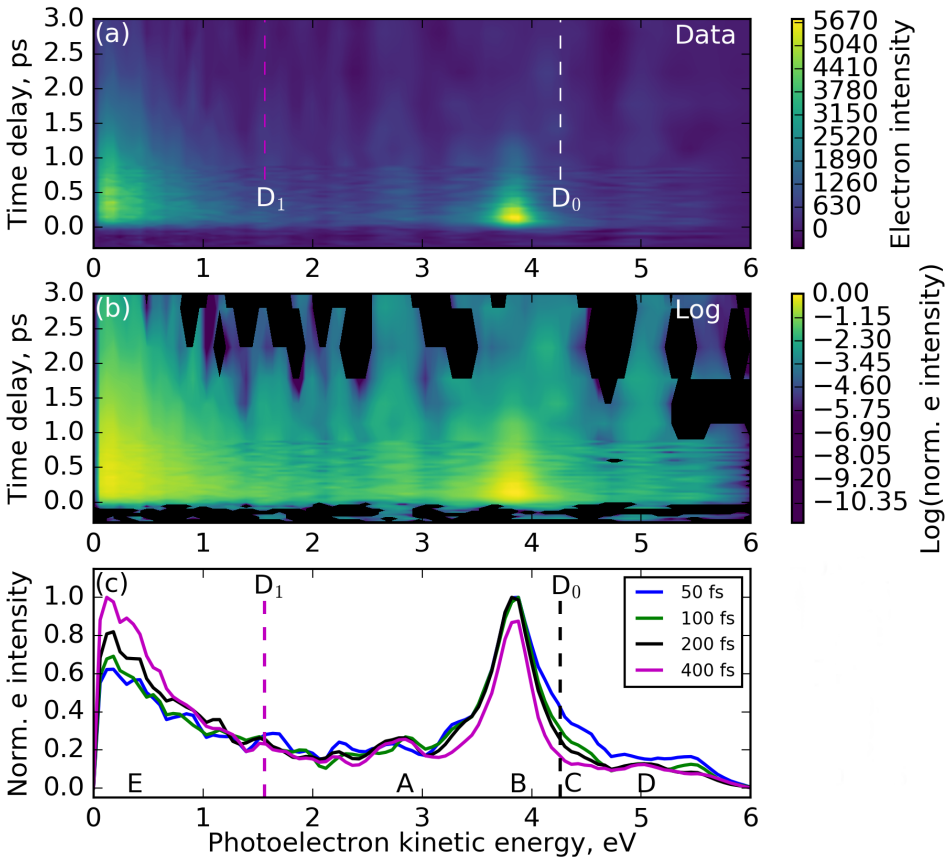

Figure 3.21: Time-resolved photoelectron spectra for acetone pumped with 7.77 eV photons and subsequently probed at 6.20 eV on both (a) linear and (b) logarithmic scales. (c) Normalised 1D cuts of the spectra presented in panel (a) for various positive pump-probe time-delays. The black/white and magenta dashed annotations the maximum possible photoelectron kinetic energies for D_0 and D_1 ionisation channels, for further details see main text. Note, similarly to Fig. 3.18, the 1D cuts are integrated over a temporal window of 60 fs. Features A-D are the same as those previously observed in Figs. 3.17-3.20 but shifted to higher kinetic energy by $\sim$1.55 eV. Feature E, previously unobserved in the lower 3ω probe photon energy data, is discussed in the main text.

exhibits the same peak structure (peak A-D) as the spectra shown in Fig. 3.17, which suggests that the ionisation continuum is relatively "flat" across the photon energy range considered in this work. If a significant difference were observed, this would be indicative of processes such as autoionisation. The higher energy probe photon does however result in a new photoelectron band being observed at lower kinetic energies (feature E in Fig. 3.21 at 0.0-1.5 eV). However, unlike the relatively

sharp features observed above 1.55 eV, this band possesses a broad FC envelope and is clearly seen in 1D temporal cuts in Fig. 3.21(c).

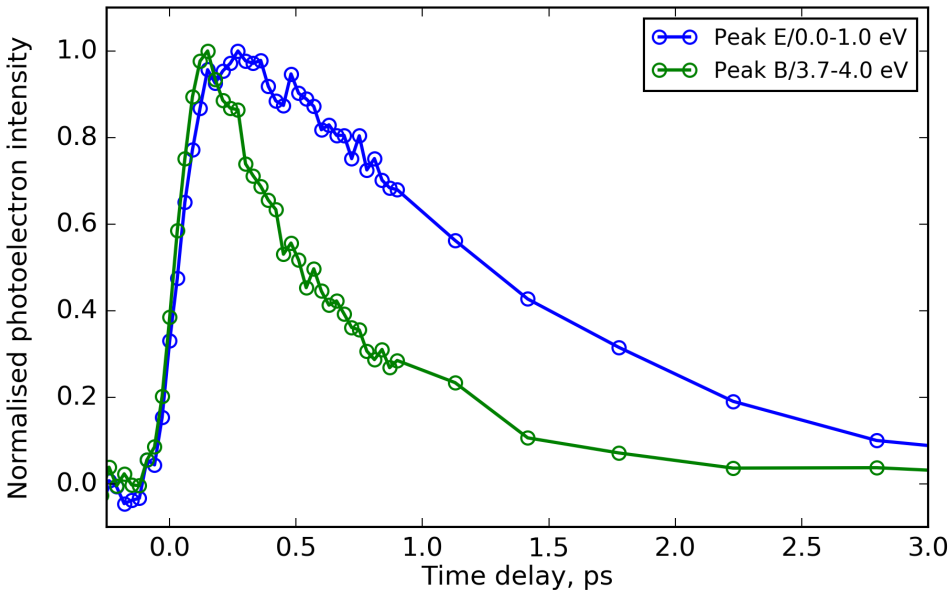

Figure 3.22: Transient photoelectron yields for the two main features (B and E) observed in Fig. 3.21. The electron kinetic energy integration regions are highlighted in each panel.

Despite the similarities between the data recorded at 4.65 eV (3ω - Fig. 3.17) and 6.20 eV (4ω - Fig. 3.21), the latter spectra has considerably worse signal-to-noise, which is in part due to: (i) an increase in electrons associated with scattered UV/VUV light ionising metal surfaces within the vacuum chamber. This is not observed with the 4.65 eV probe as that photon energy lies below the work-function of most materials within the spectrometer and; (ii) a second non-resonant two-photon ionisation signal, from the probe pulse alone, needed to be subtracted from the time-resolved data. For the 3ω +5ω experiment, the first non-resonant two-photon ionisation signal is associated with the 7.77 eV (5ω) pump pulse. These points resulted in rather noisy photoelectron images and prevented analysis of the PADs (see Fig. 3.19). However, it was possible to extract yield data (i.e. β_0) on the main transient photoelecton bands observed in Fig. 3.21. Normalised transients for the

bands are presented in Fig. 3.22. The figure highlights that the lower energy band (peak E/0.0-1.0 eV) has a delayed rise with respected to the higher energy band (peak B/3.7-4.0 eV) and reaches a maximum at approximately 300-350 fs, as can also be seen in the 1D cuts presented in Fig. 3.21(c).

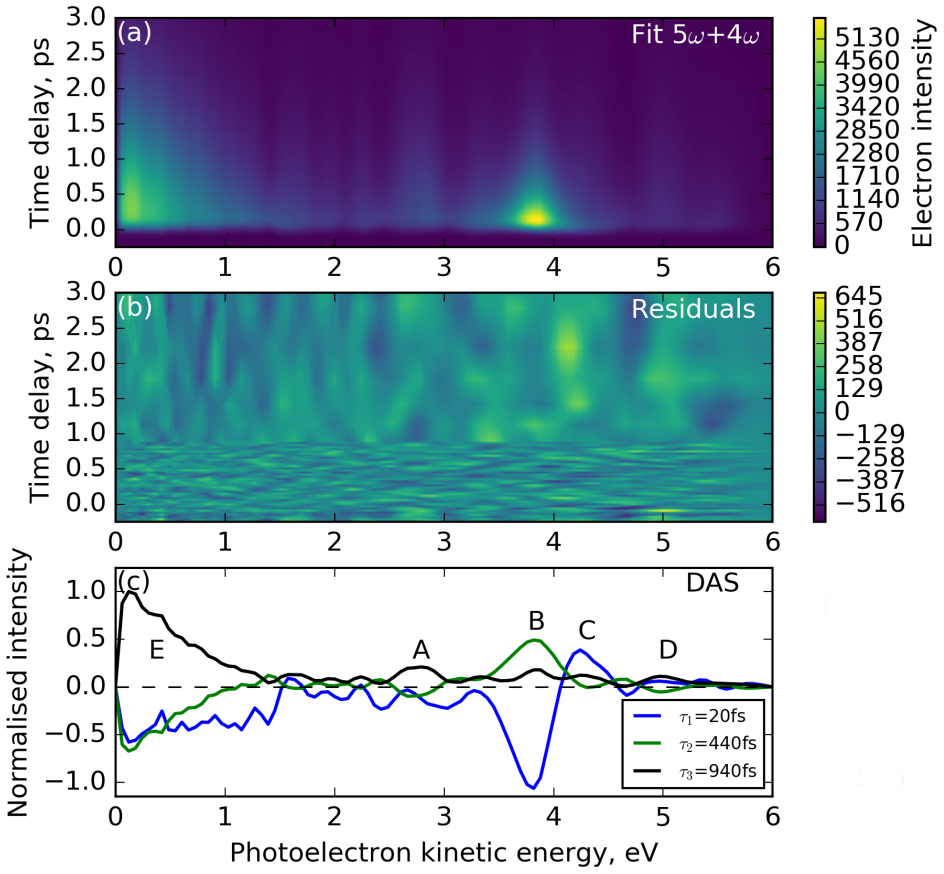

Figure 3.23: (a) A three exponential fit, using Eq. 3.3, to the photoelectron spectra in Fig. 3.21. (b) 2D plot of the residuals extracted from Fig. 3.21 and panel (a). (c) DAS obtained from the fit, the associated three exponential time constants are shown in the legend. The labeling convention of features A-E is the same as those defined in Fig. 3.21.

The presence of the slowly growing lower energy photoelectron band in the higher energy probe data necessitates a third exponential time constant in fits to the time-resolved photoelectron spectra. Fig. 3.23 show a fit to the spectra presented in

Fig. 3.21, the associated residuals, and the DAS. An experimental cross correlation of 142 fs (FWHM) was included in the fitting routine, which, similar to Sec. 3.3.3.1, was determined from non-resonant 1+1′ photoionisation of Xe. Note, the sizable increase in cross correlation width, when compared to the previous section, is due to the increased dispersion of the 4ω pulses (i.e. no prism compressor was included in the 4ω beamline for the 6.2 eV probe pulse).

The DAS extracted include three components with time constants of $\tau_1^{4\omega} \simeq 20$ fs, $\tau_2^{4\omega} \simeq 450$ fs and $\tau_3^{4\omega} \simeq 940$ fs. The short time constant, $\tau_1^{4\omega}$, describes the decay of the highest energy photoelectrons (peak C) and a rising component (positive amplitude) for the relatively sharp feature at 3.85 eV (peak B) as well as a broad photoelectron band spanning from 0.0 eV to approximately 1.5 eV. The second time constant, $\tau_2^{4\omega}$, describes the decay of the feature at 3.85 eV and exhibits a strong negative component for a lower energy band; this is indicative of sequential dynamics. This features peaks at low energies ($\sim$0.1-0.2 eV) and would likely continues to lower energies if an even shorter wavelength probe was utilised. In addition, $\tau_2^{4\omega}$ appears to capture the delayed rise of the weak feature at 2.85 eV (peak A). Finally, the subsequent decay of both negative amplitude features in the $\tau_2^{4\omega}$ spectra are accounted for by the third time constant, $\tau_3^{4\omega}$. A summary of the time constants extracted for both the 4.65 eV and 6.2 eV probe data is presented in Table. 3.2.

Table 3.2: Summary of the extracted 2D global fit parameters extracted from the time-resolved spectra presented in Figs. 3.17 (4.65 eV - 3ω) and 3.21 (6.2 eV - 4ω).

	$\tau^{3\omega}$	$\tau^{4\omega}$
pump/probe energy	7.78/4.65 eV	7.77/6.20 eV
cross correlation width (FWHM)	93 fs	142 fs
τ_1	30	20
τ_2	550	450
τ_3	N/A	940

In a similar manner to discussion outlined in Sec. 3.3.3.1, the robustness of the 2D global fit was examined by fitting multiple datasets with the three time constant

model initialising the fits with widely different starting conditions, in an attempt to sample the parameter space properly. The extracted time constants were in accord between the multiple fits and capture the same aforementioned global trends. Caution should however be placed, due to their appearance in the same decade, on the exact values extracted for $\tau_2^{4\omega}$ and $\tau_3^{4\omega}$ and whether or not the temporal behaviour of the weak feature at 2.85 eV is properly captured. The latter point relates to the discussion surrounding the inclusion of a third time constant outlined in the final paragraph of the preceding subsection. The fitting of multiple time constants within the same decade is also likely the origin of the 100 fs disparity between $\tau_2^{3\omega}$ and $\tau_2^{4\omega}$ in two different probe photon energy datasets.

3.4 Discussion

In this section, the time-resolved data presented for both 4.65 eV and 6.2 eV probe schemes will be interpreted, with the aid of previous spectroscopic data, in terms of both ultrafast Rydberg-valence coupling and internal conversion within the Rydberg manifold. The section is roughly structured such that higher kinetic energy photoelectrons are discussed first, as this broadly coincides with the evolution of the wavepacket as function of pump-probe time-delay.

The VUV absorption spectra, shown in Sec. 3.3.2, indicates that excitation at 7.77/7.78 eV prepares an excited state wavepacket with predominately $3d_{yz}$ Rydberg character but may also contain a valence contribution, likely $\pi\pi^*$, associated with the broad underlying continua. The highest-lying photoelectron feature, the short lived feature C at 2.72 eV ($\hbar\omega_{\text{probe}}$ = 4.65 eV, Fig. 3.18) and 4.26 eV ($\hbar\omega_{\text{probe}}$ = 6.20 eV, Fig. 3.21(c)), can be readily be assigned to this initially prepared state based on the following energetic argument and analysis of DAS plot. Firstly, if a photoelectron band is observed at the maximum $1+1'$ kinetic energy, for ionisation correlating to D_0, then both excitation and ionisation steps must be vertical (assuming that the neutral and ionic ground states have similar geometries) for such an energetic electron to be produced. Secondly, analysis of the DAS plots, shown in Figs. 3.20 and 3.23, reveal that the only all-positive amplitude component (i.e. a

state which does not get sequentially populated) connected with the short time constant, τ_1, is observed at the maximum possible kinetic energy. This result is also in keeping with the β_0 transient yields (Fig. 3.19), which exhibit delayed onsets for all but the highest energy band.

Despite the unambiguous assignment of the higher kinetic energy "shoulder" (peak C) to the initially prepared wavepacket, the above discussion does not provide any information of the character, either solely $3d_{yz}$ Rydberg or a mixture of this with the $\pi\pi^*$ valence state, of the state undergoing ionisation. This however can be examined by considering the role of electronic correlations (i.e. Koopmans' - see Secs 1.4 and 1.9.1) in the probe ionisation step. The single photon VUV photoelectron spectra of acetone highlights that, within a Koopmans' type picture, the D_0 and D_1 ionisation channels are n^{-1} and π^{-1} in character, respectively [263]. These correlations suggest that the $3d_{yz}$ Rydberg would preferentially ionise to D_0, whereas, any $\pi\pi^*$ component of the wavepacket would preferentially ionise to D_1. Therefore, the latter channel would not contribute significantly to a photoelectron band observed at the $1+1'$ ionisation limit for D_0. Further support for this feature (peak C) being due to ionisation of the $3d_{yz}$ Rydberg state is provided by the analysis of the PADs, shown in Fig. 3.19(c), which exhibits a high degree of anisotropy (β_2 = 0.6 and β_4 = - 0.2) for this feature, which is consistent with Rydberg state ionisation. It is also noteworthy that a β_2 of 0.6 is in accord with the previously reported value of Hüter and Temps for ionisation of the initially prepared $3d_{yz}$ Rydberg state [259]. Based on the above points, it appears reasonable to attribute peak C to ionisation of the $3d_{yz}$ Rydberg state. Note, the extracted τ_1 values of 30 fs and 20 fs for the 4.65 eV (3ω) and 6.2 eV (4ω) probe photon energies, respectively, are in agreement with the results of previous experimental investigations [259, 260]. In those prior studies, the authors observed a decay of the initial $3d_{yz}$ Rydberg state shorter than their experimental time-resolution.

The DAS plots for the decay of the $3d_{yz}$ state (τ_1) contains two negative components, indicative of sequential dynamics, at photoelectron kinetic energies corresponding to the relatively narrow peak (B) observed at 2.3 eV ($\hbar\omega_{probe}$ = 4.65 eV,

Fig. 3.18) and 3.85 eV ($\hbar\omega_{\text{probe}}$ = 6.2 eV, Fig. 3.21(c)), respectively, and the broad band at 0-1.5 eV, observed only in the 6.2 eV (4ω) DAS (see Fig. 3.23). These features exhibit very different FC envelopes, providing a hint as to the origin of each.

The higher-lying feature (peak B) will be considered first. The narrow FC envelope of this band is indicative of Rydberg state ionisation, assuming that the $\Delta v = 0$ propensity rule likely applies [163]. If this was indeed the case, then the approximations outlined in Sec. 1.9.2 of the thesis introduction likely hold and the photoelectron kinetic energy can be directly related to the energy of the state undergoing ionisation through Eq. 1.28. For the central electron kinetic energy of this peak ($\sim$2.33 eV), correlating to the D_0 continuum (IP = 9.708 eV [263]), this would correspond to a state located 7.39 eV above the ground state of neutral acetone. Based on the vertical excitation energies shown in Table. 3.1 the most likely candidate for this is the 3p Rydberg manifold, which has band origins in the 7.34-7.45 eV range [241, 242]. Determination of which member of the 3p Rydberg series gives rise to the intensity of this band is, however, challenging as all three state lie within 0.1 eV of each other: any or all of them could be populated from the initial prepared $3d_{yz}$ state. The PADs associated with this peak (see Fig. 3.19) are rather isotropic (β_2 = 0.2 and β_4 = 0.0), consistent with the conclusion that several Rydberg states may contribute to this photoelectron peak. These values differ considerably from those obtained by Hüter and Temps, β_2 = 0.6, for ionisation of the 3p Rydberg states directly prepared by two-photon excitation [259], suggesting that the a different composition of 3p states are undergoing ionisation for the sequentially populated case considered here. However, as detailed analysis of the PADs is beyond the scope of work presented here, this conclusion cannot be verified. Finally, support of the assumption that the $\Delta v = 0$ propensity rule can be applied for ionisation of Rydberg states in acetone is also provided by the experimental work of Hüter and Temps [259]. The authors report that $\leq$0.1 eV of vibrational energy was observed during single-photon ionisation for both the 3p and $3d_{yz}$ correlating to D_0 continua for this pump-photon energy. Based on analysis of the FC envelope

and invocation of the assumption that the ionisation is vertical, the photoelectron band observed at ∼2.3 eV is attributed to the 3p manifold, which is subsequently populated from the initially prepared $3d_{yz}$ (i.e. $3d_{yz} \rightarrow 3p$). The assignment of this feature to 3p is in agreement with previous PEPICO work [260]. The decay of this state will be discussed below.

Unlike the photoelectron band due to 3p ionisation, the lower-energy photoelectron band observed in the τ_1 correlated DAS plot (see Fig. 3.23(c)) exhibits a FC envelope which extends approximately to maximum cut-off for the D_1 continua (1.56 eV) from 0.0 eV. The presence of such a broad photoelectron feature is characteristic of ionisation of a valence state. The most likely candidate for a valence state that is sequentially populated from the $3d_{yz}$ is the $\pi\pi^*$ state, which is spectroscopically known to couple with 3d and 3p Rydberg states possessing the same symmetry ($^1A_1$) [241, 242]. Such an interpretation is reinforced by several theoretical investigations [241, 248] which have identified conical intersections leading to non-adiabatic coupling between valence and Rydberg states of $^1A_1$ symmetry. The decay of this state, unlike all other photoelectron bands, is not captured in the DAS analysis and hence it is hard to identify the associated decay pathway. Given the information content of the current datasets, further discussion of this channel (i.e. $3d_{yz} \rightarrow \pi\pi^* \rightarrow$ unresolved) is not pursued here.

The decay of the aforementioned 3p Rydberg state is captured by the second time constant in the DAS analysis, τ_2, for both the 4.65 eV ($\tau_2^{3\omega}$, see Fig. 3.20) and 6.2 eV ($\tau_2^{4\omega}$, see Fig. 3.23) probe photon energies. Despite the difference in absolute values (∼100 fs) between τ_2 extracted from the two different probe wavelength datasets, likely a fit artefact linked to coupling between time constants within the same decade (see. Sec. 3.3.3.1), the timescale for this decay is in reasonable agreement with several previous studies. In the two-photon TRMS work of Hüter and Temps, decays of 700-280 fs were observed in the acetone parent ion signal at photoexcitation energies of 7.748-8.0 eV (i.e. 2×3.874-2×4.0 eV), which was attributed to the decay of the 3p Rydberg state [259]. It is therefore reasonable that, for the intermediate cases of $\hbar\omega_{pump}$ = 7.77/7.78 eV presented here, the extracted τ_2

would be somewhere in between these two values. Little information was provided on the decay mechanism for the 3p Rydberg state, but the authors note that disentangling whether the decay is due to structural relaxation or electronic relaxation was not possible from their data [259]. A decay of 330 fs for the 3p Rydberg state was observed in the single photon VUV pump PEPICO study by Couch *et al.*, which was attributed, in part, to population of the lower-lying 3s Rydberg state [260]. This channel was predicted theoretically [248], but had not been previously observed in investigations employing lower photon energy probes [232, 259].

A feature (peak A) consistent with ionisation of the 3s Rydberg state is also observed in the present work. This band, similar to that observed for the 3p Rydberg state, exhibits a relatively narrow FC envelope (see Fig. 3.18) and hence can be analysed using the assumption that the ionisation is vertical. For example, in the $\hbar\omega$ = 4.65 eV (3ω) data, a photoelectron band at 1.3eV, correlating to the D_0 channel would originate from a state 6.36 eV above the ground state in neutral acetone. This is in excellent agreement with a vertical excitation energy of 6.355 eV, shown in Table 3.1. Supporting evidence for ionisation of Rydberg states of s-type character is typically provided through the analysis of PADs. In such analyses (see, for example, Refs. [284] and [285]) it is assumed the Rydberg state is atomic-like and, therefore, photoionisation with linearly polarised light should give rise to photoelectron partial waves of exclusively p_z character (i.e. large positive values of β_2). In acetone, however, the PADs for the 3s Rydberg state (see Fig 3.19(a)) deviate strongly from characteristic expectations of this simple atomic model, with $\beta_2 = 0.2$ and $\beta_4 = 0.0$. This disparity is likely linked to the 3s Rydberg in acetone having a very large quantum defect ($\delta = 0.98$ [242]) and therefore a significant departure from atomic Rydberg state behaviour.

In spite of the theoretical prediction that the 3p Rydberg state undergoes internal conversion to the lower-lying 3s state [248], this cannot be unambiguously assigned given the current datasets/analysis. The τ_2 DAS plots, associated with the decay of the 3p Rydberg state, differ considerably between the two probe wavelengths, with only $\tau_2^{4\omega}$ capturing any signature of internal conversion (see panel (c)

of Figs. 3.20 and 3.23). This apparent indication of sequential dynamics from the 3p may however be linked to the use of two time constants within the same decade and unreliable fitting. Nevertheless, the delayed onset of the β_0 transient (i.e. photoelectron yield) in Fig. 3.19(a) does agree with a mechanism in which the 3s state is sequentially populated. An additional striking feature of the photoelectron peak connected with the 3s state is its small amplitude, particularly when compared to that of the 3p state. Given the (i) narrow FC envelope of this peak (i.e. a small or no geometry change upon ionisation) and (ii) that within a Koopmans' picture the 3s should correlate well with the D_0 continuum it is then difficult to envision a mechanism resulting in a substantially smaller photoionisation cross section for the 3s Rydberg state. It is therefore more likely that the small amplitude of this signal reflects it being a minor channel in the dynamics. The subsequent decay of the 3s state is likely due to further internal conversion to the lower-lying $n\pi^*$ state or neutral dissociation. The former is known to play a significant role in the dynamics following direct excitation to the 3s state [247, 250–252]. This is not observed in the present data.

Based on $\tau_2^{4\omega}$ DAS plot (see Fig. 3.23), the dominant observed decay channel associated with the 3p Rydberg states is the sequential population of a state which gives rise to slow photoelectrons between approximately 0.0 and 1.5 eV. The broad FC envelope of this band is consistent with ionisation of valence state. This assignment is supported by the fact that the only Rydberg state which could be sequentially populated from the 3p is the lower-lying 3s: this was discussed above in the context of feature A. Given the small amplitude associated with this photoelectron band (see above discussion), it is hard to envision a Koopmans' correlation to higher-lying ionisation continuum (which is a necessity based on energetics) as being the dominant channel, since the 3s to D_0 channel is both small and Koopmans' allowed. Thus, there exist two remaining possibilities, each being a valence state which could give rise to these observed low energy photoelectrons, each of which will be discussed below.

The first possibility is that ionisation occurs from the lowest-lying singlet state,

$n\pi^*$. The electronic correlations for this state would suggest that the D_0 ionisation channel is favoured. For the case of a valence state $\Delta v = 0$ is generally not a valid approximation and hence photoelectrons can be produced up to the corresponding $1+1'$ cut-off (see. Sec. 3.3.3.2), with any deviation from this value being related to FC/geometrical arguments. As the $n\pi^*$ state would be sequentially populated from a state approximately 2.5 eV higher in energy, it would be very vibrational "hot" and hence the wavepacket would sample a large range of nuclear configurations away from the initially prepared (essentially ground state) geometry. This would give rise to a significant shift in the FC envelope towards lower kinetic energies, which is consistent with the observation in Fig. 3.21.

The second possibility, which agrees more closely with previous literature [241, 245, 248, 257], is that the lower energy band (peak E) is due to ionisation of the $\pi\pi^*$ state. Zewail and co-workers [248] calculated excited state potential energy curves of acetone along the CO stretching coordinate and observed substantial non-adiabatic coupling between the $^1A_1$ $3p_y$ Rydberg state and the $\pi\pi^*$ ($^1A_1$) valence state as a function of CO bond elongation [248]. Here the $3p_y$ Rydberg state is the main character at shorter CO distances while the $\pi\pi^*$ dominates at geometries with extended CO bond lengths. The authors note that this result was already suggested in earlier spectroscopic studies [257] and more evidence of non-adiabatic coupling was observed in subsequent REMPI work [241].

Based on the π^{-1} character of the D_1 channel, it is reasonable to assume this is the primary ionisation channel for the $\pi\pi^*$ valence state. Given the ground state vertical IP for D_1 (12.45 eV) and the total photon energy, photoelectrons could be produced for this channel up to a maximum energy of 1.56 eV (see Fig. 3.21(c)), which is at significantly higher energies than the peak ($\sim$0.2-0.3 eV) of the observed band. This deviation could be due to structural relaxation occurring on the $\pi\pi^*$ surface and a concomitant shift in the effective vertical IP. Such a mechanism would be in accord with the $\pi\pi^*$ state having a substantially different equilibrium geometry than the initially prepared Rydberg states. However, a calculation of the vertical IP in this region of coordinate space would be required to verify this.

Regardless of this ambiguity, the DAS analysis does highlight that the decay of this feature is correlated with $\tau_3^{4\omega}$ (see Fig. 3.23). If the origin of this feature was the $n\pi^*$ state, this decay may be correlated due to population of low-lying triplet states, the dominant pathway when the $n\pi^*$ state is directly excited [254, 255]. This pathway leads to triplet state fragmentation forming acetyl plus CH_3, or CO plus $2\times CH_3$ [255]. For the $\pi\pi^*$ state case, the expected decay channels are also fragmentation to acetyl plus CH_3 but here with the acetyl potentially in an electronically excited state [248]. Such a mechanism was proposed to explain the long-lived acetyl fragment ion signals in the single photon 8 eV pump TRMS work of Farmanara *et al.* [228]. However, this channel was notably absent in the single photon PEPICO work from the Murnane and Kapteyn group, perhaps related to only single photon ionisation channels being accessed in that work [260]. This was not the case in both the earlier TRMS study [228] and in recent multiphoton PEPICO work where a long-lived photoelectron peak connected with the acetyl fragment was observed [261]. If the electronically excited acetyl channel played a significant role in the present study, then (based on a calculated IP of 5.8 eV for the relevant acetyl excited state ($\tilde{A}^2A''$) [248]) this product should be observable in the 6.2 eV (4ω) dataset. Since no evidence of a long-lived transient was observed in the associated time-resolved photoelectron spectra (see Fig. 3.23), the excited state acetyl channel is not consider to be operative here.

3.5 Conclusion

The construction and implementation of the femtosecond VUV source, as well as its application to investigate Rydberg-valence coupling in acetone, was outlined this chapter. A detailed description of the optical set-up used to generate the fifth harmonic of the Ti-Sapphire 800 nm fundamental via FWDFM was provided. An attempt to characterise the resulting VUV pulse spectra and phase matching pressure, using a monochromator and VUV photodiode was described. Estimates of the VUV pulse duration were extracted from a cross correlation between the VUV pulses and an optimally compressed third harmonic pulse using non-resonant $1+1'$

photoionisation of Xe. This measurement placed an upper bound on the VUV pulse duration, $\sigma_{5\omega}$, of 62 fs. By performing this measurement in a electron VMI spectrometer the measurement can be considered as a type of frequency-resolved optical gating (FROG), where the resultant PES provides the spectral resolution through the photoelectron kinetic energy. The Xe photoelectron spectrum exhibits, as can be observed in Fig 3.14, a small spectral tilt, which, due to the fact that the third harmonic pulse was optimally compressed, can be attributed to a slight positive chirp on the VUV pulse. This observation was in somewhat accord with the dispersion associated with the relatively broadband VUV pulse passing through a CaF_2 window which separates the VUV vacuum box from the VMI spectrometer. The Xe $1+1'$ PES also serves as a convenient *in-situ* method for extracting the central wavelength of the VUV pulse, which could only previously be roughly determined from the uncalibrated monochromator plus photodiode set-up.

The fifth harmonic pulse was then utilised as a pump pulse in a series of measurements exploring the coupling between Rydberg and valence states, as well as internal conversion dynamics, in acetone. The proposed scheme for the excited state wavepacket dynamics is a follows. Vertical excitation at 7.78 eV populates a Rydberg state possessing predominately $3d_{yz}$ character, which undergoes internal conversion to the lower-lying 3p Rydberg and $\pi\pi^*$ valence state on a timescale of $\sim$30 fs. The subsequent decay of the latter is not observed in the current datasets but has previously been attributed to dissociation [228, 259]. Analysis of the photoelectron kinetic energies, through simple FC arguments, and PADs highlighted that the sequentially populated 3p Rydberg state appears to possess character from several members of this manifold. This state also exhibits further internal conversion on a $\sim$450-500 fs timescale into at least two lower-lying state. The first of these, which appears to be a minor channel, based on cross section arguments, is population of the 3s Rydberg (S_2). Most significantly, evidence is found for population of a valence state of either $n\pi^*$ or $\pi\pi^*$ character. Although this feature cannot be unambiguously assigned given the present data, the latter $\pi\pi^*$ state would be in accord with the previous spectroscopic and theoretical literature [241, 245, 248].

Further experimental and theoretical work would be required to verify the current assignments.

Chapter 4

CH_3I core-level ionisation

4.1 Introduction

In all previous chapters the time-resolved photoelectron studies have been concerned with probing excited state wavepacket dynamics via ionisation, either strong-field or weak UV, of mainly delocalised valence electrons. Recently, however, the development of both X-ray FELs and tabletop soft X-ray sources has enabled new approaches for studying time-resolved physical and chemical processes in matter [40, 75, 76, 113, 286, 287]. In particular, the use of soft X-ray absorption and ionisation as a probe of non-adiabatic processes in photoexcited polyatomic molecules has received considerable interest, due to the technique being both element and site-specific [40, 77, 288, 289]. For tabletop sources, based primarily on HHG [73], these studies have focused on utilising soft X-ray transient absorption as a probe of the ensuing chemical dynamics [75, 287]. To our best knowledge, no X-ray photoelectron spectrometry (XPS) work has been carried out at the C, N and O 1s edges. In stark contrast to this, numerous ionisation-based detection schemes have been carried out at X-ray FELs. This can partially be attributed to their high peak brightnesses compared to HHG based laboratory sources.

Typically in these pump-X-ray ionisation probe experiments, the neutral excited state is formed by the absorption of photons from a conventional but synchronised femtosecond laser, similar to the schemes outlined in Chapters 2-3, and is probed in a time-dependent manner by an X-ray photon from the FEL. These ex-

periments aim to provide insight into the evolving local electronic structure around a particular atomic site during a photochemical processes. Despite the numerous advantages of performing time-resolved studies of molecular dynamics with FELs, the interpretation of experimental observables has proved challenging due to a lack of fundamental spectroscopic information on the molecular ground state at soft X-ray wavelengths. In particular, information on absorption cross sections and binding energies, as well as angular distributions, for inner-shell processes are not available for many polyatomic molecules, when compared to the more well studied inner/outer valence shell.

In this chapter, inner-shell excitation, ionisation and decay processes for the polyatomic methyl iodide (CH_3I) are presented, with particular focus on the investigation of the I 4s, 4p and 3d sub-shell. The heavier halogen atom containing molecules have proved particularly suitable for X-ray time-resolved studies, due to high inner-shell photoionisation cross sections, and numerous studies at the I 3d edge have already been undertaken at LCLS [76, 113]. In addition to these results being highly relevant for these recent time-resolved FEL experiments, they are also of fundamental scientific interest. This is due to the fact that unlike for polyatomics, the inner-shell spectroscopic information for rare gas atoms, such as Xe, are much more extensively documented. Since halogen atoms lie adjacent to the rare gases in the periodic table they represent ideal candidate systems by which to investigate the effect of the molecular environment on the core-level spectroscopic properties of the atomic system. Additionally, the valence shell of CH_3I is also isovalent with Xe. These above points indicate that many of the photoionisation phenomena that have been studied extensively in connection with the Xe 3d, 4s and 4p levels may also occur for the I 3d, 4s and 4p atomic-like orbitals in CH_3I.

In terms of fundamental core-level spectroscopy the shallow I 4d shell of CH_3I has been studied more extensively than the I 3d, 4s and 4p shells. Hitchcock and Brion, using low resolution electron energy loss spectroscopy, reported the first experimental study of the I 4d shell and noted similarities between the corresponding shell in Xe in the 50-200 eV energy range [290]. The photoabsorption spec-

tra in both Xe and CH_3I is dominated by a broad maximum above 4d ionisation thresholds [291] and were assigned to d$\rightarrow\varepsilon$f delayed onsets [292]. A number of discrete sharp features were also observed in the pre-edge region, attributed to excitation from the 4d subshell into either valence or Rydberg states [290]. Higher resolution laser-produced continua absorption work [293], as well as synchrotron total-photoionisation-yield studies [294, 295], permitted the assignment of an additional higher-lying feature and were broadly in agreement with assignments made by Hitchcock and Brion [290].

Photoionisation, as well as PADs, of the I 4d shell has also been the subject of both experimental [97, 296] and theoretical investigations [97, 297]. Lindle *et al.* noted that 4d photoionisation in CH_3I exhibited atomic-like behavior and essentially mimics the behavior of the Xe 4d sub-shell. To date, only a handful of investigation have been conducted on the more deeply bound I 4p and 4s orbitals. Al Kα photoelectron studies by Gelius [298] and Svensson *et al.* [299] determined the binding energies of these states and noted the anomalous appearance of 4p band. The authors suggested that, similar to Xe [118, 298, 299], multielectron effects are operative during photoionisation. Similar to the case of I 4d ionisation, Lindle *et al.* also investigated the near-threshold behavior of the 4p PAD and also concluded that multielectron effects do play a significant role in I 4p photoionisation.

The only experimental investigation of processes pertaining to I 3d excitation, beyond determining the $3d_{5/2}$ ionisation threshold by X-ray photoelectron spectroscopy [300], was performed by Hitchcock and Brion [290]. The authors reported low-resolution electron energy loss spectra in the 600-700 eV region. The authors highlight that the energy loss spectra are similar to the previously reported photoabsorption spectrum of Xe [101], in the 3d region. Two broad maxima were observed above the I 3d thresholds and, similarly to the 4d shell, were assigned to d$\rightarrow\varepsilon$f shape resonances [290].

In contrast to the sparsity of studies of I 3d orbital in CH_3I, Xe 3d has been extensively studied. Initial studies carried out using laboratory based resonance line photon sources yielded a wealth of information on electronic energy levels,

lifetimes and shake-up satellites [118, 298, 299]. The complexity of the studies being undertaken has increased significantly with the development of high-flux and high-resolution soft X-ray beamlines at synchrotron radiation facilities, due the the tunability and polarisation properties of the ionisation source. These experimental efforts have focused on characterizing the 3d orbital binding energies [100] as well as shake-up satellites [298], the absorption [101–103], total ion yield [104, 105] and multicharged Xe^{q+} (q = 1-8) ion yield [106, 107] spectra in the vicinity of ionisation thresholds. The angular distribution of the 3d photoelectrons [108] and the near-threshold photoionisation behavior [109] have also been characterized. Given the wealth of information available for the corresponding processes in Xe it is therefore of interest to ascertain whether the atomic ionisation processes described above for the Xe 3d subshell are observed for the I 3d orbital of the iodine atom within CH_3I.

This chapter is structured as follows. In Sec. 4.2, a description both of the experimental apparatus and data analysis techniques are given. Sec. 4.3 provides a brief summary of the details of the supporting theoretical X-ray absorption, as well as photoionisation continuum scattering, calculations. In Sec. 4.4.1, the experimental total ion yield of CH_3I from below the I $3d_{5/2}$ ionisation threshold up to a photon energy of $\sim$690 eV are presented. These results are interpreted with the aid of the calculations outlined in Sec. 4.3. Presented in Sec. 4.4.2 are angularly resolved photoelectron spectra for the I 4s, 4p and 3d orbitals, as well as associated shake-up/shake-off structure. Finally, this study is summarised in Sec. 4.5.

4.2 Experimental apparatus and data analysis

4.2.1 Experimental setup

The measurements were performed at the soft X-ray PLÉIADES beamline at the Synchrotron SOLEIL [92]. A permanent magnet undulator, Apple II-type, with a 80 mm period provides linearly polarised synchrotron radiation in the photon energy range of 35-1000 eV. The degree of linear polarisation of the radiation is estimated to be $>$99%, and is consistent with the results of our polarisation dependent recordings of the photoelectron spectra of the C 1s and the I 4s levels in CH_3I. The

synchrotron radiation was delivered into a plane grating monochromator, operating in fixed focused mode, by means of two prefocussing mirrors. The monochromator used on the PLÉIADES beamline has variable line spacing, which allows the grating to focus in the dispersive plane at the exit slits and thus removes the requirement of an additional focusing mirror. This design permits both high efficiency and spectral resolution across a wide wavelength range. Variable groove depth gratings, in horizontal direction, were employed on the beamline. This allows the diffraction efficiency of the grating to be optimized for either maximum transmission efficiency of the first order radiation or optimum rejection of the second order. A grating with 600 lines per mm was used in this study.

The photoion and photoelectron spectra were recorded with a grating having 600 lines/mm. An exit slit width of 10 μm was chosen, resulting in a theoretical optical resolution which varies between 80 meV at $\hbar\omega$ = 630 eV and 100 meV at $\hbar\omega$ = 750 eV, for the photoelectron spectra encompassing only the I 3d peaks. An exit slit width of 70 μm was chosen, resulting in a theoretical optical resolution of 300 meV, for the complete photoelectron spectra covering the entire energy range (to include all peaks extending from those due to direct ionisation of the valence orbitals to those due to the carbon KVV Auger electrons).

Two spectrometers were utilised in the experimental studies: (i) a 40 mm channelplate detector oriented in the horizontal plane 25 mm from the interaction region separated by two mesh electrodes for measuring the ion-yield and (ii) a VG Scienta R4000 analyzer for recording electron spectra.

For the ion detector, sample gases (either methyl iodide or calibrant gas) were introduced into the chamber using a hollow needle. The needle position was adjusted with an *x*-*y*-*z* manipulator to ensure optimal overlap of the gas jet with the incoming photon beam. In the case of methyl iodide (Sigma-Aldrich purity $\geq$99%) the liquid sample has significant vapor pressure at room temperature, and therefore was introduced into the chambers without additional heating. Dissolved air and volatile impurities were removed from the sample by several freeze-pump-thaw cycles. The pressure in the chamber was varied between 1.5×10^{-7} mbar and

2.0×10^{-6} mbar depending on the sample gas being used. However, the actual pressure in the photon beam-gas interaction region was estimated to be several orders of magnitude higher than the measured values.

The design of the ion spectrometer does not allow the highly energetic fragments, formed through Coulomb explosion of the doubly or multiply charged parent molecule following inner-shell photoabsorption, to be collected with 100 % efficiency. This loss will depend upon the orientation of the ionised parent molecule and will be largest for molecules lying in a plane perpendicular to the ion propagation path towards the detector. However, this discrimination against energetic fragments is not expected to affect our ion yield measurements significantly.

The ion yield spectrum was recorded between 610 and 690 eV, in 50 meV steps, using vertically plane polarised radiation. In Fig. 4.1 we show an ion yield in the energy range 527-680 eV for a mixture of CH_3I, O_2 and Xe. These spectra were used to calibrated the photon energy scale using the established transition energies of 530.5 and 539.5 eV for the $2p\pi^*$ and $2p\sigma^*$ resonances in O_2, [301] and 674.0 eV for the $3d_{5/2}\rightarrow$ 6p Rydberg excitation in Xe [105].

Electron spectra, for emission either parallel or perpendicular to the polarisation vector of the plane polarised radiation, were recorded with the Scienta analyser. This spectrometer, mounted with the electron detection axis lying perpendicular to the plane of the electron orbit in the storage ring, was operated in the transmission mode of the electron lens. The sample gas was flowed into a differentially pumped cell, which contains a series of electrodes to correct for the plasma potentials generated along the path of the synchrotron radiation [302]. The indicated pressure was held between 4×10^{-7} and 8×10^{-7} mbar in the spectrometer chamber, but that in the differentially pumped cell was estimated to be between two and three orders of magnitude greater. Spectra were recorded using analyser pass energies of 5, 10, 20 or 50 eV, and a 0.6 mm curved entrance slit, resulting in theoretical spectrometer resolutions of 10, 20, 40 or 100 meV, respectively. These correspond to reasonable values given the literature reported lifetime widths, 500 meV, of 3d holes in

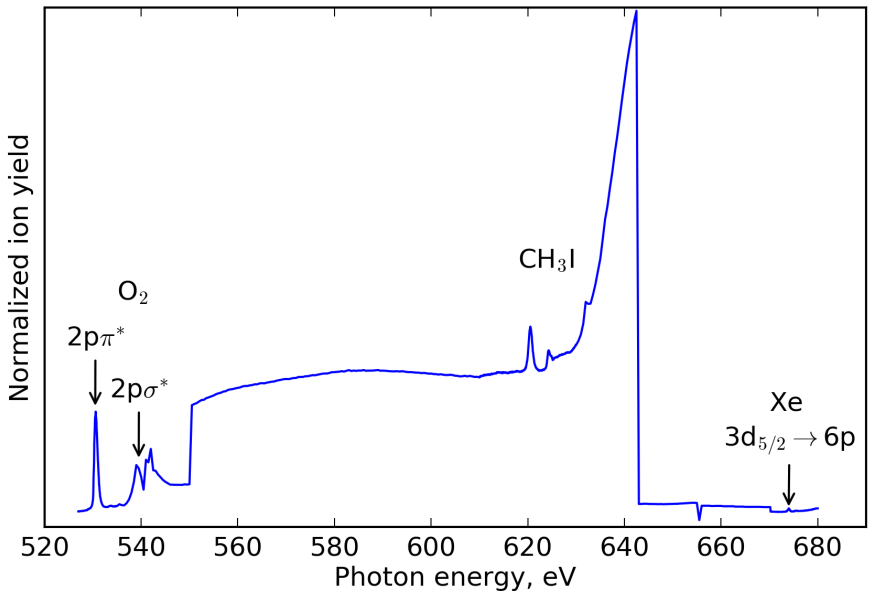

Figure 4.1: The experimental ion yield of a mixture of O_2, CH_3I and Xe recorded in the photon energy range 527-680 eV. The spectra was recorded with 1 s of integration time and the photon energy adjusted in two different step sizes: (i) 50 meV in the pre-edge region for each gas and; (ii) 0.5 eV in the regions in between. Established transition energies of the $2p\pi^*$ and $2p\sigma^*$ resonances in O_2 and $3d_{5/2} \rightarrow$ 6p Rydberg excitation in Xe was used to calibrate the photon energy scale.

Xe [303] and the inherent line widths of the Xe $M_{4,5}N_{4,5}N_{4,5}$ Auger decay [304].

Translational Doppler broadening, associated with the thermal motion of the room temperature CH_3I sample, also contributes to the overall observed peak width. The linewidth associated with this broadening, ΔE_D, is given by $\Delta E_D(\text{meV}) = 0.7215(E_{KE}T/M)^{1/2}$, where E_{KE} is the electron kinetic energy in eV, T is the temperature of the sample gas in K, and M is the molecular mass expressed in atomic units [302]. For the maximum photon energy, 750 eV, used to ionise the I 3d shell in CH_3I, $\Delta E_D(\text{meV}) = 11.5$ meV. In the case of the highest electron kinetic energies considered ($\sim$600 eV), associated with 4d photoelectron peak and shake-up structure, the translational Doppler broadening is $\Delta E_D(\text{meV}) = 25.4$ meV. Additionally, the experimental spectra are likely subject to further broadening due to unresolved vibrational structure.

The electron spectrometer employs a camera-based MCP/phosphor screen de-

tector setup and was operated in pulse counting mode. In this mode, each illuminated pixel on the CCD camera has a thresholding applied such that the signal is proportional to a single electron count. This procedure ensures good linearity, thereby allowing the number of counts to be extracted.

For completely plane polarised radiation, the photoionisation differential cross section in the electric dipole approximation, assuming randomly oriented target molecules and electron analysis in a plane perpendicular to the photon propagation direction, can be expressed in the form [305].

$$\frac{d\sigma}{d\Omega} = \frac{\sigma}{4\pi}[1 + \beta P_2(\cos\theta)] \tag{4.1}$$

where σ is the angle-integrated photoionisation cross section, β is the photoelectron anisotropy parameter, θ is the electron ejection angle relative to the major polarisation axis and P_2 is a second order Legendre polynomial: $P_2(\cos\theta) = (3\cos^2\theta\text{-}1)/2$.

The anisotropy parameter can be alternatively expressed in the experimentally convenient form [305]:

$$\beta = 2\frac{I_{para} - I_{perp}}{I_{para} + 2I_{perp}} \tag{4.2}$$

which allows β to be deduced from spectra (I_{par}) recorded at $\theta = 0^\circ$ and spectra (I_{perp}) recorded at $\theta = 90^\circ$. For the particular instrumental arrangement on the PLÉIADES beamline, I_{par} and I_{perp} correspond to spectra recorded with the plane of linear polarisation lying perpendicular or parallel, respectively, to the electron orbital plane in the storage ring.

As part of the experimental work, the I $3d_{5/2}$:I $3d_{3/2}$ branching ratio has been measured: that is, the partial photoionisation cross section of the $3d_{5/2}$ orbital (σ(I $3d_{5/2}$)) divided by that (σ(I $3d_{3/2}$)) of the $3d_{3/2}$ orbital. This has been accomplished by recording photoelectron spectra of the $3d_{5/2}$ and $3d_{3/2}$ levels. The evaluation of the branching ratio requires that the photoelectron intensity, at a particular kinetic energy, is normalized to the transmission efficiency of the electron

analyzer. The efficiency was determined as described by Jauhiainen *et al.* [306].

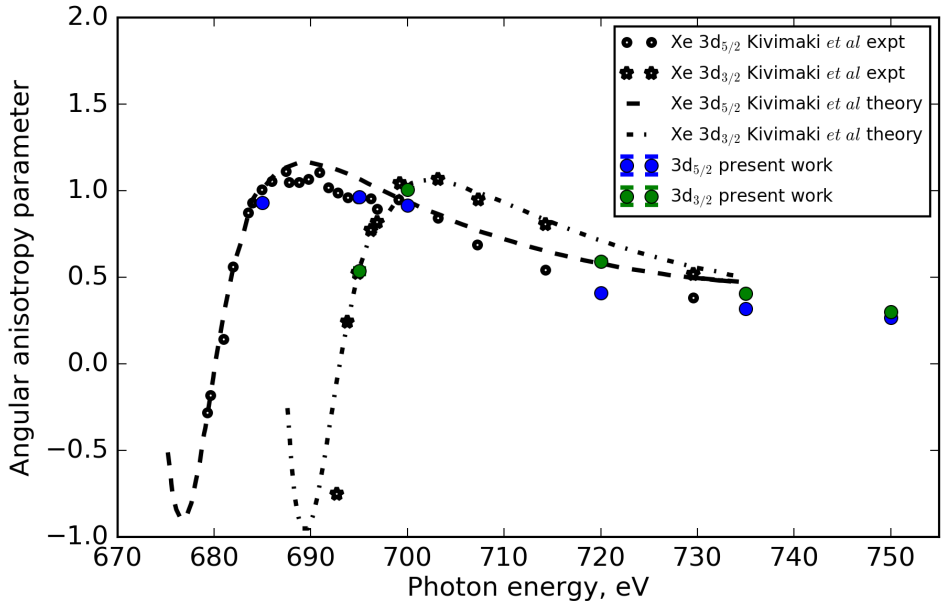

Figure 4.2: Angular anisotropy parameters, β, of the $3d_{3/2,5/2}$ photoelectron lines as a function of photon energy. Open circles and stars give the previously reported experimental β values for the $3d_{5/2}$ and $3d_{3/2}$ photoelectron peaks, respectively [109]. In blue and green circles denote the current calibration points for the $3d_{5/2}$ and $3d_{3/2}$ photoelectron peaks, respectively, measured on the PLÉIADES beamline. Additionally, dashed and dot-dashed lines depict the calculated curves for $3d_{5/2}$ and $3d_{3/2}$ photoionisation [109].

The spectra were normalized to both the pressure and the photon flux. The photon flux was measured with a photodiode located at the end of the beamline.

In order to confirm the expected performance of the beamline and the spectrometer for the measurement of electron angular distributions, angle-resolved photoelectron spectra were recorded for Xe 3d ionisation over the photon energy range used in this study. In Fig. 4.2, β parameters extracted fits (see Sec. 4.2.2) of the Xe $3d_{5/2}$ and $3d_{3/2}$ photoelectron peaks are presented. The data are in satisfactory agreement with the previously reported values [109]. Additionally, the electron kinetic energy scale was calibrated using the expected kinetic energies based on binding energies in Xe [119, 299].

4.2.2 The effect of post collision interaction on the I 3d photoelectron peak shape

In the present experiment, photoelectron spectra of the I $3d_{5/2}$ and I $3d_{3/2}$ orbitals were recorded for various photon energies between 630-750 eV, corresponding to photoelectron kinetic energies in the range of ∼5-120 eV. Due to the photon energy lying near the inner-shell ionisation potential, the slowly departing photoelectron may be additionally influenced by the faster Auger electron. The initially created $3d^{-1}_{5/3}$ and $3d^{-1}_{3/2}$ core-holes state decays through the emission of Auger electrons (see Chapter 5) having kinetic energies in the ∼350-570 eV range. The resulting interaction between the two escaping electrons, as well as the resulting ionic core, is termed post collision interaction (PCI) [307, 308]. Classically, PCI can be described as the change in the mutual shielding of the two ejected electrons. Close to the ionisation threshold, where the photoelectron kinetic energy is small, this slowly departing electron shields the Auger electron from the doubly charged ionic core. Therefore, due to energy conservation, the kinetic energy of the Auger electron increases, whereas the photoelectron kinetic energy decreases by a similar amount. For lower photoelectron excess energies, a larger shift will be observed in the electron energies, since the Auger electron will pass the photoelectron closer to the ionic core. PCI results in the photoelectron peak shape exhibiting a characteristic asymmetry towards low kinetic energies. The opposite is true for the Auger electrons, with an asymmetry being observed towards higher kinetic energies. In the limiting case, far above threshold, where the kinetic energy of the photoelectron is equivalent to, or larger than, that of the Auger electron, the observed line shape is, ignoring additional instrumental broadening, Lorentzian with a width corresponding to that of the core-hole state.

A fitting routine was adopted in the experimental analysis for both the photo and Auger electron spectra (see Chapter 5) as it provides several advantages over using the integrated signal of the photoelectron peak, namely: (i) fitting can allow for widths, which relate to the experimental, core-hole and, for the Auger electrons, final state broadening to be extracted; (ii) superfluous background intensity can be

more accurately modeled and the associated contributions removed from further analysis.

The effect of the PCI distortion on the shape of the I 3d photoelectron peaks, here from ionisation of CH_3I, was taken into account in the experimental analysis by incorporating the approximate line shape described by Armen *et al* [308]. For the case of the photoelectron peak the PCI broadened peak shape, P_{PCI}, can be expressed as:

$$P_{\mathrm{PCI}}(E_{\mathrm{kin}},E_0,\Gamma,C) = \frac{\Gamma}{2\pi}\frac{\pi C}{(\frac{\Gamma}{2})^2+(E_{\mathrm{kin}}+E_0)^2}\frac{\exp[-2C\arctan(2(E_{\mathrm{kin}}+E_0)/\Gamma)]}{\sinh(\pi C)} \tag{4.3}$$

where E_{kin} and Γ refer to the photoelectron kinetic energy and core-hole width, respectively. E_0 is the photoelectron peak position and C is a fitting parameter, which describes the distortion of the Lorentzian line shape and is dependent of photoelectron excess energy.

At each photon energy, the spectra recorded with vertically or horizontally plane polarised radiation were fitted jointly, with each of the $3d_{5/2}$ and $3d_{3/2}$ photoelectron peaks being fitted individually. Fitting the two photoelectron peaks separately allowed the number of terms associated with the background to be minimized. For all but the lowest four photon energies, only an onset and a linear term were used to describe the background. At the lower photon energies, close to threshold, a quadratic term was added to account for cascaded Auger processes (e.g. I $3d^{-1}$ $\rightarrow$I $4d^{-2}$ $\rightarrow$I $4d^{-1}V^{-2}$, , where V denotes a valence electron) which are expected to contribute to the background at low electron kinetic energies.

The following fitting function was employed

$$\begin{aligned} I(E_{\mathrm{kin}},a,b,c,\sigma,\beta,\theta,E_0,\Gamma,\alpha,C) = a+bE_{\mathrm{kin}}+cE_{\mathrm{kin}}^2+\frac{\sigma}{4\pi}[1+\beta P_2(\cos(\theta))] \\ \times[\frac{1}{\alpha\sqrt{2\pi}}\exp[\frac{-(E_{\mathrm{kin}}-E_0)^2}{2\alpha^2}] \\ \otimes P_{\mathrm{PCI}}(E_{\mathrm{kin}},E_0,\Gamma,C)] \end{aligned}$$

where a, b and c are the coefficients describing the background, α is the width of

the Gaussian function which describes the instrumental broadening (i.e. the photon bandwidth and spectrometer broadening). The peak intensity, described by Eq. A.1, was fitted to the vertical and horizontally polarised spectra by evaluating $P_2(\cos(\theta))$ at θ=0 and θ=π/2, respectively.

The global error function was then constructed from the two separate error functions associated with each of the vertically and horizontally polarised spectra. This procedure allowed β to be extracted directly from the fitting routine. Constraints were placed on the fitting parameters to ensure that the variables remained physically significant. For example, the intensities associated with the background, peak intensity as well as the peak widths were set to remain positive. The peak positions were constrained to be within $\pm$0.5 eV of their initial guesses and β to be between -1 and 2.

All the error bars shown in the figures presented in this chapter represent the standard error on the fitting parameters, which were extracted from the square root of the diagonal elements of the covariance matrix associated with each fit.

4.3 Theoretical techniques

To the best of our knowledge, no theoretical work has been undertaken on excitation and ionisation of the CH_3I 3d subshell. In the following sections a brief outline of theoretical calculations, performed by Nick Besley and Ivan Powis (University of Nottingham), is presented to aid in the interpretation of the CH_3I experimental spectra.

4.3.1 X-ray absorption spectrum

The absorption spectrum of CH_3I was computed using TDDFT within the Tamm-Dancoff approximation [309]. Details of the basis set and density function choices are outlined in Ref. [310]. The calculations explicitly neglect relativistic effects and hence the computed spectrum, due to excitation or ionisation of an I 3d electron, is denoted I $3d^{-1}_{5/2}$. The spectra connected with the I $3d^{-1}_{3/2}$ continuum are then generated by shifting I $3d^{-1}_{5/2}$ spectrum by +11.5 eV. This energy shift corresponds to the I 3d spin-orbit splitting measured in the present experiment. The spectral intensity

for features connected with I $3d_{3/2}^{-1}$ continuum was weighted according to the differences in statistical weights between I $3d_{5/2}^{-1}$ and I $3d_{3/2}^{-1}$. The ionisation energy, computed using a ΔSCF approach [311], was found to be 6.77 eV higher in energy than the lowest energy transition. This yields ionisation energies of 627.16 eV for I $3d_{5/2}^{-1}$ and 638.66 eV for I $3d_{3/2}^{-1}$. The Stieltjes imaging technique [312] was used to simulate the above threshold spectra, with discrete transition energies and intensities computed using TDDFT. The pre-edge spectra were generated by convolving the calculated intensity at each transition energy with a Gaussian function (0.5 eV FWHM). The spectrum for the pre-edge is combined with the above threshold spectrum to generate the total X-ray absorption spectrum.

4.3.2 Photoionisation cross section

The photoionisation cross sections and electron anisotropy parameters, associated with I 3d ionisation in CH_3I, were calculated using a procedure outlined in detail in Refs. [97, 297]. Briefly, however, electric dipole photoionisation matrix elements were calculated using the Continuum Multiple Scattering method with an Xα local-exchange potential (CMS-Xα) [313, 314]. A model molecular potential was constructed with the molecular volume separated into overlapping spherical region centered on each atomic site, the whole volume was then enclosed with an outer spherical region centered on the I atom. The asymptotic form of the potential was then adjusted to have the correct long range electron-ion Coulombic interaction. Wavefunctions associated with the continuum electron are then generated using multiple scattering equations with a symmetry-adapted spherical harmonic angular basis. In the calculations presented here, the basis was truncated at $l_{\max} = 8$ (outer sphere), 7 (I atom), 6 (C atom), 4 (H atoms). The orthogonal set of bound orbital functions, available from the Xα potential, were then used to calculate the one-electron (frozen core) dipole matrix elements for specific ionisation channels of interest. From these matrix elements, the photoionisation cross-sections (σ) and anisotropy parameters (β) were obtained.

4.4 Results and discussion

4.4.1 Ion yield, x-ray absorption and photoionisation cross section spectra

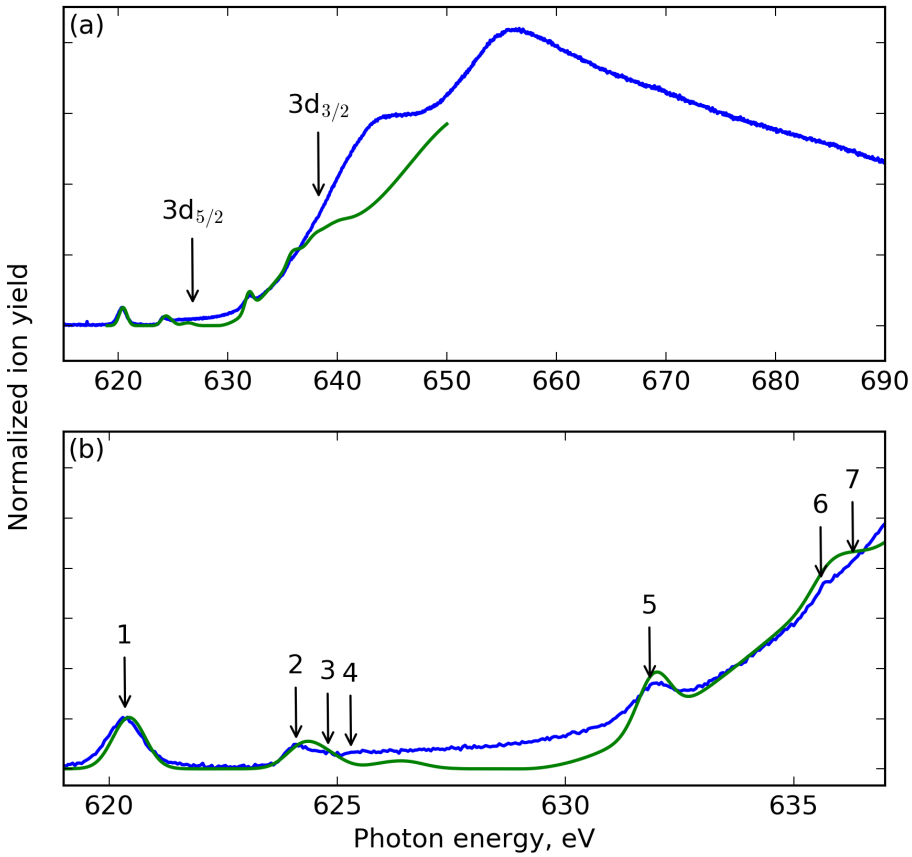

Figure 4.3: The experimental total ion yield (blue) of CH_3I recorded in the photon energy range 610-690 eV, and the theoretical absorption spectrum (green) calculated using the TDDFT method. The I $3d_{5/2}$ and I $3d_{3/2}$ ionisation thresholds at 626.8 and 638.3 eV, respectively, are marked. (b) Expanded sections of the spectra showing the threshold region in greater detail. The arrows denote the positions of resonances. The measured and predicted excitation energies of these resonances are given in Table 4.1.

In Fig. 4.3 a total-ion-yield spectrum recorded in the vicinity of the CH_3I 3d ionisation thresholds is presented. The yield, which is broadly in agreement with the

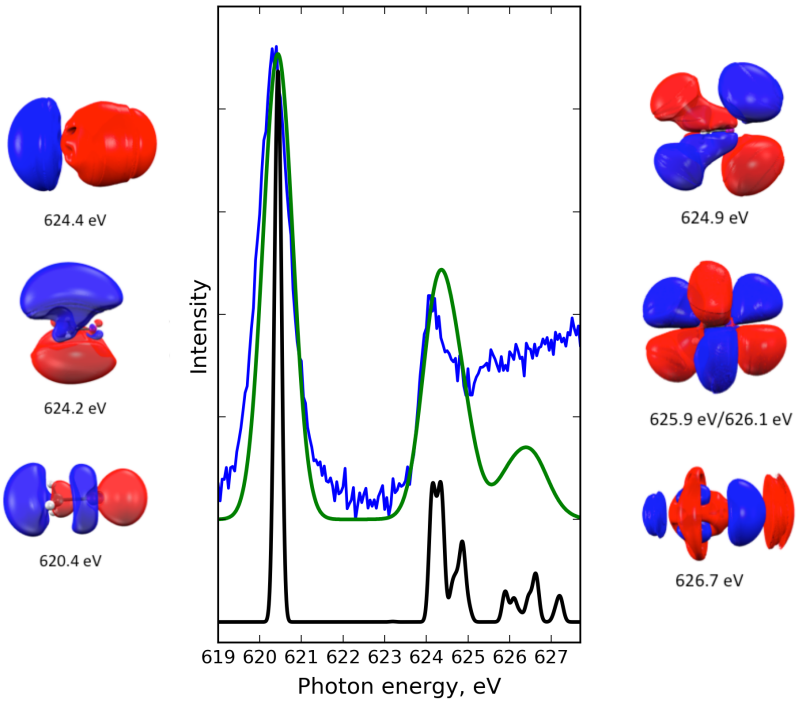

Figure 4.4: The experimental total ion yield (blue) of CH_3I in the I $3d_{5/2}$ threshold region. The theoretical (TDDFT) absorption spectrum is shown after convolution of the calculated spectral intensity at a particular excitation energy with a Gaussian of 0.1 eV (FWHM) (black) to allow the individual contributions to be discernible, and after convolution with a Gaussian of 0.5 eV (FWHM) (green) to provide a better match with the experimental spectrum. Plots of the valence and Rydberg orbitals, together with the corresponding calculated transition energies associated with excitation from the I $3d_{5/2}$ orbital, are shown.

energy loss spectrum previously measured by Hitchcock and Brion [290], exhibits a broad maximum at ∼656 eV and a shoulder at ∼644 eV. The separation (∼12 eV) between these features is comparable to the I 3d spin-orbit splitting (11.48 eV) determined in the present study. The shoulder and maximum can be attributed to the $3d_{5/2} \rightarrow \varepsilon f$ and $3d_{3/2} \rightarrow \varepsilon f$ shape resonances, respectively, based on the corresponding observed [102, 104, 106, 107, 109] and predicted [315, 316] processes in Xe.

In contrast to the energy loss spectrum [290], the experimental ion yield exhibits several pronounced resonances in the pre-edge region (Fig. 4.3). Somewhat similar structure has been observed in the Xe 3d absorption [102, 105] and ionisation [104, 107] spectra, and attributed to excitation of the $3d_{5/2,3/2}$ electrons into

p-type Rydberg orbitals. In order to help assign the nature of the transitions involved in the pre-edge region of CH_3I, the theoretical X-ray absorption spectrum, together with orbital plots for some of the low-lying excited states, are presented in Fig. 4.4. The TDDFT results were plotted after convolving the spectral intensity at a particular excitation energy with a Gaussian of 0.1 eV (FWHM), allowing the individual contributions to be discernible, and after convolving with a Gaussian of 0.5 eV (FWHM), to provide a better match with the experimental spectrum. Overall, the computed spectrum is in good agreement with the experimental measurements, particularly in the pre-edge region.

The calculations neglect an explicit description of relativistic effects and there will also be some error associated with the use of the CAM-B3LYP exchange-correlation functional for the transitions from inner-shell orbitals [317]. Therefore, it is possible that the close agreement between the calculated and experimental excitation energies arises in part from a cancellation of errors. The energies of the excitations from the different d orbitals are not degenerate, and the energies shown in Fig. 4.3 and listed in Table 4.1, correspond to the energy of the peak of the bands resulting from the convolution with the Gaussian functions.

The first band, labeled as peak 1 in Fig. 4.3, is computed to lie at 620.4 eV compared to the experimental value of 620.35 eV. This band arises from transitions from the $3d_{5/2}$ orbital into lowest unoccupied $\sigma^*(a_1)$ molecular orbital (LUMO) which has antibonding character along the carbon-iodine (C-I) axis. In a similar manner, peak 5, observed at 631.95 eV, is attributed to the $3d_{3/2} \rightarrow \sigma^*(a_1)$ transition. As the I 3d spin-orbit splitting is 11.48 eV, bands due to excitations involving the $3d_{3/2}$ orbital are embedded in the $3d_{5/2}^{-1}$ continuum.

The next distinct features in the spin-orbit split excitation series, peaks 2 and 6, are located 3.75 eV and 3.80 eV above those due to transitions into the σ^* orbital in the experimental and theoretical spectrum, respectively. Our predictions indicate that each of these peaks (2 and 6) arises from transitions into two separate p-type Rydberg orbitals, namely 6pe and $6pa_1$, lying perpendicular and parallel, respectively, to the C-I axis (Fig. 4.4). The calculated excitation energies for these two

Rydberg transitions are 624.2 and 624.4 eV, respectively. These assignments are somewhat in keeping with those proposed for the corresponding CH_3I 4d excitation by Hitchcock and Brion [290], and by O'Sullivan [293].

The following peaks, 3 and 7, at 624.8 eV and 636.4 eV, are predicted to be due to transitions into orbitals that have Rydberg d character (Fig. 4.4). These assignments differ from those proposed for the analogous peaks in the 4d excitation spectrum where the upper orbital was given as $6pa_1$ [290, 293]. The assignment of the 4d transitions has been subject to debate due to the similarity of the binding energies and relative separations for the Rydberg states of CH_3I and I_2. The analogous feature in I_2 was attributed to excitation into the 4f Rydberg orbital [318]. In atomic systems, transitions into the f-type discrete and continuum channels are usually suppressed until well above threshold due to centrifugal barriers [292]. However, in I_2, it was suggested that the anisotropic molecular potential allows sufficient mixing between the states of different l to permit access to the f channel [293]. Finally, there is tentative evidence of a transition at 625.3 eV, peak 4, which in the analogous transition in the 4d excitation spectrum was attributed to the 7p Rydberg state [293]. The nature of the orbitals for the higher energy bands, located above peak 4, becomes increasingly complex to assign in the calculations: an accurate description of the predicted and observed structure is no longer feasible.

The TDDFT calculations show that the continuum intensity arises from transitions to f orbitals. Fig. 4.5(a) illustrates two typical orbitals corresponding to the discrete states which contribute significant oscillator strength to the continuum. These orbitals have characteristic features of an f orbital localized around the I atom. The basis set used in the calculations contains functions with angular momenta up to l = 5(h). Removing the higher angular momentum functions from the basis set has the effect of removing transitions to these states from the calculations. This allows the nature of the states contributing to the continuum region to be examined. Fig. 4.5(b) shows the computed continuum region when the l = 4(g),5(h) basis functions have been removed and when the l = 3(f),4,5 basis functions have been removed. When the l = 4,5 functions are removed, there is only a minor loss

Table 4.1: Excitation energies and proposed assignments for the structure in the CH_3I ion yield due to valence and Rydberg states converging to the $3d_{5/2}$ and (ii) $3d_{3/2}$ ionisation thresholds,respectively. The $3d_{5/2}$-$3d_{5/2}$ interval is approximately 11.5 eV and is in reasonable agreement with previous XPS measurements on I_2 [304].

	Excitation energy (eV)		
Feature	Experimental	Theoretical	Assignment
(i)			
1	620.35	620.4	$3d_{5/2} \rightarrow \sigma^*(a_1)$
2	624.1	624.2/624.4	$3d_{5/2} \rightarrow 6pe/6pa_1$
3	624.8	624.9	$3d_{5/2} \rightarrow d$
4	625.4	N/A	$3d_{5/2} \rightarrow$unassigned
$3d_{5/2}$ IP	626.8	626.17	$3d_{5/2} \rightarrow \infty$
	644.4	N/A	$3d_{5/2} \rightarrow \varepsilon f$
(ii)			
5	631.95	631.9	$3d_{3/2} \rightarrow \sigma^*(a_1)$
6	635.7	635.7/635.9	$3d_{3/2} \rightarrow 6pe/6pa_1$
7	636.4	636.4	$3d_{3/2} \rightarrow d$
$3d_{5/2}$ IP	633.4	638.67	$3d_{3/2} \rightarrow \infty$
	656.0	N/A	$3d_{3/2} \rightarrow \varepsilon f$

in intensity, suggesting that these states are not the dominant contribution to the continuum. However, when the l = 3 functions are removed, the intensity in the continuum is reduced to nearly zero. This highlights that transitions to these states make the dominant contribution to the continuum. Note that the apparent higher intensity, around 630 eV, associated with the curve having the l = 3,4,5 basis functions removed compared to that having only the l = 4,5 basis functions removed, and that having all the functions present, is an artifact of the spline fitting used in the Stieltjes image fitting procedure.

The I 3d photoionisation cross section of CH3I, calculated using the CMS-Xα method [313,314], is shown in Fig. 4.6(a). To allow the role of the f-waves to be examined in more detail, the total photoionisation cross section was decomposed into its partial l-wave contributions: these results are plotted in Fig. 4.6(b). It is evident that the l = 3(f) wave makes the dominant contribution to the I 3d photoionisation cross section, as expected for an atomic-like process, in accord with the TDDFT

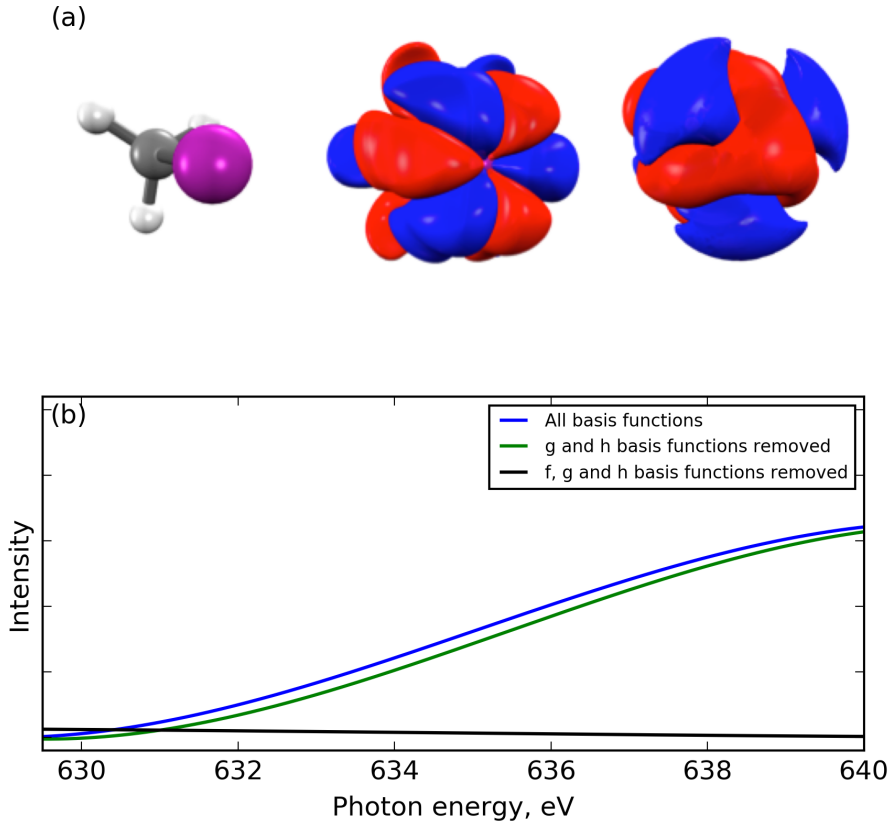

Figure 4.5: (a) Two orbitals, typical of those involved in the transitions which give rise to the oscillator strength in the continuum. The calculations highlight that these orbitals have characteristic features of an f orbital around the iodine atom. (b) Theoretical above-threshold X-ray absorption spectra, calculated using TDDFT, as a function of employed basis set.

results. In Fig. 4.6(c) we present a decomposition of the cross section into symmetry adapted combinations of the angular basis functions. In this view, it is seen that the a_1 and e symmetry continua dominate across the whole energy range. Allowing for the degeneracy of the e continuum, the a_1 and e partial cross sections are quite commensurate, with a further examination confirming that $f\sigma(a_1)$ and $f\pi$(e) waves contribute equally to the ionisation. The theoretical spectrum displays a peak at a kinetic energy 20.5 eV ($\hbar\omega$ = 652.5 eV) above the calculated ionisation threshold of 632 eV, readily attributable to the expected $3d\rightarrow\varepsilon f$ shape resonance. The eigenphase sums (Fig. 4.6(d)) identify, for both the a_1 and e continua, a sharp phase

rise of π radians at this energy, providing a signature indication of the presence of shape resonances in both of these partial channels. It should be noted, however, that apart from the region around 650 eV where the $l = 1$ component is the second most dominant partial wave, higher-l partial waves make significant contributions, thereby emphasising the molecular, multipolar nature of the ionisation process.

To the best of our knowledge, the photoabsorption spectra of molecular iodine and hydrogen iodide have not been measured in the vicinity of the I 3d thresholds. It would therefore be of interest to record the I 3d absorption spectra of these two diatomics in order to study the way in which the absorption structure evolves in going from atomic Xe, to the closely related diatomics HI and I_2, and then onto the polyatomic CH_3I.

4.4.2 Photoelectron spectra

4.4.2.1 Overview of the complete spectrum

Fig. 4.7(a) shows the photoelectron spectrum of CH3I, measured at a photon energy of 614 eV, for vertically and horizontally plane polarised radiation. This energy lies below both the I 3d ionisation thresholds and the spectrum is dominated by bands due to photoionisation of the C 1s and I 4d levels. The photoelectron bands associated with the valence shells are relatively weak, which is to be expected at large excess energies presented here. Bands due to direct photoionisation can be assigned using the previously reported binding energies of the C 1s(291.3 eV [290]), I 4s(195.4 eV [298, 299]), I 4p($\sim$129 eV [296]), I 4d(58.3 eV-$4d_{3/2}$, 56.7 eV–$4d_{5/2}$ [293]) and valence [94, 97] orbitals. Some weak structure associated with the I 4d and C 1s shake-up/shake-off transitions is also discernible.

A section of the spectrum recorded at a photon energy of 666.2 eV, which lies above both the I $3d_{5/2}$ and $3d_{3/2}$ ionisation thresholds, is plotted in Fig. 4.7(b). The additional structure occurring in this spectrum, when compared to Fig. 4.7(a), arises from various Auger decay channels associated with the I $3d_{3/2}$ (M_4) and $3d_{5/2}$ (M_5) orbitals. The photoelectron peaks due to the I $3d_{5/2,3/2}$ levels are not included in Fig. 4.7(b), and will be discussed in Sec. 4.4.2.3 – 4.4.2.4. Table 4.2 provides a summary of the photoelectron and Auger electron bands appearing in

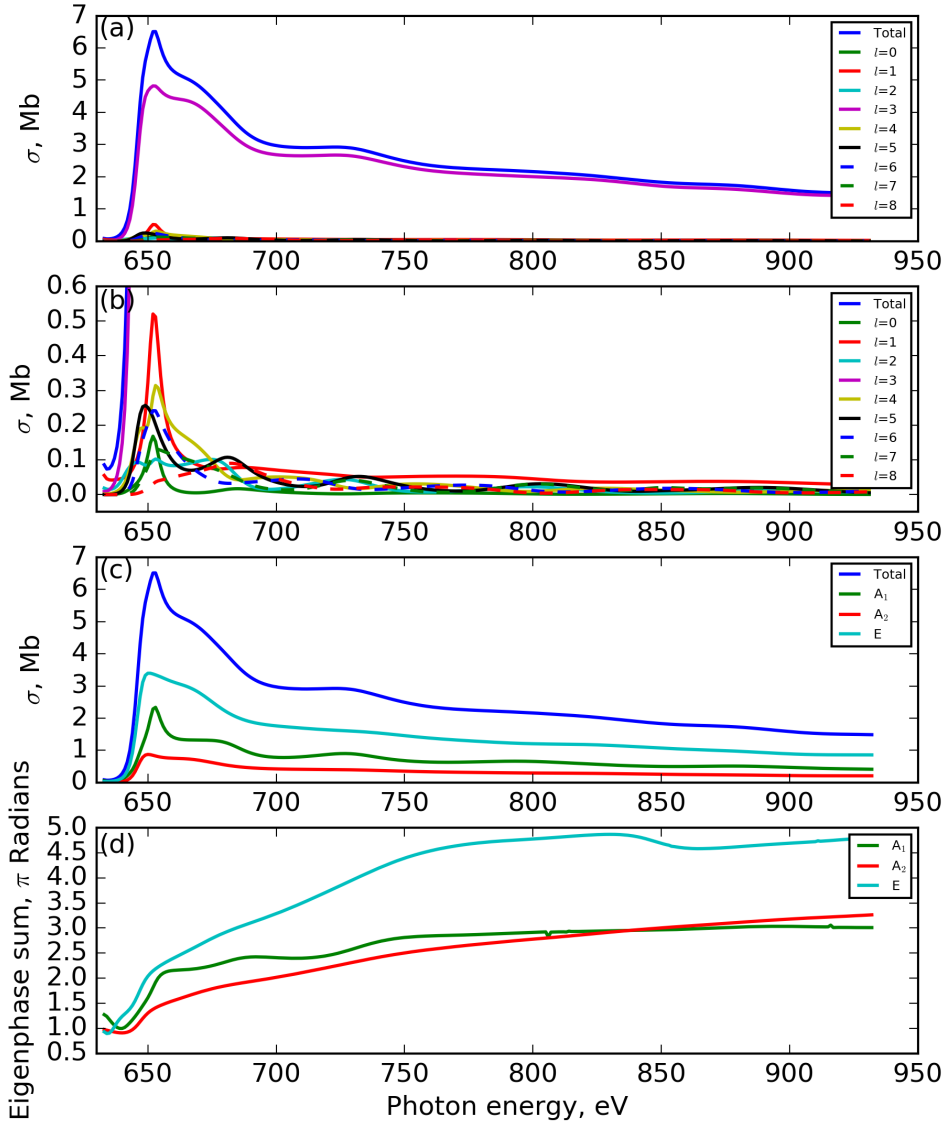

Figure 4.6: (a) Photoionisation cross section for the I 3d levels in CH_3I, calculated using the CMS-Xα, decomposed into the partial l-wave contributions, and expanded around the I atom. (b) Photoionisation cross section expanded to highlight weaker l-wave contributions. (c) Photoionisation cross sections decomposed into contributions made by symmetry adapted combinations of the angular basis functions. (d) The symmetry adapted eigenphase sums.

the experimental spectrum. Peaks due to direct photoionisation and the associated shakeup/shake-off transitions are referenced with respect to their binding energy, whereas those due to Auger decay channels are referenced with respect to their

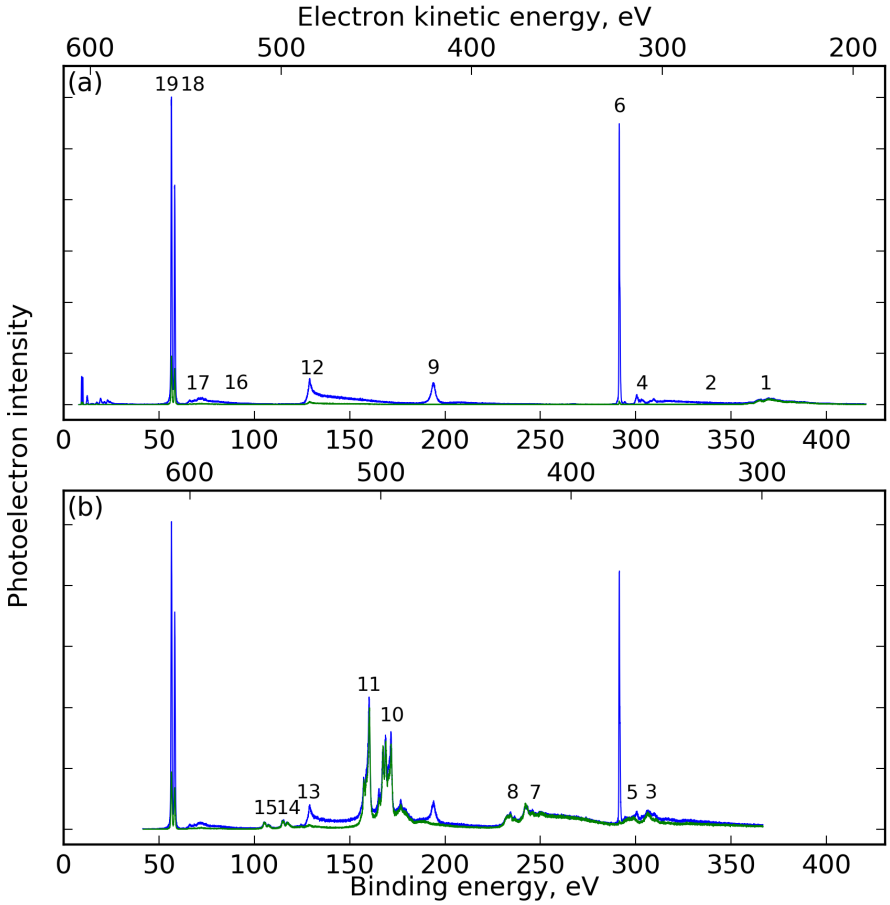

Figure 4.7: (a) The electron spectrum of CH_3I recorded at a photon energy of 614.0 eV using vertically (blue) and horizontally (green) plane polarised radiation. Most of the structure is due to direct photoionisation. (b) The electron spectrum of CH_3I recorded at a photon energy of 666.2 eV using vertically (blue) and horizontally (green) plane polarised radiation. Most of the structure in the spectrum recorded with horizontally plane polarised radiation is associated with the $M_{45}N_{45}O_{23}$, $M_{45}N_{45}V$, $M_{45}N_{45}N_{45}$, $M_{45}N_{23}N_{45}$ and $M_{45}N_1N_{45}$ Auger transitions. The numbered peaks in (a) and (b) are identified in Table 4.2.

electron kinetic energy. The electron peaks arising from Auger decay of the M_4 and M_5 subshells, and their associated angular distributions, will be discussed in detail in Chapter 5.

4.4.2.2 Photoelectron bands associated with the I 4s and I 4p orbitals

Fig. 4.8(a) shows the region of the photoelectron spectrum encompassing structure associated with the I 4s and I 4p orbitals in greater detail. Our spectrum is broadly in accord with those measured by Gelius [298] and by Svensson *et al* [299], using Al

Table 4.2: Energies and assignments of the observed transitions in the electron spectrum of CH_3I shown in Fig. 4.7. Explanation of the nomenclature for the Auger transition labeling is given in Sec. 1.6.1.

Feature	Electron kinetic energy (eV)	Binding energy (eV)	Assignment
1	∼220-265		C KVV
2		316-366	C 1s shake-off
3	∼355-363		$M_5N_1N_{45}$
4		294-316	C 1s shake-up
5	∼365-373		$M_4N_1N_{45}$
6		291.3	C 1s
7	∼413-426		$M_5N_{23}N_{45}$
8	∼426-437		$M_5N_{23}N_{45}$
9		193.8	I 4s
10	∼488-500		$M_5N_{45}N_{45}$
11	∼500-512		$M_5N_{45}N_{45}$
12		129.0	I 4p
13	∼530-545		$M_{45}N_{4.5}V$
14	∼546-554		$M_5N_{45}O_{23}$
15	∼556-564		$M_5N_{45}O_{23}$
16		76-102	I 4d shake-off
17		62-76	I 4d shake-up
18		58.3	I $4d_{3/2}$
19		56.7	I $4d_{5/2}$

Kα radiation, but is of improved quality and covers a wider binding energy range. The anomalous appearance of the photoelectron bands is similar to that observed in Xe [118, 298, 299].

The earliest indication of the unusual behavior of the Xe 4p orbital was found in the absorption spectrum [319, 320] where lines were observed converging onto what was considered to be the $4p^5\ ^2P_{3/2}$ ionisation threshold, whereas none were evident converging onto the $4p^5\ ^2P_{1/2}$ threshold. Confirmation of this anomaly was provided by the photoelectron spectrum [118,298,299] which, instead of exhibiting a well resolved spin-orbit doublet associated with the 4p orbital, showed a single structured peak in the vicinity of the expected $4p^5\ ^2P_{3/2}$ ionisation limit, together with a continuous intensity distribution which extended up to a second peak, which

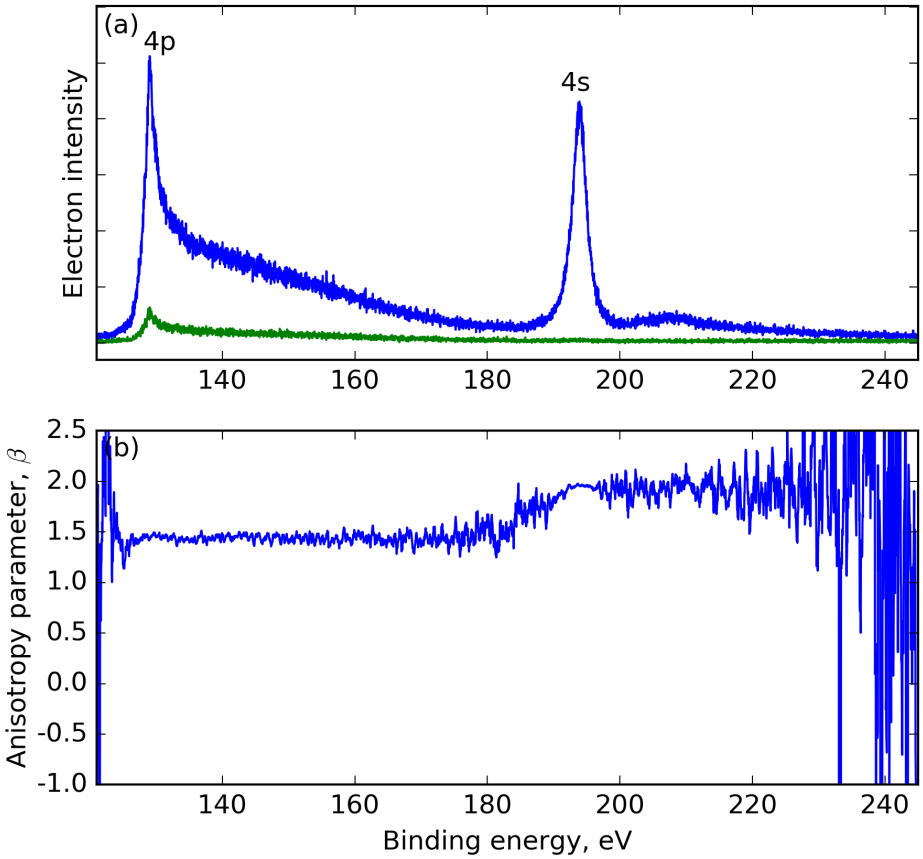

Figure 4.8: (a) Photoelectron spectrum of CH_3I, recorded at a photon energy of 614.0 eV, using vertically (blue) and horizontally (green) plane polarised radiation, in the binding energy range encompassing structure due to the I 4s and I 4p orbitals. (b) The corresponding photoelectron anisotropy parameter. A 10-point moving average has been applied to the anisotropy parameter spectra to improve the signal-to-noise ratio.

was associated with the 4s $^1S_0$ limit.

This anomalous intensity distribution is a consequence of strong electron correlation, resulting in a breakdown of the single particle model of ionisation [321] (see Sec. 1.4). Under such circumstances, the two step model of Auger decay [322], where photoionisation forms a well-defined core hole and the subsequent emission of the Auger electron is considered to be an independent process, becomes invalid. Instead, the inner-shell hole state transforms rapidly, through Coster-Kronig and super-Coster-Kronig processes, into excited states having configurations with two

excited electrons. Coster-Kronig [323] and super-Coster-Kronig [324] transitions correspond to Auger decays in which one, or both, respectively, of the holes in the final ionic state belong to the same principal shell as the initial vacancy. Such processes have very high transition rates.

In order to provide a framework by which the photoelectron spectra connected with the I 4s and 4p level in CH_3I can be interpreted, a brief summary of the theoretical investigations, performed by Wendin and Ohno [325,326], of the corresponding 4s and 4p levels in Xe is outlined as follows. For the initially formed $4p^{-1}$ state, the following decay mechanisms were considered [325, 326] (using the nomenclature adopted in previous discussions [325–327]): $4p^{-1} \rightarrow 4d^{-1}5p^{-1}$ + kl electron, Coster-Kronig transition; $4p^{-1} \rightarrow 4d^{-1}5s^{-1}$ + kl electron, Coster-Kronig transition; $4p^{-1} \rightarrow 4d^{-2}$ + kl electron, super-Coster-Kronig transition; $4p^{-1} \rightarrow 4d^{-2}$ + 4f electron, giant-Coster-Kronig transition (where k denotes a discrete or continuum orbital). The calculations showed that the dominant decay process yields $4d^{-2}$kl electron configurations and that the peak observed in the vicinity of the expected $4p^5\ ^2P_{3/2}$ threshold should be attributed to a group of satellites with electron configurations $4d^{-2}$kf, of which $4d^{-2}4f\ ^2P_{3/2}$ is the strongest component. This peak was predicted to have only 38% of the spectral intensity associated with the unperturbed 4p photoionisation, and its binding energy is shifted with respect to that calculated for the unperturbed state. The other decay mechanisms listed above are responsible for the continuum observed between the peaks due to the $4d^{-2}4f\ ^2P_{3/2}$ and the $4s\ ^1S_0$ states.

In the case of the initially formed $4s^{-1}$ state, the decay mechanisms considered in Refs [325, 326], were $4s^{-1} \rightarrow 4p^{-1}4d^{-1}$ + kl electron, $4s^{-1} \rightarrow 4p^{-1}5s^{-1}$ + kl electron and $4s^{-1} \rightarrow 4p^{-1}5p^{-1}$ + kl electron. Although, as to be expected, these interactions lead to a shift in the binding energy of the peak associated with the 4s orbital with respect to the unperturbed value, most of the spectral intensity - on the order of 80% - remains in a single peak. Thus, this dominant peak may be characterised as being due to a reasonably well defined hole having mainly 4s character. The remaining part of the 4s intensity was predicted to appear in the

super-Coster-Kronig $4p^{-1}4d^{-1}$ continuum [325, 326]. This prediction could not be verified because the experimental spectrum did not extend to sufficiently high binding energies.

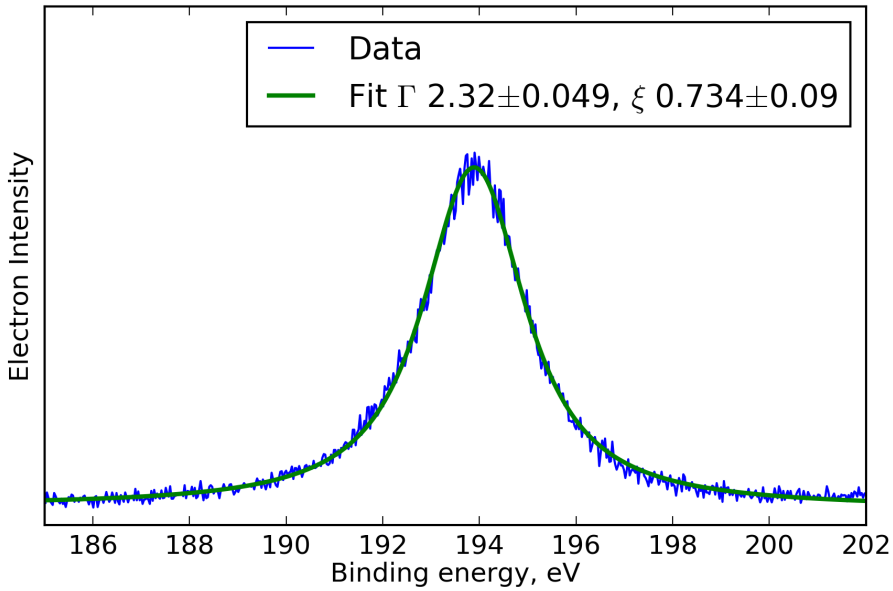

Figure 4.9: Photoelectron spectrum of CH_3I in the binding energy range covering the main peak due ionisation of I 4s orbital. The spectra recorded at a photon energy of 614.0 eV using vertically plane polarised radiation (blue). A Voigt profile fit to the experimental data (green) allows widths to be extracted for the hole state level width, Γ (FWHM), and the experimental resolution, ξ (FWHM).

The photoelectron band shapes associated with the I 4p and I 4s orbitals in CH_3I are similar to those discussed above in relation to the corresponding orbitals in Xe and, thus, similar configuration interactions and decay mechanisms appear to apply. Binding energies of 129.0 and 193.8 eV are obtained for the maxima of the peaks due to the 4p and 4s orbitals, respectively. The I 4p peak shows some hints of structure on the high binding energy side. The analogous structure observed in the Xe 4p peak was associated with multiplets within the $(4d^{-2}4f)_{3/2}$ configuration [326]. In Fig. 4.9, a fit of the 4s photoelectron peak with a Voigt profile is presented. The fit results in Lorentzian, Γ, and Gaussian, ξ, widths of 2.32±0.049 eV (FWHM) and 0.734±0.09 eV (FWHM) to be extracted for the hole state level width and experimental resolution, respectively. Thus, the level width of the peak due to the I 4s orbital is similar to that (2.7 eV [299]) for the corresponding Xe 4s peak. In

addition, the spectrum (Fig. 4.8(a)) shows a continuum in the binding energy range ∼200-250 eV. This, in a similar manner to Xe [325, 326], can be attributed to the decay of the I 4s hole state into the $4p^{-1}4d^{-1}$ continuum, via super-Coster-Kronig transitions.

Fig. 4.8(b) shows the β parameter, evaluated using Eq. 4.2, as a function of the binding energy in the region of the I 4s and 4p photoelectron peaks. It is evident that the value of the β parameter associated with the continuum occurring on the high binding energy side of the principal peak due to the 4p orbital is similar to that in the peak. The same behavior is observed for the β parameter corresponding to the 4s peak and that of the continuum appearing at higher binding energies. At a photon energy of 614 eV, a β value of ∼2.0 is obtained for the I 4s peak when integrating the electron counts across the binding energy range shown in Fig. 4.9. β parameters of 1.4, 1.1, 1.3 and 1.0 are obtained at photon energies of 614, 620.1, 656 and 666.2 eV, respectively, when we evaluate the intensity around a small energy range containing the I 4p line. These values are similar to those measured by Becker *et al* for the 4s and 4p orbitals in Xe in the vicinity of the Xe 3d threshold [328]. It was suggested that the variations in the Xe 4s β parameter, close to the 3d edge, might be due to interchannel coupling between the 4s and 3d subshells [328]. A similar type of coupling might be the cause of the variations we observe in the β values for the I 4p peak in the vicinity of the I 3d threshold.

4.4.2.3 Photoelectron bands associated with the I $3d_{5/2,3/2}$ orbitals

Fig. 4.10 shows the photoelectron spectrum of CH_3I, recorded at a photon energy of 665.6 eV, in the binding energy region encompassing the two peaks associated with the I $3d_{5/2}$ and $3d_{3/2}$ electrons. The bands exhibit a characteristic tailing towards higher binding energy due to PCI. For both of the spin-orbit split states, the peak binding energy, intensity, β parameter, and level width of the hole state were extracted by performing a weighted least-squares fit to the spectra (see Fig. 4.10(b)-(c)), as described in Sec. 4.2.2.

The binding energies of the I $3d_{5/2,3/2}$ levels in CH_3I have not been reported previously. In order to determine these, photoelectron spectra were recorded for a

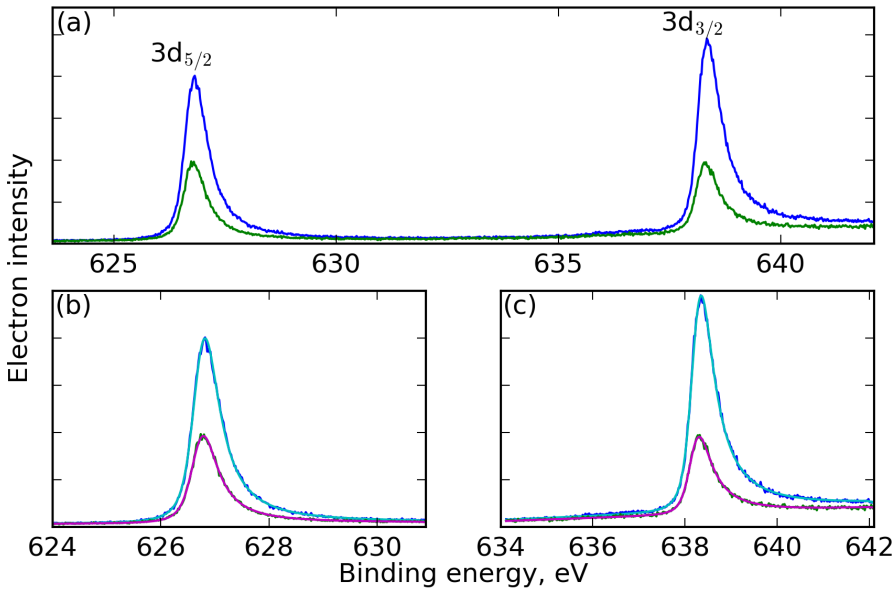

Figure 4.10: (a) Photoelectron spectrum of CH_3I, recorded at a photon energy of 665.6 eV, using vertically (blue) and horizontally (green) plane polarised radiation. The two bands are due to ionisation of the I $3d_{5/2}$ and I $3d_{3/2}$ levels. The asymmetric band shapes are the result of post collision interaction. (b) The experimental photoelectron peaks due to ionisation of the I $3d_{3/2}$ level, in the two polarisation orientations, and their fitted profiles (respectively cyan and magenta), using the functional form outlined in Sec. 4.2.2. (c) The experimental peaks, and fitted profiles of the photoelectron band due to ionisation of the I $3d_{5/2}$ level, in the two polarisation orientations.

mixture of CH_3I and Xe, in the binding energy range encompassing the I 3d and Xe 3d peaks. There are several previous measurements of the Xe $3d_{5/2,3/2}$ binding energies [298, 299, 329]. Those of Svensson *et al* [299] were used to calibrate our binding energy scale, and resulted in energies of 626.8 and 638.3 eV, with an estimated uncertainty of $\pm$0.4 eV, for the I $3d_{5/2}$ and I $3d_{3/2}$ ionisation thresholds, respectively. This uncertainty is related to the spread in the previously reported Xe binding energies [298, 299, 329] available for use as calibrations rather than to any limitation in our experimental instrumentation. The I 3d photoelectron spectra also allow the spin-orbit splitting to be determined. A value of 11.48 $\pm$ 0.01 eV was obtained by analysing photoelectron spectra recorded at thirteen separate photon energies.

In Fig. 4.11, the extracted core-level widths, instrumental broadenings and *C*

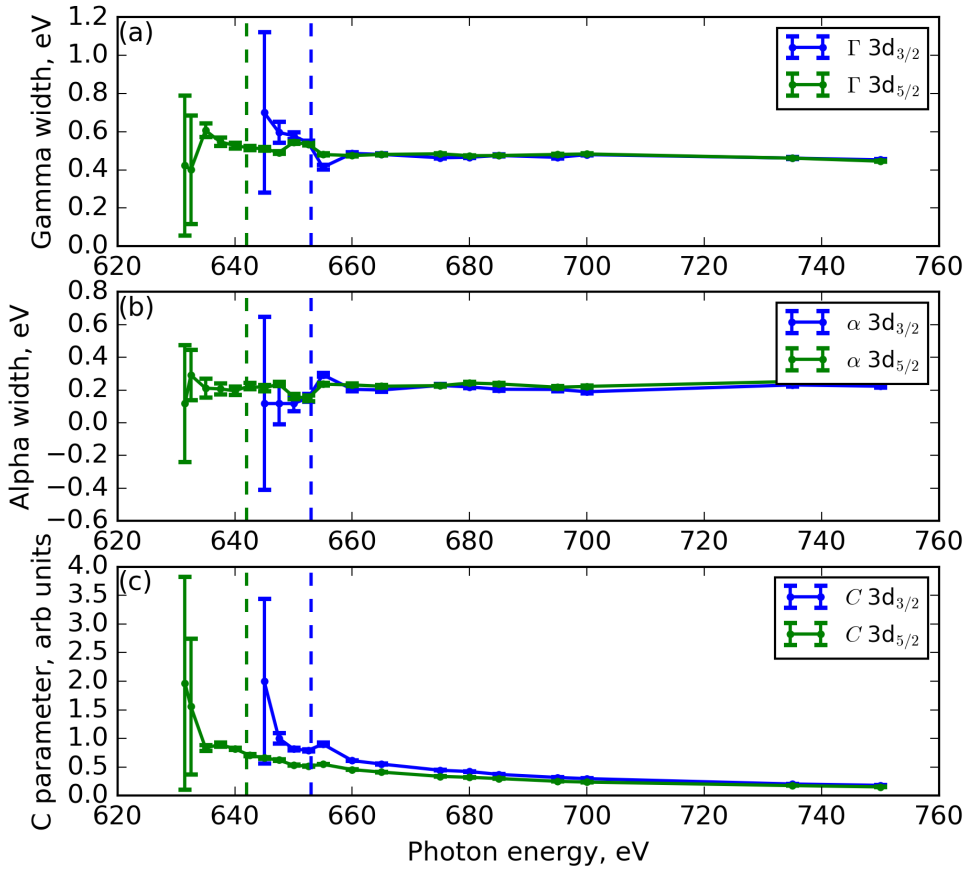

Figure 4.11: The (a) core-level widths, (b) instrumental broadenings and (c) *C* parameters extracted from the fitting routine for the I $3d_{5/2}$ (green) and I $3d_{3/2}$ (blue) levels in CH_3I. The error bars represent the standard error of the fitting parameters. The dashed lines represent the photon energy at which the adopted atomic line shape is expected to deviate from the semi-classical line shape, see main text for further discussion.

parameters are shown as a function of photon energy. The fitting procedure typically returns level widths (Fig. 4.11(a)) between 440-520 meV and 450-500 meV for the I $3d_{5/2}$ and $3d_{3/2}$ hole states in CH_3I, respectively. These values are in reasonable accord with those of $\Gamma_{5/2}$ = 510 $\pm$ 30 meV and $\Gamma_{3/2}$ = 490 $\pm$ 30 meV for the corresponding 3d hole states in Xe [303]. The instrumental broadenings, α, extracted in our fitting procedure ($\sim$190-290 meV (FWHM)) were in reasonable accord with those expected based upon predicted monochromator, electron spectrometer and Doppler contributions.

It is evident that, at lower photon energies, close to the ionisation threshold, significant discrepancies as well as large error bars, occur for fitted widths and C parameters when compared to the values extracted at higher excess energies (see Fig. 4.11). These deviations may be related to the line shape used to approximate the distortion caused by PCI. The modified Coulomb line shape, derived by Armen *et al* [308], uses the asymptotic form of the two-electron wave function and explicitly neglects the non-Coulombic structure of the cation. While the I 3d ion yield and photoelectron spectra exhibit structure similar to that occurring in the corresponding spectra in Xe, it is likely that the nature of the molecular potential plays a role at energies close to threshold. Additionally, although the adopted line shape has been shown to agree well with semi-classical line shapes at electron kinetic energies of $E_{\mathrm{kin}} \geq (\Gamma_{5/2,3/2} E_{\mathrm{Auger}})^{1/2}$ where $\Gamma_{5/2,3/2}$ and E_{Auger} are the level width of the hole state and the Auger electron energy, respectively, deviations may occur close to threshold [308]. Using $\Gamma_{5/2,3/2}$ = 475 meV and E_{Auger} = 500 eV, which are appropriate values for I 3d ionisation, results in $E_{\mathrm{kin}} = \sim$15 eV. Thus, our I $3d_{5/2}$ and I $3d_{3/2}$ photoelectron band shapes may deviate from those predicted by the formula given by Armen *et al*, at photon energies below ∼642 and 653 eV, respectively. These values are denoted by the dashed green and blue lines in Fig. 4.11 and indeed below these excess energies significant deviations do occur.

Fig. 4.12 shows the experimentally derived I $3d_{5/2}$ and I $3d_{3/2}$ photoelectron anisotropy parameters. The predictions of the (non-relativistic) CMS-Xα calculations, which have been plotted using the experimental ionisation energies of 626.8 and 638.3 eV, are in good agreement with the measured values. The β parameter is predicted to be negative near threshold, and then to rise rapidly as the photon energy increases to reach a maximum close to unity approximately 15 eV above threshold. The photon energies at which these maxima occur, 640 and 655 eV for the $3d_{5/2}$ and $3d_{3/2}$ orbitals, respectively, approximately coincide with those for the predicted $3d_{5/2} \rightarrow \varepsilon$f and $3d_{3/2} \rightarrow \varepsilon$f shape resonances. At higher photon energies, the experimental and calculated β parameters gradually decrease. Our theoretical work indicates that the dip around $\hbar\omega$ = 700 eV may be associated with a (weak)

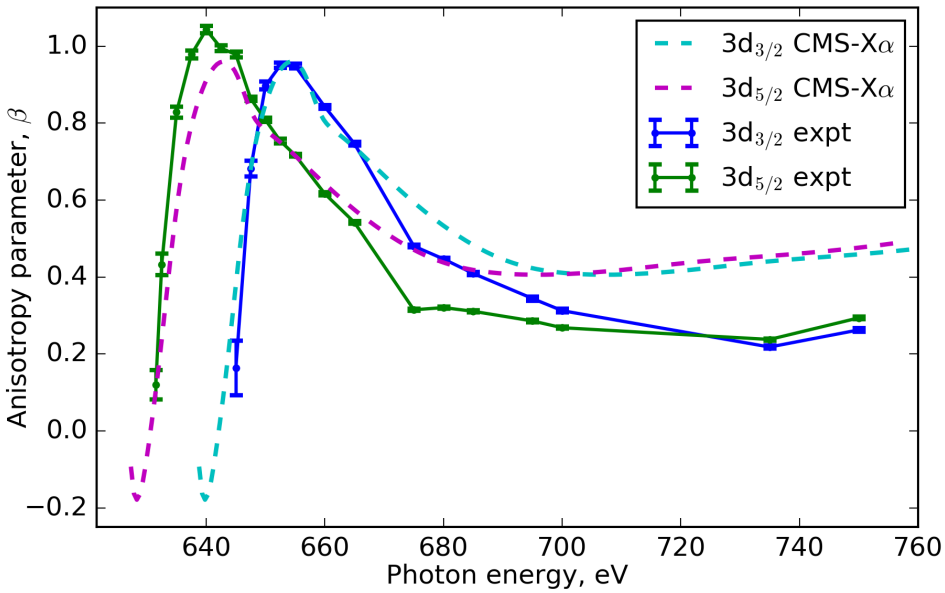

Figure 4.12: The experimentally derived photoelectron anisotropy parameters for the I $3d_{5/2}$ (green) and I $3d_{3/2}$ (blue) levels in CH_3I. The error bars represent the standard error of the β parameters extracted from the fit. The corresponding theoretical (CMS-Xα) photoelectron anisotropy parameters are plotted for the I $3d_{5/2}$ (magenta) and I $3d_{3/2}$ (cyan) levels using the experimentally determined ionisation energies.

Extended X-ray Absorption Fine Structure (EXAFS) type oscillation occurring in the a_1 symmetry continuum function (Fig. 4.6(c)). The localization of the initial 3d electrons, approximating a single site emitter, allows a simple in-phase-out-of-phase interference pattern to emerge, resulting from on-axis back-scattering from the methyl group. This back-scattering is most pronounced for a_1 symmetry outgoing waves due to the axial electron continuum density between the carbon and iodine atoms.

Overall, the photon energy dependence of the experimentally derived I $3d_{5/3,3/2}$ photoelectron anisotropy parameters is similar to that of the β parameters for the corresponding 3d orbitals in Xe [109], which, for the I $3d_{5/2}$ and $3d_{3/2}$ levels, are 1.05 and 0.95, respectively. In Xe, the β values for the $3d_{5/2}$ and $3d_{3/2}$ levels are almost the same ($\sim$1.05), which is in accord with theoretical predictions [330]. The discrepancy between the CH_3I I $3d_{3/2}$ and Xe $3d_{3/2}$ maximum β values may be linked to the fact that, in CH_3I, the main $3d_{3/2}^{-1}$ photoelectron peak

energetically overlaps with the majority of the $3d_{5/2}$ shake-up structure (see Sec. 4.4.2.4). The shake-up structure for the $3d_{5/2}$ peak will likely have a different β parameter compared to that of the main $3d^{-1}_{3/2}$ peak, which may be giving rise to the slightly lower 0.95 value. A larger difference is evident in the calculated β parameters, where those for Xe approach -1 close to threshold [109]. This deviation from the atomic Xe results close to the ionisation thresholds may be related to the fact that the multipolar nature of the molecular potential plays a more significant role at small excess energies.

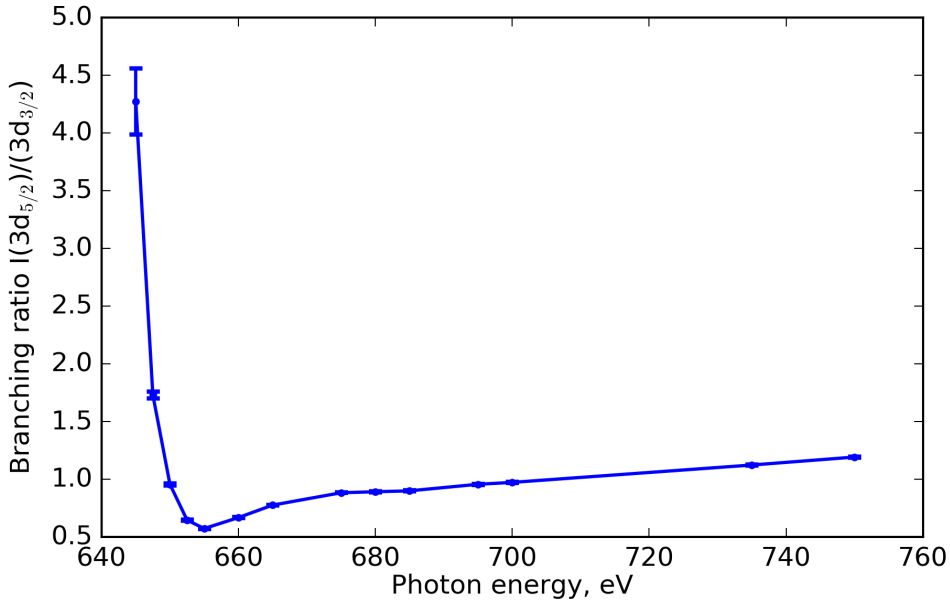

Figure 4.13: The I $3d_{5/2}$:I $3d_{3/2}$ intensity branching ratio. The error bars represent the standard error on the branching ratio, based on the standard error of the angle independent cross section extracted from the fit.

The branching ratio for photoionising the I $3d_{5/2}$ and I $3d_{3/2}$ orbitals in CH_3I (Fig. 4.13) exhibits an energy dependence similar to that observed for the $4d_{5/2}$ and $4d_{3/2}$ orbitals in Xe [331] and CH_3I [296]. Deviations from the statistical value of 1.5 are apparent. Calculations performed by Walker and Waber [332] highlight that, at a given photon energy, these deviations can be attributed to differences in the photoelectron kinetic energies and, hence, photoionisation partial cross sections, associated with the spin-orbit split components. This difference leads to a branching ratio greater than statistical when the partial cross section is rising, and to a smaller

branching ratio when the partial cross section is falling. Fig. 4.6(a) shows that the I 3d partial cross section rises rapidly from a low value at threshold to reach a maximum at $\hbar\omega$ = ∼655 eV, and then decreases. Since the I 3d spin-orbit splitting is 11.48 eV, at a given photon energy the partial cross sections for the $3d_{5/2}$ and $3d_{3/2}$ orbitals will differ considerably. These differences result in a higher than statistical branching ratio at threshold and in a lower than statistical ratio around 655 eV, coinciding with the $3d_{3/2} \rightarrow \varepsilon f$ shape resonance.

Finally, it is of note that the maximum values of the β parameters, and the minimum in the branching ratio, occur approximately 15 eV above the I 3d ionisation thresholds. This is precisely the region in which the adopted PCI line shape begins to deviate from the expected result. In order to verify the experimental results, given the assumptions in the adopted atomic model, we have evaluated the β parameters and branching ratio using the integrated intensity within a particular photoelectron peak, assuming a linear background. The results obtained using this independent procedure are in reasonable agreement with those obtained from the fitting procedure, and reproduce all the photon energy dependencies.

4.4.2.4 I 3d shake-up/shake-off spectrum

Fig. 4.14(a) shows the photoelectron spectrum of CH_3I, recorded at a photon energy of 740 eV, in the binding energy range encompassing the peaks associated with both the I $3d^{-1}_{5/2}$ and I $3d^{-1}_{3/2}$ states, and the structure due to shake-up/shake-off satellites (see Sec. 1.6). Most of the distinct satellite structure is associated with the $3d^{-1}_{3/2}$ state, as the analogous features associated with the $3d^{-1}_{5/2}$ state are energetically overlapping with the main $3d^{-1}_{3/2}$ photoelectron peak.

We start our interpretation of the satellite structure by considering peaks which can be assigned to shake-up processes accompanying $3d_{3/2}$ ionisation. Features observed at binding energies of 642.8 and 644.5 eV (labeled 3 and 4 in Fig. 4.14(b)), corresponding to energies of 4.5 and 6.2 eV above the main-line at 638.2 eV, are tentatively assigned to $3d_{3/2}$ ionisation accompanied by the $2e \rightarrow \sigma^*$ and $2e \rightarrow 6s$ excitations, respectively. In the valence shell absorption spectrum of CH_3I, the bands due to the $2e \rightarrow \sigma^*$ and $2e \rightarrow 6s$ transitions are observed at ∼4.8 and 6.2 eV,

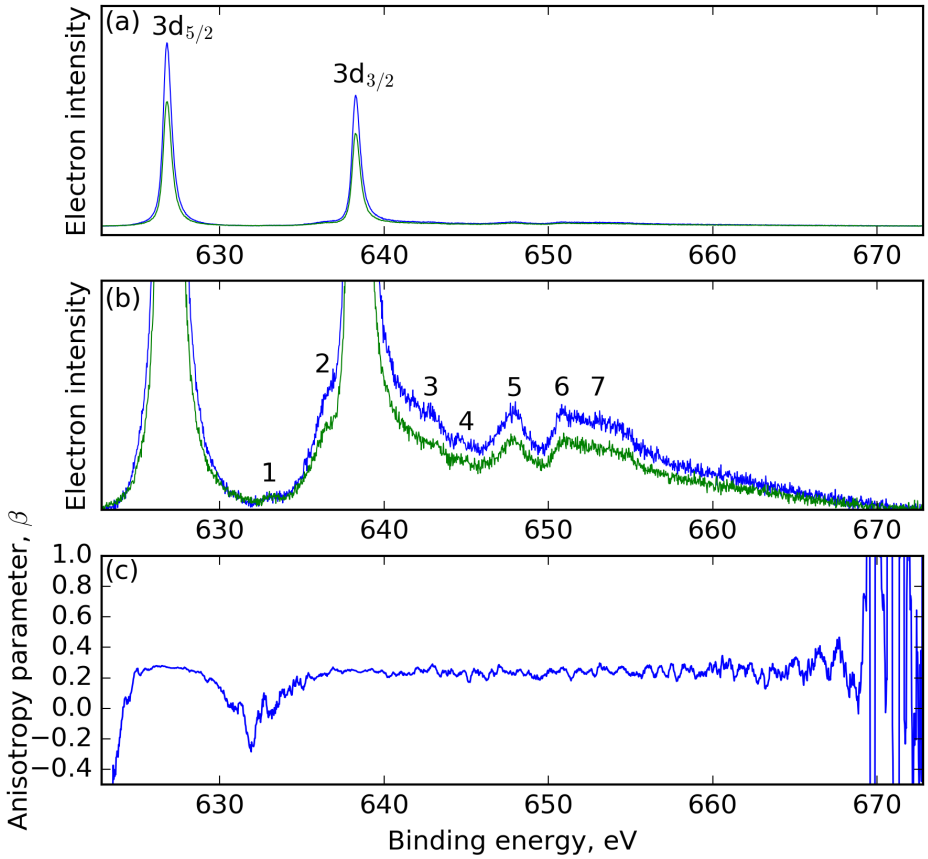

Figure 4.14: Photoelectron spectra of CH_3I, recorded at a photon energy of 740 eV, using vertically (blue) and horizontally (green) plane polarised radiation, in the binding energy range encompassing structure due to the I $3d_{5/2,3/2}$ main-lines and the associated shake-up/shake-off satellites. Panel (a) shows the entire spectrum. Panel (b) shows an expanded view, highlighting the structure due to the shake-up/shake-off satellites. Possible assignments for the numbered peaks are given in the text. Panel (c) shows the photoelectron anisotropy parameter, where a 10-point moving average has been applied to improve the signal-to-noise ratio. The dip on the β values at binding energies around 632 eV is an experimental artifact caused by the low electron intensity.

respectively [333, 334].

At higher energies, peaks observed at 647.9, 650.8 and 653.0 eV (labeled 5-7 in Fig. 4.14(b)), corresponding to energies of 9.6, 12.5 and 14.7 eV above the main-line, are tentatively assigned to $3d_{3/2}$ ionisation accompanied by excitation of another electron from the 2e, $3a_1$ or 1e orbitals, respectively, into a Rydberg orbital. Vertical ionisation energies of ∼9.5, 12.5 and 14.7 eV were reported for the $\tilde{X}^2E_{3/2}$,

$\tilde{A}^2A_1$ and $\tilde{B}^2E$ states, respectively [94].

Two features, labeled 1 and 2 in Fig. 4.14(b), are analogous to peaks 3 and 4, but involve $3d_{5/2}$ ionisation. Peak 1 at 633.0 eV, and the shoulder (peak 2) at 636.5 eV, can be assigned to shake-up satellites, where $3d_{5/2}$ ionisation is accompanied by the excitation of an electron from the outermost 2e orbital into the 6s Rydberg orbital, and by excitation from the 2e orbital into a high lying Rydberg orbital connected with the $\tilde{X}^2E_{3/2}$ limit, respectively.

In addition to these shake-up satellites, a continuum associated with shake-off transitions starts at a binding energy of ∼634 eV and extends to at least 670 eV. Fig. 4.14(c) shows that the β parameters associated with the satellite structure are similar to those of the main-lines.

4.4.2.5 Measurement of spin-orbit resolved I 3d ionisation cross sections via Auger yields

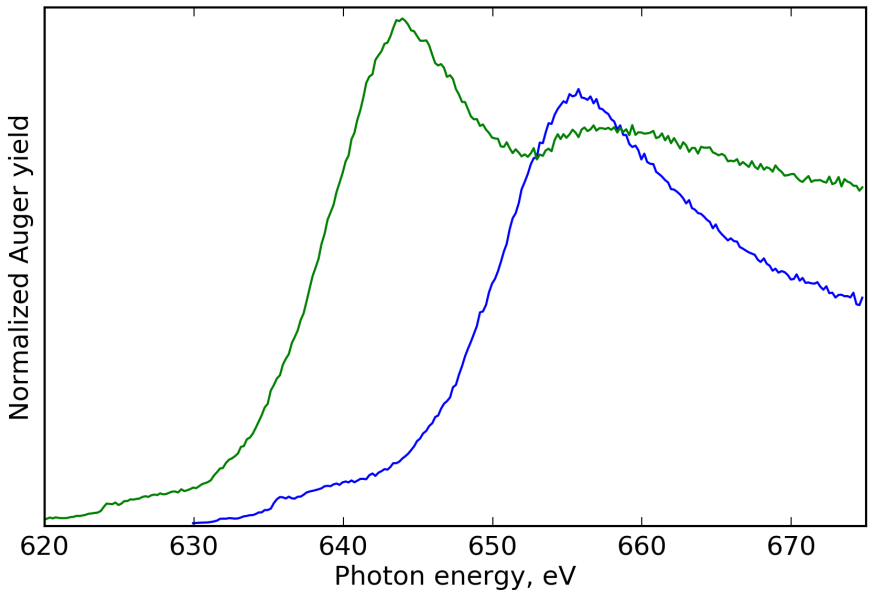

Figure 4.15: The $M_4N_{45}N_{45}$ (blue) and $M_5N_{45}N_{45}$ (green) Auger electron yields of CH_3I recorded with horizontally plane polarised radiation.

A simple, indirect method of determining the relative photoionisation cross sections of the I $3d_{5/2}$ and I $3d_{3/2}$ orbitals in CH_3I is through a measurement of the total electron yields associated with the $M_5N_{45}N_{45}$ and $M_4N_{45}N_{45}$ Auger tran-

sitions [109] (see Sec. 1.6.1 of the introduction for details on Auger nomenclature). As, for example, the first step in the $M_5N_{45}N_{45}$ Auger decay is the formation of the I $3d_{5/2}^{-1}$ core-hole state, the $M_5N_{45}N_{45}$ Auger electron yield is directly proportional to the I $3d_{5/2}$ partial photoionisation cross section. In our experiment, the $M_5N_{45}N_{45}$ and $M_4N_{45}N_{45}$ yields were determined by operating the Scienta electron analyzer in so-called "fixed" mode. This refers to mode of operation where data is acquired over a fixed electron kinetic energy window, with the width dictated by the pass energy employed. A 10 eV pass energy, resulting in a approximately 10 eV window, was used in this study. Electron kinetic energy windows centered at 495.5 eV and 507.5 eV were selected for the the $M_5N_{45}N_{45}$ and $M_4N_{45}N_{45}$ yields, respectively (Fig. 4.7(b)). These windows omit the peak due to the transition into the $^1S_0$ final state (see Chapter 5) but ensure that all of the detected Auger electron signal is associated with the selected decay. The yields shown in Fig. 4.15 were recorded using horizontally plane polarised radiation. At photon energies close to the I $3d_{5/2}$ and $3d_{3/2}$ ionisation thresholds at 626.8 and 638.3 eV, respectively, direct photoionisation of the I 4p orbital can lead to a small contribution from electrons whose kinetic energies overlap with those of the Auger electrons due to the $M_{45}N_{45}N_{45}$ transitions. Hence, the Auger electron signal remains finite at threshold. This point is highlighted in Fig. 4.16, where $M_{45}N_{45}N_{45}$ Auger electron spectra are presented as function of photon energy. In order to highlight the feature due to I 4p ionisation, the spectra are presented for vertically plane polarised radiation. Here, features due to direct photoionisation exhibit the characteristic shift to higher electron kinetic energy as the photon energy is increased, whereas those due to Auger transitions as independent of photon energy. It is evident that the 4p photoline (623-631 eV - $M_5N_{45}N_{45}$ spectra, 636-634 eV - $M_4N_{45}N_{45}$ spectra) only overlaps in kinetic energies near threshold and does not affect the shape of the yields in the regions of interest containing the shape resonances. The assignments, as well as the, associated angular distributions, of the $M_{45}N_{45}N_{45}$ Auger transitions will be discussed in Chapter 5.

The $M_5N_{45}N_{45}$ Auger electron yield (see Fig. 4.15) shows a peak at 644.0 eV,

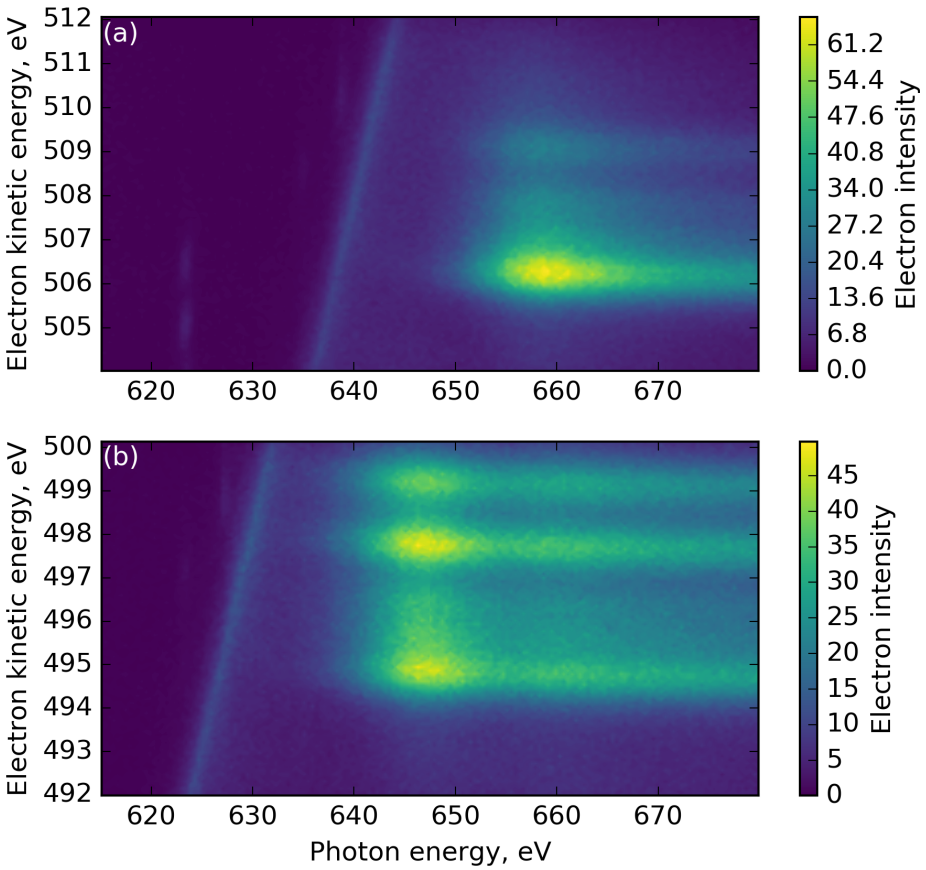

Figure 4.16: Auger electron spectra for the (a) $M_4N_{45}N_{45}$ and (b) $M_5N_{45}N_{45}$ transitions as a function of photon energy. The feature due to direct photoionisation of the I 4p orbital can be discerned due to the characteristic photon energy dependence.

corresponding to the $3d_{5/2} \rightarrow \varepsilon f$ shape resonance, followed by a broad maximum centered at approximately 657.4 eV. In contrast, the $M_4N_{45}N_{45}$ yield displays a single peak at 655.7 eV associated with the $3d_{3/2} \rightarrow \varepsilon f$ shape resonance. The photon energies corresponding to the positions of the shape resonances in the Auger electron yields coincide well with those observed in the ion yield spectra (see Fig. 4.3). The overall shape of the Auger electron yields measured in the present experiment for the I 3d level in CH_3I is similar to that of the corresponding yields determined for the Xe 3d level [109] and that of the calculated Xe 3d photoionisation partial cross sections [315, 316, 330].

In Xe, the theoretical work showed that the second maximum, located at higher

energy, in the Xe $3d_{5/2}$ photoionisation partial cross section was the result of inter-channel coupling between the $3d_{5/2}$ and $3d_{3/2}$ continua [315,316,330]. Specifically, the coupling mixes a small amount of the continuum wave functions representing the $3d_{3/2}$ channels with those representing the $3d_{5/2}$ channels [315]. However, this mixing does not occur only between states of the same energy. Thus, the second maximum in the calculated $3d_{5/2}$ cross section does not occur at exactly the same energy as the maximum in the $3d_{3/2}$ cross section [315]. For Xe, the second maximum , in the $3d_{5/2}$ channel, is observed at an energy approximately 3 eV higher than that of the peak in the $3d_{3/2}$ cross section [109].

Given the similarity between the Xe $M_{45}N_{45}N_{45}$ Auger electron yields [109] and those for the I $M_{45}N_{45}N_{45}$ transition measured in the present experiment, it appears reasonable to assert that inter-channel coupling between the I $3d_{5/2}$ and I $3d_{3/2}$ continua is responsible for the maximum observed at 657.4 eV in the M5N45N45 yield. In CH_3I, the second maximum in the $M_5N_{45}N_{45}$ yield is shifted to higher energy by approximately 1.7 eV when compared to the position of the peak in the $M_4N_{45}N_{45}$ yield.

4.5 Conclusions

The total ion yield of CH_3I has been measured using synchrotron radiation in the vicinity of the I $3d_{5/2,3/2}$ thresholds and exhibits broad maxima associated with the $3d \rightarrow \varepsilon f$ shape resonances. In addition, some weak structure, below the ionisation thresholds, can be attributed to transitions into valence or Rydberg states. The corresponding photoabsorption cross section, computed using TDDFT within the Tamm-Dancoff approximation, shows a reasonable agreement with the experimental spectrum and has aided in the assignment of the observed features. The theoretical X-ray absorption spectrum above the ionisation threshold has been simulated using the Stieltjes imaging approach and suggests that transitions into the f(l = 3) continuum channel dominate. This conclusion was independently confirmed by the partial wave resolved photoionisation cross section for the I 3d level in CH_3I, calculated with the CMS-Xα approach.

The complete photoelectron spectrum of CH_3I were recorded at several photon energies and bands due to the C 1s, I 3d, 4s, 4p and 4d atomic-like orbitals, as well as the molecular valence orbitals, were observed and assigned. The photoelectron band associated with the I 4p orbital has an unusual appearance, due to the rapid decay of the $4p^{-1}$ hole state through Coster-Kronig and super-Coster-Kronig transitions. This assignment was based upon interpretations presented in an earlier theoretical study of the analogous Xe 4p photoelectron band. A similar explanation of super-Coster-Kronig transitions can also account for the continuum which appears on the high binding energy side of the peak due to the I 4s orbital.

By utilising plane polarised synchrotron radiation, in two polarisation orientations, it was possible extract the photoelectron anisotropy (β) parameters for the bands due to photoionisation the I 3d orbital. The experimentally derived β parameters were compared to the corresponding theoretical results, calculated using the CMS-Xα approach, and a satisfactory agreement has been found. The I 3d shake-up/shake-off spectrum was recorded and some of the satellite structure was assigned. The β parameters associated with the shake-up/shake-off satellites are similar to those characterising the main photolines.

The $M_5N_{45}N_{45}$ and $M_4N_{45}N_{45}$ Auger electron yields, which are proportional to the I $3d_{5/2}$ and I $3d_{3/2}$ partial photoionisation cross sections, respectively, were measured in the photon energy range encompassing the $3d\rightarrow \varepsilon f$ shape resonances. Each of the Auger yield curves exhibits a maximum associated with the corresponding continuum resonance. In addition, the $M_5N_{45}N_{45}$ decay contains a second maximum due to interchannel coupling between the $3d_{5/2}$ and $3d_{3/2}$ continua. This second maximum in the $M_5N_{45}N_{45}$ yield is shifted to slightly higher energy as compared to the position of the maximum associated with the $3d_{3/2} \rightarrow \varepsilon f$ resonance in the $M_4N_{45}N_{45}$ yield. Similar behaviour was previously reported for the analogous Auger yield in Xe [109].

Chapter 5

Auger electron angular distributions following excitation or ionisation of the I 3d level in CH_3I

5.1 Introduction

The previous chapter discussed the necessity of having a clear understanding of ground state dynamics and spectral properties as a prerequisite for using core level X-ray spectroscopies to monitor ultrafast chemical dynamics. This is point is particularly true for the on-going experimental efforts which utilise Auger electron spectroscopy as a probe of photoexcited molecular systems [288, 335]. Time-resolved Auger spectroscopy, when compared to both X-ray absorption and photoelectron spectroscopy, offers two main advantages. Firstly, the kinetic energies of the emitted Auger electrons are independent of the photon energy used to create the initial core-hole (see Sec. 1.6.1). This has resulted in the technique being amenable to current X-ray FEL sources, which are largely based on self-amplified stimulated emission (SASE). An inherent feature of SASE process (essentially a coherent build-up from noise) is that the X-ray pulse produced from FELs exhibit fluctuations in both central wavelength and spectral line shape [54]. Unlike the first point, which is largely a limitation of current technology, the second relates to the elemental selectivity of X-rays and how they can be applied in a more subtle way to Auger decay. Recent

work by Gühr and coworkers on using Auger decay to track excited state dynamics in the nucleobase thymine highlighted this point clearly and can be summarised as follows [288]. The authors exploited the fact that the Auger decay following oxygen 1s ionisation in thymine must involve the participation of two valence electrons (since oxygen is a first row element) and, given the well localised core-hole, must involve valence transitions at the core site. This specificity allowed the authors to disentangle the roles of $\pi\pi^*$ and nπ^* states in the photochemistry of thymine since the well-localised lone pair state, in particular, gave rise to a unique Auger decay channel. Considerable efforts have also been made to use time-resolved Auger spectroscopy as a probe of photodissociation dynamics in other molecular systems, like methyl halides. However, despite the efforts by a large consortium of people across several X-ray FEL beamtimes, the interpretation of results was hindered by a lack of spectroscopic knowledge of the ground state. With this in mind, presented in this chapter are angularly-resolved electron spectra for the main Auger decay channels following ionisation of the I 3d level in CH_3I. This study,beyond providing spectroscopic assignments which may be useful for FEL experiments, provides detailed information on molecular Auger electron angular distributions - a process which has not been extensively investigated to date.

Conventional Auger electron spectroscopy, where core ionised atoms or molecules are produced by an electron beam or a resonance line photon source, has yielded a wealth of information on electronic structure and lifetimes, and associated decay mechanisms in atomic and molecular systems [90, 100]. The sophistication and versatility of the investigations being performed on Auger decay processes substantially increased with the tunability and polarisation properties of synchrotron radiation [99, 307, 336–338]. However, despite these increased capabilities, the majority of studies on molecular systems have been performed with molecules composed of low atomic number elements, especially carbon, nitrogen and oxygen. This, as outlined above, results in the Auger decay only involving valence electrons. When heavier elements such as iodine are present within a molecule Auger decay can involve inner-shell, inner-valence, and outer-valence electrons, and the

processes thus become far more complex.

The tunability of synchrotron radiation has been utilised extensively in the closely related technique of resonant Auger spectroscopy [99,307,336–338], where photoabsorption in pre-edge region (just below a core level ionisation threshold) initially leads to the formation of neutral core excited state. This intermediate state, comprised of a core hole and an electron promoted into a previously unoccupied orbital, may undergo Auger decay to produce a singly charged ion, where the kinetic energy of the ejected electron is determined by the difference between the neutral intermediate and the final ionic state energies. These resonant Auger decay channels are broadly classified into two categories. The first one, participator Auger decay, is where the initially excited electron is involved in the Auger process and results in a final state with a single hole. The final state of this process is therefore identical to that formed by direct photoionisation: thus, the spectroscopic signature of participator Auger is enhancement of photoemission lines. The second, spectator Auger decay, is where the excited electron behaves as a spectator in the decay and results in a final state with two holes and one electron in the excited orbital. This configuration results in a final state energy higher than that of both normal (non-resonant) and participator Auger decay and, therefore, Auger transitions appear at lower electron kinetic energies than the above two processes [336]. The latter decay mechanism, spectator Auger decay, will be examined extensively for case of CH_3I presented in this chapter.

In terms of molecular physics, one of the early investigations which utilised the continuous wavelength coverage of synchrotron radiation was the seminal work of Morin and Nenner, which examined the competition between Auger emission and molecular dissociation in core excited HBr [339]. This work represented one of the first studies to investigate the role of nuclear motion in inner shell absorption processes/Auger decay in detail, particularly when compared to previous work which mainly inferred details about the nuclear dynamics from energy-energy loss spectroscopy (EELS) [290,340] and photoabsorption measurements [293]. In Morin and Nenner's study, the synchrotron photon energy was tuned to be resonant with the

Br 3d $\rightarrow \sigma^*$ transition, where σ^* refers to an unoccupied antibonding orbital above the neutral ground state. Observed in the recorded electron spectra were several sharp features, which were assigned to autoionisation occurring in atomic bromine and therefore implied that dissociation of the core excited parent molecule occurs on a timescale similar to that of Auger emission (typically a few fs). A subsequent, and closely related, study by the same authors on the I 4d $\rightarrow \sigma^*$ transitions in CH_3I highlighted that instead of sharp atomic autoionisation peaks, the electron spectra were dominated by broad molecular autoionisation features; this demonstrated the role of inertia in molecular fragmentation process [295]. These pioneering studies prompted extensive experimental and theoretical investigations on HCl and other closely related halogen containing molecules. In particular, the Cl 2p $\rightarrow \sigma^*$ and Cl 2p $\rightarrow$ Rydberg excitations were the subject of numerous investigations [341–349]. More recent studies demonstrated (Ref [350] and references therein) that the competition between Auger decay and neutral dissociation is a more general phenomenon, but the rapid fragmentation in the hydrogen halide systems enhances its effects.

While the tunability of synchrotron radiation has been widely used in Auger electron studies, much less use has been made of its polarisation properties. Plane polarised light, when used in conjunction with an electron analyser with a narrow acceptance angle, allows the angular distributions of the Auger electrons to be measured. The angular distributions provide: a means to access specific interference effects [351–353] which cannot be extracted from total decay spectra and additional observable to aid in the assignment of Auger transitions. Auger electron angular distributions have, however, been exploited to investigate core-excited state relaxation dynamics in several diatomics, such as CO [351, 354, 355], NO [353, 356] and O_2 [357], as well as in polyatomic molecules such as C_2H_2 [352], CO_2 [358, 359] and H_2O [360]. These studies, despite being a considerable body of experimental and theortical work, have, however, been limited to molecules with low atomic numbers and, hence, K-shell excitation. The choice of K-shell excitation in these small molecular systems results in a state of well defined symmetry, Σ or Π, and preferentially selects molecules whose molecular axes lie parallel or perpendicu-

lar, respectively, to the photon polarisation vector [361]. This molecular alignment typically results in an anisotropic Auger electron angular distribution.

A different alignment mechanism, namely the non-statistical population of magnetic sublevels, may also lead to anisotropic Auger electron angular distributions in atomic systems [362, 363]. In this chapter, the effects of this latter type of alignment are explored for I 3d Auger emission in CH_3I. This system represented an interesting test case to determine if atomic-like properties are still operative in a polyatomic system. Auger transitions are usually considered within a two-step model [364], where the decay of the core excited (i.e. for resonant Auger) or core ionised atom is assumed to be independent of the initial formation process. Within this framework, the angular distributions of Auger electrons produced by plane polarised radiation, assuming electric dipole photoabsorption by randomly oriented target atoms, may be expressed as [365–367]:

$$\frac{\mathrm{d}W_{J_i\rightarrow J_f}(\theta_{\mathrm{Auger}})}{\mathrm{d}\Omega} = \frac{W_{J_i\rightarrow J_f}}{4\pi}[1+\beta_{\mathrm{Auger}}P_2(\cos\theta_{\mathrm{Auger}})] \tag{5.1}$$

here the form of Eq. 5.1 is broadly similar to that of Eq. 4.1 presented in Chapter 4 but now expressed in terms of the total Auger decay rate, $W_{J_i\rightarrow J_f}$, between initial and final states of total angular momentum J_i and J_f, respectively, θ_{Auger} is the angle between the momentum of the ejected Auger electron and the polarisation axis of the plane polarised radiation (i.e. the alignment axis) and β_{Auger} is a parameter describing the Auger electron angular distribution for a particular transition. Similarly to Eq. 4.1 $P_2(\cos(\theta))$ is the Legendre polynomial of second order. Under the assumption that photoabsorption and Auger decay can be considered as two separate steps, β_{Auger} may be factorised into two distinct components [365, 366]:

$$\beta_{\mathrm{Auger}} = A_{20}\alpha_2 \tag{5.2}$$

where A_{20} is a parameter reflecting the alignment of the core excited/ionic state produced by the photoabsorption in the first step, and α_2 is the intrinsic anisotropy parameter for the Auger transition. Alignment of the photo-induced atomic va-

cancy is possible if J_i is greater than 1/2 for the core-ionised state, this typically results in the anisotropic Auger electron angular distributions [362,363]. The alignment parameter, A_{20}, characterises the anisotropy of the decaying state as a result of a non-statistical population of magnetic sublevels, through initial photoabsorption. These populations are proportional to the photoionisation partial cross sections $\sigma(JM)$, where J is the total angular momentum of the intermediate state and M denotes a particular magnetic sublevel, which typically differ, resulting in alignment. In general, the degree to which alignment can be produced in the core-ionised state varies with photon energy. The intrinsic anisotropy parameter for a specific Auger channel depends on both J_i and J_f, as well as the Auger decay matrix elements, and is independent of photon energy [99, 365]. Anisotropies in Auger electron angular distributions produced from aligned core-ionised states have been studied extensively for the rare gases [99, 307, 362, 363, 367–375] and also compared in detail to theoretical predictions [363, 365–367, 376–381]

In one theoretical study, Berezhko and coworkers investigated the photoionisation induced alignment in core hole states for several rare gas atoms. Their calculations highlighted that, for photoionisation of a state with initial angular momentum l, the degree of alignment depends on the relative strengths of the photoionisation cross sections into the two dipole allowed $l \rightarrow l-1$ and $l \rightarrow l+1$ continuum channels [366]. In general, the $l \rightarrow l+1$ channel dominates the ionization process and the resulting alignment is rather small. However, higher values of alignment were predicted close to the ionization threshold, due to potential barrier effects [382], and in energy regions affected by a Cooper minimum [383], where the $l \rightarrow l-1$ channel dominates due to the change in sign of the $l+1$ matrix element. The latter theoretical prediction was confirmed an experimental study by Snell *et al.* for the $N_{45}O_{23}O_{23}$ transitions in Xe [384]. The data highlighted that significant variation in the A_{20} parameter was observed for photon energies in the vicinity of the Cooper minimum in the Xe 4d photoionisation cross section, due to the vanishing of the Xe $4d \rightarrow \varepsilon f$ continuum channel.

In this study, Auger electron spectra were recorded, using horizontally or

vertically polarised radiation, following either resonant or non-resonant excitation/ionization of the I 3d level in CH_3I. The spectra allowed the Auger electron β_{Auger} anisotropy parameters to be extracted and, for the case of the dominating $M_{45}N_{45}N_{45}$ Auger transitions, compared to the corresponding transitions in Xe. This comparison appears somewhat reasonable as iodine lies adjacent to xenon in the periodic table, and, for the valence shell, CH_3I and Xe are isovalent. For the Auger decay channels considered within this work, an atomic-like description of the initial photoionisation and subsequent Auger decay appears reasonable based on the following arguments. Firstly, the results presented in Chapter 4 on photoionisation of the I 3d in CH_3I highlighted that the ionisation dynamics of this subshell are broadly similar to atomic Xe. Secondly, the binding energies of the atomic orbitals of I are energetically well isolated from those of CH_3. In particular, the binding energies of the C and H orbitals are: C 1s $\sim$290 eV, C 2s/2p $\sim$10-20 eV, and H 1s $\sim$13 eV, whereas those of I are: 3d (M_{45}) $\sim$630 eV, 4d (N_{45}) $\sim$60 eV, and 4s/4p (N_1/N_{23}) $\sim$195/130 eV. Thus, the 4d and more tightly bound I core orbitals should not be significantly involved in the molecular bonding and should appear atomic-like and well localised. Finally, within the narrative of the Auger decay process being treated as a two step process, the first step in, for example, an $M_{45}N_{45}N_{45}$ Auger transition is an I $M_{45}N_{45}$ electron-hole interaction, which should be quite atomic-like, even in a molecular system. Any molecular behaviour would be due to the interaction between the departing N_{45} Auger electron and the delocalised charge distribution of the valence electrons and nuclei.

The above discussion provides support for the M_{45} Auger electron angular distributions to be interpreted as an atomic-like process and hence having their anisotropy being due to the non-statistical population of magnetic sublevels. In order to determine the role of the alignment of the molecular axes, which typically plays a significantly role in molecular systems and may be operative here, Continuum Multiple Scattering (CMS) were utilised to evaluate the spatial distribution of molecular axes in CH_3I in the I $3d^{-1}$ ionised state. The calculation results highlighted that, except in a small energy region close to I 3d ionisation threshold,

the molecular axes in the ionised state are essentially unaligned across the photon energy range considered in this present study. The Auger electron angular distributions emerging from both resonant or non-resonant excitation/ionisation of the I 3d level in CH_3I can be interpreted in a manner usually applied to atomic systems.

The remainder of this chapter is structured as follows. In Sec. 5.2 a brief descriptions of the experimental apparatus and Auger electron fitting procedure are provided. Sec. 5.3 contains all the experimental data, as well as associated discussion. The section is divided into three parts, with subsection 5.3.1 showing an overview of the data, subsection 5.3.2 dealing with assignment of the different Auger decay channels (i.e. $M_{45}N_{45}N_{45}$) and subsection 5.3.3 discussing the Auger electron angular distributions. Finally, the study is summarised in Sec. 5.4.

5.2 Experimental apparatus and procedure

5.2.1 Experimental setup

In contrast to the previous experimental chapters, the apparatus utilised to collect the data reported here is broadly similar to that outlined in Chapter 4, therefore only details relevant to the investigation of the CH_3I Auger electrons are given here.

Auger electron spectra were recorded using the VG Scienta R4000 hemispherical electron energy analyser, mounted on the soft X-ray undulator-based PLÉIADES beamline at the SOLEIL synchrotron radiation facility. The employed undulator allows the plane of polarisation to be chosen to lie either parallel or perpendicular to the entrance of the spectrometer, hence facilitating the collection of angularly resolved spectra.

The electron spectra were recorded with the light source using a grating having 600 lines/mm together with an exit slit width of 70 μm. This combination results in a theoretical optical resolution of approximately 300 meV and 340 meV at the lowest (614 eV) and highest (680 eV) photon energies employed in this study. The Scienta spectrometer was operated with a pass energy of 50 eV and a 0.5 mm curved entrance slit, this resulted in a theoretical spectrometer resolution of 62.5 meV. For an electron kinetic energy of 500 eV, which is appropriate to that of an Auger elec-

tron produced in the $M_{45}N_{45}N_{45}$ decay in CH_3I, the translational Doppler broadening width (see Sec. 4.2.1) is approximately 23 meV.

The angular distribution parameters β were obtained, using similar methods to those outlined in Chapter 4, from the electron intensity for parallel, I_{par}, and perpendicular, I_{perp}, polarisation orientations, respectively.

To calibrate the electron kinetic energy scale, Auger spectra due to the $M_{45}N_{45}N_{45}$ transitions in Xe were recorded. The peak positions of the Auger transitions, shown in Fig. 5.1 and summarised in Table 5.1, were in good agreement with the previously reported energies [119].

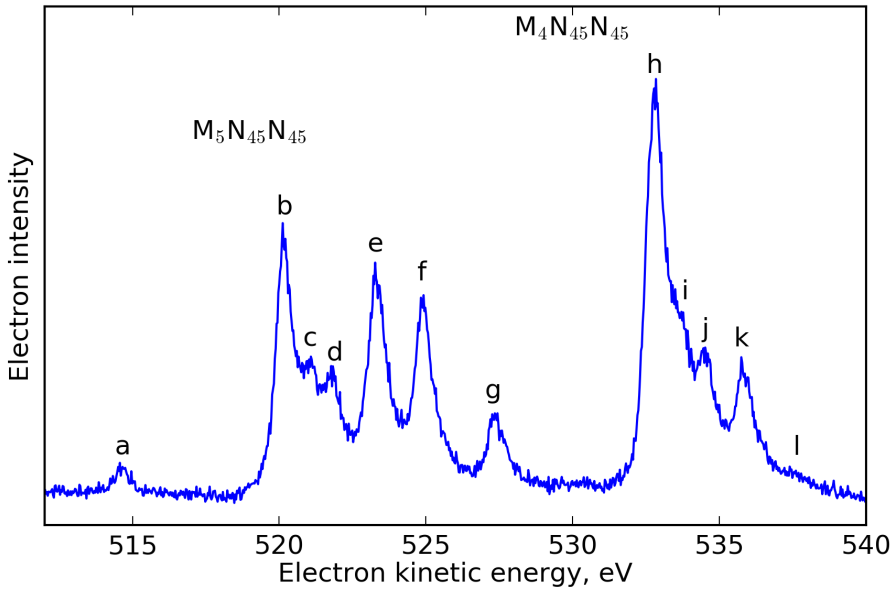

Figure 5.1: The electron spectrum of Xe recorded at a photon energy of 709 eV using vertical plane polarised radiation. The peak structure is associated with $M_{45}N_{45}N_{45}$ Auger transitions and assignments of features are given in Table. 5.1.

In a similar manner to that presented in Chapter 4, the kinetic energy dependent transmission efficiency of the electron analyser was determined using the procedure outlined by Jauhiainen *et al.* [306]. This efficiency is required to normalise the $M_{45}N_{45}N_{45}$ and $M_{45}N_{45}O_{23}$ Auger electron spectra used to evaluate the I $3d_{5/2}$:I

Table 5.1: Experimental Auger electron kinetic energies and final state assignments for the Xe $M_{45}N_{45}N_{45}$ transitions.

Transition	Final state	Peak label	Auger [a] electron kinetic energy (eV)	Auger [b] electron kinetic energy (eV)
$M_5N_{45}N_{45}$	$^1S_0$	a	514.65	514.6
	$^1D_2/^1G_4$	b	520.1	520.1
	$^3P_1/^3P_0$	c	521.1	520.0
	$^3P_2$	d	521.8	521.8
	$^3F_3/^3F_2$	e	523.3	523.3
	$^3F_4$	f	524.85	524.9
$M_4N_{45}N_{45}$	$^1S_0$	g	527.3	527.3
	$^1D_2/^1G_4$	h	532.75	532.7
	$^3P_1/^3P_0$	i	533.7	533.7
	$^3P_2$	j	534.5	534.5
	$^3F_3/^3F_2$	k	535.8	535.7
	$^3F_4$	l	537.5	537.5

[a]Auger electron kinetic energies were estimated from the spectra in Fig. 5.1.
[b]Auger electron kinetic energies obtained from Table III of Werme *et al.* [119].

$3d_{3/2}$ Auger branching ratios (i.e. the partial photoionisation cross section of the $3d_{5/2}$ orbital divided by that of the $3d_{3/2}$ orbital).

5.2.2 Auger electron peak fitting procedure

The peaks associated with the Auger electrons were fitted using the procedure described in detail in Appendix A. This procedure allowed the intensity and the angular distribution parameter (β_{Auger}) due to an individual Auger transition to be derived through a weighted non-linear least-squares fit procedure [385]. As already outlined in Sec. 4.2.2 utilising a fitting routines offers several advantages but, in the particular context of the Auger spectra, it is necessary due to many electron peaks having significant energetic overlap. This is linked to the fact many final states can be populated during the $M_{45}N_{45}N_{45}$ Auger transitions and the initial core-hole width is reasonably broad ($\sim$500 meV).

The Auger electron peak shape resulting from a non-resonant transition ex-

hibits a characteristic tailing on the high kinetic energy side, due to post-collision interaction [307]. This asymmetry was incorporated into our fitting by employing the analytical line shape formula given by Armen *et al* [308]. The total line shape (see Appendix A) is comprised of two more additional components, namely: (i) the final state broadening, associated with $4d^{-2}$ state width and; (ii) the total instrumental Gaussian broadening, due to the broadenings associated with electron analyser and the Doppler contribution.

In the fitting of the non-resonant Auger electron bands, the initial state (PCI) and experimental widths were held fixed, thus the only free width used in fitting was associated with the final, $4d^{-2}$, state. This choice was motivated by the following: (i) the widths associated with $3d^{-1}_{5/2}$ and $3d^{-1}_{3/2}$ core-hole states were extracted from the fits of the photoelectron peaks in Sec. 4.4.2.3 and; (ii) the width related to the Gaussian instrumental broadening can be estimated based on the beamline specifications.

The initial state level widths of 461 and 473 meV were used for the $3d^{-1}_{5/2}$ and $3d^{-1}_{3/2}$ states, respectively. These widths were obtained by averaging the widths extracted from the fits to the I 3d photoelectron peaks (see Fig. 4.11) for photon energies between 655 and 750 eV, corresponding to the region where the use of the atomic PCI line-shape is likely to reasonable (see discussion provided in Sec. 4.4.2.3 and Fig. 4.11). These widths, together with the instrumental broadening, resulted in level widths of 461$\pm$3 meV and 455$\pm$12 meV for the doubly ionized final states associated with the $M_{45}N_{45}N_{45}$ ($4d^{-2}$) and the $M_{45}N_{45}O_{23}$ ($4d^{-1}5p^{-1}$) Auger decays, respectively.

For resonant Auger transitions, the employed lineshape differs from the non-resonant case if the photon bandwidth is narrower than the natural level width of the neutral core-excited state (i.e. $3d^{-1}_{5/2}\sigma^*$ or $3d^{-1}_{3/2}\sigma^*$). This results in the initial state width being replaced by a Gaussian width representing the photon bandwidth [338]. We are not aware of any reported lifetimes of the core-excited valence states but an upper bound estimate can be made through examining the width of the $3d_{5/2} \rightarrow \sigma^*$ transition in the CH_3I ion yield (see Fig. 4.3). A fit of this peak with a Voigt

profile leads to a Lorentzian width of 930 meV, which is significantly larger than 390±20 meV and 450±40 meV obtained for the $3d_{5/2}^{-1}6p$ and $3d_{5/2}^{-1}7p$ Rydberg states in Xe, respectively [373]. This increase in width, when compared to the excited Rydberg states in Xe, can perhaps be linked to the antibonding dissociative nature of the populated σ^* state.

Additionally, the resonant Auger fitting procedure includes a Lorentzian for the final, singly ionized state (e.g. $4d^{-2}\sigma^*$), as this state may decay further by cascade Auger transitions. Final state broadening is typically neglected in the analysis of resonant Auger spectra involving only valence electrons due to the expected long lifetimes of the corresponding final states. Fitting of the $3d_{5/2}^{-1}$ and $3d_{3/2}^{-1}$ spectra yields final state level widths of 480 and 469 meV, respectively. The final state level widths extracted for the non-resonant Auger decay are similar to those extracted for the resonant Auger decay.

5.3 Results and discussion

5.3.1 Overview

In Fig. 5.2, an electron spectrum spanning the kinetic energy range covering all possible Auger decay transitions connected with the I $3d_{5/2}^{-1}$ (M_5) and $3d_{3/2}^{-1}$ (M_4) core-holes is presented. The spectrum was recorded with a photon energy of 666.2 eV and is presented for both the parallel (panel (a)) and perpendicular (panel (b)) polarisation orientations, respectively. The spectrum covering a wider kinetic energy range was assigned in Sec. 4.4.2.1, with features due to direct photoionisation, as well as associated shake-up/shake-off, discussed in detail. Therefore, only features associated with the M_{45} Auger transitions are considered here.

The assignments of the observed Auger electron band structure in CH_3I are based on those given by Werme *et al.* [119], Aksela *et al.* [304], and Pulkkinen *et al.* [386] for the corresponding bands in Xe. In order to examine the photon energy, and, therefore, photoinduced alignment dependence of the M_{45} Auger transitions, spectra similar to those presented in Fig. 5.2 were recorded at multiple photon

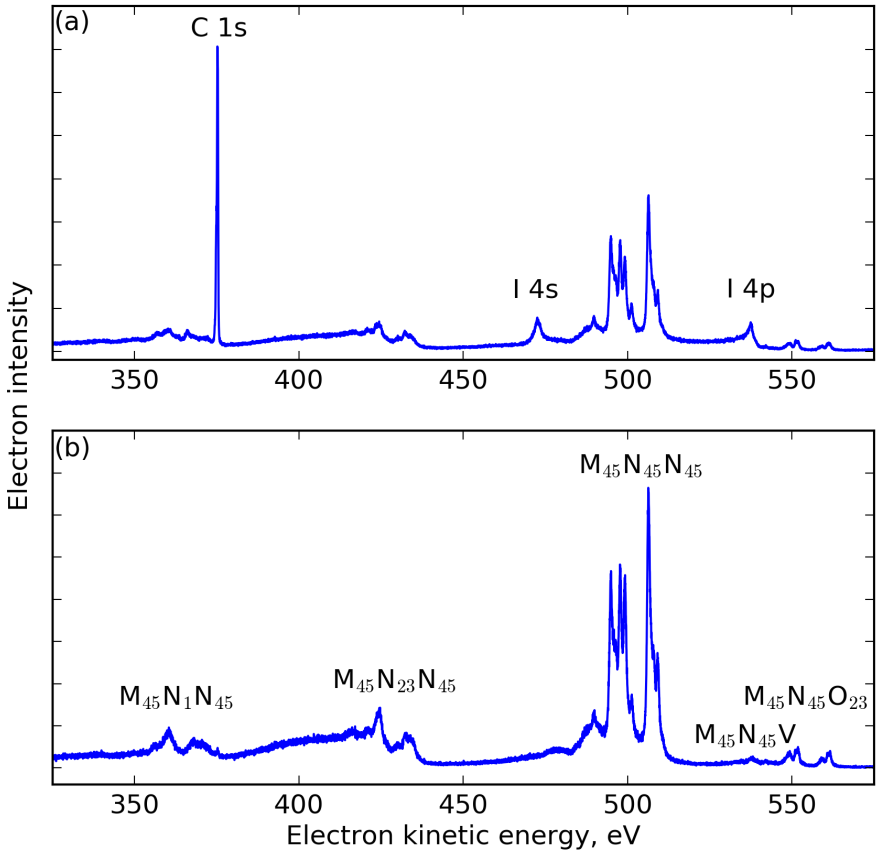

Figure 5.2: The electron spectrum of CH_3I recorded at a photon energy of 666.2 eV using (a) vertical and (b) horizontally polarised radiation. Most of the structure is associated with the $M_{45}N_{45}O_{23}$, $M_{45}N_{45}V$, $M_{45}N_{45}N_{45}$, $M_{45}N_{23}N_{45}$ and $M_{45}N_1N_{45}$ Auger transitions, although some features are due to direct ionization of the I 4p, I 4s, and C 1s orbitals, as well as the associated shake-up/shake-off transitions, are also discernible.

energies (635.8, 640.0, 646.0, 656.0 and 680.0 eV). In addition, resonantly excited Auger spectra were measured at photon energies of 620.4 and 632.0 eV, coinciding with the $3d_{5/2} \rightarrow \sigma^*$ and $3d_{3/2} \rightarrow \sigma^*$ transitions, respectively (see Sec. 4.4.1).

5.3.2 Auger electron band structure

5.3.2.1 $M_{45}N_{45}N_{45}$ transitions

Auger electron spectra encompassing both the $M_4N_{45}N_{45}$ and $M_5N_{45}N_{45}$ de-

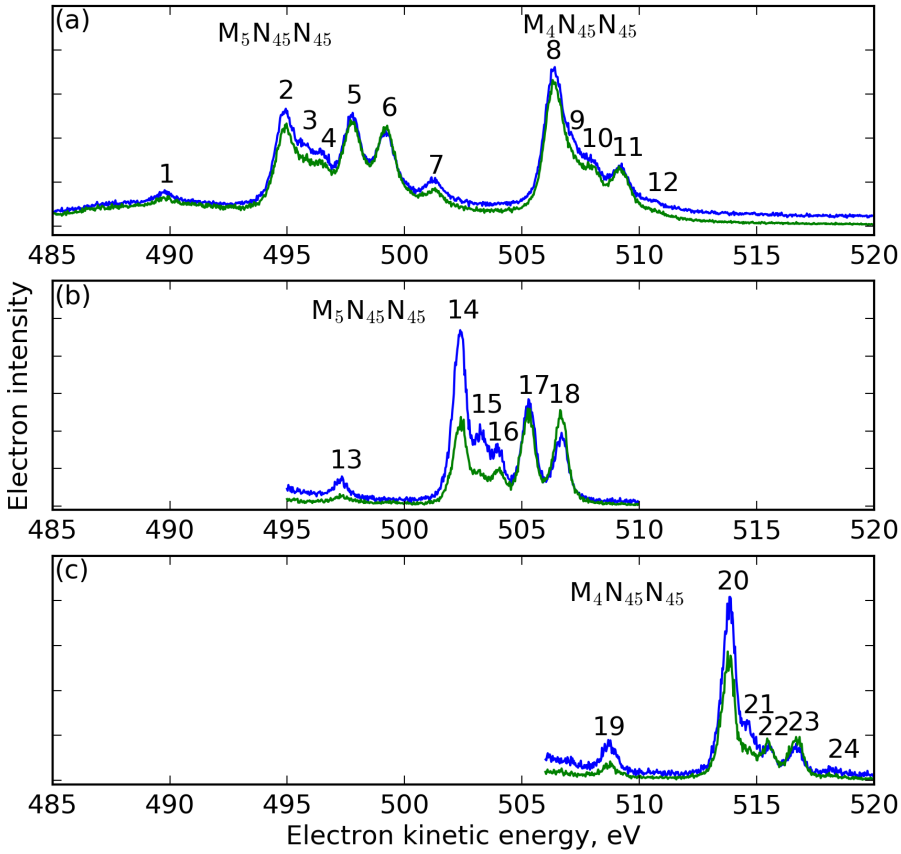

Figure 5.3: Auger electron bands due to the $M_{45}N_{45}N_{45}$ transitions in CH_3I recorded with vertically (blue) and horizontally (green) polarised radiation. The non-resonant Auger spectrum (a) was recorded at $\hbar\omega$ = 666.2 eV, whereas the resonantly excited spectra [(b) and (c)] were measured at $\hbar\omega$ = 620.4 eV and 632.0 eV, corresponding to the $3d_{5/2} \rightarrow \sigma^*$ and $3d_{3/2} \rightarrow \sigma^*$ transitions, respectively. The Auger electron kinetic energies for the peaks numbered 1-24 are given in Tables 5.2 and 5.3.

cay transitions in CH_3I are shown in Fig. 5.3 (non-resonant spectrum recorded at a photon energy of 666.2 eV, and resonantly excited spectra recorded at photon energies of 620.4 and 632.0 eV, using both vertically and horizontally polarised radiation). In order to find intensities and electron kinetic energies of the individual transitions, the weighted least-squares fit described in Sec. 5.2.2 was applied to the spectra. A total of nine two-hole $4d^{-2}$ configurations are accessible as final-states in the $M_{45}N_{45}N_{45}$ Auger decay [304], but due to the rather large broadening ($\sim$500 meV) associated with the $3d^{-1}_{5/2}$ and $3d^{-1}_{3/2}$ core-holes, not all transitions are

resolved, as is evident from Fig. 5.3. Therefore, energetically overlapping transitions were considered as a single line and a total of 6 peaks were used to fit the $M_4N_{45}N_{45}$ and $M_5N_{45}N_{45}$ Auger electron bands.

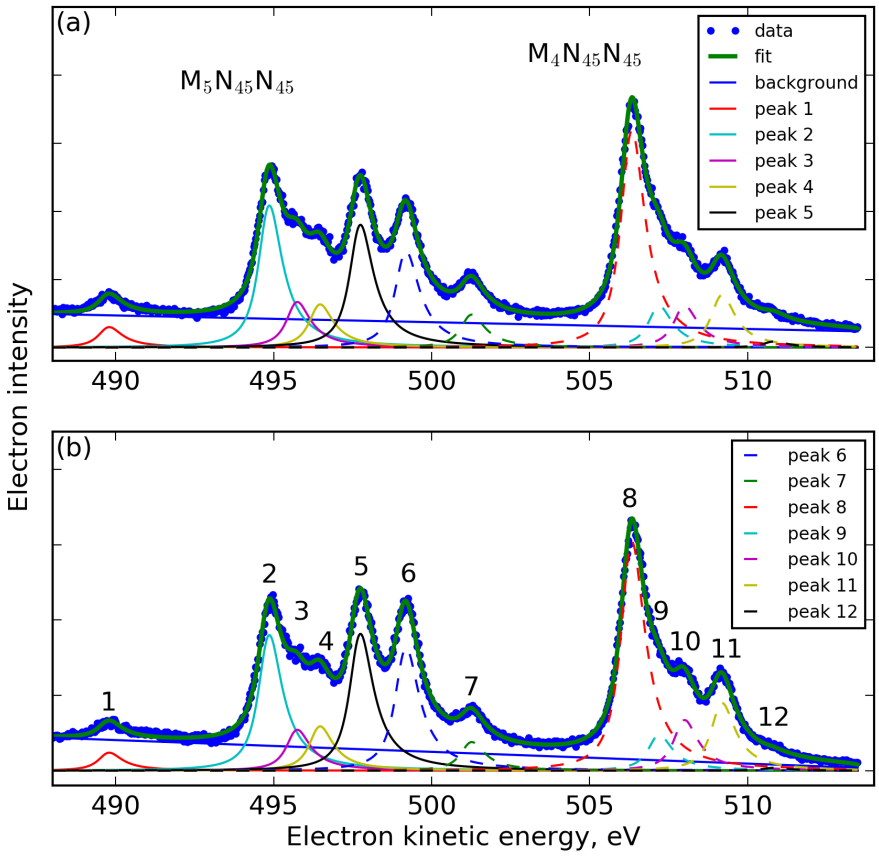

Figure 5.4: Non-resonant Auger electron bands due to the $M_{45}N_{45}N_{45}$ transitions in CH_3I recorded with vertically (a) and horizontally (b) polarised radiation at $\hbar\omega$ = 666.2 eV. The raw and the fitted data are shown (see text for details). The energies and assignments for the individual transitions numbered 1-12 are given in Table 5.2.

In Fig. 5.4, a fit of the Auger spectra recorded at $\hbar\omega$ = 666.2 eV is presented and the electron kinetic energies derived from the fitting procedure are listed in Table 5.2. The assignments were made by analogy with the Xe Auger peaks assigned previously by Aksela *et al.* [304]. The analysis yields electron kinetic energies of

494.72 and 506.20 eV for peaks 2 and 8, respectively, due to the unresolved $^1D_2$ and $^1G_4$ states. These values yield a M_4-M_5 spin-orbit splitting of 11.47±0.02 eV, which is in accord with the value of 11.48±0.01 eV obtained from the photoelectron analysis in the previous chapter and is similar to that of 11.45 eV for the corresponding splitting in I_2 vapour [304].

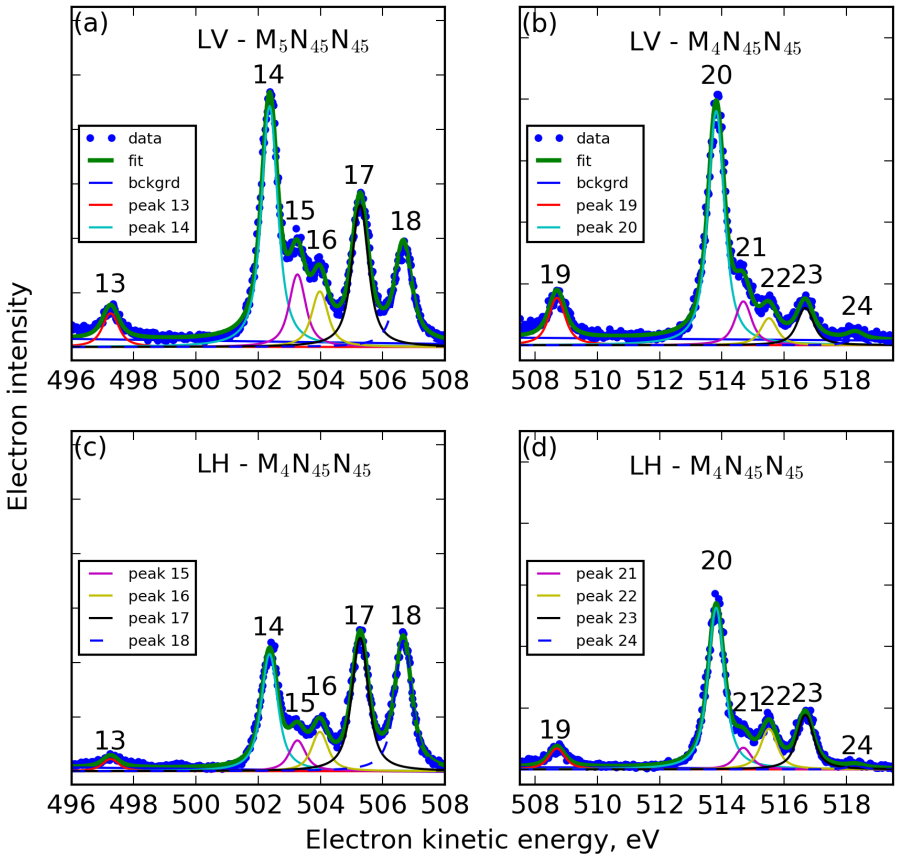

Figure 5.5: Resonant Auger electron spectra recorded at photon energies of 620.4 (panels (a)/(c)) and 632.0 eV (panels (b)/(d)), which coincide with the $3d_{5/2} \rightarrow \sigma^*$ and $3d_{3/2} \rightarrow \sigma^*$ transitions, respectively. The spectra are presented for both the vertical (panels (a)/(b)) and horizontal (panels (c)/(d)) polarised states and fitted using the methodology outlined in Appendix A. The Auger electron kinetic energies and assignments for the peaks numbered 13-24 are listed in Table 5.3.

It is of note that the spectra presented in Fig. 5.4 exhibits a polarisation dependent background on the high kinetic side of the $M_4N_{45}N_{45}$ Auger group, with

enhancement observed with vertically polarised geometry. This discrepancy can be readily attributed to the spectra containing a contribution from the low electron kinetic energy tail of the peak due to direct ionization of the I 4p orbital (see Chapter 4), which has a binding energy of 129.0 eV [296]. Since the photoelectron anisotropy parameter for the I 4p orbital has a value of 1.0 at 666.2 eV (see Sec. 4.4.2.2), the tail from the corresponding photoelectron peak provides a higher background contribution in the spectrum recorded with vertically polarised radiation than in that recorded with horizontally polarised radiation. Despite this, the higher kinetic energy background contributions appears to be satisfactorily taken into account in the fitting procedure (Fig. 3) and is, therefore, unlikely to influence the experimentally derived β_{Auger} values.

Presented in Fig. 5.5 are Auger electron spectra recorded at photon energies of 620.4 and 632.0 eV, corresponding to the $3d_{5/2} \rightarrow \sigma^*$ and $3d_{3/2} \rightarrow \sigma^*$ resonances, respectively. The spectra are shown for both the vertical and horizontal polarisation geometries and presented on the same vertical scale for each resonant Auger spectrum. This highlights the significant polarisation anisotropy for the $M_5N_{45}N_{45}$ and $M_4N_{45}N_{45}$ Auger transitions. Table 5.3 lists the Auger electron kinetic energies and assignments of the resonant Auger peaks. The final states populated during these transitions are singly ionised, with two core-holes and an electron promoted into the σ^* valence orbital, denoted, for example, as $4d^{-2}(^3F_4)\sigma^*$. The Auger electron kinetic energies, following resonant excitation at 620.4 or 632.0 eV, are shifted to higher energy by $\sim$7.62 eV compared to the corresponding values in the non-resonant Auger spectrum (Table 5.2). Finally, similarly to the polarisation dependent background on the high electron kinetic energy side of Fig. 5.3(a), a polarisation dependent background is observed in both resonant Auger spectra at lower kinetic energies (see Fig. 5.3(b) and (c)). This variation is again to contributions associated with the I 4p photoelectron peak which would appear at 491.4 eV and 503 eV for the datasets recorded at $\hbar\omega$ = 620.4 eV and 632.0 eV, respectively.

5.3.2.2 $M_{45}N_{45}O_{23}$ and $M_{45}N_{45}V$ transitions

Table 5.2: Experimental Auger electron kinetic energies and intrinsic anisotropy parameters for the I $M_{45}N_{45}N_{45}$ transitions in CH_3I, and calculated intrinsic anisotropy parameters for the $M_{45}N_{45}N_{45}$ transitions in Xe.

Transition	Final state	Peak number	Auger [a] electron kinetic energy (eV)	β_{Auger} [b,c] (expt)	α_2 [c,d] (expt)	α_2 [e] (calc)
$M_5N_{45}N_{45}$	$^1S_0$	1	489.65	0.151±0.022	-0.718±0.103	-1.069
	$^1D_2$	2	494.72	0.059±0.004	-0.279±0.018	-0.131
	$^1G_4$					-0.719
	$^3P_1$	3	495.60	0.173±0.012	-0.822±0.058	-0.748
	$^3P_0$					-1.069
	$^3P_2$	4	496.33	0.076±0.011	-0.364±0.052	-0.389
	$^3F_3$	5	497.60	0.013±0.004	-0.061±0.017	0.331
	$^3F_2$					-0.222
	$^3F_4$	6	499.04	-0.072±0.004	0.345±0.019	0.378
$M_4N_{45}N_{45}$	$^1S_0$	7	501.13	0.172±0.011	-0.862±0.053	-1.000
	$^1D_2$	8	506.20	0.038±0.003	-0.191±0.014	0.050
	$^1G_4$					-0.653
	$^3P_1$	9	507.06	0.150±0.018	-0.750±0.089	-0.799
	$^3P_0$					-1.000
	$^3P_2$	10	507.87	-0.079±0.011	0.393±0.053	0.378
	$^3F_3$	11	509.06	-0.104±0.006	0.521±0.031	0.432
	$^3F_2$					0.738
	$^3F_4$	12	510.70	0.500±0.0.77	-2.502±0.385	-0.826

[a]Auger electron kinetic energies obtained by fitting the spectrum recorded at $\hbar\omega$ = 666.2 eV.
[b]The average β_{Auger} parameter for the M_5 ($3d_{5/2}^{-1}$) core hole was obtained by averaging the values obtained at six photon energies (635.8, 640.0, 646.0, 656.0, 666.2 and 680.0 eV). The average β_{Auger} parameter for the M_4 ($3d_{3/2}^{-1}$) core hole was obtained by averaging the values obtained at three photon energies (656.0, 666.2 and 680.0 eV).
[c]The quoted uncertainty is due only to electron counting statistics and peak fitting, and does not take any systematic errors into account.
[d]The experimental α_2 parameters were obtained from the experimental β_{Auger} parameters using theoretical values $A_{20}(D_{5/2})$ = -0.21 and $A_{20}(D_{3/2})$ = -0.20.
[e]Calculated α_2 parameters for the $M_{45}N_{45}N_{45}$ transitions in Xe [378].

The highest energy Auger transitions are located between 530 and 570 eV and based on energetics must involve at least one of the CH_3I valence electrons. In Fig. 5.6, Auger spectra are presented across this energy range for two photon energies, namely 666.2 eV and 646 eV. The structure of Auger groups in the kinetic

Table 5.3: Experimental Auger electron kinetic energies, β_{Auger} parameters and intrinsic anisotropy parameters (α_2) for the I $M_{45}N_{45}N_{45}$ transitions in CH_3I following resonant excitation at 620.4 eV ($3d_{5/2} \rightarrow \sigma^*$) or 632.0 eV ($3d_{3/2} \rightarrow \sigma^*$)

Transition and final state	Peak number	Auger electron kinetic energy (eV)	β_{Auger} [a] (expt)	α_2 [a,b] (expt)
I $3d_{5/2}^{-1}\sigma^* \rightarrow 4d^{-2}\sigma^*$ [c]				
$4d^{-2}(^1S_0)\sigma^*$	13	497.26	0.741±0.056	-0.524±0.040
$4d^{-2}(^1D_2+^1G_4)\sigma^*$	14	502.36	0.520±0.016	-0.368±0.011
$4d^{-2}(^3P_{0,1})\sigma^*$	15	503.26	0.624±0.044	-0.441±0.031
$4d^{-2}(^3P_2)\sigma^*$	16	503.98	0.241±0.037	-0.170±0.026
$4d^{-2}(^3F_2+^3F_3)\sigma^*$	17	505.28	0.042±0.015	-0.030±0.011
$4d^{-2}(^3F_4)\sigma^*$	18	506.66	-0.189±0.015	0.134±0.011
I $3d_{3/2}^{-1}\sigma^* \rightarrow 4d^{-2}\sigma^*$ [d]				
$4d^{-2}(^1S_0)\sigma^*$	19	508.70	0.595±0.042	-0.421±0.029
$4d^{-2}(^1D_2+^1G_4)\sigma^*$	20	513.82	0.260±0.014	-0.184±0.010
$4d^{-2}(^3P_{0,1})\sigma^*$	21	514.69	0.507±0.061	-0.359±0.043
$4d^{-2}(^3P_2)\sigma^*$	22	515.51	-0.253±0.036	0.179±0.025
$4d^{-2}(^3F_2+^3F_3)\sigma^*$	23	516.68	-0.234±0.026	0.165±0.018
$4d^{-2}(^3F_4)\sigma^*$	24	518.29	0.534±0.159	-0.378±0.112

[a]The quoted uncertainty is due only to electron counting statistics and peak fitting, and does not take any systematic errors into account.
[b]The experimental α_2 parameters were obtained from the experimental β_{Auger} parameters using $A_{20} = -\sqrt{2}$.
[c]Auger electron kinetic energies and β_{Auger} parameters obtained by fitting the resonantly excited spectrum recorded at $\hbar\omega$ = 620.4 eV.
[d]Auger electron kinetic energies and β_{Auger} parameters obtained by fitting the resonantly excited spectrum recorded at $\hbar\omega$ = 632.0 eV.

energy range ∼545-565 eV resembles to some extent the $M_{45}N_{45}O_{23}$ transitions in both I_2 [304] and Xe [386]. Based on the calculated $M_{45}N_{45}O_{123}$ spectrum in Xe [386], the two pairs of doublets we observe at kinetic energies of approximately 550 and 560 eV in CH_3I likely correspond to the $M_{45}N_{45}O_{23}$ transitions. A fit to the $M_4N_{45}O_{23}$ and $M_5N_{45}O_{23}$ transitions (not shown) made use of five peaks for each of the Auger groups, based on the assignments of the analogous structure in Xe [304, 386]. The electron kinetic energies derived from a fit of the spectra recorded at 666.2 eV are listed in Table 5.4. In the resonantly excited spectrum recorded at $\hbar\omega$ = 620.4 eV (not shown), a peak appearing at an electron kinetic energy of

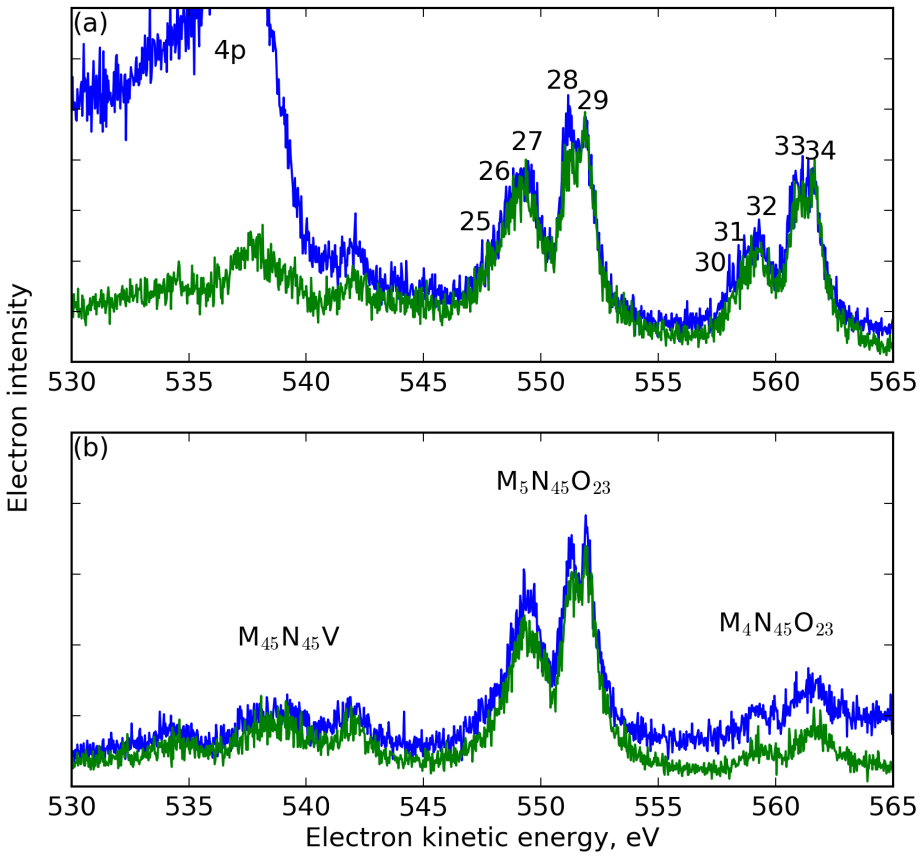

Figure 5.6: The non-resonant Auger spectrum of CH_3I showing bands due to the $M_{45}N_{45}O_{23}$ and $M_{45}N_{45}V$ transitions. The spectra are presented for (a) $\hbar\omega$ = 666.2 eV and (b) $\hbar\omega$ = 646 eV for both vertical (blue) and horizontal (green) polarised radiation. The lower kinetic energy $M_{45}N_{45}V$ transitions are obscured in panel (a) due to significant spectral overlap with the peak due to I 4p photoionisation but are clearly discernible in panel (b). The energies for the peaks numbered 25-34 are given in Table 5.4. Note that due to low photoionisation cross section (see Figs. 4.3 and 4.6) transition involving the M_4 initial state appear weak in panel (b).

558.35 eV probably corresponds to the unresolved contributions from peaks 28 and 29 (Table 5.4). Thus, the $M_{45}N_{45}O_{23}$ peaks are shifted by approximately 6.9 eV to higher energy in the resonantly excited Auger spectrum.

The broader and weaker structures observed in Fig. 5.6 between approximately 530-545 eV likely arise from transitions involving molecular valence orbitals. Note that the relatively intense peak at 537.8 eV in the spectrum recorded at $\hbar\omega$ =

666.2 eV contains a contribution from photoelectrons emitted from the I 4p level. To clearly identify features only due to Auger transitions, a section of an electron spectrum recorded at $\hbar\omega$ = 646.0 eV is also shown. At this photon energy, the 4p photoline is observed at 517 eV, which is outside the electron kinetic energy range shown in Fig. 5.6. Three broad peaks are observed at kinetic energies of 534.5, 538.7 and 542.1 eV which, based on their broad structure and appearance at higher binding energies than the $M_{45}N_{45}O_{23}$ transitions, are assigned to Auger decays involving molecular valence orbitals.

In order to obtain a better understanding of the CH_3I M_{45} Auger decays involving the iodine O-shell, atomic population of the valence orbitals were determined from electronic structure calculations, using a MP2/3-21G with Gaussian 09 [387]. Note that these calculations were performed by Ivan Powis (University of Nottingham). The results indicate that the two components of the 2e HOMO, which should therefore produce the highest kinetic energy Auger electrons, are nearly pure iodine p_x and p_y atomic orbitals. This is assignment is consistent with VUV photoelectron spectroscopy studies which show that the observed spin-orbit splitting (628 meV) in the $(2e)^{-1}$ band is similar to that of atomic iodine (629 meV) [94]. Furthermore, angle-resolved photoelectron spectroscopy measurements by Holland *et al.* highlighted that the PADs associated with 2e HOMO in CH_3I exhibit a photon energy dependence reminiscent of that predicted for the atomic I 5p Cooper minimum [97].

The calculations also demonstrated that there exists no atomic-like molecular orbital for iodine 5s, which can interact with the C, and possibly the H, atomic orbital in all the molecular orbitals possessing a_1 symmetry. The next lower-lying (HOMO-1) orbital may be characterised as a C-I σ-bonding orbital. This assignment appears to be in agreement with previous He I PEPICO [388], as well as synchrotron mass spectrometry studies [334, 389], where fission of the C-I bond is observed for removal of a HOMO-1 electron. The lowest-lying valence orbitals, $1a_1$ and $2a_1$, may be regarded as a σ/σ^* (bonding/antibonding) pair formed by the interacting I 5s and C 2s/$2p_z$ atomic orbitals. These characterisations of the valence shell molecular orbitals in terms of the atomic contributions are in accord with

those reported by Pernpointner *et al.* [390]. In particular, this work highlight that I 5p atomic populations account for over 90% of both components of the HOMO orbital. Plots of the valence orbitals are shown in the supplementary material of the publication that resulted from the work outlined in this chapter [391].

These predictions rationalise the evident similarity between the $M_{45}N_{45}O_{23}$ transitions in CH_3I and the corresponding transitions in Xe, justifying the atomic-like labeling choice of O_{23} despite the involvement of a valence orbital within a molecule. The calculations also indicate that the lack of structure observed at lower kinetic energy Auger transitions ($\sim$530-545 eV) is partially due to the lack of atomic-like character of the more deeply bound (bonding) valence orbitals. In addition, the lack of I atomic-like character in the HOMO-1, and deeply bound valence orbitals, probably accounts for the lack of oscillator strength in these transitions. Since these molecular orbitals are not well-localised on the iodine site, they will have little overlap with 3d (M_{45}) and 4d (N_{45}) electron density. The opposite is true for the I 5p doubly degenerate orbital.

Table 5.4: Auger electron kinetic energies for the iodine $M_{45}N_{45}O_{23}$, $M_{45}N_{23}N_{45}$ and $M_{45}N_1N_{45}$ transitions in CH_3I

M_5 Transition	Peak Number	Auger electron kinetic energy (eV)	M_4 Transition	Peak Number	Auger electron kinetic energy (eV)
$M_5N_{45}O_{23}$	25	547.82	$M_4N_{45}O_{23}$	30	558.02
	26	548.74		31	558.69
	27	549.46		32	559.29
	28	551.10		33	560.79
	29	551.87		34	561.55
$M_5N_{23}N_{45}$	35	415.6	$M_4N_{23}N_{45}$	40	430.3
	36	417.0		41	432.36
	37	421.1		42	433.8
	38	423.72		43	434.73
	39	434.73			
$M_5N_1N_{45}$	44	356.4	$M_4N_1N_{45}$	46	367.9
	45	360.4		47	370.5

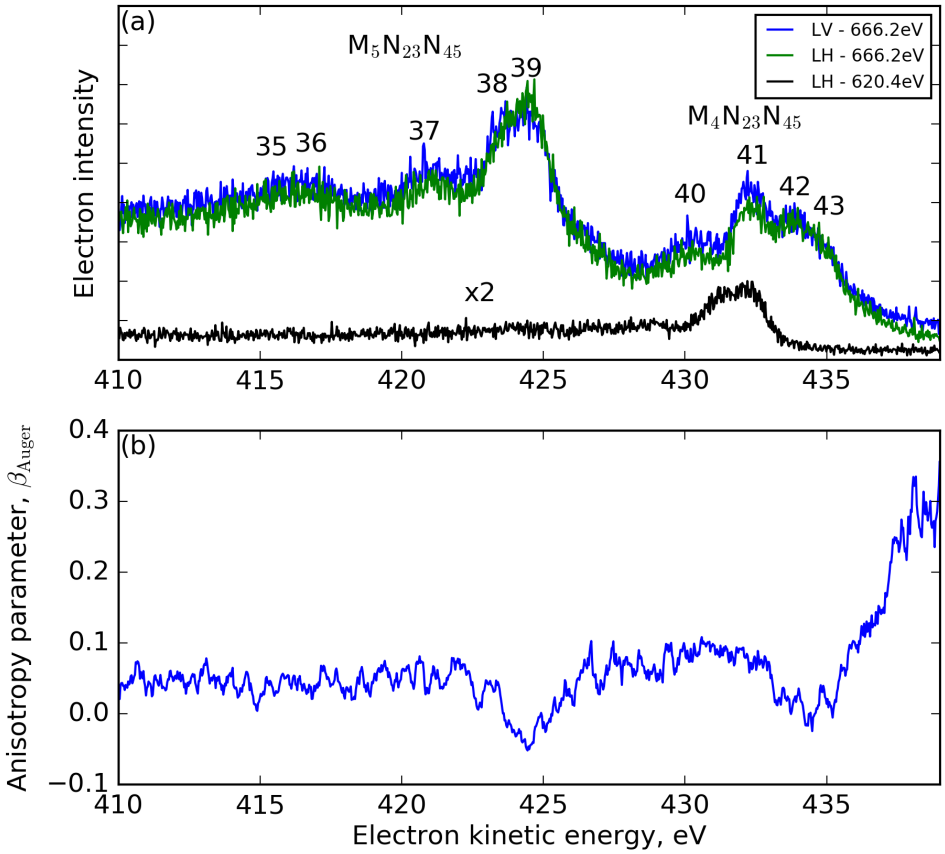

Figure 5.7: (a) Auger electron bands due to the $M_{45}N_{23}N_{45}$ transitions in CH_3I recorded at 666.2 eV using vertically (LV - blue) and horizontally (LH - green) polarised radiation, and at 620.4 eV using horizontally (black) polarised radiation. The spectra recorded with vertical polarised spectra at 620.4 eV was dominated by the photoelectron peak due to photoionisation of the I 4s orbital and is hence omitted for clarity. The energies for the peaks numbered 35-43 are given in Table 5.4. (b) The anisotropy parameter, β_{Auger}, for the $M_{45}N_{23}N_{45}$ transitions derived from the vertically and horizontally polarised spectra recorded at $\hbar\omega$ = 666.2 eV. A 10-point moving average has been applied to improve the signal-to-noise ratio.

5.3.2.3 $M_{45}N_{23}N_{45}$ transitions

Presented in Fig. 5.7 are resonant (620.4 eV) and non-resonant (666.2 eV) Auger spectra in the electron kinetic energy range spanning the $M_{45}N_{23}N_{45}$ transitions. The resonantly excited spectrum recorded with vertically polarised radiation was omitted from the figure due to being dominated by a peak arising from direct

ionisation of the I 4s level. However, this peak is absent in the spectra recorded with horizontally polarised radiation since the β parameter for the 4s electron is $\sim$2. The non-resonant Auger spectrum appears to show five peaks due to $M_5N_{23}N_{45}$ transitions and four peaks due to the $M_4N_{23}N_{45}$ transitions. Assignment of the individual transitions observed in Fig. 5.7 proved challenging despite knowledge of the calculated Auger electron energies and relative line intensities for the corresponding transitions in Xe [304, 380]. This is, in part, due to inconsistencies in the predicted ordering of the final states for the $M_{45}N_{23}N_{45}$ in Xe. The kinetic energies of the transitions observed for $M_{45}N_{23}N_{45}$ Auger transitions are summarised in Table 5.4. For the resonantly excited Auger spectrum, two peaks were observed at 431.39 and 432.11 eV. These correspond to peaks 38 and 39, associated with the $M_5N_{23}N_{45}$ transitions, shifted to higher kinetic energies by 7.67 and 7.64 eV, respectively.

In addition to the well-resolved Auger transitions observed in Fig. 5.7(a) ($\sim$415-435 eV), there exists a broad underlying continuum which extends towards lower electron kinetic energies (see Fig. 5.2). The continuum exhibits a structure reminiscent of the usual appearance of the photoelectron band associated with the I 4p orbital in CH_3I. This origin of this was discussed in detail in Sec. 4.4.2.2 of the previous chapter. Briefly, the anomalous intensity distribution of the photoline was ascribed to the rapid decay of the inner-shell hole state through Coster-Kronig and super-Coster-Kronig processes, as previously observed [299] and predicted [326] for the 4p orbital in Xe. It therefore appears reasonable to evoke a similar explanation for the the continuum underlying the Auger electron peaks due to the $M_{45}N_{23}N_{45}$ transitions.

5.3.2.4 $M_{45}N_1N_{45}$ transitions

The Auger electrons band due to $M_{45}N_1N_{45}$ transitions encompass a kinetic energy range of $\sim$350-380 eV. In Fig. 5.8(a) we show the resonantly excited spectra (620.4 and 632.0 eV) and non-resonant spectrum (666.2 eV) recorded with horizontally polarised radiation. In the corresponding spectra (not shown) recorded with vertically polarised radiation, significantly more structure was observed due to

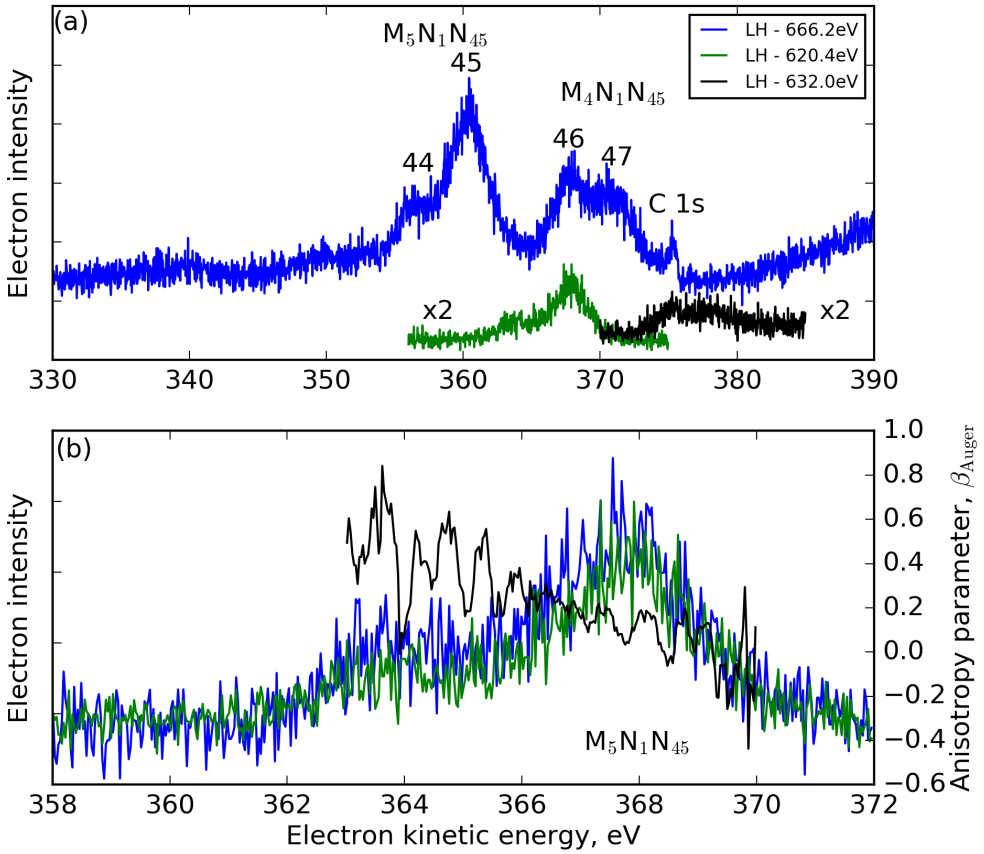

Figure 5.8: (a) Auger electron bands due to the $M_{45}N_1N_{45}$ transitions in CH_3I recorded using horizontally polarised radiation. Spectra are shown for both the non-resonant ($\hbar\omega = 666.2$ eV) and resonantly excited ($\hbar\omega = 620.4$ eV and 632.0 eV) cases. A summary of the kinetic energies for the peaks numbered 44-47 is provided in Table 5.4. Note, at $\hbar\omega = 666.2$ eV the vertical polarised spectra was omitted due significant overlap with the C 1s photoelectron peak and associated satellite structure. For further details see main text. (b) β_{Auger} (black) for the $M_5N_1N_{45}$ transition derived from the vertically (blue) and horizontally (green) polarised spectra measured at 620.4 eV. A 10-point moving average was applied to improve the signal-to-noise ratio. β_{Auger} values are omitted in regions of low electron intensity.

direct ionisation of the C 1s orbital and the associated satellite (shake-up/shake-off) states. The contributions associated with C 1s ionisation can be readily disentangled from features connected with Auger transitions due the C 1s main-line and the shake-up spectrum possessing a β of $\sim$2, whereas the anisotropy parameter associated with the $M_{45}N_1N_{45}$ Auger electrons will be close to zero. Hence, a comparison

between the spectra recorded with vertically or horizontally polarised radiation allows the Auger electron peaks to be distinguished.

In the non-resonant Auger electron spectrum, a broad doublet is assigned to each of the $M_4N_1N_{45}$ and $M_5N_1N_{45}$ transitions. The electron kinetic energies corresponding to these four peaks are listed in Table 5.4. In the spectra recorded at a photon energy corresponding to the $3d_{5/2} \rightarrow \sigma^*$ resonance at 620.4 eV, the peaks observed at 363.7 and 367.8 eV correspond to peaks 44 and 45 shifted by 7.3 and 7.4 eV, respectively, to higher kinetic energy. Similarly, in the resonant spectrum recorded with $\hbar\omega$ = 632.0 eV (i.e. coinciding with the $3d_{3/2} \rightarrow \sigma^*$), peaks 46 and 47 are shifted by 7.4 and 7.2 eV, respectively, and appear at kinetic energies of 375.3 eV and 377.7 eV. In terms of assignments of the doublets associated with the $M_5N_1N_{45}$ transitions, it is conceivable that the more intense higher energy component (360.4 eV) should be associated with the $^3D_3$ and $^3D_2$ states which, in Xe [380], are calculated to have high relative intensities, whilst the weaker component, observed at 356.4 eV, should be associated with the $^3D_1$ and $^1D_2$ states which are predicted to have lower relative intensities. Verification of these assignments would, however, benefit from additional calculations for atomic I and experimental investigation of the corresponding transitions in HI.

5.3.2.5 M_{45} Auger electron and I $3d_{5/2,3/2}$ photoelectron branching ratios

In fitting the experimental $M_{45}N_{45}N_{45}$ and $M_{45}N_{45}O_{23}$ Auger spectra a peak amplitude that contained both angularly independent and dependent terms (see Appendix A), where the former is the total Auger decay rate, or cross section, for a particular transition/final state were included. Extraction of the total decay rates for the transitions within both the M_4 and M_5 Auger group permitted the $M_4N_{45}N_{45}$:$M_5N_{45}N_{45}$ and $M_4N_{45}O_{23}$:$M_5N_{45}O_{23}$ Auger electron branching ratios to be evaluated. At each photon energy, all Auger lines produced by transitions of the M_4 and M_5 core-holes to the same CH_3I^{2+} final states were used to evaluate the

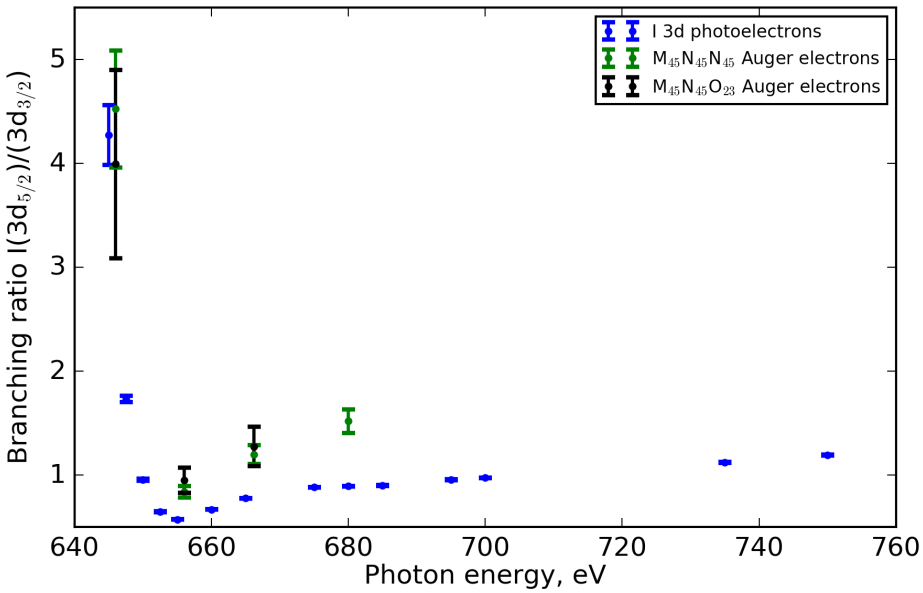

Figure 5.9: Branching ratios for the $M_4N_{45}N_{45}$:$M_5N_{45}N_{45}$, $M_4N_{45}O_{23}$:$M_5N_{45}O_{23}$ Auger transitions compared with the I $3d_{5/2}$:$3d_{3/2}$ photoelectrons.

branching ratio, with the exception of 680 eV where the $^1S_0$ state was omitted due to the recorded spectra covering an insufficient electron kinetic energy range.

These ratios are plotted in Fig. 5.9, together with that for the I $3d_{5/2}$:$3d_{3/2}$ photoelectrons (see Fig. 4.13). The $M_4N_{45}N_{45}$:$M_5N_{45}N_{45}$ and $M_4N_{45}O_{23}$:$M_5N_{45}O_{23}$ branching ratios exhibits a similar photon energy dependence as the corresponding photoelectron branching ratio. This result is expected if no variation occurs between the decay channels for the two spin-orbit split vacancies, i.e., there is no photon energy dependence in the branching ratios for transitions to the various CH_3I^{2+} final states.

Finally, although the photon energy dependence is similar, there is a clear discrepancy in vertical offset between the Auger and photoelectron branching ratios. It is, however, reasonable to assume this discrepancy is associated with the photo rather than Auger electrons, based on the following:

- The Auger electrons transitions observed following I 3d ionisation in CH_3I were all at relatively high (300-600 eV) electron kinetic energies. These energies coincide with a region where one would expect the transmission of the

spectrometer to be essentially flat (i.e. little variation as a function of electron kinetic energy), particularly across 11.6 eV energy difference, corresponding to the I $3d_{5/2}$-I $3d_{3/2}$ spin-orbit splitting observed between different core-hole state within the same Auger group.

- For each pass energy utilised in the study, a corresponding transmission function for the electron spectrometer (see Sec. 5.2.1) was required. This means for the case of photoelectrons, multiple different transmission functions were required and applied to the data in order to achieve the branching ratio spectra presented in Fig. 4.13. This decision to use multiple pass energies was motivated by a desire to achieve reasonable resolution across broad range of photoelectron kinetic energies. For the Auger spectra, however, only a single pass energy was used, meaning one transmission function was used for all data presented in Fig. 4.13).

- Finally, unlike the photoelectrons, the Auger electrons are inherently independent of photon energy meaning that, apart from the 11.6 eV difference between M_4 and M_5 Auger groups, there is no change to the energy dependent transmission function as the photon energy is scanned.

Based on the above points, it likely that the discrepancy between the photoelectron and Auger branching ratios stems from inaccurate determination of the kinetic energy dependent transmission function of the SCIENTA spectrometer provided by SOLEIL beamline scientists.

5.3.2.6 Shift in Auger electron kinetic energies between non-resonant and resonantly excited spectra

The experimental results shown in Secs. 5.3.2.1-5.3.2.4 highlighted that the electron kinetic energies connected with the $M_{45}N_{45}N_{45}$, $M_{45}N_{23}N_{45}$ and $M_{45}N_1N_{45}$ Auger decay channels are shifted to higher energy by $\sim$7.6, 7.7 and 7.3 eV in the resonantly excited spectra when compared to the corresponding energies in the non-resonant spectra. A shift is also observed, albeit a smaller one (6.9 eV), for the

$M_{45}N_{45}O_{23}$ transitions. These shifts arise from the screening provided by the electron excited into the σ^* orbital. In order to help determine the origin of the differences in kinetic energy shifts between each group of Auger transitions, calculations of the orbital ionisation energies of CH_3I^+ with a hole in the I 3d shell and neutral CH_3I with a 3d electron excited into the σ^* orbital (i.e. $3d^{-1}\sigma^*$) were performed. In these calculations, performed by Nick Besley (University of Nottingham) using the Q-chem software package [392], transitions energies were determined using a Δ self-consistent field approach with the ground and excited state energies computed using DFT with the B3LYP exchange-correlation functional [393] with the 6-311G** basis set. The maximum overlap method [311, 394] was used to prevent variational collapse in the calculation of the core excited states. Presented in Table 5.5 is a summary of the state binding energies relevant for the Auger decay channels considered in this work. Full details of addition state binding energies and associated orbital plots are shown in the supplementary material of Ref. [391].

Table 5.5: Theoretical orbital ionisation energies for I 3d ionised and I 3d core excited states ($3d^{-1}\sigma^*$) in CH_3I

Orbital	Ionisation energy (eV)		
	I 3d ionised state [a]	I 3d excited state [b]	Difference (eV)
N_1	199.31	191.65	7.66
N_{23}	154.41	146.85	7.56
N_{45}	78.10	70.46	7.64
$1a_1$	28.05	20.37	7.68
$2a_1$	31.20	23.50	7.7
1e	21.62	14.17	7.45
$3a_1$	20.80	12.99	7.81
2e	18.71	11.68	7.03

[a]The ionised state corresponds to a hole in the I 3d shell
[b]The neutral excited state corresponds to an I 3d electron excited into the σ^* orbital (i.e. $3d^{-1}\sigma^*$)

The kinetic energies of Auger transitions following non-resonant photoabsorption can be estimated by using the measured value for the ionisation energy (626.8 eV) of the $3d_{5/2}$ orbital (see Chapter 4) and the calculated ionisation energy of 78.1 eV for the N_{45} orbital in ionised CH_3I with a 3d hole. This leads to an

estimated Auger electron kinetic energy of 470.6 eV for the $M_5N_{45}N_{45}$ transitions. Similarly, the kinetic energies of the resonant Auger transitions can be approximated using the experimental value of 620.4 eV for the excitation energy of the $3d_{5/2} \rightarrow \sigma^*$ transitions, and the calculated ionisation energy of 70.5 eV for the N_{45} orbital in CH_3I $3d^{-1}\sigma^*$. This results an estimated Auger electron kinetic energy of 479.4 eV for the $M_5N_{45}N_{45}$ transitions. The resulting shift, based on the calculated ionisation energies, is 8.8 eV, compared to the experimental value of 7.6 eV. Thus, despite the estimated Auger electron kinetic energies being somewhat lower than the experimental values ($\sim$25 eV), determination of the shift, between the resonant and non-resonant Auger spectra, from theoretical orbital ionisation energies in 3d excited and 3d ionised CH_3I appears somewhat reasonable. Application of the same procedure to the $M_5N_{23}N_{45}$ and $M_5N_1N_{45}$ transitions results in estimated shifts of 8.7 and 8.8 eV, respectively. The corresponding experimental values were approximately (depending on the peak analysed) 7.65 and 7.35 eV, respectively. In spite of the $\sim$1 eV shift between calculated and experimentally measured values, the calculations do reproduce the observation that little variation in the shifts is seen between the $M_5N_{45}N_{45}$, $M_5N_{23}N_{45}$ and $M_5N_1N_{45}$ transitions. Finally, for the $M_5N_{45}O_{23}$ transitions an estimated shift of 8.2 eV was extracted. This value appears to be in accord with smaller observed shift of 6.9 eV. Therefore, the predicted and measured shifts in the Auger electron kinetic energies appear to follow the same trends.

5.3.3 Auger electron angular distributions

The theoretical investigation carried out by Berezhko *et al.* [366] showed that, in the non-relativistic limit, the alignment (A_{20} parameters) resulting from inner shell photoionisation of an atomic d orbital can be expressed as [395]:

$$A_{20}(D_{5/2}) = \frac{-2}{5}\sqrt{\frac{2}{7}}\frac{(1+\frac{7}{2}\gamma)}{(1+\gamma)} \tag{5.3}$$

$$A_{20}(D_{3/2}) = \frac{-1}{5}\frac{(1+\frac{7}{2}\gamma)}{(1+\gamma)} \tag{5.4}$$

$$\gamma = \frac{2}{3}\frac{R^2_{3d\rightarrow\varepsilon p}}{R^2_{3d\rightarrow\varepsilon f}} \tag{5.5}$$

where $R_{3d\rightarrow\varepsilon p}$ and $R_{3d\rightarrow\varepsilon f}$ denote the radial dipole matrix elements for photoionisation of the 3d electrons into the p (l-1) and f (l+1) continua, respectively.

For the non-spherical potential of a molecule, a considerably larger number of partial waves are expected to contribute to both the cross section and angular distribution. However, as was made evident in Chapter 4, the photoionisation dynamics of the 3d orbital in CH_3I are fairly atomic-like. The partial wave resolved photoionisation cross section (see Fig. 4.6) demonstrated that, apart from in the near-threshold region the l = 3 partial wave dominates, the total I 3d photoionisation cross section. This is in accord with the expectation from atomic photoionisation, where the l = 3 cross section is expected to be much larger than the l = 1 cross section, except close to threshold where the l = 3 component is suppressed by the centrifugal barrier in the effective potential [382].

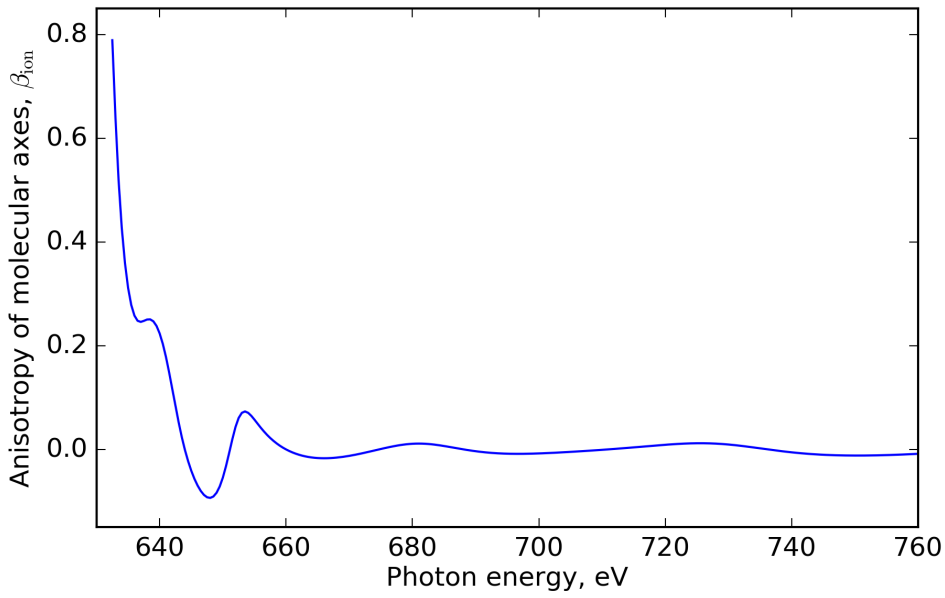

Figure 5.10: The calculated, normalised, angular distribution parameter (β_{ion}) characterising the spatial distribution of molecular axes in CH_3I in the I $3d^{-1}$ ionised state.

Using the same photoionisation calculations, it is also possible to determine the contributions to the alignment associated with the molecular axes rather than the non-statistical population of magnetic sublevels. Here the spatial distribution of molecular axes, $I(\theta)$, in the I $3d^{-1}$ core-ionised state can be evaluated from a rotation of the molecular frame dipole matrix elements into the lab frame, and integration over all azimuthal orientation and all electron emission directions. The alignment of molecular axes can be expressed as a distribution having the form [396]:

$$I(\theta_{\text{ion}}) = 1 + \beta_{\text{ion}} P_2(\cos(\theta_{\text{ion}})) \tag{5.6}$$

where β_{ion} is the normalised angular distribution parameter, $P_2(\cos(\theta_{\text{ion}}))$ is a second order Legendre polynomial and θ_{ion} is the angle between the polarisation axis of the plane polarised radiation and the principle molecular axis (C-I axis in CH_3I). The results of these calculations, shown in Fig. 5.10, highlight that, apart from in a small energy range close to the ionisation threshold, the molecular axes in the core-ionised state are not aligned to any significant extent.

For the remainder of this section, it is assumed that the Auger electron angular distributions, following either excitation or ionisation of the I 3d electron in CH_3I, can be treated largely as an atomic phenomenon and that Eqs. 5.3 - 5.5 are applicable. This assumption appears valid based on the following: (i) the observation that the 3d electron density is well-localised about the I atom, and well isolated from delocalised molecular orbitals; (ii) the peak structure observed in the majority of the M_{45} Auger decay channels are broadly similar to the corresponding transitions in Xe and; (iii) the calculated negligible molecular axis alignment in the $3d^{-1}$ core-ionised state, apart from close to threshold.

For the non-resonant Auger transitions due to direct photoionisation, the dominance of the l = 3 partial wave across the photon energy range, 635.8-680 eV, utilised in the present experimental measurements results in $\gamma \rightarrow 0$. In this limit [366],

$$A_{20}(\mathrm{D}_{5/2}) = -0.21 \text{ and } A_{20}(\mathrm{D}_{3/2}) = -0.20 \tag{5.7}$$

where these values of the alignment parameter refer to plane polarised radiation with the quantisation axis parallel to the electric vector of the radiation. The convention adopted here differs from that used in the earlier theoretical work, and requires the A_{20} parameters reported by Berezhko *et al.* to be multiplied by a factor of 2 to allow comparison with the present experiment [366]. This theoretical work showed that significantly larger values of the alignment parameter may be reached near the photoionisation threshold. In the limit $\gamma \rightarrow$ inf, $A_{20}(\mathrm{D}_{5/2})$ = -0.75 and $A_{20}(\mathrm{D}_{3/2})$ = -0.70. The values of the alignment parameter given in Eq. 5.7 have been used to evaluate the Auger electron intrinsic anisotropy parameter (α_2), following I 3d photoionisation, using Eq A.7, where the β_{Auger} parameter is obtained from our fitting of the Auger electron spectra. The results of Berezhko *et al.* also highlighted that, for a vacancy in the Xe $3d_{5/2}$ subshell, the achievable degree of alignment reaches a relatively constant value at excess energies more than a few eV above the ionisation threshold [366]. This is in accord with the photoionisation cross section being dominated by a single continuum. By analogy, the alignment due to a $3d_{3/2}$ vacancy would be expected to exhibit a similar energy dependence. The lowest photon energies, 635.8 and 646 eV, used for ionisation of $3d_{5/2}$ and $3d_{3/2}$ subshells, correspond to excess energies of approximately 9.0 and 7.7 eV and therefore the ionisation dynamics are likely dominated by the l = 3 continua. Thus, the use of the limiting values of A_{20}, given in Eq. 5.7, for the evaluation of the I 3d Auger electron intrinsic anisotropy parameters appears reasonable.

For resonant Auger processes the A_{20} value, with photoexcitation by plane polarised radiation from an atomic ground state with J = 0 to an excited state having J = 1, has the energy independent value of -$\sqrt{2}$ [377]. If the effect of the rotational structure of the molecule - i.e. the distribution of molecular axes - is ignored, then the atomic value of A_{20} can be used to obtain the α_2 (intrinsic anisotropy) parameters from the β_{Auger} parameters associated with each Auger transition in the resonantly excited spectra recorded at 620.4 and 632.0 eV.

In Fig. 5.11, the β_{Auger} parameters extracted from fits to the non-resonant Auger spectra are shown as a function of photon energy. It is evident that, for a particular final state, the β_{Auger} values exhibit little variation with photon energy, with the majority of the data points lying within or close to the error bar limits. The observed trend is consistent with the expectation that the alignment does not vary significantly across the photon energy range over which these measurements were taken. It should be noted that the discrepancy between β_{Auger} parameters extracted for the $M_4N_{45}N_{45}$ group at $\hbar\omega$ = 646 eV, when compared to all other photon energies, may be attributed to: (i) a breakdown of the adopted PCI line shape close to the ionisation threshold (see Sec. 4.4.2.3) or simply; (ii) difficultly in reliably fitting the Auger transitions due to spectral overlap with the broad continua associated with I 4p photoelectron peak (see Sec. 4.4.2.2) or small signal strength close to threshold. As outlined above a photon energy of 646 eV would correspond to an excess energy of 7.7 eV, a region with low photoionisation cross section.

The values for α_2 parameters, obtained from the β_{Auger} parameters and the A_{20} values in Eq. 5.7, are listed in Table 5.2. The β parameters used for a specific final state were an average obtained across all available photon energies, with exception of $M_4N_{45}N_{45}$ transitions at $\hbar\omega$ = 646 eV. The theoretical α_2 parameters for the corresponding $M_{45}N_{45}N_{45}$ transitions in Xe, calculated by Chen using the multi-configuration Dirac-Fock model [378], are also given in Table 5.2. Despite the fact that not all final states are resolved, the overall agreement between the I $M_{45}N_{45}N_{45}$ transitions in CH_3I and those predicted for Xe is good. This overall agreement is not unexpected because both the initial and final states involved in the $M_{45}N_{45}N_{45}$ transitions in Xe are essentially the same as those involved in the corresponding transitions in CH_3I. The matrix elements connected with a particular Auger transitions will have an energy dependence associated with the Auger electron kinetic energy. However, for the transitions considered, the electron kinetic energies in Xe ($\sim$527 eV) and CH_3I ($\sim$500 eV) are similar. Hence, the kinetic energy dependence of the matrix element may not significantly affect the comparison made here.

The α_2 results are in reasonable accord with values obtained by Karvonen and

co-workers for the non-resonant $M_{45}N_{45}N_{45}$ Auger spectrum in Xe, although there are some significant discrepancies [367]. However, those authors do report strong deviations from the calculated values [378], for several transitions, when the photon energy is tuned below the M_4 threshold, hinting that additional channels leading to the $4d^{-2}$ final state configuration may be operative.

The validity of the assumption that $\gamma \rightarrow 0$, due to the photoionisation cross section being dominated by the l+1 ionisation continua, can be examined by considering the transitions leading to a two-hole final state with total angular momentum J = 0. For these transitions, the Auger electron is characterized by a single partial wave, irrespective of the coupling scheme [395], and leads to α_2 = -1.0 for the $M_4N_{45}N_{45}$ $^1S_0$ and $^3P_0$ states, and α_2 = -1.069 for the $M_5N_{45}N_{45}$ $^1S_0$ and $^3P_0$ states. Using the β_{Auger} value of 0.172±0.011 obtained for the $M_4N_{45}N_{45}$ $^1S_0$ state, together with the theoretically predicted α_2 value of -1.0, results in A_{20} = -0.172±0.011, which is in reasonable accord with the theoretical value of -0.20 assumed here. For the $M_5N_{45}N_{45}$ $^1S_0$ final state, an A_{20} value of -0.141±0.02 was extracted, which is in slightly poorer agreement with the theoretical prediction of -0.21. This discrepancy may be partially due to difficulties of the fitting routine in reliably extracting the relatively weak intensity associated with the $M_5N_{45}N_{45}$ $^1S_0$ peak.

For the $3d_{3/2,5/2} \rightarrow \sigma^*$ resonantly excited Auger spectra, there are no experimental or theoretical α_2 parameters with which to compare the experimental results presented here. Summarised in Table 5.3 are both the β_{Auger} and α_2 parameters for the singly ionised $4d^{-2}\sigma^*$ final states. In general, the Auger electron angular distributions following resonant excitation are more anisotropic than those associated with non-resonant ionisation. This reflects the higher degree of alignment induced in the photoexcited neutral state.

Presented in Fig. 5.12 are the β_{Auger} parameters extracted for the five peaks associated with the $M_4N_{45}O_{23}$ and the $M_5N_{45}O_{23}$ transitions. Similar to the data

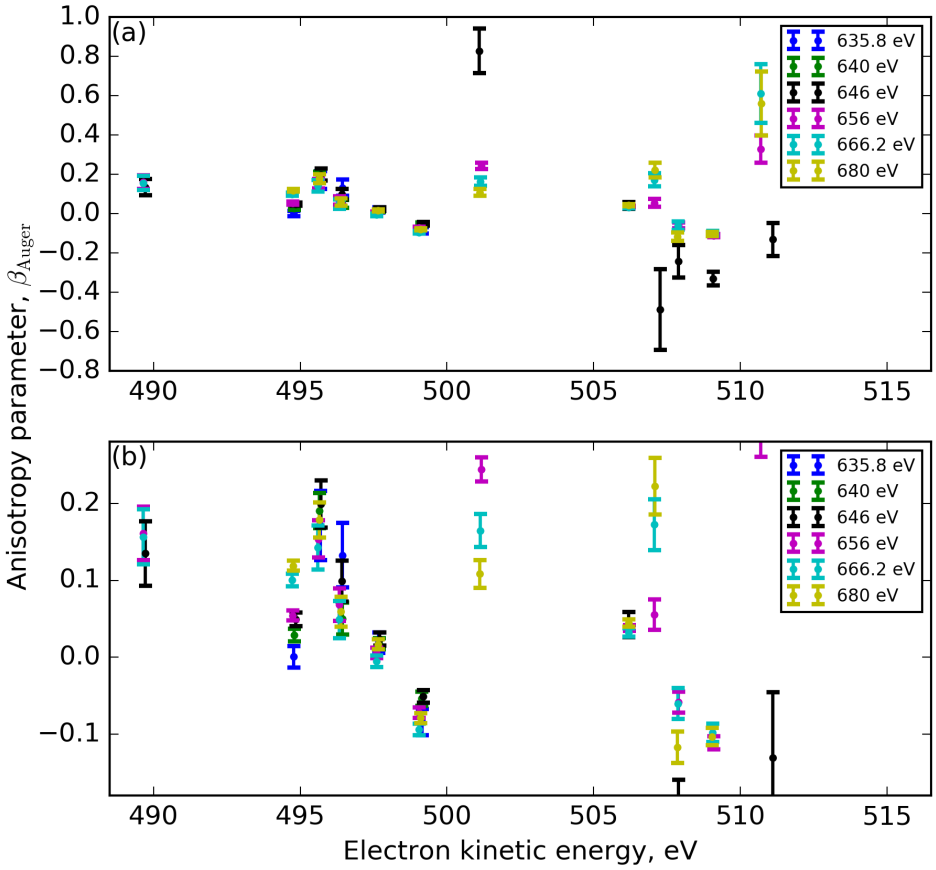

Figure 5.11: (a) The β_{Auger} parameters for the $M_{45}N_{45}N_{45}$ transitions in CH_3I derived from the non-resonant Auger spectra recorded with vertically and horizontally polarised radiation (see Fig. 5.4). (b) Zoom of the β_{Auger} parameter between -0.18 and 0.28. Both the β_{Auger} and intrinsic anisotropy parameters for these final states are listed in Table 5.2.

presented for the $M_{45}N_{45}N_{45}$ transitions in Fig. 5.11, the β_{Auger} parameters for these decay channels exhibit little variation with photon energy, again, as expected from the dominance of the $l = 3$ ionisation continuum. For the data recorded at $\hbar\omega =$ 646 eV, very small signals were observed in peaks connected with $M_4N_{45}O_{23}$ Auger transitions. This resulted in insufficient data quality to reliably extract the angular distributions at this photon energy, the results are therefore omitted. Unfortunately, there are no theoretically predicted α_2 values for these transitions in Xe or I so further analysis/comparison was not possible.

Theoretical values for the α_2 parameters associated with the $M_4N_{23}N_{45}$ [378]

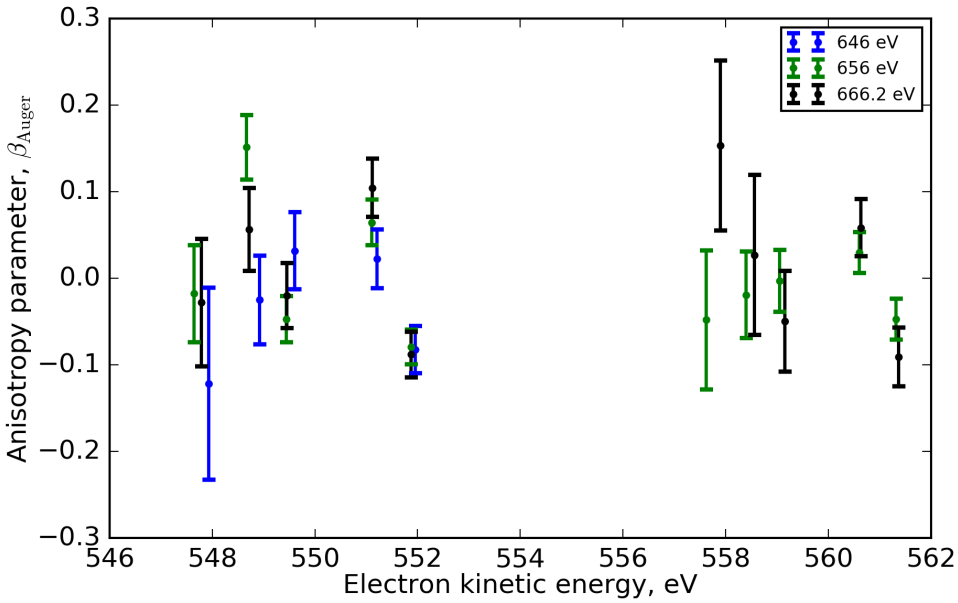

Figure 5.12: (a) The β_{Auger} parameters for the $M_{45}N_{45}O_{23}$ transitions in CH_3I as a function of photon energy. These values were extracted from fits (see Appendix A) to non-resonant Auger spectra recorded with vertically and horizontally polarised radiation.

and the $M_5N_{23}N_{45}$ [378, 380] transitions in Xe have been reported and the results from these two calculations are in good agreement with each other. However, as outlined in Sec. 5.3.2.3, it is not straightforward to correlate these predictions with the experimental data shown in Fig. 5.7, due to final state orderings. The experimental results indicate that β_{Auger} is slightly positive throughout most of the electron kinetic energy range covered by the $M_{45}N_{23}N_{45}$ transitions, apart from the two regions containing the doublets. In contrast, the theoretical values for Xe exhibit a marked dependence on the final state. Similar comments can be made for the β_{Auger} parameter associated with the $M_{45}N_1N_{45}$ transitions (Fig. 5.8) for the resonantly excited spectrum recorded at a photon energy of 620.4 eV. The experimental data show that β_{Auger} is close to zero across the entire band structure whereas the theoretical predictions for Xe, although in good agreement with each other, predict widely ranging values [378, 380]. Additional calculations to determine both the final state ordering and α_2 parameters for atomic I would likely be required in order to facilitate detailed comparisons.

5.4 Conclusions

Presented in this chapter was a study of the Auger decay channels following excitation (resonant) and ionisation (non-resonant) of the I 3d orbital in CH_3I. Horizontally and vertically plane polarised synchrotron radiation was employed to extract the electron anisotropy parameter, β_{Auger}, which characterises the Auger electron angular distribution. Across the photon energy range considered within this work, the I 3d photoionisation cross section appears to behave somewhat atomic-like and is dominated by transitions into the εf continuum. Under these conditions, the theoretical value of the alignment parameter characterising the intermediate, core-ionised, state of an atom remains constant, independent of the photon energy. This theoretical value was used to obtain the Auger electron intrinsic anisotropy parameters (α_2) from the measured β_{Auger} parameters.

The extracted α_2 parameters were compared with theoretically determined values for the corresponding transitions for Xe 3d. For the $M_{45}N_{45}N_{45}$ decay channel, the I 3d Auger spectra exhibits a similar structure to that previously observed for Xe 3d [119,304,367], as well as I_2 [304], and the α_2 parameters are in accord with those calculated for the corresponding transitions in Xe [367]. The Auger electron spectra associated with the $M_{45}N_{23}N_{45}$ and $M_{45}N_1N_{45}$ transitions generally resemble those for the corresponding transitions in Xe and molecular iodine, but some differences are apparent. In particular, for the $M_{45}N_{23}N_{45}$ Auger decay a broad continuum, similar to that previously observed for I_2 [304], extending towards lower kinetic energies was observed. This continuum was attributed to multielectron effects in the intermediate state, similar to those outlined in Sec. 4.4.2.2 for the 4p photoline in CH_3I. The experimentally determined α_2 parameters for the $M_{45}N_{23}N_{45}$ and $M_{45}N_1N_{45}$ transitions do not exhibit the marked dependence on the final ionic state that is predicted in Xe. The Auger electron spectrum due to the $M_{45}N_{45}O_{23}$ transitions shows little molecular character, despite now involving ejection of an electron from the valence shell, and resembles that due to the corresponding transitions in Xe. This observation is consistent with the presented calculations which show that the outermost 2e orbital retains a strong atomic I 5p lone-pair character.

The Auger electron kinetic energy associated with a specific transition in the normal spectrum is shifted to higher energy in the resonantly excited spectrum. The observed shift has been verified using calculated transition energies for I 3d excited and I 3d ionised CH_3I. Finally, a large increase in anisotropy is observed for resonantly excited $M_{45}N_{45}N_{45}$ Auger spectra when compared to the non-resonant case. This was attributed to an increase in the alignment of the intermediate state due to resonant photoabsorption.

Chapter 6

General conclusions and outlook

6.1 Strong-field ionisation of NO_2

The results presented in Chapter 2 highlight the complexity of tracking non-adiabatic dynamics in polyatomic molecules using SFI, due the presence of multiple electronic continua accessed during ionisation and difficulties in disentangling the number of pump photon (i.e. 2 versus 3) involved in some of the channels. The latter point will generally occur in measurement schemes not directly sensitive to the number of pump photons involved. In spite of these complications, it was possible to: (i) identify the signature of ground state repopulation, from the first optically bright state, in several ionisation channels; (ii) observe a channel consistent with wavepacket motion (IVR) occurring on the ground state; (iii) associate different series of ATI combs in the photoelectron spectra with accessing different final cation states and; (iv) separate out single versus multiphoton excitation pathways. Identification of these different dynamical features was only possible by exploiting a differential measurement, namely photoelectron and fragment coincidences. If a less differential measurement, such as time-resolved mass spectroscopy, had been employed, extracting the contributions of each of these features would have been challenging.

Future extensions of this work to investigate the pump wavelength effect on the experimental observables would be of interest due to the pump wavelength lying close to first dissociation limit of neutral NO_2 [191]. Such a study may permit

statistical dissociation dynamics and processes like roaming [192] to be investigated in the time domain. In terms of increasing the differentiability of the multiple ionisation continuum operative during SFI of NO_2, one approach could be to perform a series of time-resolved experiments at multiple probe wavelengths. Such a scheme has been utilised in identifying the presence of multiple ionisation continua in the polyatomic molecule SF_6 [149], where other methods based on molecular alignment, such as angle-and-channel-resolved ATI [153], would not be possible due to molecular symmetry (O_h point group). Implementation of this scheme in a pump-probe setting would however be challenging due to increased experimental data acquisition times, which are already lengthy for coincidence/covariance experiments presented here. These constraints may however be addressed by the development and use of significantly higher repetition rate lasers systems based on, for example, optical parametric chirped pulse amplification (OPCPA) [397].

Finally, another area of continued research would be to conduct a similar experiment in an coincidence spectrometer capable of recording ion fragment kinetic energy releases. Utilising such a spectrometer would likely help separate out contributions associated with 2/3 pump photon processes as the kinetic energy release in the NO^+ fragment is unlikely to be the same for these two channels. This sensitivity would arise from the fact that the two-photon pathway accesses the $\tilde{D}^2B_2$ state, which is know to predissociate on $<$100 fs timescale, whereas the three photon pathway accesses a presumably longer-lived Rydberg state. A study which utilises an ion momentum resolved spectrometer and coincident electron detection to study photodissociation dynamics in NO_2 has already been undertaken in collaboration with the groups of Paul Corkum and André Staudte at the NRC in Ottawa. This study made use of a Cold Target Recoil Ion Momentum Spectrometry (COLTRIMS) [398] to achieve the desired momentum resolution for both the ion and electron. Analysis of this highly multidimensional dataset is currently underway and will likely appear in a future publication.

6.2 Femtosecond VUV and Rydberg valence coupling in acetone

Presented in the second experimental chapter were details surrounding the implementation and characterisation of a femtosecond VUV source capable of generating the fifth harmonic (5ω) of the Ti-Sapphire 800 nm fundamental via FWDFM. By using a VUV monochromator and a photodiode it was possible to estimate the spectral bandwidth of the VUV pulse and to optimise phase matching conditions. Characterisaion of both the central photon energy, as well as the pulse duration, was achieved by examining the photoelectron spectra following non-resonant 1+1′ photoionisation of Xe in a electron VMI spectrometer. The calibrated 5ω pulses were then utilised as a pump in an series of time-resolved studies exploring the coupling between Rydberg and valence states, as well as internal conversion dynamics, in acetone. This study highlighted that relatively complex parallel decay channels can arise when photoexcitation takes place in the VUV region of the spectrum. The initially prepared wavepacket on the 3d Rydberg state was seen to decay onto the lower-lying 3p Rydberg manifold, as well as a valence $\pi\pi^*$ state, on a timescale of $\sim$30 fs. The photoelectron peak connected with the 3p state subsequently decayed on a $\sim$450-550 fs timescale into two channels: a minor one with internal conversion taking place to the lower-lying 3s Rydberg state; the dominant one connected with population of a valence state. The latter channel could not be unambiguously assigned to a state of either nπ^* or $\pi\pi^*$ character but was correlated with a decay with a time constant of 940 fs.

High-level molecular dynamics calculations using, for example, methods like *ab initio* multiple spawning (AIMS) [399] or multi-configurational time-dependent Hartree (MCTDH) [400] would be highly desirable to help verify the current assignments. Even if full dynamics calculations could not be performed determination of the IP at various geometries on both the nπ^* and $\pi\pi^*$ would be of great benefit to assign the low-energy photoelectron transient. Such calculations are currently being undertaken by Drs. Michael Schuurman and Simon Neville (NRC/University of Ottawa). With these results in hand it should be possible to form a more complete

picture of VUV excited state dynamics of acetone, which, as the simplest aliphatic ketone, likely has implications for the photochemistry of all aldehydes and ketones. Preliminarily results, collected within the NRC molecular photonic group, on various substituted linear and cyclic ketones suggest that is is indeed the case and many of the internal conversion mechanisms outlined here are also operative in these systems.

In terms of further development of the current femtosecond VUV source there are several areas of possible continued research and development; some of these include:

- The inclusion of a dedicated VUV spectrometer in the gas cell/optics box. This addition would provide a convenient method for monitoring the 5ω spectrum while optimising the spatial and temporal overlap in the FWM process. The current method adjusting the signal on power, although convenient, may not correspond to a situation where a Gaussian spectrum is produced. A spectrometer for this purpose has been purchased but has not yet been installed in the beamline.

- In addition to the spectrometer, further characterisation of the VUV pulses could be achieved by using: (i) VUV sensitive camera to measure the generated beam profile, allowing properties such as the quality of the spatial mode to be extracted; (ii) a power meter or a calibrated photodiode to determine the VUV flux. In related work (not presented herein) on generation of 133 nm pulses we have utilised a standard thermopile power meter to extract pulse energies reliably down to 50 nJ; a similar method could likely be utilised for 160 nm pulses.

- A method to provide shorter VUV pulses and to control the dispersion associated with passing the relatively broadband pulse through the VMI entrance window. This point was highlighted due to the fact that, despite the inclusion of a prism compressor in the other arm of the pump-probe set-up and measured cross correlations of 75-95 fs, some experiments would benefit

for shorter VUV pulses. One previously demonstrated method which could achieve both these aims would be to replace the fundamental pulse in the FWM with a spectrally broadened pulse from the output of a hollow-core fiber [401]. In this work the authors demonstrated that VUV pulse durations below 20 fs could be measured inside a mass spectrometer despite the insertion of a MgF_2 window in the VUV beam path. Compensation of the dispersion associated with this optical element was achieved by the inclusion of a pair of fused silica wedges in broadband seed beam, thus adding a positive chirp to the pulse. This spectral chirp is then transferred to the FWM pulse with the opposite sign, resulting in a shorter pulse duration in the experimental chamber. In spite of the appealing nature of this scheme, it does however need to be applied with caution as only the even orders of the spectral chirp are transferred to the FWM pulse with opposite sign, whereas odd orders of the transferred chirp do not change the sign. This distinction was discussed in detail in the FWM work performed by Zuo *et al.* [402].

- Development of a wavelength tunable femtosecond VUV source. The ability to tune the VUV photon energy is advantageous for both the situation when the pulse is being used as a pump and as a probe. The acetone results presented in this chapter provide a nice illustrative example of where a tunable VUV pump photon would be applicable as it would allow the exact vertical excitation energy of the $\pi\pi^*$ state to be extracted. For the case of the VUV pulse being used as a probe in a TPRES measurement the main advantage would be the ability to shift the wavelength away from resonant features and ensure that the resulting spectra contained limited contributions associated with probe-pump dynamics. A scheme capable of tuning between approximately 147-153 nm has already been demonstrated by Noack and co-workers where tunability was achieved by replacing the fundamental in the FWM process with the signal of an infrared optical parametric amplifier (OPA) [403]. Further tunability, on both the longer and shortest energy sides of 160 nm, could be achieved by replacing the third harmonic in the FWM with another

UV colour generated by conventional sum-frequency mixing in crystals of an OPA output. Tunable VUV four-wave mixing schemes similar to this have been previously demonstrated using, for example, nanosecond lasers [404].

Other than the FWDFM schemes outlined above another route to generate both widely tunable potentially short (<10 fs) VUV pulses would be to exploit gas filled hollow-core photonic crystal fibres [405]. It has been recently demonstrated that theses sources can produce extremely short (4 fs) pulses in the DUV region [406], as well as generation of light down to 113 nm [407], with good conversion efficiency (e.g. 5 μJ of 800 nm input goes to 75 nJ DUV output). However, despite these impressive specifications, this may not provide sufficient flux for a gas-phase time-resolved experiment; particularly when this small pulse energy is spread over such a large range of wavelengths required to generate such short pulse durations.

Finally, generation of shorter wavelength, high flux (i.e. >100 nJ), VUV radiation has been achieved by a number of groups exploiting wave mixing of either 400 nm or 267 nm femtosecond pulses yielding light at 133 nm [408, 409] and 89 nm [410], respectively. These relatively high flux sources provide an interesting photon energies for the probe in TRPES measurements as it would allow photo-products, which typically have large IPs, as well as ground state re-population, to be detected. An application of an 89 nm source to both of these situations has been recently demonstrated in investigations by Suzuki and co-workers [158, 411]. It is difficult to envision generation of shorter wavelengths than <89 nm through wave mixing sources; this would be better suited to HHG based methods, which are starting to now be applied in TRPES [160].

6.3 CH_3I core-level ionisation

The investigation presented in Chapter 4 provides a comprehensive view of the electronic structure of soft X-ray photoexcited and photoionised CH_3I by using polarised synchrotron radiation at the PLÉIADES beamline at the Synchrotron SOLEIL [92]. A particular focus of this study was on the photoionisation dynamics of the I 3d shell as it facilitates comparison with the much more extensively studied

Xe 3d orbital [100, 108, 109, 298]. This comparison provides a means to investigate how core-level spectroscopic properties evolve from an atomic to a closely related molecular system. The experimental work, through comparison with both theoretical X-ray absorption spectra and photoionisation cross sections/angular distributions, highlighted that this orbital shows atomic-like behaviour across the majority of the photon energy range considered in this work. Apart from being of spectroscopic interest the study also provides information which will be useful for future dynamical studies, in particular at FELs, where CH_3I is a very popular system [40,76,111–113,115,116]. In addition, to the 3d subshell, photoelectron spectra for the I 4s and 4p orbitals has also been presented. The latter shows an unusual photoelectron peak structure associated with the breakdown of the single particle model of ionisation [321] through the inner-shell hole state transforming rapidly via Coster-Kronig [323] and super-Coster-Kronig [324] processes.

Although not shown within this thesis, there is on-going analysis of data connected with both photoexcitation and photoionisation of the C 1s and I 4d shells in CH_3I. This data was collected during the same beamtimes as the I 3d data presented here. Despite the analysis being preliminary, the total ion yield measurements connected with the C 1s and I 4d pre-edges reveal additional substructure which was not previously observed in much lower resolution EELS [290, 389, 412] or X-ray absorption [293, 295] measurements. Comparison of this I 4d ion yield data with TDDFT calculations of the X-ray absorption cross section has suggested that reinterpretation of peak assignments may also be required. This point may have implications for the interpretations of previous transient X-ray absorption spectroscopy studies on CH_3I [413,414]. The point also nicely highlights the need for high resolution ground state spectra as a precursor to performing time-resolved studies, particularly with recent investigations reaching photon energies at the C K-edge [75,287], where a large fraction of the available spectroscopic literature is recorded by EELS.

One area of possible further study, as an extension of the work shown here, would be to investigate the PADs from aligned CH_3I at photoexcitation energies coinciding with the I 3d shape resonance. Such an investigation could be performed on

either a FEL or synchrotron using the following experimental schemes. For FELs it would be possible to utilise laser based alignment techniques to either field-free 3D align [415–417] or extract the molecular frame through a fitting-based methodology [154], and use the FEL as the ionisation source. A second method would be exploit a COLTRIMS/a reaction microscope spectrometer to extract molecular frame PADs through measurement of the fragment recoil direction [91]. Although the later is applicable to both synchrotron and FELs it is, however, limited to dissociative ionisation and situations where the axis recoil approximation holds.

6.4 Auger electron angular distributions for the I 3d level in CH_3I

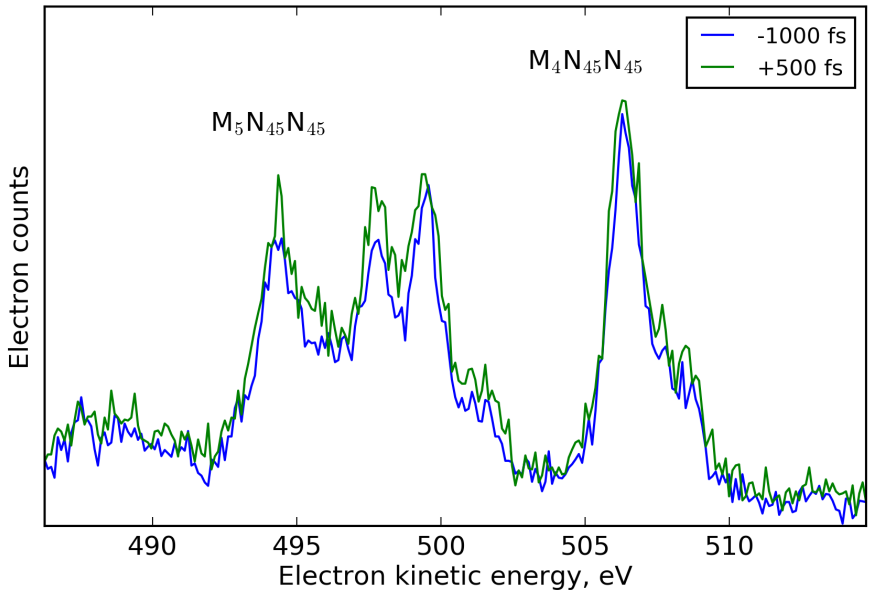

Figure 6.1: Time-resolved Auger spectra of CH_3I recorded at the Linac Coherent Light Source (LCLS) of photodissociation dynamics in CH_3I. Here a femtosecond pump pulse centered at 4.65 eV was used to excited the dissociative σ^* orbital and the ensuing dynamics tracked using Auger decay $M_{45}N_{45}N_{45}$ Auger decay following I 3d (M_{45}) photoionisation at 727 eV. Thanks go to Profs. Daniel Rolles and Artem Rudenko (Kansas State University) for providing the unpublished data used to generate this figure.

In the final experimental chapter the Auger decay channel following either

excitation or photoionisation of the I 3d shell in CH_3I were assigned and characterised using synchrotron radiation. The use of plane polarised radiation allowed the electron anisotropy parameters, describing the Auger electron angular distributions, to be extracted. These anisotropy parameters were compared to the intrinsic anisotropy parameters of the corresponding transitions in Xe by assuming an atomic-like model of the Auger transitions. The validity of atomic model was confirmed by calculating the molecular alignment parameter expected due to 3d vacancy creation. These calculations permitted the source of the Auger anisotropy to be attributed mainly to unequal distribution of magnetic sublevels in the core-ionised state rather than a non-isotropic distribution of molecular axis in the core-hole ensemble. This type of analysis, to the best of our knowledge, is novel and can likely be applied investigate the source of Auger anisotropy in other molecular systems. With this in mind, analysis of the Auger transitions connected with the more shallow I 4d orbital in CH_3I is already underway from datasets recorded during the same beamtimes as the work presented here. For the I 4d level, preliminary theoretical calculations highlight a higher degree of molecular frame alignment, compared to the I 3d shell, which will likely result in more complex Auger electron angular distributions as a function of photoexcitation energy.

The spectroscopic information and assignments obtained on the I 3d Auger transitions in this study will also feed into on-going analysis of Linac Coherent Light Source (LCLS) data on time-resolved Auger spectroscopy of CH_3I. In this work a UV photon, generated via third harmonic generation of a conventional Ti:sapphire laser system, initiates photodissociation of CH_3I by excitation to the dissociative σ^* valence state. Presented in Fig. 6.1 are sample Auger spectra for two pump-probe time-delays corresponding to the UV pulse preceding the 727 eV probe pulse by 500 fs and UV pulse arriving 1000 fs after the X-ray pulse (i.e not resonantly exciting the σ^* state in CH_3I). Despite the poorer signal-to-noise, compared to synchrotron spectra shown in this thesis, the Auger spectra do exhibit pump laser dependent changes to the peak branching ratios and perhaps widths. The spectra do not however exhibit prominent shifts in Auger electron kinetic energies,

similar to the ones observed by Gühr and coworkers [288]. This is likely linked to the atomic-like nature of the I $M_{45}N_{45}N_{45}$ Auger transitions which, based on similar Auger electron kinetic energy spectra observed from both CH_3I and I_2 [304], are not particularly sensitive to the surrounding molecular environment. It therefore appears reasonable to suggest that little variation would be observed in the Auger electron kinetic energies between atomic iodine and I embedded in CH_3I. A more sensitive observable to the photodissociation dynamics would be the C KVV and I NVV Auger transitions as these both involve valence electrons, in a similar manner to Ref. [288].

6.5 Concluding remarks

Given that since the beginning of this PhD thesis (2014) the number of X-ray FELs has almost doubled (4 to 7), and several more are under construction, it appears reasonable to suggest that one area of continued research in photoionisation will be time-resolved core-level spectroscopies. Photoelectron spectroscopy in particular will be an area of development at these new light sources which employ seeding strategies rather than relying on the SASE processes to generate the X-ray pulses. For laboratory based experiments, ultrafast laser technology will continue to advance and result in higher-power shorter pulse laser systems at higher repetition rates. The latter point is particularly interesting for differential spectroscopic methods such coincidence imaging technique, which have only been employed in a handful of time-resolved studies to date [24, 28, 37, 184, 186]. If such PEPICO coincidence methods were utilised with new light sources in VUV/XUV spectra region this may provide a route to detection of the complete reaction path without suffering from, for example, windowing effects.

Appendix A

Fitting of the Auger spectra in CH_3I

A.1 Fitting of the non-resonant Auger spectra

The overall line shape associated with a non-resonant Auger transition arises from three contributions: (i) The initial state level width that can be distorted by PCI between the photoelectron and the subsequently emitted Auger electron in the field of the positively charged ion. The effect of PCI broadening can be taken into account by implementing an approximate line shape in the analysis of the CH_3I 3d photoelectron peaks. The PCI broadening peak shape, $P^{\mathrm{PCI}}(E^{\mathrm{kin}})$, can be expressed using an analytical formula given in Armen *et al* [308]:

$$P^{\mathrm{PCI}}(E^{\mathrm{kin}},E^0,\Gamma,C) = \frac{\Gamma}{2\pi}\frac{\pi C}{\frac{1}{4}\Gamma^2+(E^{\mathrm{kin}}-E^0)^2} \times \frac{\exp[-2C\arctan(2(E^{\mathrm{kin}}-E^0)/\Gamma)]}{\sinh(\pi C)} \tag{A.1}$$

where E^{kin}, E^0 and Γ refer to the Auger electron kinetic energy, peak position and core-hole width, respectively. C is a fitting parameter, which describes the distortion of the Lorentzian line shape and is dependent on electron excess energy.

(ii) The final state (symmetrical) level width, Γ^{f}, that is represented by a Lorentzian profile, $L^{\mathrm{Auger}}(E^{\mathrm{kin}},\Gamma^{\mathrm{f}})$:

$$L^{\mathrm{Auger}}(E^{\mathrm{kin}},\Gamma^{\mathrm{f}}) = \frac{1}{2\pi}\frac{\Gamma^{\mathrm{f}}}{(\frac{\Gamma^{\mathrm{f}}}{2})^2+(E^{\mathrm{kin}}-E^0)^2} \tag{A.2}$$

(iii) The total instrumental broadening: a Gaussian due to the convolution of the Gaussian broadenings associated with the spectrometer (62.5 meV) and the Doppler contribution (23 meV). This corresponds to a Full Width Half Maximum (FWHM) of the instrument broadening of 66.6 meV. The photon resolution does not play a role and the associated peak shape is given by:

$$G(E^{\text{kin}},\sigma) = \frac{1}{\sigma\sqrt{2\pi}}\exp\left[\frac{-E^{\text{kin}\ 2}}{2\sigma^2}\right] \tag{A.3}$$

The peak shape for a specific normal (non-resonant) Auger transitions can therefore be expressed as:

$$\begin{aligned} P(E^{\text{kin}},\theta^{\text{Auger}},\sigma,\Gamma^{\text{f}},\Gamma,C,E^0,W^{\text{T}}_{i\to f},\beta^{\text{Auger}}) = \frac{W^{\text{T}}_{i\to f}}{4\pi}[1+\beta^{\text{Auger}}P_2(\cos(\theta^{\text{Auger}}))] \\ \times [P^{\text{PCI}}(E^{\text{kin}},E^0,\Gamma,C) \\ * L^{\text{Auger}}(E^{\text{kin}},\Gamma^{\text{f}}) * G(E^{\text{kin}},\sigma)] \end{aligned} \tag{A.4}$$

where the amplitude of the peak is related to the angularly resolved differential cross section:

$$\frac{W_{i\to f}(\theta)}{d\Omega} = \frac{W^{\text{T}}_{i\to f}}{4\pi}[1+\beta^{\text{Auger}}P_2(\cos(\theta^{\text{Auger}}))] \tag{A.5}$$

where $W^{\text{T}}_{i\to f}$ is the total Auger decay rate for a particular transition between intermediate and final ionic states, β^{Auger} is the electron anisotropy parameter, $P_2(\cos(\theta^{\text{Auger}}))$ is Legendre polynomial of second order and θ^{Auger} is the Auger electron ejection angle relative to the polarisation axis of the plane polarised radiation.

The fitting function for a non-resonant Auger group, connected with a single core hole, is therefore:

$$\begin{aligned} & I_{\text{M}_i}(E^{\text{kin}},\theta^{\text{Auger}},\sigma_j,\Gamma^{\text{f}}_j,\Gamma_{\text{M}_i},C_j,E^0_j,W^{\text{T}}_{i\to f,j},\beta^{\text{Auger}}_j) \\ &= \sum_{j=1}^{j^{\max}} P(E^{\text{kin}},\theta^{\text{Auger}},\sigma_j,\Gamma^{\text{f}}_j,\Gamma_{\text{M}_i},C_j,E^0_j,W^{\text{T}}_{i\to f,j},\beta^{\text{Auger}}_j) \end{aligned} \tag{A.6}$$

here j is used to denote the peak number in an Auger group and $j^{\max}$ denotes the total number of peaks within the group. M_i is used to express whether the intensity of a particular Auger group, connected with a particular intermediate state, is either a M_5 ($3d_{5/2}^{-1}$) or M_4 ($3d_{3/2}^{-1}$) core-hole.

The functional form used to fit the Auger spectra at a particular photon energy can therefore be expressed as:

$$\begin{aligned} I(E^{\mathrm{kin}}, a, b, \theta, \sigma_{j,j'}, \Gamma^{\mathrm{f}}_{j,j'}, \Gamma_{\mathrm{M}_i}, C_{j,j'}, E^0_{j,j'}, W^{\mathrm{T}}_{i\to f,j,j'}, \beta_{j,j'}) &= a + bE^{\mathrm{kin}} \\ &+ \sum_{j=1}^{j^{\max}} I_{\mathrm{M}_5}(E^{\mathrm{kin}}, \theta^{\mathrm{Auger}}, \sigma_j, \Gamma^{\mathrm{f}}_j, \Gamma_{\mathrm{M}_5}, C_j, E^0_j, W^{\mathrm{T}}_{i\to f,j}, \beta^{\mathrm{Auger}}_j) \\ &+ \sum_{j'=1}^{j'^{\max}} I_{\mathrm{M}_4}(E^{\mathrm{kin}}, \theta^{\mathrm{Auger}}, \sigma_{j'}, \Gamma^{\mathrm{f}}_{j'}, \Gamma_{\mathrm{M}_4}, C_{j'}, E^0_{j'}, W^{\mathrm{T}}_{i\to f,j'}, \beta^{\mathrm{Auger}}_{j'}) \end{aligned} \tag{A.7}$$

The double indices of j and j' is used to denote the number of peaks in the M_5 and M_4 Auger groups, respectively. The coefficients a and b are used to describe a linear energy dependent background, which can be used to remove superfluous counts not associated with the Auger decay process.

The peak intensity, for the total spectrum at a particular photon energy, was fitted to the spectra recorded with vertically or horizontally plane polarised radiation using $\theta_{\mathrm{Auger}} = 0^\circ$ or $\theta_{\mathrm{Auger}} = 90^\circ$, respectively. The global minimisation function was then constructed from the two separate minimisation functions, associated with each of the vertically and horizontally polarised spectra.

In the fitting routine, both widths in the peak shape (associated with the total instrumental and final state broadening) were constrained to be equivalent for all peaks regardless of the intermediate core-hole state and for both polarisation states, such that σ_j=...=$\sigma_{j^{\max}}$ and Γ^{f}_j=...=$\Gamma^{\mathrm{f}}_{j^{\max}}$, for both $\theta^{\mathrm{Auger}} = 0^\circ$ or $\theta^{\mathrm{Auger}} = 90^\circ$, respectively.

Bounds were placed on the fitting parameters such that they had to have physically significant values. For example, the widths, peak intensities and peak positions had to be positive and β^{Auger} parameter value must lie between -1 and 2.

Finally, it should be noted that the width associated with the total instrumental

broadening and that associated with the intermediate state core-hole broadening were not treated as a fitting parameters but were held fixed during the weighted least squared fitting routine. The exact values used were determined based on the extracted width from fits of the $3d_{5/2}$ and $3d_{3/2}$ photolines and from estimates of the beamline resolution.

A.2 Fitting of the resonant Auger spectra

For resonant Auger transitions, if the photon bandwidth is narrower than the level width of the neutral excited state ($3d_{5/2}^{-1}\sigma^*$ or $3d_{3/2}^{-1}\sigma^*$ in our case), then the initial state width can be neglected and replaced by a Gaussian representing the photon bandwidth [338]. As a resonantly excited state is being prepared and there is no photoelectron produced during initial photoexcitation, the effects of PCI are also not considered here.

The total lineshape for a specific Auger transition is therefore given by the convolution of two contributions: (i) The total instrumental broadening: a Gaussian due to the convolution of the Gaussian broadenings associated with the spectrometer (62.5 meV), the Doppler contribution (23 meV) and the photon bandwidth ($\approx$300 meV) and; (ii) The final state ($4d^{-2}\sigma^*$) level width that is represented by a Lorentzian profile. The total lineshape used in the fitting routine is based on the details given in Ref [418]. Since the lineshape is given by a convolution of a Gaussian profile $G(x,\sigma)$ and a Lorentzian profile $L(x,\gamma^{\mathrm{f}})$, a Voigt lineshape $V(x,\sigma,\gamma^{\mathrm{f}})$ is used in fitting routine:

$$V(x,\sigma,\gamma^{\mathrm{f}}) = \int_{-\infty}^{\infty} G(x',\sigma)L(x-x',\gamma^{\mathrm{f}})\mathrm{d}x' \tag{A.8}$$

$$G(x,\sigma) = \frac{1}{\sigma\sqrt{2\pi}}\exp\left[\frac{-x^2}{2\sigma^2}\right] \tag{A.9}$$

$$L(x,\gamma^{\mathrm{f}}) = \frac{\gamma^{\mathrm{f}}/\pi}{x^2+\gamma^{\mathrm{f}\,2}} \tag{A.10}$$

Here γ^{f} is the half-width at half-maximum (HWHM) of the Lorentzian profile connected with the final state level width and σ is the standard deviation of the

Gaussian profile related to the total instrumental broadening. The HWHM, α, is 155 meV and is related to σ by α=$\sigma\sqrt{2\ln 2}$. In terms of electron kinetic energy, E^{kin}, x=E^{kin}-E^0, where E_0 is the central kinetic energy of an Auger peak. There is no closed form for the Voigt profile, but it is related to the real part of the Faddeeva function, $w(z)$ by:

$$V(x,\sigma,\gamma_{\mathrm{f}}) = \frac{\mathrm{Re}[w(z)]}{\sigma\sqrt{2\pi}}, \text{where } z = \frac{x+i\gamma^{\mathrm{f}}}{\sigma\sqrt{2}} \tag{A.11}$$

The peak shape for a specific resonant Auger transitions can therefore be expressed as:

$$\begin{aligned} P^{\mathrm{Res}}(E^{\mathrm{kin}},\theta^{\mathrm{Auger}},\sigma,\gamma^{\mathrm{f}},E^0,W^{\mathrm{T}}_{i\to f},\beta^{\mathrm{Auger}}) = \frac{W^{\mathrm{T}}_{i\to f}}{4\pi}[1+\beta^{\mathrm{Auger}}P_2(\cos(\theta^{\mathrm{Auger}}))] \\ \times V(E^{\mathrm{kin}},E^0,\sigma,\gamma^{\mathrm{f}}) \end{aligned} \tag{A.12}$$

where the amplitude of the peak is again related to the angularly resolved differential cross section.

The total fitting function for a given resonant Auger group, containing multiple peaks and terms associated with background electron intensity, is given by:

$$\begin{aligned} I(E^{\mathrm{kin}},a,b,\theta^{\mathrm{Auger}},\sigma_k,\gamma^{\mathrm{f}}_k,E^0_k,W^{\mathrm{T}}_{i\to f,k},\beta^{\mathrm{Auger}}_k) = a+bE^{\mathrm{kin}} \\ + \sum_{k=1}^{k^{\mathrm{max}}} P^{\mathrm{Res}}(E^{\mathrm{kin}},\theta^{\mathrm{Auger}},\sigma_k,\gamma^{\mathrm{f}}_k,E^0_k,W^{\mathrm{T}}_{i\to f,k},\beta^{\mathrm{Auger}}_k) \end{aligned} \tag{A.13}$$

here k is used to denote the peak number in a particular resonant Auger group and k_{max} denotes the total number of peaks within the group. At a given photon energy, the above function form was fitted to the spectra recorded with vertically or horizontally plane polarised radiation, simultaneously. This made use of a global minimisation function constructed, in a manner similar to that described in relation to the normal Auger spectra, from the individual functions associated with the vertically and horizontally polarised spectra. In addition, bounds were placed on the fitting parameters to ensure they had physically significant values and the width

associated with the total instrumental broadening was held fixed during the fitting routine.

Bibliography

[1] G. A. Worth and L. S. Cederbaum. “Beyond Born-Oppenheimer: molecular dynamics through a conical intersection”. *Annu. Rev. Phys. Chem.*, **55**:127, (2004).

[2] I. Prigogine and S. A. Rice, editors. *Adv. Chem. Phys.*, volume **100** of *Adv. Chem. Phys.* John Wiley & Sons, Inc., Hoboken, NJ, USA, (1997).

[3] J. F. Rabek and G. W. Scott. *“Photochemistry and photophysics, volume 1”*. CRC Press, (1989).

[4] W. Domcke, D. Yarkony, and H. Köppel. *“Conical intersections: Electronic structure, dynamics & spectroscopy”*. World Scientific, (2004).

[5] R. Schoenlein, L. Peteanu, R. Mathies, and C. Shank. “The first step in vision: femtosecond isomerization of rhodopsin”. *Science*, **254**(5030):412, (1991).

[6] L. A. Peteanu, R. W. Schoenlein, Q. Wang, R. A. Mathies, and C. V. Shank. “The first step in vision occurs in femtoseconds: complete blue and red spectral studies”. *Proc. Natl. Acad. Sci. U.S.A.*, **90**(24):11762, (1993).

[7] G. R. Fleming. *“Chemical applications of ultrafast spectroscopy”*. (1986).

[8] Y-C. Cheng and G. R. Fleming. “Dynamics of light harvesting in photosynthesis”. *Annu. Rev. Phys. Chem.*, **60**:241, (2009).

[9] G. Herzberg. “Molecular spectra and molecular structure. Vol.2: Infrared and Raman spectra of polyatomic molecules”. (1945).

[10] G. Herzberg. "Molecular spectra and molecular structure. Vol.1: Spectra of diatomic molecules". *New York: Van Nostrand Reinhold*, (1950).

[11] G. Herzberg. "Molecular spectra and molecular structure. Vol.3: Electronic spectra and electronic structure of polyatomic molecules". *New York: Van Nostrand*, (1966).

[12] T. Suzuki and B. J. Whitaker. "Non-adiabatic effects in chemistry revealed by time-resolved charged-particle imaging". *Int. Rev. Phys. Chem.*, **20**(3):313, (2001).

[13] A. Stolow, A. E. Bragg, and D. M. Neumark. "Femtosecond time-resolved photoelectron spectroscopy". *Chem. Rev.*, **104**(4):1719, (2004).

[14] A. Stolow and J. G. Underwood. "Time-resolved photoelectron spectroscopy of nonadiabatic dynamics in polyatomic molecules". *Adv. Chem. Phys.*, **139**:497, (2008).

[15] R. G. W. Norrish and G. Porter. "Chemical reactions produced by very high light intensities", (1949).

[16] G. Porter. "Flash photolysis and spectroscopy. A new method for the study of free radical reactions". *Proc. R. Soc. Lond. A Math. Phys. Sci.*, **200**(1061):284, (1950).

[17] Ahmed H. Zewail. "Femtochemistry: Atomic-scale dynamics of the chemical bond". *J. Phys. Chem. A*, **104**(24):5660, (2000).

[18] F. Krausz and M. Y. Ivanov. "Attosecond physics". *Rev. Mod. Phys.*, **81**:163, (2009).

[19] S. Toshinori. "Time-resolved photoelectron spectroscopy of non-adiabatic electronic dynamics in gas and liquid phases". *Int. Rev. Phys. Chem.*, **31**(2):265, (2012).

[20] R. Spesyvtsev, J. G. Underwood, and H. H. Fielding. *"Time-resolved photoelectron spectroscopy for excited state dynamics"*, page 99. Springer International Publishing, (2014).

[21] K. L. Reid. "Photoelectron angular distributions". *Ann. Rev. Phys. Chem.*, **54**:397, (2003).

[22] C. J. Danby and J. H. D. Eland. "Photoelectron-photoion coincidence spectroscopy". *Int. J. Mass Spectrom. Ion. Process.*, **8**(2):153, 1972.

[23] J. H. D. Eland. "Photoelectron-photoion coincidence spectroscopy". *Int. J. Mass Spectrom. Ion Process.*, **8**(2):143, (1972).

[24] J. A. Davies, J. E. LeClaire, R. E. Continetti, and C. C. Hayden. "Femtosecond time-resolved photoelectron–photoion coincidence imaging studies of dissociation dynamics". *J. Chem. Phys.*, **111**(1):1, (1999).

[25] V. Stert, W. Radloff, C.P. Schulz, and I.V. Hertel. "Ultrafast photoelectron spectroscopy: Femtosecond pump-probe coincidence detection of ammonia cluster ions and electrons". *Eur. Phys. J. D*, **5**(1):97, (1999).

[26] C. Z. Bisgaard, O. J. Clarkin, G. Wu, A. M. D. Lee, O. Gessner, C. C. Hayden, and A. Stolow. "Time-resolved molecular frame dynamics of fixed-in-space CS_2 molecules". *Science*, **323**(5920):1464, (2009).

[27] P. Hockett, C. Z. Bisgaard, O. J. Clarkin, and A. Stolow. "Time-resolved imaging of purely valence-electron dynamics during a chemical reaction". *Nat. Phys.*, **7**(8):612, (2011).

[28] P. Hockett, E. Ripani, A. Rytwinski, and A. Stolow. "Probing ultrafast dynamics with time-resolved multi-dimensional coincidence imaging: butadiene". *J. Mod. Opt.*, **60**(17):1409, (2013).

[29] D. R. Cyr and C. C. Hayden. "Femtosecond time-resolved photoionization and photoelectron spectroscopy studies of ultrafast internal conversion in 1,3,5-hexatriene". *J. Chem. Phys.*, **104**(2):771, (1996).

[30] V. Blanchet, M. Z. Zgierski, T. Seideman, and A. Stolow. "Discerning vibronic molecular dynamics using time-resolved photoelectron spectroscopy". *Nature*, **401**(6748):52, (1999).

[31] T. Horio, T. Fuji, Y. Suzuki, and T. Suzuki. "Probing ultrafast internal conversion through conical intersection via time-energy map of photoelectron angular anisotropy". *J. Amer. Chem. Soc.*, **131**(30):10392, (2009).

[32] R. S. Minns, D. S. N. Parker, T. J. Penfold, G. A. Worth, and H. H. Fielding. "Competing ultrafast intersystem crossing and internal conversion in the "channel 3" region of benzene". *Phys. Chem. Chem. Phys.*, **12**:15607, (2010).

[33] Y. Suzuki, T. Fuji, T. Horio, and T. Suzuki. "Time-resolved photoelectron imaging of ultrafast $S_2 \rightarrow S_1$ internal conversion through conical intersection in pyrazine". *J. Chem. Phys.*, **132**(17):174302, (2010).

[34] B. Kim, C. P. Schick, and P. M. Weber. "Time-delayed two-color photoelectron spectra of aniline, 2-aminopyridine, and 3-aminopyridine: Snapshots of the nonadiabatic curve crossings". *J. Chem. Phys.*, **103**(16):6903, (1995).

[35] D. S. N. Parker, R. S. Minns, T. J. Penfold, G. A. Worth, and H. H. Fielding. "Ultrafast dynamics of the S_1 excited state of benzene". *Chem. Phys. Lett.*, **469**(1):43, (2009).

[36] V. Blanchet and A. Stolow. "Nonadiabatic dynamics in polyatomic systems studied by femtosecond time-resolved photoelectron spectroscopy". *J. Chem. Phys.*, **108**(11):4371, (1998).

[37] O. Gessner, A. M. D. Lee, J. P. Shaffer, H. Reisler, S. V. Levchenko, A. I. Krylov, J. G Underwood, H. Shi, A. L. L. East, D. M. Wardlaw, E. T. H. Chrysostom, C. C. Hayden, and A. Stolow. "Femtosecond multidimensional imaging of a molecular dissociation". *Science*, **311**(5758):219, (2006).

[38] "R. de Nalda and J. Durá and A. García-Vela and J. G. Izquierdo and J. González-Vázquez and L. Bañares". "A detailed experimental and theoretical study of the femtosecond A-band photodissociation of CH_3I". *J. Chem. Phys.*, **128**(24):244309, (2008).

[39] T. Horio, R. Spesyvtsev, Y. Furumido, and T. Suzuki. "Real-time detection of $S(^1D_2)$ photofragments produced from the $^1B_2(^1\Sigma_u^+)$ state of CS_2 by vacuum ultraviolet photoelectron imaging using 133 nm probe pulses". *J. Chem. Phys.*, **147**(1):013932, (2017).

[40] F. Braußе, G. Goldsztejn, K. Amini, R. Boll, S. Bari, C. Bomme, M. Brouard, M. Burt, B. C. de Miranda, S. Düsterer, . Erk, M. Géléoc, R. Geneaux, A. S. Gentleman, R. Guillemin, I. Ismail, P. Johnsson, L. Journel, T. Kierspel, H. Köckert, J. Küpper, P. Lablanquie, J. Lahl, J. W. L. Lee, S. R. Mackenzie, S. Maclot, B. Manschwetus, Andrey S. M., T. Mullins, P. K. Olshin, J. Palaudoux, S. Patchkovskii, F. Penent, M. N. Piancastelli, D. Rompotis, T. Ruchon, A. Rudenko, E. Savelyev, N. Schirmel, S. Techert, O. Travnikova, S. Trippel, J. G. Underwood, C. Vallance, J. Wiese, M. Simon, D. M. P. Holland, T. Marchenko, A. Rouzée, and D. Rolles. "Time-resolved inner-shell photoelectron spectroscopy: From a bound molecule to an isolated atom". *Phys. Rev. A*, **97**:043429, (2018).

[41] T. Brabec and F. Krausz. "Intense few-cycle laser fields: Frontiers of nonlinear optics". *Rev. Mod. Phys.*, **72**:545, (2000).

[42] P. Agostini, F. Fabre, G. Mainfray, G. Petite, and N. K. Rahman. "Free-free transitions following six-photon ionization of xenon atoms". *Phys. Rev. Lett.*, **42**(17):1127, (1979).

[43] R. R. Freeman, P. H. Bucksbaum, H. Milchberg, S. Darack, D. Schumacher, and M. E. Geusic. "Above-threshold ionization with subpicosecond laser pulses". *Phys. Rev. Lett.*, **59**(**10**):1092, (1987).

[44] G. G. Paulus, W. Nicklich, Huale Xu, P. Lambropoulos, and H. Walther. "Plateau in above threshold ionization spectra". *Phys. Rev. Lett.*, **72**:2851, (1994).

[45] A. McPherson, G. Gibson, H. Jara, U. Johann, T. S. Luk, I. A. McIntyre, K. Boyer, and C. K. Rhodes. "Studies of multiphoton production of vacuum-ultraviolet radiation in the rare gases". *J. Opt. Soc. Am. B*, **4**(4):595, (1987).

[46] M. Ferray, A. L'Huillier, X. F. Li, L. A. Lompre, G. Mainfray, and C. Manus. "Multiple-harmonic conversion of 1064 nm radiation in rare gases". *J. Phys. B: At., Mol. Opt. Phys.*, **21**(3):L31, (1988).

[47] P. B. Corkum. "Plasma perspective on strong field multiphoton ionization". *Phys. Rev. Lett.*, **71**(13):1994, (1993).

[48] M. Meckel, D. Comtois, D. Zeidler, A. Staudte, D. Pavičić, H. C. Bandulet, H. Pépin, J. C. Kieffer, R. Dörner, D. M. Villeneuve, and P. B. Corkum. "Laser-Induced electron tunneling and diffraction". *Science*, **320**(5882):1478, (2008).

[49] S. Baker, J. S. Robinson, C. A. Haworth, H. Teng, R. A. Smith, C. C. Chirila, M. Lein, J. W. G. Tisch, and J. P. Marangos. "Probing proton dynamics in molecules on an attosecond time scale". *Science*, **312**(5772):424, (2006).

[50] H. J. Wörner, J. B. Bertrand, D. V. Kartashov, P. B. Corkum, and D. M. Villeneuve. "Following a chemical reaction using high-harmonic interferometry". *Nature*, **466**(7306):604, (2010).

[51] H. J. Wörner, J. B. Bertrand, P. B. Corkum, and D. M. Villeneuve. "High-harmonic homodyne detection of the ultrafast dissociation of Br_2 molecules". *Phys. Rev. Lett.*, **105**:103002, (2010).

[52] C. I. Blaga, J. Xu, A. D. DiChiara, E. Sistrunk, K. Zhang, P. Agostini, T. A. Miller, L. F. DiMauro, and C. D. Lin. "Imaging ultrafast molecular dynamics with laser-induced electron diffraction". *Nature*, **483**:194, (2012).

[53] B. Wolter, M. G. Pullen, A.-T. Le, M. Baudisch, K. Doblhoff-Dier, A. Senftleben, M. Hemmer, C. D. Schröter, J Ullrich, T. Pfeifer, R Moshammer, Gräfe, S., O Vendrell, C. D. Lin, and J. Biegert. "Ultrafast electron diffraction imaging of bond breaking in di-ionized acetylene". *Science*, **354**:308, (2016).

[54] P. Emma, K. Bane, M. Cornacchia, Z. Huang, H. Schlarb, G. Stupakov, and D. Walz. "Femtosecond and subfemtosecond X-Ray pulses from a self-amplified spontaneous-emission-based free-electron laser". *Phys. Rev. Lett.*, **92**:074801, (2004).

[55] Tetsuya *et al.* Ishikawa. "A compact X-ray free-electron laser emitting in the sub-ångström region". *Nat. Photon.*, **6**:540, (2012).

[56] H. Ihee, V. A. Lobastov, U. M. Gomez, B. M. Goodson, R. Srinivasan, C.-Y. Ruan, and A. H. Zewail. "Direct imaging of transient molecular structures with ultrafast diffraction". *Science*, **291**(5503):458, (2001).

[57] B. J. Siwick, J. R. Dwyer, R. E. Jordan, and R. J. D. Miller. "An atomic-level view of melting using femtosecond electron diffraction". *Science*, **302**(5649):1382, (2003).

[58] J. B. Hastings, F. M. Rudakov, D. H. Dowell, J. F. Schmerge, J. D. Cardoza, J. M. Castro, S. M. Gierman, H. Loos, and P. M. Weber. "'Ultrafast time-resolved electron diffraction with megavolt electron beams". *Appl. Phys. Lett.*, **89**(18):184109, (2006).

[59] M. P. Minitti, J. M. Budarz, A. Kirrander, J. S. Robinson, D. Ratner, T. J. Lane, D. Zhu, J. M. Glownia, M. Kozina, H. T. Lemke, M. Sikorski, Y. Feng, S. Nelson, K. Saita, B. Stankus, T. Northey, J. B. Hastings, and P. M. Weber. "Imaging molecular motion: Femtosecond X-Ray scattering of an electrocyclic chemical reaction". *Phys. Rev. Lett.*, **114**:255501, (2015).

[60] J. M. Glownia, A. Natan, J. P. Cryan, R. Hartsock, M. Kozina, M. P. Minitti, S. Nelson, J. Robinson, T. Sato, T. van Driel, G. Welch, C. Weninger,

D. Zhu, and P. H. Bucksbaum. "Self-referenced coherent diffraction X-Ray movie of Ångstrom- and femtosecond-scale atomic motion". *Phys. Rev. Lett.*, **117**:153003, (2016).

[61] J. Yang, M. G "uhr, X. Shen, R. Li, T. Vecchione, R. Coffee, J. Corbett, A. Fry, N. Hartmann, C. Hast, K. Hegazy, K. Jobe, I. Makasyuk, J. Robinson, M. S. Robinson, S. Vetter, S. Weathersby, C. Yoneda, X. Wang, and M. Centurion. "Diffractive imaging of coherent nuclear motion in isolated molecules". *Phys. Rev. Lett.*, **117**:153002, (2016).

[62] J. Yang, X. Zhu, T. J. A. Wolf, Z. Li, J. P. F. Nunes, R. Coffee, J. P. Cryan, M. Gühr, K. Hegazy, T. F. Heinz, K. Jobe, R. Li, X. Shen, T. V., Stephen W., Kyle J. W., C. Yoneda, Q. Zheng, T. J. Martinez, M. Centurion, and X. Wang. "Imaging CF_3I conical intersection and photodissociation dynamics with ultrafast electron diffraction". **361**(6397):64, (2018).

[63] L. J. Frasinski, K. Codling, P. Hatherly, J. Barr, I. N. Ross, and W. T. Toner. "Femtosecond dynamics of multielectron dissociative ionization by use of a picosecond laser". *Phys. Rev. Lett.*, **58**:2424, (1987).

[64] H. Stapelfeldt, E. Constant, H. Sakai, and P. B. Corkum. "Time-resolved Coulomb explosion imaging: A method to measure structure and dynamics of molecular nuclear wave packets". *Phys. Rev. A*, **58**:426, (1998).

[65] F. Légaré, Kevin F. Lee, I. V. Litvinyuk, P. W. Dooley, S. S. Wesolowski, P. R. Bunker, P. Dombi, F. Krausz, A. D. Bandrauk, D. M. Villeneuve, and P. B. Corkum. "Laser Coulomb-explosion imaging of small molecules". *Phys. Rev. A*, **71**:013415, (2005).

[66] H. Ibrahim, B. Wales, S. Beaulieu, B. E. Schmidt, N. Thiré, E. P. Fowe, É. Bisson, C. T. Hebeisen, V. Wanie, M. Giguére, J.-C. Kieffer, M. Spanner, A. D. Bandrauk, J. Sanderson, M. S. Schuurman, and F. Légaré. "Tabletop imaging of structural evolutions in chemical reactions demonstrated for the acetylene cation". *Nat. Comm.*, **5**:4422, (2014).

[67] C. E. Liekhus-Schmaltz, I. Tenney, T. Osipov, A. Sanchez-Gonzalez, N. Berrah, R. Boll, C. Bomme, C. Bostedt, J. D. Bozek, S. Carron, R. Coffee, J. Devin, B. Erk, K. R. Ferguson, R. W. Field, L. Foucar, L. J. Frasinski, J. M. Glownia, M. Gühr, A. Kamalov, J. Krzywinski, H. Li, J. P. Marangos, T. J. Martinez, B. K. McFarland, S. Miyabe, B. Murphy, A. Natan, D. Rolles, A. Rudenko, M. Siano, E. R. Simpson, L. Spector, M. Swiggers, D. Walke, S. Wang, T. Weber, P. H. Bucksbaum, and V. S. Petrovic. "Ultrafast isomerization initiated by X-ray core ionization". *Nat. Comm.*, **6**:8199, (2015).

[68] Z. Li, L. Inhester, C. E. Liekhus-Schmaltz, B. F. E. Curchod, J. W. Snyder, N. Medvedev, J. P. Cryan, T. Osipov, S. Pabst, O. Vendrell, P. H. Bucksbaum, and T. J. Martinez. "Ultrafast isomerization in acetylene dication after carbon K-shell ionization". *Nat. Comm.*, **8**:453, (2017).

[69] M. Burt, R. Boll, J. W. L. Lee, K. Amini, H. Köckert, C. Vallance, A. S. Gentleman, S. R. Mackenzie, S. Bari, C. Bomme, S. Düsterer, B. Erk, B. Manschwetus, E. Müller, D. Rompotis, E. Savelyev, N. Schirmel, S. Techert, R. Treusch, J. Küpper, S. Trippel, J. Wiese, H. Stapelfeldt, B. C. de Miranda, R. Guillemin, I. Ismail, L. Journel, T. Marchenko, J. Palaudoux, F. Penent, M. N. Piancastelli, M. Simon, O. Travnikova, F. Brausse, G. Goldsztejn, A. Rouzée, M. Géléoc, R. Geneaux, T. Ruchon, J. Underwood, D. M. P. Holland, A. S. Mereshchenko, P. K. Olshin, P. Johnsson, S. Maclot, J. Lahl, A. Rudenko, F. Ziaee, M. Brouard, and D. Rolles. "Coulomb-explosion imaging of concurrent CH_2BrI photodissociation dynamics". *Phys. Rev. A*, **96**:043415, (2017).

[70] K. Amini, E. Savelyev, F. Braußе, N. Berrah, C. Bomme, M. Brouard, M. Burt, L. Christensen, S. Düsterer, B. Erk, H. Höppner, T. Kierspel, F. Krecinic, A. Lauer, J. W. L. Lee, M. Müller, E. Müller, T. Mullins, H. Redlin, N. Schirmel, J. Thøgersen, S. Techert, S. Toleikis, R. Treusch, S. Trippel, A. Ulmer, C. Vallance, J. Wiese, P. Johnsson, J. Küpper, A. Rudenko, A. Rouzée, H. Stapelfeldt, D. Rolles, and R. Boll. "Photodisso-

ciation of aligned CH_3I and $C_6H_3F_2I$ molecules probed with time-resolved Coulomb explosion imaging by site-selective extreme ultraviolet ionization". *Struct. Dyn.*, **5**(1):014301, (2018).

[71] Ch. Spielmann, N. H. Burnett, S. Sartania, R. Koppitsch, M. Schnürer, C. Kan, M. Lenzner, P. Wobrauschek, and F. Krausz. "Generation of coherent X-rays in the water window Using 5-femtosecond laser pulses". *Science*, **278**(5338):661, (1997).

[72] Z. Chang, A. Rundquist, H. Wang, M. M. Murnane, and H. C. Kapteyn. "Generation of coherent soft X-Rays at 2.7 nm using high harmonics". *Phys. Rev. Lett.*, **79**:2967, (1997).

[73] A. Rundquist, C. G. Durfee, Z. Chang, C. Herne, S. Backus, M. M. Murnane, and H. C. Kapteyn. "Phase-matched generation of coherent soft X-rays". *Science*, **280**(5368):1412, (1998).

[74] E. J. Takahashi, T. Kanai, K. L. Ishikawa, Y. Nabekawa, and K. Midorikawa. "Coherent water window X Ray by phase-matched high-order harmonic generation in neutral media". *Phys. Rev. Lett.*, **101**:253901, (2008).

[75] A. R. Attar, A. Bhattacherjee, C. D. Pemmaraju, K. Schnorr, K. D. Closser, D. Prendergast, and S. R. Leone. "Femtosecond x-ray spectroscopy of an electrocyclic ring-opening reaction". *Science*, **356**(6333):54, (2017).

[76] B. Erk, R. Boll, S. Trippel, D. Anielski, L. Foucar, B. Rudek, S. W. Epp, R. Coffee, S. Carron, S. Schorb, K. R. Ferguson, M. Swiggers, J. D. Bozek, M. Simon, T. Marchenko, J. Küpper, I. Schlichting, J. Ullrich, C. Bostedt, D. Rolles, and A. Rudenko. "Imaging charge transfer in iodomethane upon x-ray photoabsorption". *Science*, **345**(6194):288, (2014).

[77] A. Picón, C. S. Lehmann, C. Bostedt, A. Rudenko, A. Marinelli, T. Osipov, D. Rolles, N. Berrah, C. Bomme, M. Bucher, G. Doumy, B. Erk, K. R. Ferguson, T. Gorkhover, P. J. Ho, E. P. Kanter, B. Krässig, J. Krzywinski, A. A.

Lutman, A. M March, D. Moonshiram, D. Ray, L. Young, S. T. Pratt, and S. H. Southworth. "Hetero-site-specific X-ray pump-probe spectroscopy for femtosecond intramolecular dynamics". *Nat. Comms.*, **7**:11652, (2016).

[78] M. Seel and W. Domcke. "Model studies on femtosecond time-resolved ionization spectroscopy of excited-state vibrational dynamics and vibronic coupling". *Chem. Phys.*, **151**(1):59, (1991).

[79] Y. Arasaki, K. Takatsuka, K. Wang, and V. McKoy. "Femtosecond energy- and angle-resolved photoelectron spectra". *Chem. Phys. Lett.*, **302**(5):363, (1999).

[80] L. J. Butler. "Chemical reaction dynamics beyond the Born-Oppenheimer approximation". *Annu. Rev. Phys. Chem.*, **49**:125, (1998).

[81] L. S. Cederbaum, H. Köppel, and W. Domcke. "Multimode vibronic coupling effects in molecules". *Int. J. Quantum Chem.*, **20**(S15):251, (2009).

[82] E. B. Wilson, J. C. Decius, and P. C. Cross. *"Molecular vibrations: The theory of infrared and Raman vibrational spectra"*. Courier Corporation, (1955).

[83] B. H. Bransden and C. J. Joachain. *"Physics of atoms and molecules"*. Prentice Hall, (2003).

[84] H. W. Kroto. *"Molecular rotation spectra"*. Dover Publications, (2003).

[85] R. N. Zare. *"Angular momentum: understanding spatial aspects in chemistry and physics"*. Wiley, (1988).

[86] E. U. Condon. "A theory of intensity distribution in band systems". *Phys. Rev.*, **28**:1182, (1926).

[87] J. Franck and E. G. Dymond. "Elementary processes of photochemical reactions". *Trans. Faraday Soc.*, **21**:536, (1926).

[88] E. U. Condon. "Nuclear motions associated with electron transitions in diatomic molecules". *Phys. Rev.*, **32**:858, (1928).

[89] D. W. Turner. "A Discussion on photoelectron spectroscopy - Molecular photoelectron spectroscopy". *Philos. Trans. Royal Soc. A*, **268**(1184):7, (1970).

[90] T. A. Carlson. "Photoelectron spectroscopy". *Annu. Rev. Phys. Chem.*, **26**(1):211, (1975).

[91] A. Yagishita, K. Hosaka, and J-I. Adachi. "Photoelectron angular distributions from fixed-in-space molecules". *J. Electron Spectrosc. Relat. Phenom.*, **142**(3):295, (2005).

[92] http://www.synchrotron-soleil.fr/Recherche/LignesLumiere/PLEIADES.

[93] A. W. Potts, H. J. Lempka, D. G. Streets, and W. C. Price. "A Discussion on photoelectron spectroscopy - Photoelectron spectra of halides of elements in groups III, IV, V and VI". *Philos. Trans. Royal Soc. A*, **268**(1184):59, (1970).

[94] L. Karlsson, R. Jadrny, L. Mattsson, F. T. Chau, and K. Siegbahn. "Vibrational and vibronic structure in the valence electron spectra of CH 3 X molecules (X=F, Cl, Br, I, OH)". *Phys. Scr.*, **16**(5-6):225, (1977).

[95] W. von Niessen, L. Åsbrink, and G. Bieri. "30.4 nm He (II) photoelectron spectra of organic molecules Part VI. Halogeno-compounds (C, H, X; X = Cl, Br, I)". *J. Electron. Spectrosc. Relat. Phenom.*, **26**(2):173, (1982).

[96] Thomas A. Carlson, Anders Fahlman, Manfred O. Krause, Paul R. Keller, James W. Taylor, Timothy Whitley, and Frederick A. Grimm. "Angle resolved photoelectron spectroscopy of the valence shells in HI and CH_3I as a function of photon energy from 13 to 90 eV". *J. Chem. Phys.*, **80**(8):3521, (1984).

[97] D. M. P. Holland, I. Powis, G. Åhrwall, L. Karlsson, and W. von Niessen. "A study of the photoionisation dynamics of chloromethane and iodomethane". *Chem. Phys.*, **326**(2):535, (2006).

[98] L. S. Cederbaum, W. Domcke, J. Schirmer, and W. Von Niessen. "Correlation effects in the ionization of molecules: breakdown of the molecular orbital picture". *Adv. Chem. Phys*, **65**(115):75, (1986).

[99] *"VUV and soft X-Ray photoionization"*. Springer US, (1996).

[100] K. Siegbahn, C. Nordling, G. Johansson, J. Hedman, P. F. Heden, K. Hamrin, U. Gelius, T. Bergmark, L. O. Werme, R. Manne, and Y. Baer. *"ESCA applied to free molecules"*. North Holland, Amsterdam, (1969).

[101] R. D. Deslattes. "Photoionization of the M Shell of Xenon". *Phys. Rev. Lett.*, **20**(10):483, (1968).

[102] O. Yagci and J. E. Wilson. "3d photoabsorption in gaseous and solid xenon". *J. Phys. C*, **16**(2):383, (1983).

[103] B. Sonntag, T. Nagata, Y. Sato, Y. Satow, A. Yagishita, and M. Yanagihara. "Collapse of the f-symmetric final-state wavefunction in the 3d excitation spectra of atomic Xe, Cs and Ba". *J. Phys. B: At., Mol. Opt. Phys.*, **17**(2):L55, (1984).

[104] U. Arp, K. Iemura, G. Kutluk, T. Nagata, S. Yagi, and A. Yagishita. "3d photoionization of Xe, Cs and Ba and the collapse of the 4f wavefunction". *J. Phys. B: At., Mol. Opt. Phys.*, **32**(5):1295, (1999).

[105] M. Kato, Y. Morishita, M. Oura, H. Yamaoka, Y. Tamenori, K. Okada, T. Matsudo, T. Gejo, I. H. Suzuki, and N. Saito. "Absolute photoionization cross sections with ultra-high energy resolution for Ar, Kr, Xe and N_2 in inner-shell ionization regions". *J. Electron. Spectrosc. Relat. Phenom.*, **160**(1):39, (2007).

[106] N. Saito and I. H. Suzuki. "Yields of multicharged Xe ions in the M-shell transition region". *J. Phys. B: At., Mol. Opt. Phys.*, **25**(8):1785, (1992).

[107] S. H. Southworth, R. Wehlitz, A. Picón, C. S. Lehmann, L. Cheng, and J. F. Stanton. "Inner-shell photoionization and core-hole decay of Xe and XeF_2". *J. Chem. Phys.*, **142**(22):224302, (2015).

[108] U. Becker, H. Kerkhoff, M. Kupsch, B. Langer, D. Szostak, and R. Wehlitz. "Photoionization of Xenon with Soft X-rays". *J. Phys. Colloq.*, **48**(C9):497, (1987).

[109] A. Kivimäki, U. Hergenhahn, B. Kempgens, R. Hentges, M. N. Piancastelli, K. Maier, A. Rüdel, J. J. Tulkki, and A. M. Bradshaw. "Near-threshold study of Xe 3d photoionization". *Phy. Rev. A*, **63**(1):012716, (2000).

[110] J. Viefhaus, M. Braune, S. Korica, A. Reinköster, D. Rolles, and U. Becker. "Auger cascades versus direct double Auger: relaxation processes following photoionization of the Kr 3d and Xe 4d, 3d inner shells". *J. Phys. B: At., Mol. Opt. Phys.*, **38**(21):3885, (2005).

[111] K. Motomura, E. Kukk, H. Fukuzawa, S.-I. Wada, K. Nagaya, S. Ohmura, S. Mondal, T. Tachibana, Y. Ito, R. Koga, T. Sakai, K. Matsunami, A. Rudenko, C. Nicolas, X.-J. Liu, C. Miron, Y. Zhang, Y. Jiang, J. Chen, M. Anand, D. E. Kim, K. Tono, M. Yabashi, M. Yao, and K. Ueda. "Charge and nuclear dynamics induced by deep inner-shell multiphoton ionization of CH_3I molecules by intense X-ray free-electron laser pulses". *J. Phys. Chem. Lett.*, **6**(15):2944, (2015).

[112] K. Nagaya, K. Motomura, E. Kukk, Y. Takahashi, K. Yamazaki, S. Ohmura, H. Fukuzawa, S. Wada, S. Mondal, T. Tachibana, Y. Ito, R. Koga, T. Sakai, K. Matsunami, K. Nakamura, M. Kanno, A. Rudenko, C. Nicolas, X.-J. Liu, C. Miron, Y. Zhang, Y. Jiang, J. Chen, M. Anand, D. E. Kim, K. Tono, M. Yabashi, M. Yao, H. Kono, and K. Ueda. "Femtosecond charge and molecular dynamics of I-containing organic molecules induced by intense X-ray free-electron laser pulses". *Faraday Discuss.*, **194**:537, (2016).

[113] R. Boll, B. Erk, R. Coffee, S. Trippel, T. Kierspel, C. Bomme, J. D. Bozek, M. Burkett, S. Carron, K. R. Ferguson, L. Foucar, J. Küpper, T. Marchenko, C. Miron, M. Patanen, T. Osipov, S. Schorb, M. Simon, M. Swiggers, S. Techert, K. Ueda, C. Bostedt, D. Rolles, and A. Rudenko. "Charge transfer in dissociating iodomethane and fluoromethane molecules ionized by intense femtosecond X-ray pulses". *Struct. Dyn.*, **3**(4):043207, (2016).

[114] K. Nagaya, K. Motomura, E. Kukk, H. Fukuzawa, S. Wada, T. Tachibana, Y. Ito, S. Mondal, T. Sakai, K. Matsunami, R. Koga, S. Ohmura, Y. Takahashi, M. Kanno, A. Rudenko, C. Nicolas, X.-J. Liu, Y. Zhang, J. Chen, M. Anand, Y. H. Jiang, D.-E. Kim, K. Tono, M. Yabashi, H. Kono, C. Miron, M. Yao, and K. Ueda. "Ultrafast dynamics of a nucleobase analogue illuminated by a short intense X-ray free electron laser pulse". *Phys. Rev. X*, **6**:021035, (2016).

[115] A. Rudenko, L. Inhester, K. Hanasaki, X. Li, S. J. Robatjazi, B. Erk, R. Boll, K. Toyota, Y. Hao, O. Vendrell, C. Bomme, E. Savelyev, B. Rudek, L. Foucar, S. H. Southworth, C. S. Lehmann, B. Kraessig, T. Marchenko, M. Simon, K. Ueda, K. R. Ferguson, M. Bucher, T. Gorkhover, S. Carron, R. Alonso-Mori, J. E. Koglin, J. Correa, G. J. Williams, S. Boutet, L. Young, C. Bostedt, S.-K. Son, R. Santra, and D. Rolles. "Femtosecond response of polyatomic molecules to ultra-intense hard X-rays". *Nature*, **546**:129, (2017).

[116] K. Amini, E. Savelyev, F. BrauSSe, N. Berrah, C. Bomme, M. Brouard, M. Burt, L. Christensen, S. Düsterer, B. Erk, H. Höppner, T. Kierspel, F. Krecinic, A. Lauer, J. W. L. Lee, M. Müller, E. Müller, T. Mullins, H. Redlin, N. Schirmel, J. Thøgersen, S. Techert, S. Toleikis, R. Treusch, Sebastian Trippel, Anatoli Ulmer, Claire Vallance, Joss Wiese, P. Johnsson, J. Küpper, A. Rudenko, A. Rouzée, H. Stapelfeldt, D. Rolles, and R. Boll. "Photodissociation of aligned CH_3I and $C_6H_3F_2I$ molecules probed with time-resolved Coulomb explosion imaging by site-selective extreme ultraviolet ionization". *Struct. Dyn.*, **5**(1):014301, (2018).

[117] S. Svensson, B. Eriksson, N. Mårtensson, G. Wendin, and U. Gelius. "Electron shake-up and correlation satellites and continuum shake-off distributions in X-Ray photoelectron spectra of the rare gas atoms". *J. Electron. Spectrosc. Relat. Phenom.*, **47**:327, (1988).

[118] S. Svensson, B. Eriksson, N. Mårtensson, G. Wendin, and U. Gelius. "Electron shake-up and correlation satellites and continuum shake-off distributions in X-Ray photoelectron spectra of the rare gas atoms". *J. Electron. Spectrosc. Relat. Phenom.*, **47**:327, (1988).

[119] L. O. Werme, T. Bergmark, and K. Siegbahn. "The high resolution $L_{2,3}MM$ and $M_{4,5}NN$ Auger spectra from krypton and $M_{4,5}NN$ and $N_{4,5}OO$ Auger spectra from xenon". *Phys. Scr.*, **6**(2-3):141, (1972).

[120] T. A. Carlson and M. O. Krause. "Experimental evidence for double electron emission in an Auger process". *Phys. Rev. Lett.*, **14**:390, (1965).

[121] T. A. Carlson and M. O. Krause. "Measurement of the electron energy spectrum resulting from a double Auger process in argon". *Phys. Rev. Lett.*, **17**:107, (1966).

[122] J. Viefhaus, A.N. Grum-Grzhimailo, N.M. Kabachnik, and U. Becker. "Electron–electron coincidence study of double Auger processes in atoms". *J. Electron. Spectrosc. Relat. Phenom.*, **141**(2):121, (2004).

[123] A. D. Bandruk. *"Atomic and molecular processes with short intense laser pulses"*. Plenum Press, (1988).

[124] M. Protopapas, C. H. Keitel, and P. L. Knight. "Atomic physics with super-high intensity lasers". *Rep. Prog. Phys.*, **60**(4):389, (1997).

[125] P. B. Corkum, M. Yu. Ivanov, and J. S. Wright. Subfemtosecond processes in strong laser fields. *Annu. Rev. Phys. Chem.*, **48**(1):387, (1997).

[126] F. Fabre, G. Petite, P. Agostini, and M. Clement. "Multiphoton above-threshold ionisation of xenon at 0.53 and 1.06μm". *J. Phys. B: At., Mol. Opt. Phys.*, **15**(9):1353, (1982).

[127] M. P. Hertlein, P. H. Bucksbaum, and H. G. Muller. "Evidence for resonant effects in high-order ATI spectra". *J. Phys. B: At., Mol. Opt. Phys.*, **30**(6):L197, (1997).

[128] Y. Gontier and M. Trahin. "Energetic electron generation by multiphoton absorption". *J. Phys. B: At., Mol. Opt. Phys.*, **13**(22):4383, (1980).

[129] V. P. Krainov M. V. Ammosov, N. B. Delone. "Tunnel ionization of complex atoms and of atomic ions in an alternating electromagnetic field ". *JETP*, **64**(6):1191, (1988).

[130] G. L. Yudin and M. Y. Ivanov. "Nonadiabatic tunnel ionization: Looking inside a laser cycle". *Phys. Rev. A*, **64**:013409, (2001).

[131] L. V. Keldysh. Ionization in the field of a string electromagnetic wave. *J. Exp. Theor. Phys*, **20**(5):1307, (1965).

[132] I. V. Litvinyuk, K. F. Lee, P. W. Dooley, D. M. Rayner, D. M. Villeneuve, and P. B. Corkum. "Alignment-dependent strong field ionization of molecules". *Phys. Rev. Lett.*, **90**(23):233003, (2003).

[133] C. Guo, M. Li, J. P. Nibarger, and G. N. Gibson. "Single and double ionization of diatomic molecules in strong laser fields". *Phys. Rev. A*, **58**(6):R4271, (1998).

[134] T. K. Kjeldsen, C. Z. Bisgaard, L. B. Madsen, and H. Stapelfeldt. "Role of symmetry in strong-field ionization of molecules". *Phys. Rev. A*, **68**:063407, (2003).

[135] J. Muth-Böhm, A. Becker, and F. H. M. Faisal. "Suppressed molecular ionization for a class of diatomics in intense femtosecond laser fields". *Phys. Rev. Lett.*, **85**:2280, (2000).

[136] A. J. Becker, A. Becker, and F. H. M. Faisal. "Ionization of N_2, O_2, and linear carbon clusters in a strong laser pulse". *Phys. Rev. A*, **69**:023410, (2004).

[137] M. Ivanov, T. Seideman, P. Corkum, F. Ilkov, and P. Dietrich. "Explosive ionization of molecules in intense laser fields". *Phys. Rev. A*, **54**:1541, (1996).

[138] T. Zuo and A. D. Bandrauk. "Charge-resonance-enhanced ionization of diatomic molecular ions by intense lasers". *Phys. Rev. A*, **52**:R2511, (1995).

[139] Tamar Seideman, M. Yu. Ivanov, and P. B. Corkum. "Role of electron localization in intense-field molecular ionization". *Phys. Rev. Lett.*, **75**:2819, (1995).

[140] E. Constant, H. Stapelfeldt, and P. B. Corkum. "Observation of enhanced ionization of molecular ions in intense laser fields". *Phys. Rev. Lett.*, **76**:4140, (1996).

[141] K. Codling, L. J. Frasinski, and P. A. Hatherly. "On the field ionisation of diatomic molecules by intense laser fields". *J. Phys. B: At., Mol. Opt. Phys.*, **22**(12):L321, (1989).

[142] B. K. McFarland, J. P. Farrell, P. H. Bucksbaum, and M. Gühr. "High harmonic generation from multiple orbitals in N_2". *Science*, **322**(5905):1232, (2008).

[143] H. Akagi, T. Otobe, A. Staudte, A. Shiner, F. Turner, R. Dörner, D. M. Villeneuve, and P. B. Corkum. "Laser tunnel ionization from multiple orbitals in HCl". *Science*, **325**(5946):1364, (2009).

[144] O. Smirnova, Y. Mairesse, S. Patchkovskii, N. Dudovich, D. Villeneuve, P. Corkum, and M. Y. Ivanov. "High harmonic interferometry of multi-electron dynamics in molecules". *Nature*, **460**(7258):972, (2009).

[145] R. Torres, T. Siegel, L. Brugnera, I. Procino, Jonathan G. Underwood, C. Altucci, R. Velotta, E. Springate, C. Froud, I. C. E. Turcu, S. Patchkovskii,

M. Yu. Ivanov, O. Smirnova, and J. P. Marangos. "Revealing molecular structure and dynamics through high-order harmonic generation driven by mid-IR fields". *Phys. Rev. A*, **81**(5):051802, (2010).

[146] W. Li, X. Zhou, R. Lock, S. Patchkovskii, A. Stolow, H. C. Kapteyn, and M. M. Murnane. "Time-resolved dynamics in N_2O_4 probed using high harmonic generation". *Science*, **322**(5905):1207, (2008).

[147] M. Spanner, J. Mikosch, A. E. Boguslavskiy, M. M. Murnane, A. Stolow, and S. Patchkovskii. "Strong-field ionization and high-order-harmonic generation during polyatomic molecular dynamics of N_2O_4". *Phys. Rev. A*, **85**(3):033426, (2012).

[148] Q. Ji, S. Cui, X. You, X. Gong, Q. Song, K. Lin, H. Pan, J. Ding, H. Zeng, F. He, and J. Wu. "Orbital-resolved strong-field single ionization of acetylene". *Phys. Rev. A*, **92**(4):043401, (2015).

[149] A. Ferré, A. E. Boguslavskiy, M. Dagan, V. Blanchet, B. D. Bruner, F. Burgy, A. Camper, D. Descamps, B. Fabre, N. Fedorov, J. Gaudin, G. Geoffroy, J. Mikosch, S. Patchkovskii, S. Petit, T. Ruchon, H. Soifer, D. Staedter, I. Wilkinson, A. Stolow, N. Dudovich, and Y. Mairesse. "Multi-channel electronic and vibrational dynamics in polyatomic resonant high-order harmonic generation". *Nat. Comms.*, **6**:5952, (2015).

[150] M. Lezius, V. Blanchet, D. M. Rayner, D. M. Villeneuve, A. Stolow, and M. Y. Ivanov. "Nonadiabatic multielectron dynamics in strong field molecular ionization". *Phys. Rev. Lett.*, **86**(1):51, (2001).

[151] M. Lezius, V. Blanchet, Misha Yu. Ivanov, and Albert Stolow. "Polyatomic molecules in strong laser fields: Nonadiabatic multielectron dynamics". *J. Chem. Phys.*, **117**(4):1575, (2002).

[152] A. E. Boguslavskiy, J. Mikosch, A. Gijsbertsen, M. Spanner, S. Patchkovskii, N. Gador, M. J. J. Vrakking, and A. Stolow. "The multielectron ioniza-

tion dynamics underlying attosecond strong-field spectroscopies". *Science*, **335**(6074):1336, (2012).

[153] J. Mikosch, A. E. Boguslavskiy, I. Wilkinson, M. Spanner, S. Patchkovskii, and A. Stolow. "Channel- and angle-resolved above threshold ionization in the molecular frame". *Phys. Rev. Lett.*, **110**(2):023004, (2013).

[154] V. Makhija, X. Ren, D. Gockel, A. T. Le, and V. Kumarappan. "Orientation resolution through rotational coherence spectroscopy". *arXiv*, **1611.06476**, (2016).

[155] R. Signorell and F. Merkt. "General symmetry selection rules for the photoionization of polyatomic molecules". *Mol. Phys.*, **92**(5):793, (1997).

[156] C. N. Yang. "On the angular distribution in nuclear reactions and coincidence measurements". *Phys. Rev.*, **74**:764, (1948).

[157] D. Dill. "Fixed-molecule photoelectron angular distributions". *J. Chem. Phys.*, **65**(3):1130, (1976).

[158] S. Adachi, M. Sato, and T. Suzuki. "Direct observation of ground-state product formation in a 1,3-cyclohexadiene ring-opening reaction". *J. Phys. Chem. Lett.*, **6**(3):343, (2015).

[159] L. Nugent-Glandorf, M. Scheer, D. A. Samuels, A. M. Mulhisen, E. R. Grant, X. Yang, V. M. Bierbaum, and S. R. Leone. "Ultrafast time-resolved soft X-Ray photoelectron spectroscopy of dissociating Br_2". *Phys. Rev. Lett.*, **87**:193002, (2001).

[160] D. Smith, A, E. M. Warne, D. Bellshaw, D. A. Horke, M. Tudorovskya, E. Springate, A. J. H. Jones, C. Cacho, R. T. Chapman, A. Kirrander, and R. S. Minns. "Mapping the complete reaction path of a complex photochemical reaction". *Phys. Rev. Lett.*, **120**:183003, (2018).

[161] V. Blanchet, M. Z. Zgierski, and A. Stolow. "Electronic continua in time-resolved photoelectron spectroscopy. I. Complementary ionization correlations". *J. Chem. Phys.*, **114**(3):1194, (2001).

[162] M. Schmitt, S. Lochbrunner, J. P. Shaffer, J. J. Larsen, M. Z. Zgierski, and Albert Stolow. "Electronic continua in time-resolved photoelectron spectroscopy. II. Corresponding ionization correlations". *J. Chem. Phys.*, **114**(3):1206, (2001).

[163] S. T. Pratt. "Excited-state molecular photoionization dynamics". *Rep. Prog. Phys.*, **58**(8):821, (1995).

[164] S. Matsika, M. Spanner, M. Kotur, and T. C. Weinacht. "Ultrafast relaxation dynamics of uracil probed via strong field dissociative ionization". *J. Phys. Chem. A*, **117**(48):12796, (2013).

[165] H. J. Wörner, J. B. Bertrand, B. Fabre, J. Higuet, H. Ruf, A. Dubrouil, S. Patchkovskii, M. Spanner, Y. Mairesse, V. Blanchet, E. Mével, E. Constant, P. B. Corkum, and D. M. Villeneuve. "Conical intersection dynamics in NO_2 probed by homodyne high-harmonic spectroscopy". *Science*, **334**(6053):208, (2011).

[166] H. Ruf, C. Handschin, A. Ferré, N. Thiré, J. B. Bertrand, L. Bonnet, R. Cireasa, E. Constant, P. B. Corkum, D. Descamps, B. Fabre, P. Larregaray, E. Mével, S. Petit, B. Pons, D. Staedter, H. J. Wörner, D. M. Villeneuve, Y. Mairesse, P. Halvick, and V. Blanchet. "High-harmonic transient grating spectroscopy of NO_2 electronic relaxation". *J. Chem. Phys.*, **137**(22):224303, (2012).

[167] P. M. Kraus, Y. Arasaki, J. B. Bertrand, S. Patchkovskii, P. B. Corkum, D. M. Villeneuve, K. Takatsuka, and H. J. Wörner. "Time-resolved high-harmonic spectroscopy of nonadiabatic dynamics in NO_2". *Phys. Rev. A*, **85**(4):043409, (2012).

[168] A. Tehlar and H. J. Wörner. "Time-resolved high-harmonic spectroscopy of the photodissociation of CH_3I and CF_3I". *Mol. Phy.*, **111**(14-15):2057, (2013).

[169] M. Lewenstein, P. Balcou, M. Y. Ivanov, A. L'Huillier, and P. B. Corkum. "Theory of high-harmonic generation by low-frequency laser fields". *Phys. Rev. A*, **49**(3):2117, (1994).

[170] V. H. Le, A. T. Le, R. H. Xie, and C. D. Lin. "Theoretical analysis of dynamic chemical imaging with lasers using high-order harmonic generation". *Phys. Rev. A*, **76**:013414, (2007).

[171] A. T. Le, R. R. Lucchese, S. Tonzani, T. Morishita, and C. D. Lin. "Quantitative rescattering theory for high-order harmonic generation from molecules". *Phys. Rev. A*, **80**:013401, (2009).

[172] R. E. Smalley. "Laser spectroscopy of supersonic molecular beams: Application to the NO_2 spectrum". *J. Chem. Phys.*, **61**(10):4363, (1974).

[173] H. Zacharias. "Laser photofragment spectroscopy of the NO_2 dissociation at 337 nm. A nonstatistical decay process". *J. Chem. Phys.*, **74**(1):218, (1981).

[174] L. Bigio and E. R. Grant. "Optical-selection in the double resonant two-photon photodissociation of NO_2". In *AIP Conference Proceedings*, volume **146**, page 501. AIP, (1986).

[175] L. Bigio and E. R. Grant. "Two-photon photodissociation dynamics of state-selected NO_2". *J. Chem. Phys.*, **87**(1):360, (1987).

[176] S. A. Reid and H. Reisler. "Unimolecular reaction of NO_2 : Overlapping resonances, fluctuations, and the transition state". *J. Phys. Chem.*, **100**(2):474, (1996).

[177] G. K. Jarvis, Y. Song, C. Y. Ng, and E. R. Grant. "A characterization of vibrationally and electronically excited NO_2^+ by high-resolution threshold photoionization spectroscopy". *J. Chem. Phys.*, **111**(21):9568, (1999).

[178] I. Bezel, P. Ionov, and C. Wittig. "Photoinitiated unimolecular decomposition of NO_2: Rotational dependence of the dissociation rate". *J. Chem. Phys.*, **111**(20):9267, (1999).

[179] I. Bezel, D. Stolyarov, and C. Wittig. "Unimolecular Reaction Rate Constants of NO_2 Just above D_0". *J. Phys. Chem. A*, **103**(49):10268, (1999).

[180] M. Brouard, R. Cireasa, A. P. Clark, T. J. Preston, and C. Vallance. "The photodissociation dynamics of NO_2 at 308 nm and of NO_2 and N_2O_4 at 226 nm". *J. Chem. Phys.*, **124**(6):64309, (2006).

[181] R. B. L'opez-Martens, T. W. Schmidt, and G. Roberts. "Femtosecond fluorescence depletion spectroscopy of NO_2 multiphoton dissociation dynamics". *J. Chem. Phys.*, **111**(16):7183, (1999).

[182] A. T. J. B. Eppink, B. J. Whitaker, E. Gloaguen, B. Soep, A. M. Coroiu, and D. H. Parker. "Dissociative multiphoton ionization of NO_2 studied by time-resolved imaging". *J. Chem. Phys.*, **121**(16):7776, (2004).

[183] N. T. Form, B. J. Whitaker, L. Poisson, and B. Soep. "Time-resolved photoion and photoelectron imaging of NO_2". *PCCP*, **8**(25):2925, (2006).

[184] A. Vredenborg, W. G. Roeterdink, and M. H. M. Janssen. "Femtosecond time-resolved photoelectron-photoion coincidence imaging of multiphoton multichannel photodynamics in NO_2". *J. Chem. Phys.*, **128**(20):204311, (2008).

[185] B. Liu, J. Zhu, B. Wang, Y. Wang, and L. Wang. "Time-resolved dynamics of NO_2 in its conical intersection region". *J. Phys. Chem. A*, **113**(50):13839, (2009).

[186] D. Irimia, I. D. Petsalakis, G. Theodorakopoulos, and M. H. M. Janssen. "Coherent oscillatory femtosecond dynamics in multichannel photodynamics of NO_2 studied by spatially masked electron imaging". *J. Phys. Chem. A*, **114**(9):3157, (2010).

[187] J. B. Hamard, R. Cireasa, B. Chatel, V. Blanchet, and B. J. Whitaker. "Quantum interference in NO_2". *J. Phys. Chem. A*, **114**(9):3167, (2010).

[188] I. Wilkinson and B. J. Whitaker. "Some remarks on the photodynamics of NO_2". *Annual Reports Section C*, **106**:274, (2010).

[189] U. Manthe and H. Köppel. "Dynamics on potential energy surfaces with a conical intersection: Adiabatic, intermediate, and diabatic behavior". *J. Chem. Phys.*, **93**(3):1658, (1990).

[190] Y. Arasaki, K. Takatsuka, K. Wang, and V. McKoy. "Time-resolved photoelectron spectroscopy of wavepackets through a conical intersection in NO_2". *J. Chem. Phys.*, **132**(12):124307, (2010).

[191] S. I. Ionov, G. A. Brucker, C. Jaques, Y. Chen, and C. Wittig. "Probing the $NO_2 \rightarrow$NO+O transition state via time resolved unimolecular decomposition". *J. Chem. Phys.*, **99**(5):3420, (1993).

[192] A. G. Suits. "Roaming atoms and radicals: a new mechanism in molecular dissociation". *Acc. Chem. Res.*, **41**(7):873, (2008).

[193] M. Sanrey and M. Joyeux. "Slow periodic oscillations in time domain dynamics of NO_2". *J. Chem. Phys.*, **126**(7):074301, (2007).

[194] S. M. Hankin, D. M. Villeneuve, P. B. Corkum, and D. M. Rayner. "Intense-field laser ionization rates in atoms and molecules". *Phys. Rev. A*, **64**:013405, (2001).

[195] I. Wilkinson, A. E. Boguslavskiy, J. Mikosch, J. B. Bertrand, H. J. Wörner, D. M. Villeneuve, M. Spanner, S. Patchkovskii, and A. Stolow. "Excited state dynamics in SO_2. I. Bound state relaxation studied by time-resolved photoelectron-photoion coincidence spectroscopy". *J. Chem. Phys.*, **140**(20):204301, (2014).

[196] A. E. Boguslavskiy, O. Schalk, N. Gador, W. J. Glover, T. Mori, T. Schultz , M.l S. Schuurman, T. J. Martínez, and A. Stolow. "Excited state non-adiabatic dynamics of the smallest polyene, trans 1,3-butadiene. I. Time-resolved photoelectron-photoion coincidence spectroscopy". *J. Chem. Phys.*, **148**(16):164302, (2018).

[197] H. K. Roscoe and A. K. Hind. "The equilibrium constant of NO_2 with N_2O_4 and the temperature dependence of the visible spectrum of NO_2: A critical review and the implications for measurements of NO_2 in the polar stratosphere". *J. Atmos. Chem.*, **16**(3):257, (1993).

[198] T. Tsuboi, E. Y. Xu, Y. K. Bae, and K. T. Gillen. "Magnetic bottle electron spectrometer using permanent magnets". *Rev. Sci. Instrum.*, **59**(8):1357, (1988).

[199] W. C. Wiley and I. H. McLaren. "Time-of-flight mass spectrometer with improved resolution". *Rev. Sci. Instrum.*, **26**(12):1150, (1955).

[200] L. J. Frasinski, K. Codling, and P. A. Hatherly. "Covariance mapping: a correlation method applied to multiphoton multiple ionization". *Science*, **246**(4933):1029, (1989).

[201] L. J. Frasinski, M. Stankiewicz, P. A. Hatherly, G. M. Cross, K. Codling, A. J. Langley, and W. Shaikh. "Molecular H_2 in intense laser fields probed by electron-electron, electron-ion, and ion-ion covariance techniques". *Phys. Rev. A*, **46**(11):R6789, (1992).

[202] M. Spanner and S. Patchkovskii. "One-electron ionization of multielectron systems in strong nonresonant laser fields". *Phys. Rev. A*, **80**(6):063411, (2009).

[203] M. Spanner and S. Patchkovskii. "Molecular strong field ionization and high harmonic generation: A selection of computational illustrations". *Chem. Phys.*, **414**:10, (2013).

[204] D. M. Hirst. "Ab initio potential energy surfaces for excited states of the NO_2^+ molecular ion and for the reaction of N^+ with O_2". *J. Chem. Phys.*, **115**(20):9320, (2001).

[205] V. Schyja, T. Lang, and H. Helm. "Channel switching in above-threshold ionization of xenon". *Phys. Rev. A*, **57**:3692, (1998).

[206] P. H. Bucksbaum, A. Zavriyev, H. G. Muller, and D. W. Schumacher. "Softening of the H_2^+ molecular bond in intense laser fields". *Phys. Rev. Lett.*, **64**:1883, (1990).

[207] S. Mahapatra, H. Köppel, L.S. Cederbaum, P. Stampfuß, and W. Wenzel. "Nonadiabatic wave packet dynamics on the coupled X^2A_1/A^2B_2 electronic states of NO_2 based on new ab initio potential energy surfaces". *Chem. Phys.*, **259**(2):211, (2000).

[208] J. H. D. Eland and L. Karlsson. "Dissociative photoionisation of NO_2 up to 26 eV". *Chem. Phys.*, **237**(1-2):139, (1998).

[209] J. Schirmer, L. S. Cederbaum, and W. Von Niessen. "Two-hole-one-particle configuration interaction approach for the ionization of open-shell molecules: Application to NO_2". *Chem. Phys.*, **56**(3):285, (1981).

[210] R. P. Singhal, H. S. Kilic, K. W. D. Ledingham, C. Kosmidis, T. McCanny, A. J. Langley, and W. Shaikh. "Multiphoton ionisation and dissociation of NO_2 by 50 fs laser pulses". *Chem. Phys. Lett.*, **253**(1-2):81, (1996).

[211] A. C. Vandaele, C. Hermans, P. C. Simon, M. Carleer, R. Colin, S. Fally, M. F. Mérienne, A. Jenouvrier, and B. Coquart. "Measurements of the NO_2 absorption cross-section from 42 000 cm^{-1} to 10 000^{-1} (238-1000 nm) at 220 K and 294 K". *J. Quant. Spectrosc. Radiat. Transfer*, **59**(3):171, (1998).

[212] K. Tsuji, M. Ikeda, J. Awamura, A. Kawai, and K. Shibuya. "Vibrational level dependence of lifetime of NO_2 in the $\tilde{D}^2B_2$ state". *Chem. Phys. Lett.*, **374**(5-6):601, (2003).

[213] L. Bigio and E. R. Grant. "Polarized absorption spectroscopy of Λ-doublet molecules: Transition moment vs electron density distribution". *J. Chem. Phys.*, **87**(10):5589, (1987).

[214] R. S. Tapper, R. L. Whetten, G. S. Ezra, and E. R. Grant. "The role of near-resonant intermediate states in the two-photon excitation of nitrogen dioxide: origin bands in bent-to-linear transitions". *J. Phys. Chem.*, **88**(7):1273, (1984).

[215] M. B. Knickelbein, K. S. Haber, L. Bigio, and E. R. Grant. "High-resolution two-photon spectroscopy of the NO_2 $3p\sigma$ $^2\Sigma_u^+$ Rydberg state". *Chem. Phys. Lett.*, **131**(1-2):51, (1986).

[216] K. S. Haber, J. W. Zwanziger, F. X. Campos, R. T. Wiedmann, and E. R. Grant. "Direct determination of the adiabatic ionization potential of NO_2 by multiresonant optical absorption". *Chem. Phys. Lett.*, **144**(1):58, (1988).

[217] D. M. Neumark. "Time-resolved photoelectron spectroscopy of molecules and clusters". *Annu. Rev. Phys. Chem.*, **52**(1):255, (2001).

[218] T. Suzuki. "Femtosecond time-resolved photoelectron imaging". *Annu. Rev. Phys. Chem.*, **57**(1):555, (2006).

[219] L. Nugent-Glandorf, M. Scheer, D. A. Samuels, V. M. Bierbaum, and S. R. Leone. "Ultrafast photodissociation of Br_2: Laser-generated high-harmonic soft x-ray probing of the transient photoelectron spectra and ionization cross sections". *J. Chem. Phys.*, **117**(13):6108, (2002).

[220] D. Strasser, F. Goulay, and S. R. Leone. "Transient photoelectron spectroscopy of the dissociative $Br_2(^1\Pi_u)$ state". *J. Chem. Phys.*, **127**(18):184305, (2007).

[221] Ph. Wernet, M. Odelius, K. Godehusen, J. Gaudin, O. Schwarzkopf, and W. Eberhardt. "Real-time evolution of the valence electronic structure in a dissociating molecule". *Phys. Rev. Lett.*, **103**:013001, (2009).

[222] P. Farmanara, O. Steinkellner, M. T. Wick, M. Wittmann, G. Korn, V. Stert, and W. Radloff. "Ultrafast internal conversion and photodissociation of molecules excited by femtosecond 155 nm laser pulses". *J. Chem. Phys.*, **111**(14):6264, (1999).

[223] S. L. Sorensen, O. Björneholm, I. Hjelte, T. Kihlgren, G. Öhrwall, S. Sundin, S. Svensson, S. Buil, D. Descamps, A. L'Huillier, J. Norin, and C. G. Wahlström. "Femtosecond pump-probe photoelectron spectroscopy of predissociative Rydberg states in acetylene". *J. Chem. Phys.*, **112**(18):8038, (2000).

[224] P. Trabs, F. Buchner, M. Ghotbi, A. Lübcke, H-H. Ritze, M. J. J. Vrakking, and A. Rouzée. "Time-, angle- and kinetic-energy-resolved photoelectron spectroscopy of highly excited states of NO". *J. Phys. B: At., Mol. Opt. Phys.*, **47**(12):124016, (2014).

[225] M. Ghotbi, M. Beutler, and F. Noack. "Generation of 2.5μJ vacuum ultraviolet pulses with sub-50 fs duration by noncollinear four-wave mixing in argon". *Opt. Lett.*, **35**(20):3492, (2010).

[226] H. Tao, T. K. Allison, T. W. Wright, A. M. Stooke, C. Khurmi, J. van Tilborg, Y. Liu, R. W. Falcone, A. Belkacem, and T. J. Martinez. "Ultrafast internal conversion in ethylene. I. The excited state lifetime". *J. Chem. Phys.*, **134**(24):244306, (2011).

[227] T. K. Allison, H. Tao, W. J. Glover, T. W. Wright, A. M. Stooke, C. Khurmi, J. van Tilborg, Y. Liu, R. W. Falcone, T. J. Martinez, and A. Belkacem. "Ultrafast internal conversion in ethylene. II. Mechanisms and pathways for quenching and hydrogen elimination". *J. Chem. Phys.*, **136**(12):124317, (2012).

[228] P. Farmanara, V. Stert, and W. Radloff. "Ultrafast photodissociation dynamics of acetone excited by femtosecond 155 nm laser pulses". *Chem. Phys. Lett.*, **320**(5):697, (2000).

[229] M. Dantus, M. H. M. Janssen, and A. H. Zewail. "Femtosecond probing of molecular dynamics by mass-spectrometry in a molecular beam". *Chem. Phys. Lett.*, **181**(4):281, (1991).

[230] M. H. M. Janssen, M. Dantus, H. Guo, and A. H. Zewail. "Femtosecond reaction dynamics of Rydberg states. Methyl iodide". *Chem. Phys. Lett.*, **214**(3):281, (1993).

[231] J. K. Song, M. Tsubouchi, and T. Suzuki. "Femtosecond photoelectron imaging on pyrazine: Spectroscopy of 3s and 3p Rydberg states". *J. Chem. Phys.*, **115**(19):8810, (2001).

[232] N. Rusteika, K. B. Møller, and T. I. Sølling. "New insights on the photodynamics of acetone excited with 253-288nm femtosecond pulses". *Chem. Phys. Lett.*, **461**(4):193, (2008).

[233] O. Schalk, A. E. Boguslavskiy, and A. Stolow. "Two-photon excited state dynamics of dark valence, Rydberg, and superexcited states in 1,3-Butadiene". *J. Phys. Chem. Lett.*, **5**(3):560, (2014).

[234] C. G. Durfee, A. R. Rundquist, S. Backus, C. Herne, M. M. Murnane, and H. C. Kapteyn. "Phase matching of high-order harmonics in hollow waveguides". *Phys. Rev. Lett.*, **83**:2187, (1999).

[235] D. Rompotis, T. Gebert, M. Wieland, F. Karimi, and M. Drescher. "Efficient generation of below-threshold harmonics for high-fidelity multi-photon physics in the VUV spectral range". *Opt. Lett.*, **40**(8):1675, (2015).

[236] P. Tzankov, O. Steinkellner, J. Zheng, M. Mero, W. Freyer, A. Husakou, I. Babushkin, J. Herrmann, and F. Noack. "High-power fifth-harmonic generation of femtosecond pulses in the vacuum ultraviolet using a Ti:sapphire laser". *Opt. Express*, **15**(10):6389, (2007).

[237] P. Zuo, T. Fuji, T. Horio, S. Adachi, and T. Suzuki. "Simultaneous generation of ultrashort pulses at 158 and 198nm in a single filamentation cell by cascaded four-wave mixing in Ar". *Appl. Phys. B*, **108**(4):815, (2012).

[238] T. Horio, R. Spesyvtsev, and T. Suzuki. "Generation of sub-17 fs vacuum ultraviolet pulses at 133 nm using cascaded four-wave mixing through filamentation in Ne". *Opt. Lett.*, **39**(20):6021, (2014).

[239] Yehuda Haas. "Photochemical α-cleavage of ketones: revisiting acetone". *Photochem. Photobiol. Sci.*, **3**:6, (2004).

[240] D. W. Liao, A. M. Mebel, M. Hayashi, Y. J. Shiu, Y. T. Chen, and S. H. Lin. "Ab initio study of the n-π* electronic transition in acetone: Symmetry-forbidden vibronic spectra". *J. Chem. Phys.*, **111**(1):205, (1999).

[241] D. H. A. ter Steege, A. C. Wirtz, and W. J. Buma. "Vibronic coupling in excited states of acetone". *J. Chem. Phys.*, **116**(2):547, (2002).

[242] M. Nobre, A. Fernandes, F. Ferreira da Silva, R. Antunes, D. Almeida, V. Kokhan, S. V. Hoffmann, N. J. Mason, S. Eden, and P. Limao-Vieira. "The VUV electronic spectroscopy of acetone studied by synchrotron radiation". *Phys. Chem. Chem. Phys.*, **10**:550, (2000).

[243] R. McDiarmid and A. Sabljić. "Experimental assignments of the 3p Rydberg states of acetone". *The Journal of Chemical Physics*, **89**(10):6086, (1988).

[244] S. N. Thakur, D. Guo, T. Kundu, and L. Goodman. "Two-photon photoacoustic spectroscopy of acetone 3p Rydberg states". *Chem. Phys. Lett.*, **199**(3):335, (1992).

[245] M. Merchán, B. O. Roos, R. McDiarmid, and X. Xing. "A combined theoretical and experimental determination of the electronic spectrum of acetone". *J. Chem. Phys.*, **104**(5):1791, (1996).

[246] S. R. Gwaltney and R. J. Bartlett. "An application of the equation-of-motion coupled cluster method to the excited states of formaldehyde, acetaldehyde, and acetone". *Chem. Phys. Lett.*, **41**(1):26, (1995).

[247] J. C. Owrutsky and A. P. Baronavski. "Ultrafast photodissociation dynamics of the S_1 and S_2 states of acetone". *J. Chem. Phys.*, **110**(23):11206, (1999).

[248] E. W. G. Diau, C. Kötting, T. I. Sølling, and A. H. Zewail. "Femtochemistry of Norrish Type-I reactions: III. Highly excited ketones-theoretical". *ChemPhysChem*, **3**(1):57, (2001).

[249] L. Favero, G. Granucci, and M. Persico. "Dynamics of acetone photodissociation: a surface hopping study". *Phys. Chem. Chem. Phys.*, **15**:20651, (2013).

[250] J. C. Owrutsky and A. P. Baronavski. "Ultrafast studies of the photodissociation of the acetone 3s Rydberg state at 195 nm: Formation and unimolecular dissociation of the acetyl radical". *J. Chem. Phys.*, **108**(16):6652, (1998).

[251] W. K. Chen, J. W. Ho, and P. Y. Cheng. "Ultrafast photodissociation dynamics of acetone at 195 nm: I Initial-state, intermediate, and product temporal evolutions by femtosecond mass-selected multiphoton ionization spectroscopy". *J. Phys. Chem. A*, **109**(31):6805, (2005).

[252] W. K. Chen and P. Y. Cheng. "Ultrafast photodissociation dynamics of acetone at 195 nm:II. Unraveling complex three-body dissociation dynamics by femtosecond time-resolved photofragment translational spectroscopy". *J. Phys. Chem. A*, **109**(31):6818, (2005).

[253] Q. Zhong, L. Poth, and A. W. Castleman. "Ultrafast dissociation dynamics of acetone: A revisit to the S1 state and 3s Rydberg state". *J. Chem. Phys.*, **110**(1):192, (1999).

[254] T. Shibata and T. Suzuki. "Photofragment ion imaging with femtosecond laser pulses". *Chem. Phys. Lett.*, **262**(1):115, (1996).

[255] E. W.-G. Diau, C. Kötting, and A. H. Zewail. "Femtochemistry of Norrish Type-I reactions: I. Experimental and theoretical studies of acetone and related ketones on the S_1 surface". *Chem. Phys. Chem.*, **2**(5):273, (2001).

[256] R. Y. Brogaard, T. I. Sølling, and K. B. Møller. "Initial dynamics of The Norrish Type I reaction in acetone: Probing wave packet motion". *J. Phys. Chem. A*, **115**(5):556, (2011).

[257] R. McDiarmid and X. Xing. "Nonadiabatic coupling of the 3p Rydberg and $\pi\pi^*$ valence states of acetone". *J. Chem. Phys.*, **107**(3):675, (1997).

[258] S. K. Kim, S. Pedersen, and A. H. Zewail. "Direct femtosecond observation of the transient intermediate in the α-cleavage reaction of $(CH_3)_2CO$ to $2CH_3$+CO: Resolving the issue of concertedness". *J. Chem. Phys.*, **103**(1):477, (1995).

[259] O. Hüter and F. Temps. "Ultrafast α-CC bond cleavage of acetone upon excitation to 3p and 3d Rydberg states by femtosecond time-resolved photoelectron imaging". *J. Chem. Phys.*, **145**(21):214312, (2016).

[260] D. E. Couch, H. C. Kapteyn, M. M. Murnane, and W. K. Peters. "Uncovering highly-excited state mixing in acetone using ultrafast VUV pulses and coincidence imaging techniques". *J. Phys. Chem. A*, **121**(12):2361, (2017).

[261] P. Maierhofer, M. Bainschab, B. Thaler, P. Heim, W. E. Ernst, and M. Koch. "Disentangling multichannel photodissociation dynamics in acetone by time-resolved photoelectron-photoion coincidence spectroscopy". *J. Phys. Chem. A*, **120**(32):6418, (2016).

[262] M. Koch, B. Thaler, P. Heim, and W. E. Ernst. "The role of Rydberg–valence coupling in the ultrafast relaxation dynamics of acetone". *J. Phys. Chem. A*, **121**(34):6398, (2017).

[263] E. E. Rennie, A.-M. Boulanger, P. M. Mayer, D. M. P. Holland, D. A. Shaw, L. Cooper, and L. G. Shpinkova. "A photoelectron and TPEPICO investigation of the acetone radical cation". *J. Phys. Chem. A*, **110**(28):8663, (2006).

[264] M. Beutler, M. Ghotbi, F. Noack, and I. V. Hertel. "Generation of sub-50-fs vacuum ultraviolet pulses by four-wave mixing in argon". *Opt. Lett.*, **35**(9):1491, (2010).

[265] J. F. Reintjes. *"Nonlinear optical parametric processes in Liquids and Gases"*. (1984).

[266] C. Homann, N. Krebs, and E. Riedle. "Convenient pulse length measurement of sub-20-fs pulses down to the deep UV via two-photon absorption in bulk material". *Appl. Phys. B*, **104**(4):783, (2011).

[267] U. Even. "Pulsed supersonic beams from high pressure source: Simulation results and experimental measurements". *Adv. Chem.*, **2014**:636042, (2014).

[268] S. Y. Liu, K. Alnama, J. Matsumoto, K. Nishizawa, H. Kohguchi, Y. P. Lee, and T. Suzuki. "He I ultraviolet photoelectron spectroscopy of benzene and pyridine in supersonic molecular beams using photoelectron imaging". *J. Phys. Chem. A*, **115**(14):2953, (2011).

[269] A. T. J. B. Eppink and D. H. Parker. "Velocity map imaging of ions and electrons using electrostatic lenses: Application in photoelectron and photofragment ion imaging of molecular oxygen". *Rev. Sci. Instrum.*, **68**(9):3477, (1997).

[270] Y. T. Cho and S. J. Na. "Application of Abel inversion in real-time calculations for circularly and elliptically symmetric radiation sources". *Meas. Sci. Technol.*, **16**(3):878, (2005).

[271] J. E. Hansen and W. Persson. "Revised analysis of singly ionized xenon, Xe II". *Phys. Scr.*, **36**(4):602, (1987).

[272] G. Wu, A. E. Boguslavskiy, O. Schalk, M. S. Schuurman, and A. Stolow. "Ultrafast non-adiabatic dynamics of methyl substituted ethylenes: The π3s Rydberg state". *J. Chem. Phys.*, **135**(16):164309, (2011).

[273] O. Schalk, A. E. Boguslavskiy, and A. Stolow. "Substituent effects on dynamics at conical intersections: cyclopentadienes". *J. Phys. Chem. A*, **114**(12):4058, (2010).

[274] J. O. F. Thompson, L. B. Klein, T. I. Sølling, M. J. Paterson, and D. Townsend. "The role of novel Rydberg-valence behaviour in the non-adiabatic dynamics of tertiary aliphatic amines". *Chem. Sci.*, **7**:1826, (2016).

[275] J. J. John, M. Brouard, A. Clark, J. Crooks, E. Halford, L. Hill, J. W. L. Lee, A. Nomerotski, R. Pisarczyk, I. Sedgwick, C. S. Slater, R. Turchetta, C. Vallance, E. Wilman, B. Winter, and W. H. Yuen. "PImMS, a fast event-triggered monolithic pixel detector with storage of multiple timestamps". *J. Instrum.*, **7**(08):C08001, (2012).

[276] A. Zhao, M. van Beuzekom, B. Bouwens, D. Byelov, I. Chakaberia, C. Cheng, E. Maddox, A. Nomerotski, P. Svihra, J. Visser, V. Vrba, and T. Weinacht. "Coincidence velocity map imaging using Tpx3Cam, a time stamping optical camera with 1.5 ns timing resolution". *Rev. Sci. Instrum.*, **88**(11):113104, (2017).

[277] R. Forbes, V. Makhija, K. Veyrinas, A. Stolow, J. W. L. Lee, M. Burt, M. Brouard, C. Vallance, I. Wilkinson, R. Lausten, and P. Hockett. "Time-resolved multi-mass ion imaging: Femtosecond UV-VUV pump-probe spectroscopy with the PImMS camera". *J. Chem. Phys.*, **147**(1):013911, (2017).

[278] B. M. Cheng, H. F. Chen, H. C. Lu, H. K. Chen, M. S. Alam, S. L. Chou, and M. Y. Lin. "Absorption cross section of gaseous acetylene at 85K in the wavelength range 110-155nm". *Astrophys. J. S.*, **196**(1):3, (2011).

[279] A. B. F. Duncan. "The absorption spectrum of acetone vapor in the far ultra-violet". *J. Chem. Phys.*, **3**(3):131, (1935).

[280] E. E. Barnes and W. T. Simpson. "Correlations among electronic transitions for carbonyl and for carboxyl in the vacuum ultraviolet". *Journal Chem. Phys.*, **39**(3):670, (1963).

[281] P. Brint, L. O'Toole, S. Couris, and D. Jardine. "Multiphoton ionisation spectroscopy of the 3s(2 + 2, 1) and 4s(3 + 1) Rydberg states of acetone: evidence for a molecular valence state at 153 nm". *J. Chem. Soc. Faraday Trans.*, **87**:2891, (1991).

[282] H. Keller-Rudek, G. K. Moortgat, R. Sander, , and R. Sörensen. "The MPI-Mainz UV/VIS spectral atlas of gaseous molecules of atmospheric interest". *Earth Syst. Sci. Dat*, **5**:365, (2013).

[283] O. Schalk and P. Hockett. "Rotational dephasing of symmetric top molecules: Analytic expressions and applications". *Chem. Phys. Lett.*, **517**(4):237, (2011).

[284] R. Spesyvtsev, O. M. Kirkby, and H. H. Fielding. "Ultrafast dynamics of aniline following 269-238 nm excitation and the role of the $S_2(\pi 3s/\pi\sigma^*)$ state". *Faraday Discuss.*, **157**:165, (2012).

[285] T. Kobayashi, T. Horio, and T. Suzuki. "Ultrafast deactivation of the $\pi\pi^*$(V) state of ethylene studied using sub-20 fs time-resolved photoelectron imaging". *J. Phys. Chem. A*, **119**(36):9518, (2015).

[286] V. S. Petrović, M. Siano, J. L. White, N. Berrah, C. Bostedt, J. D. Bozek, D. Broege, M. Chalfin, R. N. Coffee, J. Cryan, L. Fang, J. P. Farrell, L. J. Frasinski, J. M. Glownia, M. Gühr, M. Hoener, D. M. P. Holland, J. Kim, J. P. Marangos, T. Martinez, B. K. McFarland, R. S. Minns, S. Miyabe, S. Schorb, R. J. Sension, L. S. Spector, R. Squibb, H. Tao, J. G. Underwood, and P. H. Bucksbaum. "Transient X-Ray fragmentation: Probing a prototypical photoinduced ring opening". *Phys. Rev. Lett.*, **108**:253006, (2012).

[287] Y. Pertot, C. Schmidt, M. Matthews, A. Chauvet, M. Huppert, V. Svoboda, A. von Conta, A. Tehlar, D. Baykusheva, J-P Wolf, and H. J. Wörner. "Time-

resolved x-ray absorption spectroscopy with a water window high-harmonic source". *Science*, **355**(6322):264, (2017).

[288] B. K. McFarland, J. P. Farrell, S. Miyabe, F. Tarantelli, A. Aguilar, N. Berrah, C. Bostedt, J. D. Bozek, P. H. Bucksbaum, J. C. Castagna, R. N. Coffee, J. P. Cryan, L. Fang, R. Feifel, K. J. Gaffney, J. M. Glownia, T. J. Martinez, M. Mucke, B. Murphy, A. Natan, T. Osipov, V. S. Petrović, S. Schorb, T. Schultz, L. S. Spector, M. Swiggers, I. Tenney, S. Wang, J. L. White, W. White, and M. Gühr. "Ultrafast X-ray Auger probing of photoexcited molecular dynamics". *Nat. Comms.*, **5**:4235, (2014).

[289] T. J. A. Wolf, R. H. Myhre, J. P. Cryan, S. Coriani, R. J. Squibb, A. Battistoni, N. Berrah, C. Bostedt, P. H. Bucksbaum, G. Coslovich, R. Feifel, K. J. Gaffney, J. Grilj, T. J. Martinez, S. Miyabe, S. P. Moeller, M. Mucke, A. Natan, R. Obaid, T. Osipov, O. Plekan, S. Wang, H. Koch, and M. Gühr. "Probing ultrafast $\pi\pi^*$/nπ^* internal conversion in organic chromophores via K-edge resonant absorption". *Nat. Comms.*, **8**(1):29, (2017).

[290] A. P. Hitchcock and C. E. Brion. "Inner shell excitation of CH_3F, CH_3Cl, CH_3Br and CH_3I by 2.5 keV electron impact". *J. Electron. Spectrosc. Relat. Phenom.*, **13**(3):193, (1978).

[291] J. B. West, P. R. Woodruff, K. Codling, and R. G. Houlgate. "The 4d, 5s and 5p partial photoionization cross sections of xenon above the 4d threshold". *J. Phys. B: At., Mol. Opt. Phys.*, **9**(3):407, (1976).

[292] U. Fano and J. W. Cooper. "Spectral distribution of atomic oscillator strengths". *Rev. Mod. Phys.*, **40**(3):441, (1968).

[293] G. O'Sullivan. "The absorption spectrum of CH_3I in the extreme VUV". *J. Phys. B: At., Mol. Opt. Phys.*, **15**(9):L327, (1982).

[294] G. Dujardin, L. Hellner, D. Winkoun, and M.J. Besnard. "Valence and inner shell electronic processes in dissociative double photoionization of CH_3I". *Chem. Phys.*, **105**(1-2):291, (1986).

[295] P. Morin and I. Nenner. "Photoionization decay of core excited molecules". *Phys. Scr.*, **T17**:171, (1987).

[296] D. W. Lindle, P. H. Kobrin, C. M. Truesdale, T. A. Ferrett, P. A. Heimann, H. G. Kerkhoff, U. Becker, and D. A. Shirley. "Inner-shell photoemission from the iodine atom in CH_3I". *Phys. Rev. A*, **30**(1):239, (1984).

[297] I. Powis. "A theoretical CMS-X α treatment of CH_3I photoionization dynamics: outer valence shell and iodine 4d levels". *Chem. Phys.*, **201**(1):189, (1995).

[298] U. Gelius. "Recent progress in ESCA studies of gases". *J. Electron. Spectrosc. Relat. Phenom.*, **5**(1):985, (1974).

[299] S. Svensson, N. Mårtensson, E. Basilier, P. A. Malmquist, U.Gelius, and K. Siegbahn. "Lifetime Broadening and CI-Resonances Observed in ESCA". *Phys. Scr.*, **14**(4):141, (1976).

[300] J. A. Hashmall, B. E. Mills, D. A. Shirley, and A. Streitwieser. "Comparison of valence shell and core ionization potentials of alkyl iodides". *J. Am. Chem. Soc.*, **94**(13):4445, (1972).

[301] N. Kosugi, E. Shigemasa, and A. Yagishita. "High-resolution and symmetry-resolved oxygen K-edge spectra of O_2". *Chem. Phys. Lett.*, **190**(5):481, (1992).

[302] P. Baltzer, L. Karlsson, M. Lundqvist, and B. Wannberg. "Resolution and signal-to-background enhancement in gas-phase electron spectroscopy". *Rev. Sci. Instrum.*, **64**(8):2179, (1993).

[303] M. Jurvansuu, A. Kivimäki, and S. Aksela. "Inherent lifetime widths of Ar $2p^{-1}$, Kr $3d^{-1}$, Xe $3d^{-1}$, and Xe $4d^{-1}$ states". *Phys. Rev. A*, 64(1):012502, 2001.

[304] S. Aksela, H. Aksela, and T. D. Thomas. $M_{4,5}N_{4,5}X$ auger electron spectra of iodine and xenon. many-body effects. *Phys. Rev. A*, **19**(2):721, (1979).

[305] J. Cooper and R. N. Zare. "Angular Distribution of Photoelectrons". *J. Chem. Phys.*, **48**(2):942, (1968).

[306] J. Jauhiainen, A. Ausmees, A. Kivimäkia, S. J. Osborne, A. Naves de Briton, S. Aksela, S. Svensson, and H. Aksela. "A method to determine a transmission correction for electron spectrometers using synchrotron radiation". *J. Electron. Spectrosc. Relat. Phenom.*, **69**(3):181, (1994).

[307] V. Schmidt. *Electron spectrometry of toms using synchrotron radiation*. (1997).

[308] G. B. Armen, J. Tulkki, T. Aberg, and B. Crasemann. "Quantum theory of post-collision interaction in inner-shell photoionization: Final-state interaction between two continuum electrons". *Phys. Rev. A*, **36**(12):5606, (1987).

[309] M. Stener, G. Fronzoni, and M. de Simone. "Time dependent density functional theory of core electrons excitations". *Chem. Phys. Lett.*, **373**(1-2):115, (2003).

[310] R. Forbes, A. De Fanis, C. Bomme, D. Rolles, S. T. Pratt, I. Powis, N. A. Besley, M. Simon, S. Nandi, A. R. Milosavljević, C. Nicolas, J. D. Bozek, J. G. Underwood, and D.M.P. Holland. "Photoionization of the iodine 3d, 4s and 4p orbitals in methyl iodide - Accepted". *J. Chem. Phys.*, **149**(13), (2018).

[311] N. A. Besley, A. T. B. Gilbert, and P. M. W. Gill. "Self-consistent-field calculations of core excited states". *J. Chem. Phys.*, **130**(12):124308, (2009).

[312] M. Stener, P. Decleva, and A. Lisini. "Molecular photoionization cross sections by the local density LCAO Stieltjes imaging approach". *J. Electron. Spectrosc. Relat. Phenom.*, **74**(1):29, (1995).

[313] D. Dill and J. L. Dehmer. "Electron-molecule scattering and molecular photoionization using the multiple-scattering method". *J. Chem. Phys.*, **61**(2):692, (1974).

[314] J. W Davenport. *Dissertation*. PhD thesis, University of Pennsylvania, (1976).

[315] M. Ya. Amusia, L. V. Chernysheva, S. T. Manson, A. M. Msezane, and V. Radojević. Strong electron correlation in photoionization of spin-orbit doublets. *Phys. Rev. Lett.*, **88**:093002, (2002).

[316] D. Toffoli, M. Stener, and P. Decleva. "Application of the relativistic time-dependent density functional theory to the photoionization of xenon". *J. Phys. B: At., Mol. Opt. Phys.*, **35**(5):1275, (2002).

[317] N. A. Besley and F. A. Asmuruf. "Time-dependent density functional theory calculations of the spectroscopy of core electrons". *Phys. Chem. Chem. Phys.*, **12**(38):12024, (2010).

[318] F. J. Comes, U. Nielsen, and W. H. E. Schwarz. "Inner electron excitation of iodine in the gaseous and solid phase". *J. Chem. Phys.*, **58**(6):2230, (1973).

[319] A. P. Lukirskii, I. A. Brytov, and T. M. Zimkina. Photoionization absorption of He, Kr, Xe, CH_4, and methylal in the 23.6-250 Å region. *Optics and Spectroscopy*, **17**:234, (1964).

[320] K. Codling and R. P. Madden. "Newly observed structure in the photoionization continua of Kr and Xe below 160 Å". *Appl. Opt.*, **4**(11):1431, (1965).

[321] L. S. Cederbaum, W. Domcke, J. Schirmer, and W. Von Niessen. *"Correlation effects in the ionization of molecules: Breakdown of the molecular orbital picture"*, page 115. (2007).

[322] B. Crasemann, editor. *"Atomic inner-shell physics"*. Springer US, (1985).

[323] D. Coster and R. De L. Kronig. "New type of auger effect and its influence on the x-ray spectrum". *Physica*, **2**(1):13, (1935).

[324] E. J. McGuire. "Atomic M-Shell Coster-Kronig, Auger, and Radiative Rates, and Fluorescence Yields for Ca-Th". *Phys. Rev. A*, **5**:1043, (1972).

[325] G. Wendin and M. Ohno. *Proc. 2nd int. conf. on inner shell ionization phenomena (Freiburg)*, (1976).

[326] G. Wendin and M. Ohno. "Strong dynamical effects of many-electron interactions in photoelectron spectra from 4 s and 4 p core levels". *Phys. Scr.*, **14**(4):148, (1976).

[327] V Schmidt. "Photoionization of atoms using synchrotron radiation". *Rep. Prog. Phys.*, **55**(9):1483, (1992).

[328] U. Becker, D. Szostak, H. G. Kerkhoff, M. Kupsch, B. Langer, R. Wehlitz, A. Yagishita, and T. Hayaishi. "Subshell photoionization of Xe between 40 and 1000 eV". *Phys. Rev. A*, **39**:3902, (1989).

[329] T. X. Carroll, R. W. Shaw, T. D. Thomas, C. Kindle, and N. Bartlett. "Electron distribution in the xenon fluorides and xenon oxide tetrafluoride by ESCA and evidence for orbital independence in the xenon-fluorine bonding". *J. Am. Chem. Soc.*, **96**(7):1989, (1974).

[330] V. Radojević, D. M. Davidović, and M. Ya. Amusia. "Near-threshold photoionization of the Xe 3d spin-orbit doublet: Relativistic, relaxation, and intershell interaction effects". *Phys. Rev. A*, **67**:022719, (2003).

[331] S. P. Shannon, K. Codling, and J. B. West. "The absolute photoionization cross sections of the spin-orbit components of the xenon 4d electron from 70-130 eV". *J. Phys. B: At., Mol. Opt. Phys.*, **10**(5):825, (1977).

[332] T. E. H. Walker and J. T. Waber. "Spin-orbit coupling photoionization". *J. Phys. B: At., Mol. Opt. Phys.*, **7**(6):674, (1974).

[333] A. Fahr, A. K. Nayak, and M. J. Kurylo. "The ultraviolet absorption cross sections of CH_3I temperature dependent gas and liquid phase measurements". *Chem. Phys.*, **197**(2):195, (1995).

[334] R. Locht, B. Leyh, H.W. Jochims, and H. Baumgärtel. "Medium and high resolution vacuum UV photoabsorption spectroscopy of methyl iodide

(CH_3I) and its deuterated isotopomers CD_3I and CH_2DI. A Rydberg series analysis". *Chem. Phys.*, **365**(3):109, (2009).

[335] C. S. Lehmann, A. Picón, C. Bostedt, A. Rudenko, A. Marinelli, D. Moonshiram, T. Osipov, D. Rolles, N. Berrah, C. Bomme, M. Bucher, G. Doumy, B. Erk, K. R. Ferguson, T. Gorkhover, P. J. Ho, E. P. Kanter, B. Krässig, J. Krzywinski, A. A. Lutman, A. M. March, D. Ray, L. Young, S. T. Pratt, and S. H. Southworth. "Ultrafast x-ray-induced nuclear dynamics in diatomic molecules using femtosecond x-ray-pump–x-ray-probe spectroscopy". *Phys. Rev. A*, **94**:013426, (2016).

[336] G. B. Armen, H. Aksela, T. Åberg, and S. Aksela. "The resonant Auger effect". *J. Phys. B: At., Mol. Opt. Phys.*, **33**(2):R49, (2000).

[337] M. N. Piancastelli. "Auger resonant Raman studies of atoms and molecules". *J. Phys. B: At., Mol. Opt. Phys.*, **107**(1):1, (2000).

[338] K. Ueda. "High-resolution inner-shell spectroscopies of free atoms and molecules using soft-x-ray beamlines at the third-generation synchrotron radiation sources". *J. Phys. B: At., Mol. Opt. Phys.: At. Mol. Phys*, **36**(4):1, (2003).

[339] P. Morin and I. Nenner. "Atomic autoionization following very fast dissociation of core-excited HBr". *Phys. Rev. Lett.*, **56**:1913, (1986).

[340] G. C. King D. A. Shaw, D. Cvejanovtc and F. H. Reid. "Inner-shell and outer-shell excitation of HCl, HBr and Br_2 by electron impact with high resolution". *J. Phys. B: At., Mol. Opt. Phys.*, **17**(6):1173, (1984).

[341] H. Aksela, S. Aksela, M. Ala-Korpela, O-P. Sairanen, M. Hotokka, G. M. Bancroft, K. H. Tan, and J. Tulkki. "Decay channels of core-excited HCl". *Phys. Rev. A*, **41**:6000, (1990).

[342] A. Menzel, B. Langer, J. Viefhaus, S.B. Whitfield, and U. Becker. "Competition between direct dissociation and resonant Auger decay: a quasi-classical

model applied to the $2p^{-1}$ σ^* states of HCl, DCl and Cl_2". *Chem. Phys. Lett.*, **258**(1):265, (1996).

[343] E. Kukk, H. Aksela, O.-P. Sairanen, S. Aksela, A. Kivimäki, E. Nõmmiste, A. Ausmees, A. Kikas, S. J. Osborne, and S. Svensson. "Auger decay of the dissociating core-excited states in the HCl and DCl molecules". *J. Chem. Phys.*, **104**(12):4475, (1996).

[344] E. Kukk, H. Aksela, O.-P. Sairanen, E. Nõmmiste, S. Aksela, S. J. Osborne, A. Ausmees, and S. Svensson. "Core-to-Rydberg excitations and their Auger decay in the HCl and DCl molecules". *Phys. Rev. A*, **54**:2121, (1996).

[345] O. Björneholm, S. Sundin, S. Svensson, R. R. T. Marinho, A. Naves de Brito, F. Gel'mukhanov, and H. Ågren. "Femtosecond dissociation of core-excited HCl monitored by frequency detuning". *Phys. Rev. Lett.*, **79**:3150, (1997).

[346] A. Kivimäki, E. Kukk, J. Karvonen, J. Mursu, E. Nõmmiste, H. Aksela, and S. Aksela. "Angular distribution of electronic decay following molecular and Rydberg excitations at the Cl 2p edge of HCl". *Phys. Rev. A*, **57**:2724, (1998).

[347] R. Feifel, F. Burmeister, P. Sałek, M. N. Piancastelli, M. Bässler, S. L. Sorensen, C. Miron, H. Wang, I. Hjelte, O. Björneholm, A. Naves de Brito, F. Kh. Gel'mukhanov, H. Ågren, and S. Svensson. "Observation of a continuum-continuum interference hole in ultrafast dissociating core-excited molecules". *Phys. Rev. Lett.*, **85**:3133, (2000).

[348] E. Sokell, A. A. Wills, M. Wiedenhoeft, X. Feng, D. Rolles, and N. Berrah. "An investigation of dissociative resonant photoionization in HCl and DCl using two-dimensional photoelectron spectroscopy". *J. Phys. B: At., Mol. Opt. Phys.*, **38**(10):1535, (2005).

[349] H. Sann, T. Havermeier, C. Müller, H.-K. Kim, F. Trinter, M. Waitz, J. Voigtsberger, F. Sturm, T. Bauer, R. Wallauer, D. Schneider, M. Weller, C. Goihl,

J. Tross, K. Cole, J. Wu, M. S. Schöffler, H. Schmidt-Böcking, T. Jahnke, M. Simon, and R. Dörner. "Imaging the temporal evolution of molecular orbitals during ultrafast dissociation". *Phys. Rev. Lett.*, **117**:243002, (2016).

[350] P. Morin and C. Miron. "Ultrafast dissociation: An unexpected tool for probing molecular dynamics". *J. Electron. Spectrosc. Relat. Phenom.*, **185**(8):259, (2012).

[351] Ph. V. Demekhin, I. D. Petrov, V. L. Sukhorukov, W. Kielich, P. Reiss, R. Hentges, I. Haar, H. Schmoranzer, and A. Ehresmann. "Interference effects during the Auger decay of the C^*O $1s^{-1}\pi^*$ resonance studied by angular distribution of the $CO^+(A)$ photoelectrons and polarization analysis of the $CO^+(A-X)$ fluorescence". *Phys. Rev. A*, **80**:063425, (2009).

[352] C. Miron, V. Kimberg, P. Morin, C. Nicolas, N. Kosugi, S. Gavrilyuk, and F. Gel'mukhanov. "Vibrational scattering anisotropy generated by multichannel quantum interference". *Phys. Rev. Lett.*, **105**:093002, (2010).

[353] Ph. V. Demekhin, I. D. Petrov, V. L. Sukhorukov, W. Kielich, A. Knie, H. Schmoranzer, and A. Ehresmann. "Symmetry-forbidden electronic state interference observed in angularly resolved $NO^+(A\ ^1\Pi)$ deexcitation spectra of the $\mathbf{N^*O}(2\sigma^{-1}2\pi^2)$ resonance". *Phys. Rev. Lett.*, **104**:243001, (2010).

[354] E. Kukk, J. D. Bozek, W.-T. Cheng, R. F. Fink, A. A. Wills, and N. Berrah. "Auger decay of the C $1s^1 2pi^*$ resonance in carbon monoxide: Vibrationally and angularly resolved spectra". *J. Chem. Phys.*, **111**(21):9642, (1999).

[355] O. Hemmers, F. Heiser, J. Viefhaus, K. Wieliczek, and U. Becker. "Angle-resolved resonant Auger electron spectroscopy of CO after vibrationally resolved C 1s $\rightarrow$ $nl\lambda$ excitations". *J. Phys. B: At., Mol. Opt. Phys.*, **32**(15):3769, (1999).

[356] H. Wang, R. F. Fink, M. N. Piancastelli, M. Bässler, I. Hjelte, O. Björneholm, F. Burmeister, R. Feifel, A. Giertz, C. Miron, S. L. Sorensen, K. Wiesner, and

S. Svensson. "Is there interference in the resonant Auger electron spectra of N 1s and O 1s$\rightarrow 2\pi$ core excited NO?". *Chem. Phys.*, **289**(1):31, (2003).

[357] A. Lindblad, V. Kimberg, J. Söderström, C. Nicolas, O. Travnikova, N. Kosugi, F. Gel'mukhanov, and C. Miron. "Vibrational scattering anisotropy in O_2 dynamics beyond the Born–Oppenheimer approximation". *New J. Phys.*, **14**(11):113018, (2012).

[358] Y. Shimizu, H. Ohashi, Y. Tamenori, Y. Muramatsu, H. Yoshida, K. Okada, N. Saito, H. Tanaka, I. Koyano, S. Shin, and K. Ueda. "Sub-natural-width angle-resolved resonant Auger electron spectroscopy of atoms and molecules on the high resolution soft X-ray monochromator at SPring-8". *J. Electron. Spectrosc. Relat. Phenom.*, **114-116**:63, (2001).

[359] E. Antonsson, M. Patanen, C. Nicolas, S. Benkoula, J. J. Neville, V. L. Sukhorukov, J. D. Bozek, Ph. V. Demekhin, and C. Miron. "Dynamics of the C $1s \rightarrow \pi^*$ excitation and decay in CO_2 probed by vibrationally and angularly resolved Auger spectroscopy". *Phys. Rev. A*, **92**:042506, (2015).

[360] I. Hjelte, L. Karlsson, S. Svensson, A. De Fanis, V. Carravetta, N. Saito, M. Kitajima, H. Tanaka, H. Yoshida, A. Hiraya, I. Koyano, K. Ueda, and M. N. Piancastelli. "Angular distribution of different vibrational components of the X and B states reached after resonant Auger decay of core-excited H_2O: Experiment and theory". *J. Chem. Phys.*, **122**(8):084306, (2005).

[361] D. Dill, J. R. Swanson, S. Wallace, and J. L. Dehmer. "Angular distribution of molecular *K*-shell Auger electrons: Spectroscopy of photoabsorption anisotropy". *Phys. Rev. Lett.*, **45**:1393, (1980).

[362] B. Cleff and W. Mehlhorn. "On the angular distribution of Auger electrons". *Phys. Lett. A*, **37**(1):3, (1971).

[363] S. Flügge, W. Mehlhorn, and V. Schmidt. Angular distribution of auger electrons following photoionization. *Phys. Rev. Lett.*, **29**:7, (1972).

[364] W. Mehlhorn. *"Auger-electron spectrometry of core levels of atoms"*, page 119. Springer US, Boston, MA, (1985).

[365] E. G. Berezhko and N. M. Kabachnik. "Theoretical study of inner-shell alignment of atoms in electron impact ionisation: angular distribution and polarisation of X-rays and Auger electrons". *J. Phys. B: At., Mol. Opt. Phys.*, **10**(12):2467, (1977).

[366] E. G. Berezhko, N. M. Kabachnik, and V. S. Rostovsky. "Potential-barrier effects in inner-shell photoionisation and their influence on the anisotropy of X-rays and Auger electrons". *J. Phys. B: At., Mol. Opt. Phys.*, **11**(10):1749, (1978).

[367] J. Karvonen, A. Kivimäki, H. Aksela, S. Aksela, R. Camilloni, L. Avaldi, M. Coreno, M. de Simone, and K. C. Prince. "Angular distribution in xenon M4,5N4,5N4,5 Auger decay". *Physical Review A*, **59**(1):315–319, (1999).

[368] S. H. Southworth, P. H. Kobrin, C. M. Truesdale, D. Lindle, S. Owaki, and D. A. Shirley. "Photoelectron and Auger electron asymmetries: Alignment of $Xe^{+2}D_{\frac{5}{2}}$ by photoionization". *Phys. Rev. A*, **24**:2257, (1981).

[369] S. Southworth, U. Becker, C. M. Truesdale, P. H. Kobrin, D. W. Lindle, S. Owaki, and D. A. Shirley. "Electron-spectroscopy study of inner-shell photoexcitation and ionization of Xe". *Phys. Rev. A*, **28**:261, (1983).

[370] T. A. Carlson, D. R. Mullins, C. E. Beall, B. W. Yates, J. W. Taylor, D. W. Lindle, B. P. Pullen, and F. A. Grimm. "Unusual degree of angular anisotropy in the resonant Auger spectrum of Kr". *Phys. Rev. Lett.*, **60**:1382, (1988).

[371] T. A. Carlson, D. R. Mullins, C. E. Beall, B. W. Yates, J. W. Taylor, D. W. Lindle, and F. A. Grimm. "Angular distribution of ejected electrons in resonant Auger processes of Ar, Kr, and Xe". *Phys. Rev. A*, **39**:1170, (1989).

[372] B. Kammerling, B. Krassig, and V. Schmidt. "Connection between the angular distribution of Auger electrons and spectator autoionization electrons

following 4d ionization/excitation in xenon". *J. Phys. B: At., Mol. Opt. Phys.*, **23**(24):4487, (1990).

[373] R. Sankari, A. Kivimäki, M. Huttula, H. Aksela, S. Aksela, M. Coreno, G. Turri, R. Camilloni, M. de Simone, and K. C. Prince. "Angular distribution in resonant Auger spectra of xenon excited below the $3d_{5/2}$ ionization threshold". *Phys. Rev. A*, **63**(3):032715, (2001).

[374] A. De Fanis, N. Saito, M. Kitajima, Y. Shimizu, K. Okada, H. Tanaka, I. Koyano, and K. Ueda. "High resolution measurement for the resonant Auger emission of Xe following 3d 5/2 →6p excitation". *J. Phys. B: At., Mol. Opt. Phys.*, **34**(11):L377, (2001).

[375] M. Kitajima, M. Okamoto, M. Hoshino, H. Tanaka, S. Fritzsche, N. M. Kabachnik, I. P. Sazhina, Y. Shimizu, and K. Ueda. "Experimental and theoretical study of the Auger cascade following 4d → 6p photoexcitation in Xe". *J. Phys. B: At., Mol. Opt. Phys.*, **35**(15):3327, (2002).

[376] N. M. Kabachnik. "Alignment of inner atomic shells in nuclear α decay". *J. Phys. B: At., Mol. Opt. Phys.*, **18**(13):L423, (1985).

[377] U. Hergenhahn, N. M. Kabachnik, and B. Lohmann. "Angular distribution in resonant Auger decay". *J. Phys. B: At., Mol. Opt. Phys.*, **24**(22):4759, (1991).

[378] M. H. Chen. "Effect of intermediate coupling on angular distribution of Auger electrons". *Phys. Rev. A*, **45**:1684, (1992).

[379] S. Fritzsche. "Angular distribution parameters in the resonant xenon $4d^{-1}6p$ Auger spectra". *Phys. Lett. A*, **180**(3):262, (1993).

[380] J. Tulkki, N. M. Kabachnik, and H. Aksela. "Effects of channel interaction, exchange, and relaxation on the angular distribution and spin polarization of Auger electrons from noble-gas atoms". *Phys. Rev. A*, **48**:1277, (1993).

[381] J. Tulkki, H. Aksela, and N. M. Kabachnik. "Evolution of the anisotropy of the Auger decay of $2p_{3/2}^{-1}$ns resonances into anisotropy of L_3MM Auger decay in Ar". *Phys. Rev. A*, **48**:2957, (1993).

[382] S. T. Manson and J. W. Cooper. "Photo-Ionization in the Soft x-Ray Range: 1Z Dependence in a Central-Potential Model". *Phys. Rev.*, **165**:126, (1968).

[383] J. W. Cooper. "Photoionization from outer atomic subshells. A model study". *Phys. Rev.*, **128**:681, (1962).

[384] G. Snell, E. Kukk, B. Langer, and N. Berrah. "Angular distribution measurements of the xenon $N_{4,5}O_{2,3}O_{2,3}$ Auger electrons: Determination of alignment and intrinsic parameters". *Phys. Rev. A*, **61**:042709, (2000).

[385] E. Jones, T. Oliphant, P. Peterson, et al. "SciPy: Open source scientific tools for Python", (2001).

[386] H. Pulkkinen, H. Aksela, and S. Aksela. "Correlation effects in the $M_{4,5}N_{4,5}O$ Auger spectra of Xe". *Phys. Rev. A*, **34**:1195, (1986).

[387] M. J. Frisch, G. W. Trucks, H. B. Schlegel, G. E. Scuseria, M. A. Robb, J. R. Cheeseman, G. Scalmani, V. Barone, B. Mennucci, G. A. Petersson, H. Nakatsuji, M. Caricato, X. Li, H. P. Hratchian, A. F. Izmaylov, J. Bloino, G. Zheng, J. L. Sonnenberg, M. Hada, M. Ehara, K. Toyota, R. Fukuda, J. Hasegawa, M. Ishida, T. Nakajima, Y. Honda, O. Kitao, H. Nakai, T. Vreven, J. A. Montgomery, Jr., J. E. Peralta, F. Ogliaro, M. Bearpark, J. J. Heyd, E. Brothers, K. N. Kudin, V. N. Staroverov, R. Kobayashi, J. Normand, K. Raghavachari, A. Rendell, J. C. Burant, S. S. Iyengar, J. Tomasi, M. Cossi, N. Rega, J. M. Millam, M. Klene, J. E. Knox, J. B. Cross, V. Bakken, C. Adamo, J. Jaramillo, R. Gomperts, R. E. Stratmann, O. Yazyev, A. J. Austin, R. Cammi, C. Pomelli, J. W. Ochterski, R. L. Martin, K. Morokuma, V. G. Zakrzewski, G. A. Voth, P. Salvador, J. J. Dannenberg, S. Dapprich, A. D. Daniels, Ö. Farkas, J. B. Foresman, J. V. Ortiz, J. Cioslowski, and D. J. Fox. "Gaussian09 Revision E.01". Gaussian Inc. Wallingford CT (2009).

[388] J. H. D. Eland, R. Frey, A. Kuestler, H. Schulte, and B. Brehm. "Unimolecular dissociations and internal conversions of methyl halide ions". *Int. J. Mass Spectrom.*, **22**(1):155, (1976).

[389] T. N Olney, G. Cooper, and C. E. Brion. "Quantitative studies of the photoabsorption (4.5-488 eV) and photoionization (9-59.5 eV) of methyl iodide using dipole electron impact techniques". *Chem. Phys.*, **232**(1):211, (1998).

[390] M. Pernpointner, J. P. Zobel, E. Fasshauer, and A. N. Sil. "Spin–orbit effects, electronic decay and breakdown phenomena in the photoelectron spectra of iodomethane". *Chem. Phys.*, **407**:39, (2012).

[391] R. Forbes, A. De Fanis, C. Bomme, D. Rolles, S. T. Pratt, I. Powis, N. A. Besley, S. Nandi, C. Nicolas, J. D. Bozek, J. G. Underwood, and D. M. P. Holland. "Auger electron angular distributions following excitation or ionization of the I 3d level in methyl iodide". *J. Chem. Phys.*, **149**(9):094304, (2018).

[392] Yihan Shao *et al.* "Advances in molecular quantum chemistry contained in the Q-Chem 4 program package". *Mol. Phys.*, **113**(2):184, (2015).

[393] P. J. Stephens, F. J. Devlin, C. F. Chabalowski, and M. J. Frisch. "Ab initio calculation of vibrational absorption and circular dichroism spectra using density functional force fields". *J. Phys. Chem.*, **98**(45):11623, (1994).

[394] A. T. B. Gilbert, N. A. Besley, and P. M. W. Gill. "Self-consistent field calculations of excited states using the maximum overlap method (MOM)". *J. Phys. Chem. A*, **112**(50):13164, (2008).

[395] B. Kammerling, V. Schmidt, W. Mehlhorn, W. B. Peatman, F. Schaefers, and T. Schroeter. "Auger decay parameters α_2 for krypton $M_{4,5}$-$N_{2,3}$-$N_{2,3}$ transitions". *J. Phys. B: At., Mol. Opt. Phys.*, **22**(20):597, (1989).

[396] S. M. Bellm, J. A. Davies, P. T. Whiteside, J. Guo, I. Powis, and K. L. Reid. "An unusual π^* shape resonance in the near-threshold photoionization of S_1 para-difluorobenzene". *J. Chem. Phys.*, **122**(22):224306, (2005).

[397] O. Chalus, P. K. Bates, M. Smolarski, and J. Biegert. "Mid-IR short-pulse OPCPA with micro-Joule energy at 100kHz". *Opt. Express*, **17**(5):3587, (2009).

[398] J. Ullrich, R. Moshammer, A. Dorn, R. Dörner, L. Ph. H. Schmidt, and H. Schmidt-Böcking. "Recoil-ion and electron momentum spectroscopy: reaction-microscopes". *Rep. Prog. Phys*, **66**(9):1463, (2003).

[399] B. G. Levine, J. D. Coe, A. M. Virshup, and T. J. Martinez. "Implementation of *ab initio* multiple spawning in the Molpro quantum chemistry package". *Chem. Phys.*, **347**(1):3, (2008). Ultrafast Photoinduced Processes in Polyatomic Molecules.

[400] H.-D. Meyer, U. Manthe, and L. S. Cederbaum. "The multi-configurational time-dependent Hartree approach". *Chem. Phys. Lett.*, **165**(1):73, (1990).

[401] M. Beutler, M. Ghotbi, and F. Noack. "Generation of intense sub-20-fs vacuum ultraviolet pulses compressed by material dispersion". *Opt. Lett.*, **36**(19):3726, (2011).

[402] P. Zuo, T. Fuji, and T. Suzuki. "Spectral phase transfer to ultrashort UV pulses through four-wave mixing". *Opt. Express*, **18**(15):16183, (2010).

[403] M. Ghotbi, P. Trabs, M. Beutler, and F. Noack. "Generation of tunable sub-45 femtosecond pulses by noncollinear four-wave mixing". *Opt. Lett.*, **38**(4):486, (2013).

[404] J. P. Marangos, N. Shen, H. Ma, M. H. R. Hutchinson, and J. P. Connerade. "Broadly tunable vacuum-ultraviolet radiation source employing resonant enhanced sum–difference frequency mixing in krypton". *J. Opt. Soc. Am. B*, **7**(7):1254, (1990).

[405] P. St. J. Russell, P. Hölzer, W. Chang, A. Abdolvand, and J. C. Travers. "Hollow-core photonic crystal fibres for gas-based nonlinear optics". *Nat. Photon.*, **8**:278, (2014).

[406] A. Ermolov, H. Valtna-Lukner, J. C. Travers, and P. St. J. Russell. "Characterization of few-fs deep-UV dispersive waves by ultra-broadband transient-grating XFROG". *Opt. Lett.*, **41**(23):5535, (2016).

[407] A. Ermolov, K. F. Mak, M. H. Frosz, J. C. Travers, and P. St. J. Russell. "Supercontinuum generation in the vacuum ultraviolet through dispersive-wave and soliton-plasma interaction in a noble-gas-filled hollow-core photonic crystal fiber". *Phys. Rev. A*, **92**:033821, (2015).

[408] P. Trabs, H. Ritze, and F. Noack. "Generation of 800 nJ, 133 nm femtosecond vacuum UV pulses by third harmonic generation in argon". In *2016 Conference on Lasers and Electro-Optics (CLEO)*, pages 1–2, (2016).

[409] R. Forbes, V. Makhija, J. G. Underwood, A. Stolow, I. Wilkinson, P. Hockett, and R. Lausten. "Quantum-beat photoelectron-imaging spectroscopy of Xe in the VUV". *Phys. Rev. A*, **97**, (2018).

[410] S. Adachi, T. Horio, and T. Suzuki. "Generation of intense single-order harmonic pulse in the vacuum ultraviolet region using a deep ultraviolet driving laser". *Opt. Lett.*, **37**(11):2118, (2012).

[411] S. Adachi, H. Kohguchi, and T. Suzuki. "Unravelling the electronic state of NO_2 product in ultrafast photodissociation of nitromethane". *J. Phys. Chem. Lett.*, **9**(2):270, (2018).

[412] A.P. Hitchcock and C.E. Brion. "K-shell excitation spectra of CO, N_2 and O_2". *J. Electron. Spectrosc. Relat. Phenom.*, **18**(1):1, (1980).

[413] A. R. Attar, A. Bhattacherjee, and S. R. Leone. "Direct Observation of the Transition-State Region in the Photodissociation of CH_3I by Femtosecond

Extreme Ultraviolet Transient Absorption Spectroscopy". *J. Phys. Chem. Lett.*, **6**(24):5072, (2015).

[414] L. Drescher, M. C. E. Galbraith, G. Reitsma, J. Dura, N. Zhavoronkov, S. Patchkovskii, M. J. J. Vrakking, and J. Mikosch. "XUV transient absorption spectroscopy of iodomethane and iodobenzene photodissociation". *J. Chem. Phys.*, **145**(1):011101, (2016).

[415] K. F. Lee, D. M. Villeneuve, P. B. Corkum, A. Stolow, and J. G. Underwood. "Field-free three-dimensional alignment of polyatomic molecules". *Phys. Rev. Lett.*, **97**:173001, (2006).

[416] A. Rouzée, S. Guérin, O. Faucher, and B. Lavorel. "Field-free molecular alignment of asymmetric top molecules using elliptically polarized laser pulses". *Phys. Rev. A*, **77**:043412, (2008).

[417] X. Ren, V. Makhija, and V. Kumarappan. "Multipulse three-dimensional alignment of asymmetric top molecules". *Phys. Rev. Lett.*, **112**:173602, (2014).

[418] The voigt profile. `https://scipython.com/book/chapter-8-scipy/examples/the-voigt-profile/`.